Doctoral Dissertation
Doctoral Program in Metrology (38th cycle)

Innovations in Transition-Edge Sensors as superconductive single-particle detectors

By

Hobey Garrone

******

Supervisor(s):
Dr. M. Rajteri, Supervisor
Dr. E. Monticone, Co-Supervisor

Doctoral Examination Committee:
Prof. Loredana Parlato , Referee, University of Naples Federico II
Dott. Emanuele Taralli, Referee, SRON-Netherlands Institute for Space Research

Politecnico di Torino
2025

Declaration

I hereby declare that, the contents and organization of this dissertation constitute my own original work and does not compromise in any way the rights of third parties, including those relating to the security of personal data.

Hobey Garrone
2025

* This dissertation is presented in partial fulfillment of the requirements for **Ph.D. degree** in the Graduate School of Politecnico di Torino (ScuDo).

To all those who have taught me and helped me grow. Your guidance and support have been invaluable. This work is a testament to your influence and generosity. Thank you.

Abstract

This thesis presents a comprehensive study on Transition-Edge Sensors (TESs), superconducting detectors with single-particle sensitivity, focusing on their design, fabrication, modeling, and optimization for both photon and electron detection.

The introductory chapter outlines the operational principles of TESs, introducing the electro-thermal feedback model and the physics governing the superconducting transition, including the two-fluid and weak-link models. A comparative analysis of the main superconducting photon detectors—TESs, Kinetic Inductance Detectors (KIDs) and Superconducting Nanowire Single-Photon Detectors (SNSPDs) concludes the chapter, contextualizing the specific advantages of TES technology.

Chapter 2 details the microfabrication processes developed for TES devices, focusing on the core steps of photolithography, thin-film deposition and patterning. The experimental setups for morphological, electrical and optical characterization are also described.

In Chapter 3, the research addresses the development of fast-response detectors within the framework of the SEQUME project. Aluminum-based TESs are investigated for their high-speed potential, highlighting challenges related to fabrication reproducibility. To effectively accelerate the thermal response, the integration of lateral gold banks on standard TiAu TESs is explored. The results demonstrate that this geometric modification significantly reduces the recovery time to the order of hundreds of nanoseconds.

Chapter 4 presents a preliminary study on the application of TESs for single-electron detection within the PTOLEMY project context. The challenges related to scattered and secondary electron (SE) emission and backscattering are discussed, with kinematic estimates suggesting that time-of-flight are very fast compared to the detector response and do not allow discrimination of the SEs from their primary electron. Simplified geometrical considerations are then applied to modeling the

collection probability of scattered electrons, offering initial design guidelines to improve efficiency.

In Chapter 5, the longitudinal proximity effect induced by the wiring on the TES bilayer is investigated. Systematic measurements of the critical temperature (T_C) and transition width (ΔT_C) are conducted on strips with varying lengths and wiring materials (Nb, Ti, Al). The study evaluates different configurations, including the use of a top Titanium layer, which is shown to effectively suppress the longitudinal proximity effect.

Chapter 6 addresses the enhancement of photon detection efficiency. Anti-reflection (AR) coatings fabricated achieve measured efficiencies up to 85%. Furthermore, the potential of plasmonic metasurfaces is explored as an alternative absorption strategy; numerical simulations of optical micrometric gratings are presented alongside ellipsometric characterization of test structures with reflectivities as low as 5%.

Supplementary material, including the fundamental theory on superconductivity, SQUIDS and detailed fabrication and measurement procedures, is provided in the Appendices. This work contributes to the technological advancement of TESs at INRiM, pushing the boundaries of high-efficiency single-particle detection and temporal resolution necessary for quantum technologies and fundamental physics experiments.

Contents

List of Figures

List of Tables

Chapter 1

Concepts

The research presented here represents a direct continuation of the activity initiated during my Master thesis [1]; consequently, this chapter incorporates material originally developed in that context.

This thesis presents a comprehensive study on Transition-Edge Sensors (TESs), superconducting detectors with single-particle sensitivity. The work focuses on their design, fabrication, modeling, and optimization for both photon and electron detection. In this introductory chapter, we outline the fundamental principles of the electro-thermal model of TESs and compare them with other superconducting single-photon detectors.

1.1 Transition-Edge Sensor

TES devices consist of at least one superconducting material. However, to tune its critical temperature it is possible to add another layer of a normal material, in order to exploit the proximity effect explained in App. A. These layers, or films, for the TES devices discussed in this thesis, have thicknesses of a few tens of nanometers and areas from $20 \times 20\,\mu\text{m}^2$ to $60 \times 60\,\mu\text{m}^2$. The TES is operated at temperatures and currents corresponding to a point in the transition region of the superconducting material's phase diagram. When biased at an operating point, with resistance R_0 set at a certain percentage of the normal resistance R_n, small temperature variations cause large changes in resistance, making a TES work as a transducer and an amplifier. An incident photon with energy E_γ will cause a temperature increase:

$$\Delta T = \frac{E_\gamma}{C}, \tag{1.1}$$

where C is the heat capacity of the TES.

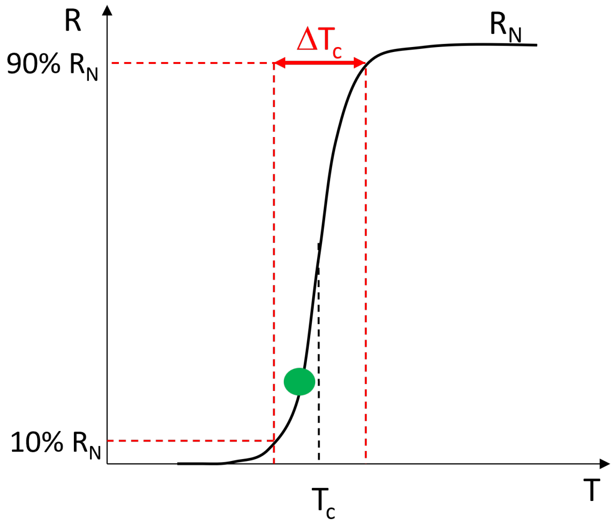

Fig. 1.1 TES phase transition showing how the electrical resistance change rapidly with small variation of its temperature near the working point (green dot).

1.1.1 Electro-Thermal Model

As proposed by Hilton and Irwin [2], TES devices are voltage-biased by placing a shunt resistance R_{sh} (or R_{bias}) in parallel with the detector and biasing the circuit with a constant current. Crucially, the condition $R_{\text{sh}} \ll R_{\text{TES}}$ must be satisfied to ensure a stiff voltage bias across the TES. The detector branch also contains a parasitic resistance R_{par} and an inductance L, through which the TES current I_{TES} flows. This inductance is magnetically coupled to a DC-biased SQUID operating in FLL mode. This configuration allows temperature variations ΔT to translate into resistance variations ΔR, which then induce current variations ΔI in the TES branch. Finally, these variations are measured as output voltage changes:

$$\Delta V_{\text{out}} = G_{\text{SQUID}} \Delta I. \tag{1.2}$$

This setup is illustrated in the circuit diagram in Fig. 1.2.

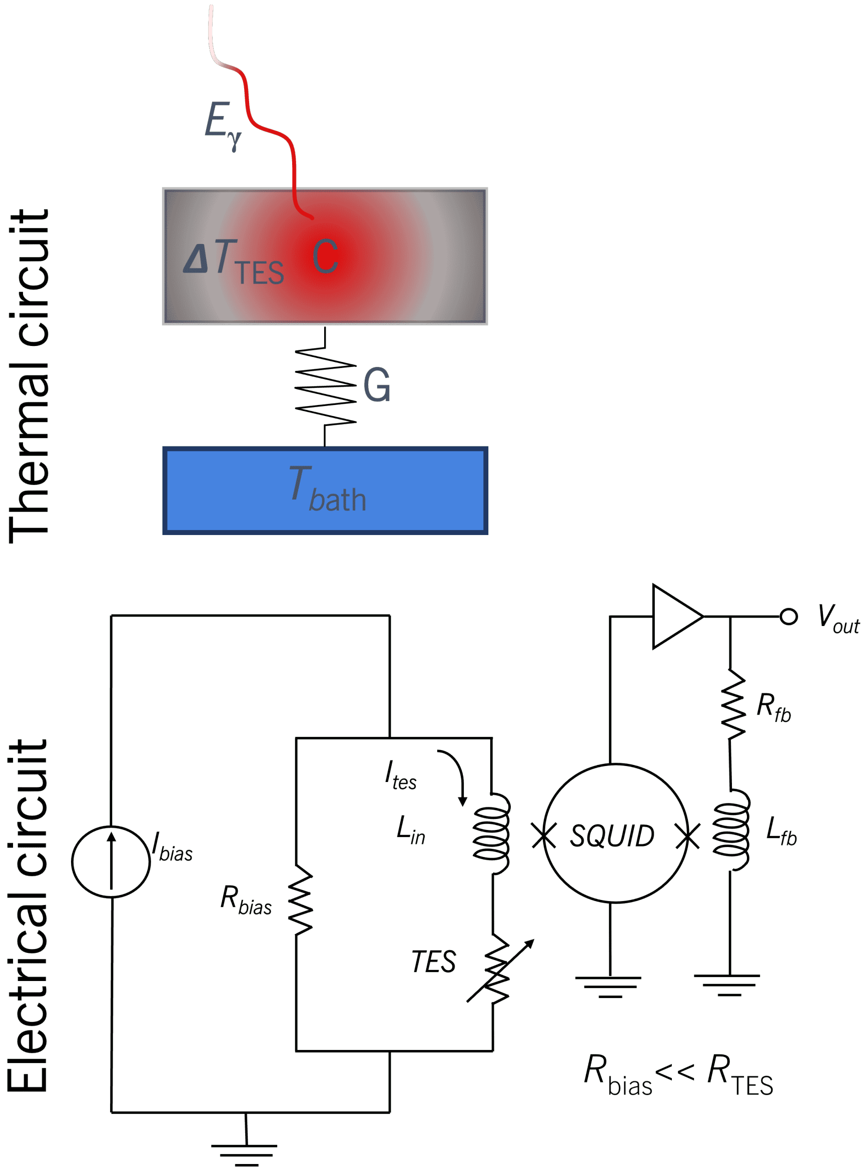

Fig. 1.2 TES operating configuration proposed by Irwin and Hilton.

The primary advantage of this configuration is the electro-thermal feedback (ETF), which allows for faster device response.

Electro-Thermal Feedback Mechanism

The fundamental operating principle of a voltage-biased TES is the negative Electro-Thermal Feedback (ETF). This mechanism exploits the steep dependence of resistance on temperature to stabilize the detector and speed up its response. Since the TES is biased with a constant voltage $V_{\mathrm{TES}} \approx V_{\mathrm{th}}$ (thanks to the condition $R_{\mathrm{sh}} \ll R_{\mathrm{TES}}$), the Joule power dissipated in the film is given by:

$$P_J = \frac{V_{\mathrm{TES}}^2}{R(T)}. \tag{1.3}$$

When energy (e.g., a photon) is absorbed, the electron temperature T increases. Since the device is in the superconducting transition, this leads to a sharp increase in resistance $R(T)$. Consequently, the Joule heating power P_J decreases. This reduction in electrical power creates a net cooling effect that counteracts the initial temperature rise, restoring the equilibrium conditions much faster than the natural thermal relaxation of the system.

This feedback provides two main advantages:

1. **Linearization and Stability:** The ETF maintains the TES at the working point on the transition edge, self-regulating against small drifts in the bath temperature.

2. **Fast Response:** The feedback reduces the effective thermal time constant of the detector. While the intrinsic thermal relaxation time is $\tau = C/G$, the effective response time becomes:

   $$\tau_{\mathrm{eff}} \approx \frac{\tau}{1+\mathscr{L}}, \tag{1.4}$$

   where $\mathscr{L}$ is the loop gain, a parameter quantifying the strength of the feedback, defined as:

   $$\mathscr{L} = \frac{\alpha P_{J0}}{GT_0}. \tag{1.5}$$

For $\mathscr{L} \gg 1$, the detector is significantly faster than its intrinsic thermal limit, enabling higher count rates.

In addition to the electrical circuit, the TES is embedded within a thermal circuit. The physical parameters involved include an input thermal power P_x from incident photons, the TES heat capacity C, the TES thermal conductance G, the power transferred from the TES to the thermal bath P_C, and the temperatures of the TES (T_{TES}) and the bath (T_{bath}). The transition to the superconducting state does not alter the lattice-specific heat, which remains $c_{\mathrm{ph}} = \beta T^3$, where β is a parameter unchanged by the superconducting transition. However, there is a variation in the electronic specific heat. The transition is second-order, meaning that latent heat is not involved. From BCS theory, the jump in specific heat is given by:

$$\Delta c_e = 1.43 \cdot \gamma T_{\mathrm{c}}, \tag{1.6}$$

and the electronic heat capacity decreases in the superconducting state following:

$$c_e \propto e^{-b\frac{T_{\mathrm{c}}}{T}}, \tag{1.7}$$

as reported in [3]. When operating at the critical temperature T_{c}, the total heat capacity is given by:

$$C = C_{\mathrm{ph}} + C_e \approx C_e, \tag{1.8}$$

since heat capacities are proportional to their respective specific heats. Additionally, phonons are assumed to have an energy equivalent to the thermal bath energy, meaning that there is no heat exchange between the phonon gas and the bath. The thermal conductance G considered is the one between electrons and phonons within the TES itself. To describe the entire system, we use the Thevenin equivalent circuit in voltage biasing mode, allowing us to write the coupled equations governing the system. The Thevenin equivalent components are:

$$V_{\mathrm{th}} = I_{\mathrm{bias}} R_{\mathrm{bias}}, \quad R_{\mathrm{th}} = R_{\mathrm{bias}} + R_{\mathrm{par}}. \tag{1.9}$$

From which the coupled equations are derived:

$$\begin{cases} L\frac{dI}{dt} = V_{\mathrm{th}} - IR_{\mathrm{th}} - IR_{\mathrm{TES}}, \\ C\frac{dT}{dt} = P_x + P_J - P_{\mathrm{bath}}. \end{cases} \tag{1.10}$$

These equations contain nonlinear terms that complicate their solution. However, they can be linearized under small-signal approximation around steady-state values $R_{\mathrm{TES}} \to R_0$, $T \to T_0$, and $I \to I_0$. The detailed derivations of the equations presented in this section can be found in Irwin's chapter [4]. The final results of the analysis include the exponential decay of current and temperature variations, the signal rise and fall times, the energy resolution, and the saturation energy. The solutions describing exponential decays are given by:

$$\Delta T(t) = \frac{\varepsilon E_\gamma}{C} e^{-\frac{t}{\tau_{\mathrm{etf}}}}. \tag{1.11}$$

Using this expression, the current variation is found as:

$$\Delta I(t) = -I_0 \alpha \frac{\Delta T(t)}{T} = -\Delta I_0 e^{-\frac{t}{\tau_{\mathrm{etf}}}}. \tag{1.12}$$

Solving instead with the variable transformation approach used by Linderman in [2], we obtain:

$$\delta I(t) \propto \left(e^{-\frac{t}{\tau_+}} - e^{-\frac{t}{\tau_-}} \right), \tag{1.13}$$

where τ_+ is the signal rise time and τ_- is the recovery time. If the inductance L is sufficiently small, making $\tau_+ \ll \tau_-$, a condition observed experimentally in the TES devices analyzed in this thesis, we obtain:

$$\tau_+ \to \tau_{\mathrm{el}} = \frac{L}{R_{\mathrm{th}} + R_0(1+\beta_I)}, \tag{1.14}$$

$$\tau_- \to \tau_{\mathrm{etf}} = \tau \frac{1 + \beta_I + \frac{R_{\mathrm{th}}}{R_0}}{1 + \beta_I + \frac{R_{\mathrm{th}}}{R_0} + (1 - \frac{R_{\mathrm{th}}}{R_0})\mathscr{L}}. \tag{1.15}$$

Here, the loop gain $\mathscr{L}$ is an important parameter in determining the response dynamics of the TES. It is defined as:

$$\mathscr{L} \equiv \frac{P_{J0}\alpha}{GT_0}, \tag{1.16}$$

We can write τ_{etf} in a way to explicit only measurable values as:

$$\tau_{\text{etf}} \sim \left[\tau^{-1} + \frac{i_0^2 R_0}{E_{\text{sat}}} \frac{1 - \frac{R_{\text{th}}}{R_0}}{1 + \frac{R_{\text{th}}}{R_0}} \right]^{-1}, \tag{1.17}$$

where E_{sat} will be explained in the next section.

1.1.2 Energy resolution and saturation energy

The energy resolution ΔE_{FWHM} is one of the most important figures of merit for TES devices, as it determines the ability to resolve the number of photons or, more precisely, the energy corresponding to a given number of photons. Given that a TES operates as a calorimeter, in a first approximation it is possible to assume a Gaussian noise distribution and express the resolution as:

$$\Delta E_{\text{FWHM}} = 2\sqrt{2\ln 2} \left[\int_0^\infty \frac{4}{S_{P_{\text{tot}}}(f)} df \right]^{-1/2}, \tag{1.18}$$

where f denotes frequency and $S_{P_{\text{tot}}}$ is the sum of all spectral power density (PSD) contributions. The more rigorous approach used in this thesis is necessary when nonlinear elements are present. The power spectral density of a resistance subject to voltage noise follows:

$$S_V = 4k_{\text{B}}TR, \tag{1.19}$$

where R accounts for all series or parallel resistances in the Thevenin equivalent circuit. In the non-linear approach, noise is determined under the assumption that the system remains close to equilibrium, but β_I and R_0 are stationary with bias current I_0. For noise components associated with resistances in the circuit, the PSD linked to the load resistance R_{th} remains unchanged:

$$S_{V_{\text{th}}} = 4k_{\text{B}}T_0R_{\text{th}}, \tag{1.20}$$

while the TES resistance contribution becomes:

$$S_{V_{\text{TES}}} = 4k_{\text{B}}T_0R_0\zeta(I), \tag{1.21}$$

where the dimensionless factor $\zeta(I)$ accounts for the deviation from standard Johnson noise due to the non-linear nature of the superconducting transition.

The thermal fluctuation noise is given by:

$$S_{P_{\text{TFN}}} = 4k_{\text{B}}T_0^2 \cdot F(T_0, T_{\text{bath}}), \tag{1.22}$$

where $F(T_0, T_{\text{bath}})$ accounts for thermal dissipation properties. The final energy resolution expression contains all this terms and is written in [4], combined with the Joule heating power at equilibrium P_{J0}, the thermal conductance between the TES and the thermal bath G, the equilibrium temperature T_0 and the loop gain Eq. 1.16 that quantifies the strength of the electrothermal feedback (ETF) mechanism (which stabilizes the TES by reducing temperature variations through self-regulation). The energy resolution ΔE_{FWHM} defines the ability of the TES to resolve different photon numbers or the corresponding deposited energy. While the complete derivation with the noise terms in [4] provide a detailed understanding, a sufficiently accurate formula for practical purposes is:

$$\Delta E_{\text{FWHM}} \simeq 7\sqrt{k_{\text{B}}E_{\text{sat}}T_{\text{c}}\sqrt{(1+2\beta)(1+M^2)}}, \tag{1.23}$$

where the term $(1+M^2)$ represents the excess noise. In our typical operation conditions, we empirically find $M \approx 3$. While historically treated as an unexplained noise component, recent studies suggest that this excess noise can be physically explained by internal thermal fluctuations arising from finite thermal conductance effects within the sensor itself (e.g. within the bilayer) [5].

E_{sat} is the saturation energy, the energy beyond which the TES can no longer discriminate photon numbers using the same method applicable at lower energies. An approximate expression for the saturation energy is given by:

$$E_{\text{sat}} \sim \frac{CT_0}{\alpha_I}, \tag{1.24}$$

Finally, the parameters α and β describe the sensitivity of the TES resistance to changes in temperature and current, respectively. They are defined as:

$$\alpha_I \equiv \frac{T_0}{R_0}\left(\frac{\partial R}{\partial T}\right)_{I_0}, \tag{1.25}$$

$$\beta_I \equiv \frac{I_0}{R_0}\left(\frac{\partial R}{\partial I}\right)_{T_0}. \tag{1.26}$$

Here, R_0 is the TES resistance at the operating point, T_0 is the equilibrium temperature, and I_0 is the operating bias current. The parameter α_I quantifies how much the resistance changes with temperature, and β_I quantifies the dependence of resistance on current. Additionally, it is worthwhile to note the proportionality between energy resolution, TES area, and critical temperature follows:

$$\Delta E_{\mathrm{FWHM}} \propto \sqrt{k^{-1} A T_{\mathrm{c}}^3}. \tag{1.27}$$

Here, A is the active area of the TES and we have the quality factor from [6]:

$$k = \frac{\alpha}{\sqrt{1+2\beta}}. \tag{1.28}$$

The parameter k, together with the excess noise M, serves as an indicator of the intrinsic quality of a TES, independent of its physical dimensions and critical temperature. This allows for a meaningful comparison between TES devices with different areas and T_{c} values, ensuring that their performance is evaluated on a normalized basis. While, the proportionality of the saturation energy is

$$E_{\mathrm{sat}} \propto A T_{\mathrm{c}}^2. \tag{1.29}$$

1.2 Modelling

1.2.1 Two-Fluid Model

To describe the dependence of resistance R on temperature T and current I, the two-fluid model is often employed. This model, proposed by Irwin et al. [7], is physically justified by the Phase Slip Line (PSL) theory. To understand the physical origin of these resistive features, it is useful to recall the distinction between superconducting classes. Unlike Type I superconductors, which completely expel magnetic flux up to a critical field (Meissner effect), Type II superconductors allow magnetic flux to penetrate the material in the form of quantized vortices above a lower critical field $H_{\mathrm{c}1}$. In the 2D thin-film limit, typical of TES devices, the resistive transition is governed by the dynamics of these vortices. Specifically, the unbinding and motion of vortex-antivortex pairs across the superconductor generate phase slips, leading to energy dissipation.

Based on this phenomenology, the model treats the current as flowing through two parallel channels: a superconducting channel and a normal one. The resulting resistance in the transition region can be expressed phenomenologically as:

$$R(I,T) = c_R R_{\mathrm{N}} \left(1 - c_I \frac{I_{\mathrm{c}}(T)}{I}\right), \tag{1.30}$$

where R_{N} is the normal-state resistance, $I_{\mathrm{c}}(T)$ is the critical current (often approximated by the Ginzburg-Landau power law), and c_R, c_I are parameters related to the normal and superconducting conduction channels. From this constitutive equation, the sensitivity parameters α_I and β_I essential for detector characterization can be derived. Specifically, experimental works [8] have shown that α_I scales with the current ratio as:

$$\alpha_I \propto \left(\frac{I_{\mathrm{c}0}}{I_0}\right)^{2/3}. \tag{1.31}$$

This model provides a useful framework for fitting transition shapes and understanding the trade-off between transition sharpness and current dependence.

1.2.2 Weak Link Model

An alternative description treats the TES as a weak link, where the superconducting properties are suppressed by the proximity effect from the leads. In this scenario, the device behaves similarly to a long SNS (Superconductor-Normal-Superconductor) junction. Assuming the Resistively Shunted Junction (RSJ) limit, the resistance for currents $I > I_\mathrm{c}$ can be described by:

$$R(T,I) = R_\mathrm{N}\sqrt{1-\left(\frac{I_\mathrm{c}(T)}{I}\right)^2}. \tag{1.32}$$

This model predicts different constraints for the detector sensitivities compared to the two-fluid model. In the limit of a long junction, it implies a specific relationship between the logarithmic sensitivities:

$$\beta_I = \frac{R_\mathrm{N}^2}{R^2} - 1. \tag{1.33}$$

Both models serve as limiting cases or fitting functions to describe the resistive transition of real devices, depending on the specific geometry and material properties (e.g., dirty vs. clean limit, strength of proximity effect).

1.2.3 Mapping of α and β

The models presented above doesn't fit any TESs. In particular, in our case, neither a combination of the two-fluid and weak-link model explain the behavior of this 2 fundamental parameters α_I and β_I. [6] reveal that while the overall current-voltage characteristics appear smooth, subtle oscillations are present. These fine features, which are amplified in the derived quantities α_I and β_I, indicate that the conventional models miss key details. Notably, variations in the external magnetic field can produce significant effects, suggesting that interference phenomena are intrinsic to TES operation. However, this sensitivity strongly depends on the geometry of the TES; for small TESs or those with a high aspect ratio, the sensitivity to magnetic fields is actually quite poor within a range of $\pm 2\,\mu\mathrm{T}$ or even more [9]. Moreover, the observed fine structures are stable and reproducible—aside from high-voltage regions prone to instabilities—underscoring that they are inherent to the device physics rather than mere measurement artifacts. This high sensitivity implies that factors like spatial non-uniformities and self-field effects, typically neglected in simpler models, play a critical role. In essence, while the two-fluid and weak-link models provide a useful framework, Zhang's work highlights the need for more sophisticated approaches that incorporate these subtle, yet crucial, effects. Enhanced models accounting for these nuances will be vital for accurately predicting TES behavior and optimizing sensor design.

1.3 Superconducting Photon Detectors

Photon/particle detection is a fundamental requirement in a wide range of scientific and technological applications, from astrophysics and quantum information to biomedical imaging and optical communication. Traditional semiconductor-based photon detectors, such as silicon photodiodes and avalanche photodiodes (APDs), operate at room temperature and provide satisfactory performance in many scenarios. However, these devices suffer from fundamental limitations in terms of noise, timing jitter, and sensitivity at low photon fluxes. Superconducting photon detectors, including Transition Edge Sensors (TESs), Kinetic Inductance Detectors (KIDs), and Superconducting Nanowire Single-Photon Detectors (SNSPDs), have emerged as promising alternatives due to their unique operating principles and extreme sensitivity. Despite requiring cryogenic cooling, modern refrigeration techniques, such as closed-cycle cryostats, have made superconducting detectors increasingly practical for laboratory and field applications. Their unique combination of ultra-low noise, high efficiency, and high spectral resolution positions them as essential tools for advancing quantum optics, astronomical observations, and next-generation photon detection technologies.

1.3.1 TESs

As explained above, TESs are highly sensitive superconducting photon detectors that operate based on the sharp resistance transition between the normal and superconducting states. A TES consists of a thin superconducting film maintained at its critical temperature T_c, where small changes in absorbed energy E_γ cause resistance variation and measurable current $\Delta R, \Delta I$. The TES operates by being voltage-biased in the superconducting-to-normal transition region. When a photon with energy E_γ is absorbed, it causes a temperature increase given by:

$$\Delta T = \frac{E_\gamma}{C}, \tag{1.34}$$

which in turn produces a proportional resistance variation ΔR.

The TES is embedded in an electrothermal feedback loop, which stabilizes its temperature at T_c and allows precise measurements of absorbed photon energy. When a photon is absorbed, it increases the TES temperature, leading to a resistance change and so a current reduction that can be detected by a SQUID amplifier. Modern TESs have demonstrated exceptional performance across various applications:

- **Energy Resolution:** TESs have outstanding energy resolution, enabling photon-number resolution (PNR) in multiple wavelength ranges. In the X-ray regime, TESs have achieved energy resolutions as low as 0.9 eV at 1.5 keV [7], while in NIR regime TESs have achieved energy resolutions as low as 67 meV at 0.8 eV [10].
- **Photon Discrimination:** TESs are inherently capable of resolving individual photon events and determining the number of photons in a pulse due to their intrinsic energy resolution. This property makes them uniquely suited for applications requiring photon-number-resolving (PNR) capabilities, such as quantum optics and quantum information processing. In the near-infrared, TESs have been demonstrated to resolve up to 55 incident photons [11].
- **Response Time:** TESs have slower response times compared to SNSPDs, but faster than KIDs, typically in the range of $1 - 100\ \mu$s. However, their thermal response can be optimized by engineering the thermal conductance and heat capacity of the sensor reaching recovery times of about 186 ns–250 ns at 0.8 eV [12, 13].
- **Detection Efficiency:** TESs can have very high internal quantum efficiency, thanks to anti-reflective coatings. The system detection efficiency (SDE) can be above 95 % at 1550 nm and 98 % at 850 nm [14, 15].
- **Operating Temperature:** TESs require dilution refrigerators or ADR to maintain temperatures in a typical range around 20 mK and 300 mK, which

limits their portability and scalability for some applications. However, their unparalleled sensitivity justifies the need for cryogenic cooling in specialized fields.

- **Dark Count Rate:** Due to their extremely low operating temperatures and intrinsic detection mechanism, TESs have an exceptionally low dark count rate. Recent measurements have demonstrated intrinsic dark count rates below 4×10^{-4} Hz [16], making them comparable to or better than SNSPDs for ultra-low background applications.
- **Multiplexing Capability:** The multiplexing capability of TESs is primarily limited by the SQUID readout bandwidth. Modern TES arrays have been demonstrated with SQUID multiplexing techniques, allowing large-scale arrays to be read out efficiently. Currently, arrays with hundreds to thousands of pixels are successfully used in astrophysical applications, such as X-ray and Gamma-ray spectroscopy [7, 17]. However, for quantum optics applications, the fast response times required (MHz bandwidth) pose significant challenges for standard SQUID multiplexing, limiting current implementations to small-scale arrays. New researches are overcoming this limitation using Kinetic Inductance Current Sensors (KICS) instead of SQUIDs [18, 19].

In summary, TESs provide unmatched photon-number resolution and energy discrimination capabilities, making them ideal for applications requiring precise photon counting and energy measurement with extremely low noise and dark count rate. Their primary limitations are their moderately slow response times, the difficulty of multiplexing caused by the use of SQUIDs and the need for deep cryogenic cooling, but their superior energy resolution and high detection efficiency make them a powerful tool in quantum optics, astrophysics, and X-ray spectroscopy.

1.3.2 KIDs

Kinetic Inductance Detectors (KIDs) [20] are superconducting sensors that exploit changes in the kinetic inductance of a superconducting film when it absorbs energy. The KID is placed in a circuit with a capacitor, forming a resonant circuit. The kinetic inductance, L_k, of a KID is related to the density of Cooper pairs n_s as:

$$L_k \propto \frac{1}{n_s}, \tag{1.35}$$

A decrease in the density of Cooper pairs leads to an increase in the kinetic inductance. The resonant frequency f_0 of the resonator is given by

$$f_0 = \frac{1}{2\pi\sqrt{LC}}, \tag{1.36}$$

where $L = L_k + L_g$ is the total inductance, including both the kinetic inductance L_k and the geometric inductance L_g, and C, the capacitance of the resonator. When a photon is absorbed by the detector, its energy breaks Cooper pairs, thereby reducing n_s and increasing L_k. This change in kinetic inductance causes a fractional frequency shift in the resonator. This frequency shift is measured via a microwave readout line, providing a sensitive probe of the absorbed energy. Modern KIDs have demonstrated outstanding performance:

- **Energy Resolution:** Advanced KIDs can achieve energy resolutions on the order of $\sim$ 10–20 eV for x-ray applications and resolutions of $\Delta E < 5$ eV for single 6 keV photons as in [21]. In [22] an energy resolution of 0.17 eV at 808 nm is reported, while in [23] a resolution of 42 meV at 1545 nm has been obtained using SiN membranes.

- **Photon Discrimination:** As TESs, KIDs are capable of resolving individual photon events. Since the number of broken Cooper pairs is proportional to the absorbed energy, they can discriminate between multiple simultaneous photon events. For example, in [24] they resolved up to 7 photons per pulse.

- **Response Time:** The detectors exhibit intrinsic response times often around $\sim$ 1 ms for X-rays applications [25] and can have a timing resolution of $\sim 1\ \mu$s [26].

- **Detection Efficiency:** Recent advancements have led to significant improvements in the absorption efficiency of KIDs. In particular, a 61% detector efficiency at 500 nm was demonstrated in [27], where the application of a 54 nm SiN anti-reflective (AR) coating to the β-Ta inductor should theoretically enhance the absorption efficiency from $\sim$ 40% to $\sim$ 80% at 600 nm. The measured efficiency accounts for the absorption efficiency of the superconducting inductor, the effective fill factor of the absorber, and the lens coupling efficiency. Further enhancements are expected by implementing multi-layer optical stacks to achieve near-unity absorption.

- **Multiplexing Capability:** Arrays containing thousands of KIDs have been fabricated, enabling simultaneous readout of large numbers of detectors through a single microwave feedline [28]. This scalability makes KIDs especially attractive for applications in astronomical instrumentation and large-scale quantum experiments.
- **Operating Temperature:** These detectors operate at temperatures, typically between 100 mK up to some Kelvin.

In summary, KIDs convert photon-induced changes in the superconducting state into measurable shifts in the resonator's frequency. When photons are absorbed, they break Cooper pairs, reducing the Cooper pair density n_s, increasing the kinetic inductance L_k, and shifting the resonance frequency. With superior energy resolution, rapid response times, and the ability to integrate thousands of detectors in an array, KIDs represent a powerful and versatile technology for a wide range of applications, in particular in astrophysics.

1.3.3 SNSPD

Superconducting Nanowire Single-Photon Detectors (SNSPDs) [29] are superconducting detectors that rely on the formation of a resistive hotspot when a photon is absorbed by a thin nanowire biased close to its critical current. The SNSPD is typically designed as a meandering nanowire to maximize absorption while maintaining a high-speed response. The basic principle of SNSPD operation is as follows: A superconducting nanowire, biased just below its critical current I_c, carries a uniform supercurrent. When a photon with sufficient energy is absorbed, it disrupts local superconductivity, creating a resistive region known as a "hotspot." If the resulting redistribution of current leads to a local current density exceeding I_c, a voltage pulse is generated, marking the detection of a photon. The resistance change in an SNSPD can be described by a time-dependent resistance function $R(t)$, which follows the thermal relaxation dynamics of the hotspot. The recovery time τ_R of the detector is determined by the kinetic inductance L_k of the nanowire and the impedance of the readout circuit:

$$\tau_R = \frac{L_k}{Z}, \tag{1.37}$$

where Z is the characteristic impedance of the detection circuit. This parameter defines the reset time of the SNSPD, which impacts its maximum achievable count rate. SNSPD are already commercial detectors and performances in literature are the following:

- **Response Time:** The response time of SNSPDs is extremely fast, with timing jitter on the order of a few picoseconds [30], with timing jitter as low as 15 ps when using cryogenic amplifiers. Detectors in the same batch achieved sub-20 ps jitter and a timing resolution of 26 ps at 1425 nm with cryogenic amplification [31]. These properties make SNSPDs ideal for applications requiring high timing precision, such as quantum optics and time-correlated single-photon detection.

- **Detection Efficiency:** Recent advancements in SNSPDs have led to system detection efficiencies (SDE) exceeding 99.5 % at 1350 nm and 98 ± 2.07 % at 1425 nm [31]. The high efficiency is achieved through optimized NbTiN superconducting films with saturated internal efficiency, broadband membrane cavity coupling, and precise system efficiency calibration with narrow-linewidth tunable lasers.

- **Dark Count Rate:** SNSPDs exhibit dark count rates lower than semiconductor-based photon counters, in [32] has been obtained a dark count rate of ~ 6 μHz with SNSPDs. This make them well-suited for ultra-low-light applications [33] at temperatures around $2-3$ K. However, as clearly depicted in [34], high bias currents lead to better detection efficiencies, but also to higher dark counts rates. Then, low dark count rates are a trade off with detection efficiencies.

- **Spectral Range and MIR Performance:** While traditionally dominant in the near-infrared, SNSPD technology is rapidly expanding into the mid-infrared (MIR). Recent developments have demonstrated saturated internal detection efficiency at wavelengths up to 29 μm using WSi nanowires [35]. Furthermore, optimized NbTiN devices have achieved high system detection efficiencies

($> 70\%$) with high time resolution in the $2-4\ \mu$m window [36], opening new possibilities for molecular spectroscopy and sensing.

- **Operating Temperature:** Unlike TESs, which require temperatures below 500 mK, modern SNSPDs can achieve high efficiency and low jitter at temperatures between 2.5 K and 2.8 K. This compatibility with more compact closed-cycle cryostats simplifies integration into real-world applications, such as space-based photon detection and long-range optical communication [37].
- **Multiplexing Capability:** While SNSPDs are traditionally limited by the need for complex readout electronics, recent efforts in cryogenic CMOS electronics have enabled the multiplexing of large arrays of SNSPDs for single-photon imaging [38] reaching a single-photon camera of 400 k – pixels [39], where each pixel is an SNSPD. Future developments of large-scale detector arrays are rapidly evolving [40].

In summary, SNSPDs provide high-speed, high-efficiency single-photon detection. However, their cryogenic operating temperatures and trade-off between detection efficiency and dark counts are the only limiting factors for widespread deployment in certain applications. Their relatively small dark count respect to room temperature and comparable with TESs, with their only a posteriori PNR capability for arrays, operating temperature higher than the one necessary for TESs, low costs and commercial availability could be an advantage or disadvantage depending on the application.

1.3.4 SPD Comparison

In conclusion, SPDs (TESs, KIDs, and SNSPDs) offer unique advantages over traditional semiconductor-based detectors. A direct comparison of their key performance metrics is summarized in Table 1.1. Before discussing the values, it is important to clarify the distinction between related metrics. **Photon Number Resolving (PNR) vs. Sensitivity:** While all three detectors possess single-photon sensitivity (the ability to detect the arrival of a single quantum of light), PNR refers specifically to the capability of distinguishing the number of photons in a multi-photon pulse. TESs and KIDs are intrinsic PNR detectors due to their proportional energy response, whereas standard SNSPDs are binary ("click") detectors unless spatially or temporally multiplexed. **Response Time vs. Timing Jitter:** The temporal performance is defined by two distinct parameters. The *response time* (or recovery time and often the main contribution for the time resolution) indicates how fast the detector resets after a detection event, determining the maximum count rate. The *timing jitter* represents the uncertainty in determining the exact arrival time of the photon. As shown in the table, SNSPDs excel in both metrics, while TESs are significantly slower but offer superior energy resolution.

Table 1.1 Comparison of key performance metrics for Transition-Edge Sensors (TES), Kinetic Inductance Detectors (KID), and Superconducting Nanowire Single-Photon Detectors (SNSPD). Values represent the state-of-the-art reported in literature.

Metric	**TES**	**KID**	**SNSPD**
Energy Res.	67 meV @ 0.8 eV [10] 0.9 eV @ 1.5 keV [7]	42 meV @ 0.8 eV [23] 0.17 eV @ 1.5 eV [22]	–
PNR Capability	Up to 55 photons [11]	Up to 7 photons [24]	Up to 65 (arrays) [41]
Time Resolution	186–250 ns [12, 13]	$\sim 1\,\mu$s [26]	26 ps [31]
SDE	$> 95\%$ @ 1550 nm [14] 98% @ 850 nm [15]	61% @ 500 nm [27]	$> 99.5\%$ @ 1350 nm [31]
Dark Count	$< 4 \cdot 10^{-4}$ Hz [16]	–	$\sim 6\,\mu$Hz [32]
Multiplexing	Hundreds [7, 17]	Thousands	400 k – pixels [39]
Op. Temp.	20–300 mK	100 mK – 1 K	2.5–2.8 K

While no single detector type dominates in all metrics, the choice depends on the specific application. TESs are the reference for energy resolution and PNR, SNSPDs for timing and speed, and KIDs for large-scale multiplexing.

Chapter 2

Experimental set-up and fabrication processes

2.1 Fabrication

2.1.1 TES fabrication process

The fabrication of TESs is a multi-step process that requires micro-fabrication precision, material uniformity, and process reproducibility. This chapter describes the fabrication procedure used for TES devices at INRiM, from wafer preparation to the final device. The entire process was carried out at the QRLab facility of INRiM.

The TES basic fabrication loop requires the following steps and is depicted in Fig. 2.1:

- **Mask design:** This is the fundamental step required for any project, defining the TES, wiring, and overall chip geometry, along with other features like anti-reflective coatings and shields described later in the thesis.
- **Photoresist spin-coating:** This procedure covers the chip with photoresist, a removable polymeric material that can be patterned with a laser.
- **Positive photolithography:** The resist is treated with a Laser Writer or a mask and UV exposure, then chemically developed to remove the resist exposed

to UV, creating a pattern. The resist now covers the chip except where the material needs to be deposited.

- **Sputter etching:** The chip with resist is cleaned through ion bombardment to guarantee clean surfaces before deposition.
- **Deposition:** The desired thickness of the material is deposited on the chip in a UHV/HV chamber by evaporation or sputtering.
- **Lift-off:** The resist on the sample is chemically and physically removed. In this way, only the material adhering to the exposed surface remains, forming a patterned chip.
- **Iteration:** The previous steps are repeated for the wiring, anti-reflective coating, and any additional structures.

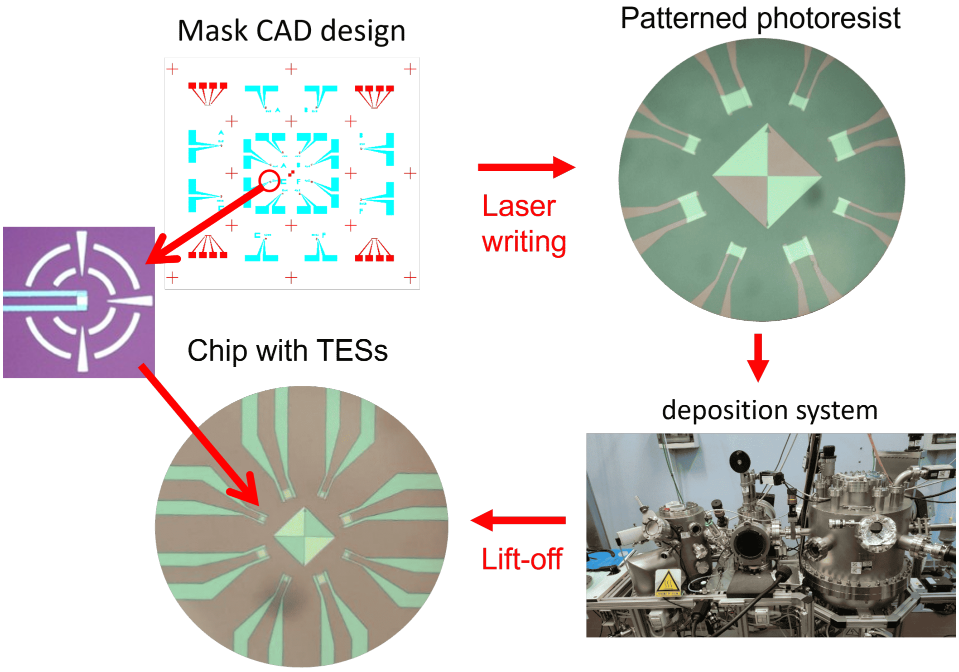

Fig. 2.1 Fabrication workflow. The first step is the design of a CAD file serving as the mask for the photolithographic process (red geometries for TES areas, blue for wirings). After spin-coating, laser writing, and development, the result is a patterned photoresist. The brighter areas are TiAu TES areas, while the grey-brown ones are "holes" in the photoresist ready for wiring deposition. Then, the desired materials are evaporated or sputtered, covering both the resist and the exposed areas. Finally, the lift-off process removes the photoresist, leaving the deposited materials only in the patterned areas.

Photoresist spin-coating

The process usually begins with a (2×2) cm^2 chip of Si (500 μm)/ SiO$_2$ (140 μm)/ SiN$_x$ (480 μm), which serves as the substrate.

The choice of SiN$_x$ is motivated by several factors:

- First, it allows for the fabrication of TESs on suspended membranes if required by the application.
- Second, since the fabrication process was originally established and optimized on this substrate, maintaining it ensures consistency and reproducibility.
- Third, the SiN$_x$ layer acts as a phonon barrier, attenuating phonons generated in the Silicon substrate by stray photons that do not land directly on the TES, thereby reducing the background noise contribution.

We clean the chip in the cleanroom via an ultrasonic bath. This cleaning method is based on the generation of high-frequency sound waves (typically in the range of $20-40$ kHz) in a liquid medium, such as acetone, ethanol, or isopropanol. These ultrasonic waves produce rapid pressure variations in the liquid, leading to the formation and collapse of microscopic bubbles due to cavitation. The implosion of these bubbles near the sample surface generates localized high-pressure jets that dislodge contaminants and particles without mechanical abrasion. The procedure consists of 5 min in acetone and another 5 min in ethanol, both at 40 °C at maximum power, followed by drying with a nitrogen gun before photoresist spin-coating. This step ensures the removal of organic residues, dust, and particulate matter, providing a clean and homogeneous surface for subsequent processing. After this initial step, we proceed with spin-coating. Photoresist is a light-sensitive polymeric material used in lithographic processes to form patterns on a substrate. When exposed to ultraviolet (UV) light or other forms of radiation through a photomask or with a laser writer, the photoresist undergoes chemical changes that alter its solubility in a developer solution. There are two main types of photoresists:

- **Positive photoresist:** The exposed regions become more soluble in the developer and are removed, leaving a pattern that replicates the mask.
- **Negative photoresist:** The exposed regions become less soluble due to cross-linking, and the unexposed regions are removed during development.

Photoresists are typically spin-coated onto substrates to form a uniform thin film. After exposure and development, the resulting patterned layer serves as a mask for etching or deposition processes, enabling precise control over micro-scale structures.

The spin-coating process (first images in Fig. 2.2) is a technique used to deposit uniform thin films of photoresist onto flat substrates. First, the photoresist is spun on the substrate and then baked. The spinning procedure involves dispensing a liquid-phase photoresist solution onto the center of a substrate and rapidly spinning it to spread the material evenly by centrifugal force. The final film thickness depends on several factors, including the spin speed and the viscosity of the resist, while the time influences the uniformity of the distribution.

In this work, we use Microchemicals GmbH AZ1505 positive photoresist, a commonly used material for fine-feature lithography. After the spinning step, the sample undergoes a soft bake on a hot plate to remove residual solvents and improve adhesion. This process results in a uniform resist film with a typical thickness of approximately 500 nm. For a thickness of approximately 1 μm with the same resist, we simply change the spin speed to 1000 rpm using the same recipe.

The process parameters are as follows:

- Spin speed: 4000 rpm
- Spin time: 30 s
- Bake temperature: 100 °C
- Bake time: 50 s

The coated substrate is then ready for UV exposure and subsequent development.

Photolithography and development

The lithographic process is performed using a Heidelberg μPG 101 (second images in Fig. 2.2), a micrometric-precise maskless laser writer for direct writing of photolithographic patterns. It employs a focused laser beam at a wavelength of 405 nm to expose a positive or negative photoresist, reproducing the design of a CAD file loaded from its software.

This technique is particularly valuable for flexible and rapid prototyping, as it eliminates the need for photomasks, reduces cost and time, and allows for pattern correction and iteration during development.

In the system, the substrate is mounted on a precision stage that moves in the xy plane. Through an air flux system, the laser can auto-focus on the chip and find its edges to automatically calculate the center. Once the design is loaded, the center found, and parameters set, writing can begin. The laser spot remains in a fixed position and is modulated (on/off) while the stage moves according to the pattern layout. Writing is performed by moving the stage in the x direction for a length equal to the distance between the outer geometries in the CAD, and then moving to the next line in the y direction. The resolution depends on the optimization of the overall process and can ideally reach 1 μm, while the precision is sub-micrometric. For the first lithography on the chip, these are the only steps required. For subsequent steps, it is necessary to load the chip in the same orientation as the first lithography and calculate the offset between the center found by the laser writer and the real center of the previous pattern, along with any rotation caused by manual loading. For these operations, the Heidelberg μPG 101 is equipped with a camera mounted above the movable stage, allowing the user to view the structures on the chip. For this reason, it is essential that at least the first lithographic CAD includes alignment markers to determine the chip's center and rotation, as shown in red in the first image of Fig. 2.1.

The key parameters of the writing process are:

- **Laser Power:** The exposure dose is controlled by adjusting the laser power, which must be optimized according to the resist type and thickness, feature dimensions, and substrate reflectivity. For our standard SiO_2-SiN_x(500 nm) substrates and 500 nm-thick AZ1505 resist, we use 4 mW for TES areas and 2 mW for wiring. For Si substrates, the power is halved. Small structures on the TES require $1-2$ mW. Conversely, with AZ1505 spun at 1000 rpm for large structures (e.g., the shield in Chapter 4), 7 mW is required.

- **Power Filter:** The Heidelberg μPG 101 is equipped with an optical filter to reduce the power below 1 mW, the laser's minimum selectable power. The percentage is selectable via software. For example, the plasmonic structures in Chapter 4 ($2-3$ μm on a highly reflective mirror) were lithographed with 1 mW and a 30% filter.

- **External Filter:** An additional manual lens filter can be placed in the beam path to halve the power.
- **Writing Time:** Depends only on the CAD dimensions (distance between the farthest geometries).
- **Resolution:** The μPG 101 can achieve feature sizes down to 1 μm or below, depending on the process optimization.

After UV exposure, the substrate undergoes a chemical process called "development". The AZ1505 photoresist undergoes a chemical modification in the regions where the laser beam has passed. Being a positive-tone photoresist, the exposed regions become more soluble in the developer solution (AZ Developer). Specifically, UV exposure breaks the chemical bonds of the photoactive compound within the resist, degrading the polymer chain in the exposed regions. Consequently, these areas become soluble in the alkaline AZ Developer, while the unexposed regions remain relatively insoluble.

During the development step (third images in Fig. 2.2), the sample is immersed in a diluted AZ Developer solution ($1:1$ with deionized water) for 20 s at room temperature and agitated manually to improve uniformity. A shorter time leads to incomplete development, while a longer time causes over-development, risking wider features and rough edges, or merging distinct patterns.

After development, the sample is rinsed in deionized water for 30 s to stop the reaction and remove residues, then dried with a nitrogen gun. Rinsing is performed in two separate beakers (15 s each) to minimize contamination. All beakers are cleaned with IPA, and a full dummy cycle is performed before the actual process. At this point, the chip is covered in patterned resist, ready for deposition.

Evaporation and lift-off

The patterned photoresist serves as a sacrificial mask defining the material deposition areas. Before deposition, the chip undergoes Oxygen Plasma Etching and Ion Milling. The plasma etching is described in Section B.1.2, and Ion Milling in Section B.1.3.

A thin metallic or dielectric layer is then deposited over the entire sample (fourth image in Fig. 2.2), covering both the substrate and the resist. Deposition uses

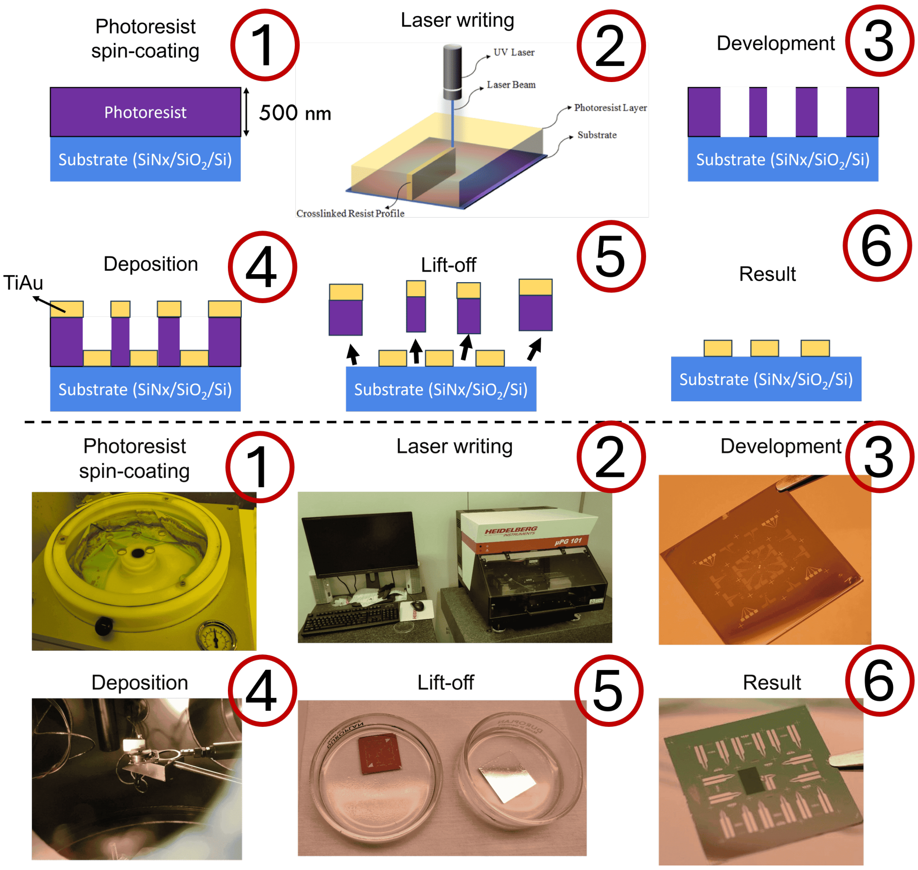

Fig. 2.2 Top: Scheme of the overall fabrication process sequence. Bottom: Images of real processes, results, or systems corresponding to the steps in the scheme.

techniques like e-beam or thermal evaporation to ensure directional flux and high-quality film growth. Details on the deposition systems are reported in Section B.1.4.

Following deposition, the lift-off process is performed by immersing the sample in acetone, which selectively dissolves the resist (Fig. 2.2). This removes the resist and the material atop it, leaving only the material in direct contact with the substrate. Ultrasonic agitation in an Ultrasonic Bath (UB) is used carefully to facilitate clean lift-off without damaging fine structures.

We follow these steps:

- **Soaking:** The sample soaks in acetone (fifth image in Fig. 2.2) to initiate resist degradation. Time ranges from minutes to overnight. A rinse typically removes large portions of weakened resist.
- **Pre-cleaning:** The lift-off beaker is cleaned with two UB steps (acetone then IPA) at 40°C for 5 minutes at full power.
- **Cleaning:** The sample undergoes the same procedure, but with UB power reduced to 50%.

This results in well-defined structures replicating the laser-written pattern (last images in Fig. 2.2). Edge quality, positioning precision, and interface cleanliness are crucial for well-behaved TESs, especially at small dimensions.

To investigate the edge profile—a critical factor for vortex entry and pinning mechanisms as discussed in Chapter 1—Scanning Electron Microscopy (SEM) imaging was performed on a (230×230) μm^2 square TES (Fig. 2.3). The electron micrographs, acquired at a 15° tilt and 350x magnification, reveal slight undulations along the edges of the superconducting strip and wiring. These imperfections are likely attributable to the photolithography or development limitations, indicating that further process refinement is required to achieve sharper edge definitions.

Other details can be found in App. B.1.

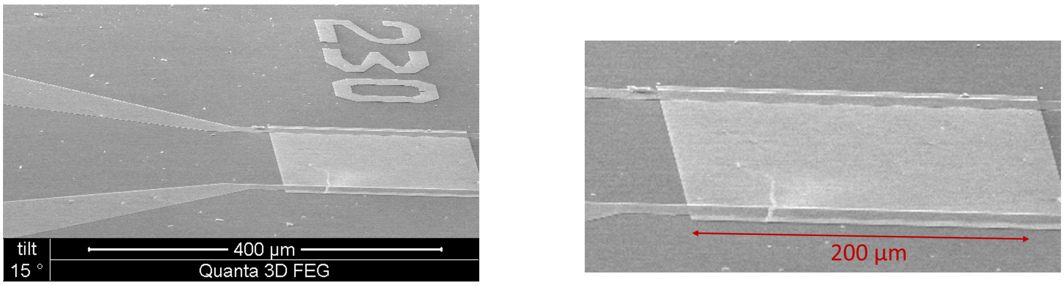

(a) Overview of the $(230 \times 230)\ \mu\text{m}^2$ TES.

(b) Digital zoom highlighting edge roughness.

Fig. 2.3 SEM characterization of a $(230 \times 230)\ \mu\text{m}^2$ TES acquired with a 15° tilt. (a) Overview of the device. (b) Detail of the edges showing slight waviness, likely resulting from the lithographic or development steps.

2.2 Characterization Set-up

2.2.1 Thickness measurements

AFM

We use a Park System NX20 Atomic Force Microscope (AFM) in non-contact mode. It maps surface morphology with nanometer resolution using a cantilever tip scanning at ~ 3 nm distance. Deflection due to van der Waals/electrostatic forces (Lennard-Jones potential, Fig. 2.4a) is measured via laser reflection (Fig. 2.4b) and kept constant by a feedback loop controlling a piezoelectric stage.

Vertical resolution is ~ 0.3 nm, lateral ~ 10 nm (tip size). Max scan area: $100 \times 100\ \mu\text{m}^2$. Measurement steps: Calibration (align cantilever/laser), Sample loading, Measurement (scan), Analysis (leveling, artifact removal). Resist residues at edges can affect thickness estimation.

AFM measurements were performed on test samples (Fig. 2.5) to calibrate the thickness monitor. We measured central squares $(50 \times 50\ \mu\text{m}^2)$ in 4 regions to get average thickness $\langle h \rangle$ and deviation σ. Two Ti samples (reference 20 nm and 25 nm) were analyzed.

Results (Fig. 2.6): Ti (20 nm ref) measured (24 ± 2) nm; Ti (25 nm ref) measured (25.4 ± 0.3) nm. Measurements agree with reference values.

Furthermore, a previous study performed on a $1 \times 1\ \mu\text{m}^2$ scan area revealed a TES surface roughness of approximately $1 - 1.5$ nm.

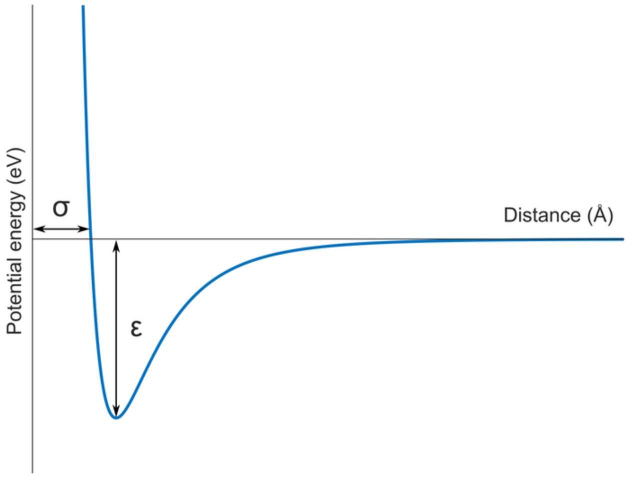

(a) Lennard-Jones potential: $V(r) = 4\varepsilon((\frac{\sigma}{r})^{12} - (\frac{\sigma}{r})^{6})$.

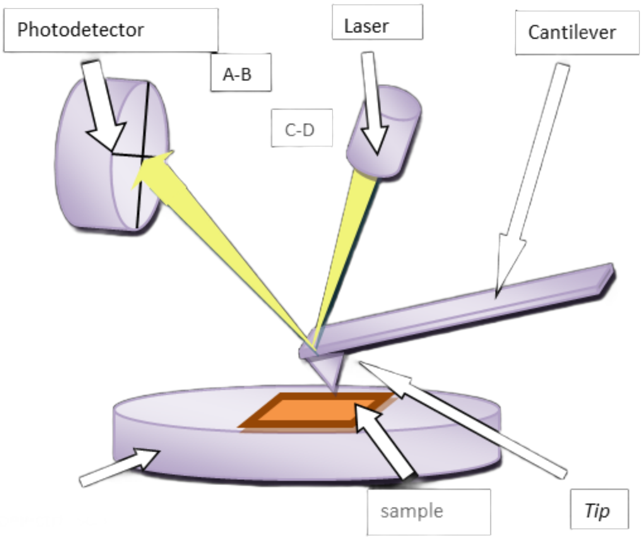

(b) Schematic of an AFM with laser feedback system.

Fig. 2.4 AFM working principle and potential.

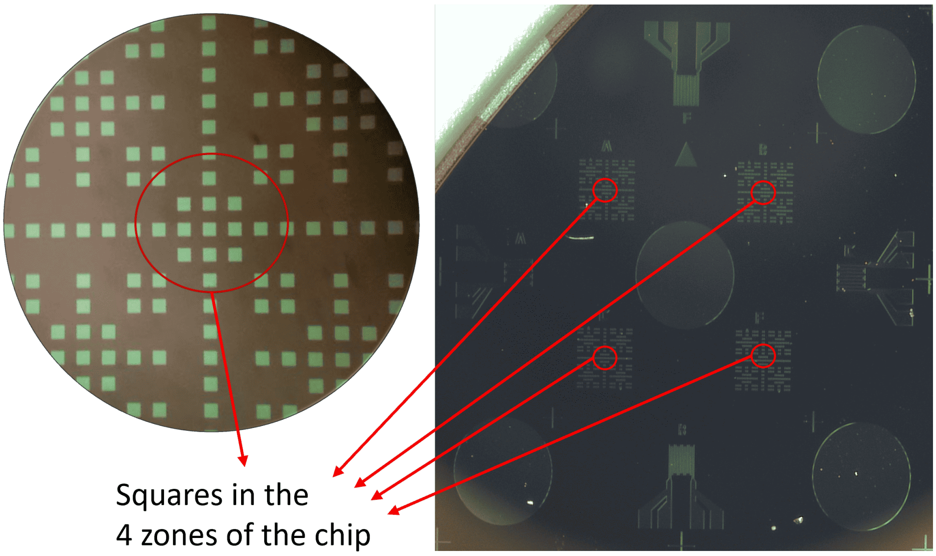

Fig. 2.5 Overview of the test chip geometries (right) and zoom of one zone (left).

Stylus Profilometer

The stylus profilometer physically traces the surface with a diamond tip, measuring vertical displacement via a transducer. It allows scanning large areas for step heights and roughness. Vertical resolution ~ 1 nm, lateral ~ 100 nm (tip radius $\sim 2\,\mu$m). It is suitable for robust materials but not delicate plasmonic gratings. Measurements were done on Ti (20 nm) and Ti (5 nm)/Au (30 nm) samples. Meanders and circles were measured. Profiles were leveled and steps calculated (ISO 5436, Fig. 2.7). Results (Fig. 2.8): TiAu measured $\langle h \rangle = (38 \pm 4)$ nm; Ti measured $\langle h \rangle = (22 \pm 4)$ nm, compatible with references. Uncertainties are $\sigma = \sqrt{\sigma_1^2 + \sigma_2^2}$.

Derivation of the uncertainty budget of the thickness during the deposition

We assign an uncertainty u_t to the deposition process using an Ishikawa diagram (Fig. 2.9) to classify sources (instrumentation, environment, etc.) [42]. Sources include: profilometer measurement (σ), thickness monitor precision (~ 0.2 nm, consistent with $1-5\%$), and sample positioning (misalignment and tilt, Fig. 2.10). The misalignment effect is negligible for our geometry. Tilt effects are included in the AFM σ. The final standard error is $u_t = \sqrt{\frac{\Sigma \sigma_{ti}^2}{n}}$.

Based on measurements:

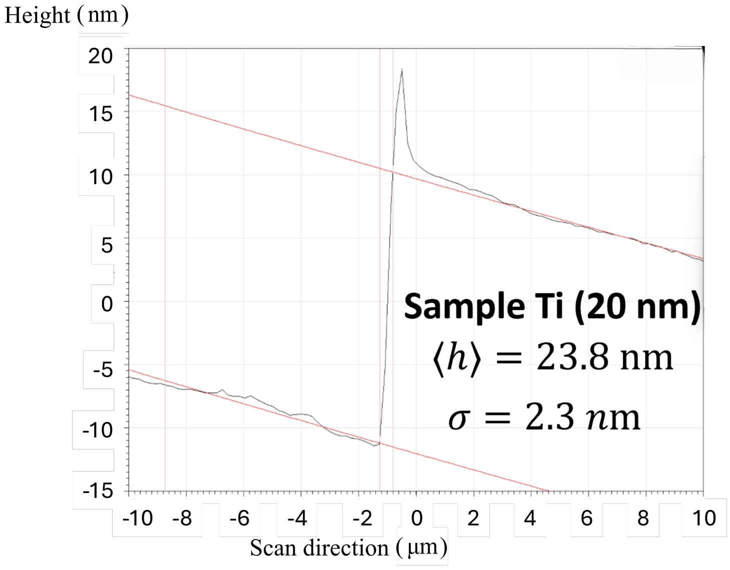

(a) Backward measurement, 20 nm sample.

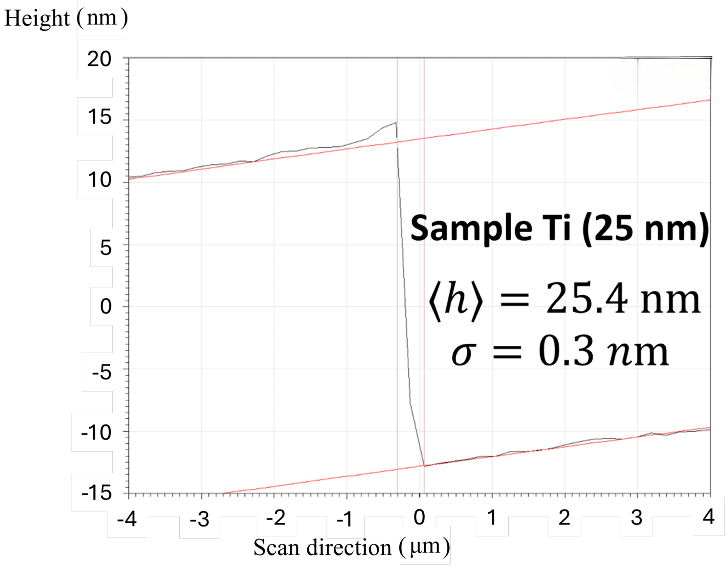

(b) Forward measurement, 25 nm sample.

Fig. 2.6 AFM measurements of Ti samples.

- Ti (20 nm): $u_{\mathrm{Ti},20} = 2$ nm
- Ti (25 nm): $u_{\mathrm{Ti},25} = 0.25$ nm
- Au (30 nm): $u_{\mathrm{Au},30} = 1.6$ nm

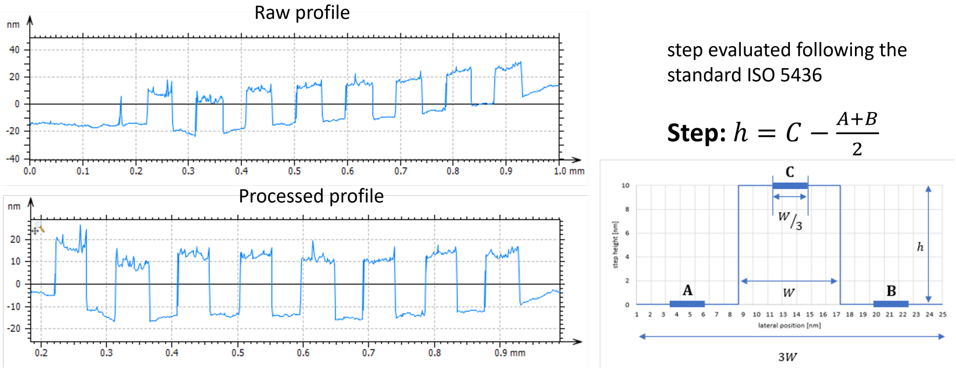

Fig. 2.7 Left: Raw and leveled meander profiles. Right: ISO 5436 step evaluation.

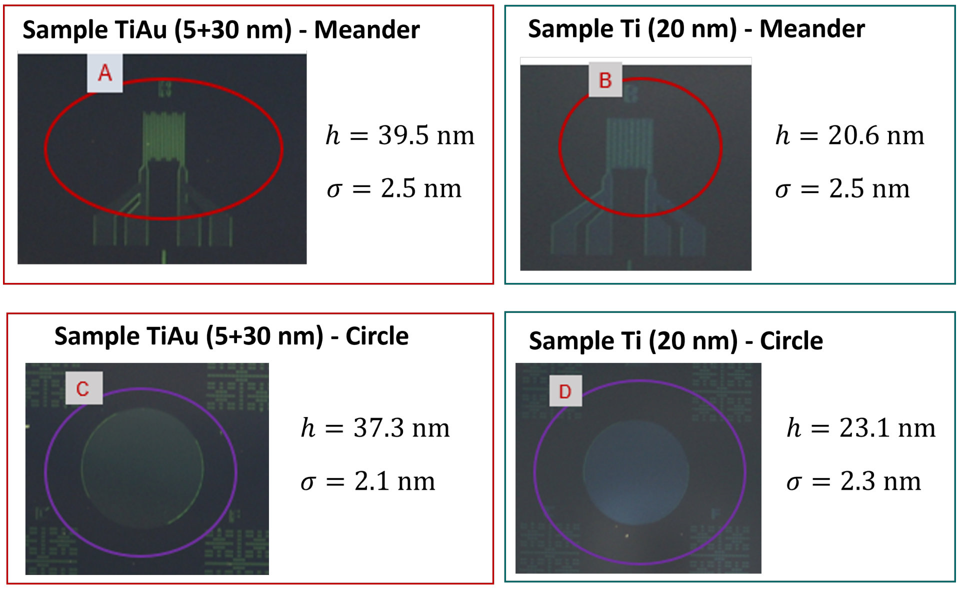

Fig. 2.8 Profilometer results for TiAu (red) and Ti (green) samples.

We assign a relative standard uncertainty of $\approx 5.5\%$ for Gold and $\approx 10\%$ for Titanium:

$$u_{\mathrm{Ti,rel}} = \sqrt{\left(\frac{0.25}{25}\right)^2 + \left(\frac{2}{20}\right)^2} \approx 0.10. \tag{2.1}$$

This observed difference in uniformity can be attributed to the distinct deposition techniques employed. Gold is evaporated using a Knudsen-type effusion cell equipped with a chimney, which generates a thermally equilibrated, broad molecular beam characterized by a stable and highly uniform spatial distribution. Conversely, Titanium is deposited via electron-beam evaporation (e-gun). In this method, the high-energy electron beam focuses on a small spot within the crucible, effectively

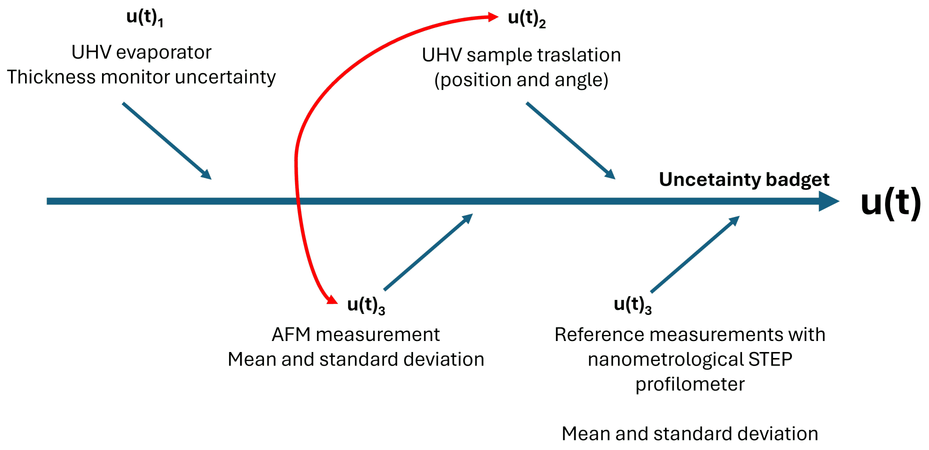

Fig. 2.9 Ishikawa diagram for deposition thickness uncertainty.

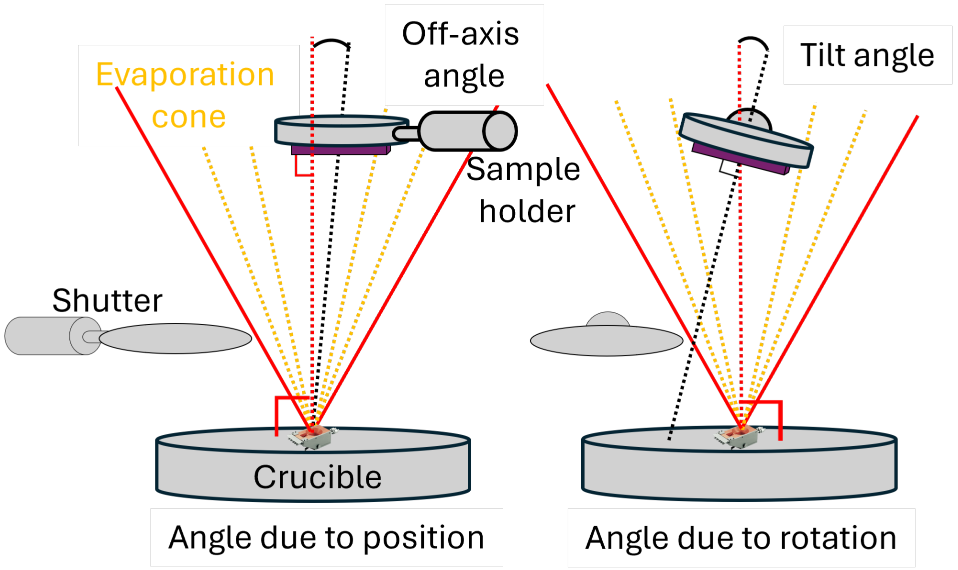

Fig. 2.10 Schematic of positioning uncertainties: off-axis misalignment (left) and tilt (right).

acting as a point source. This results in a flux distribution that is typically more directional (narrower angular lobes) and sensitive to variations in the melt shape and beam position, inherently leading to a steeper thickness gradient across the substrate compared to the effusion cell.

Modifications to the UHV evaporator (Fig. 2.11), including rotary sample holders, are planned to improve uniformity.

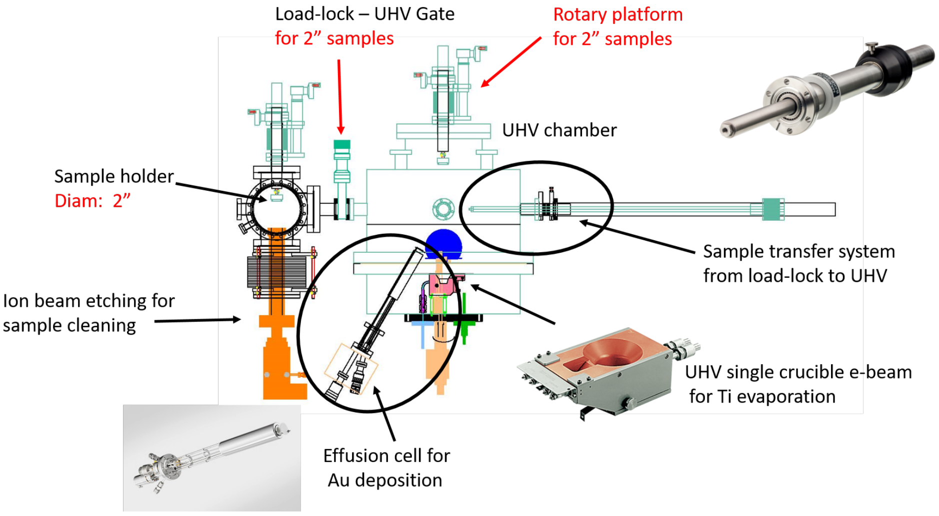

Fig. 2.11 Planned modifications: 2-inch sample holders, new effusion cell, and rotary platform.

2.2.2 Superconductivity measurements

This section incorporates concepts, visual materials, and structural elements previously included in my earlier thesis [1].

A foundational measurement that is consistently performed at the laboratories of the INRiM is the measurement of resistance of superconducting samples as a function of temperature. The main instrument used for this purpose is the cryostat, which allows temperatures lower than the superconducting transition temperature of the materials under test. To determine the critical temperature of the samples, the resistance is accurately measured as a function of temperature using a resistance bridge or a Lock-In amplifier.

The characterization of the TES devices is performed in two distinct stages. First, the resistance as a function of temperature (R vs T) is evaluated using a four-wire measurement configuration. From these curves, the normal resistance R_N and the critical temperature T_c are estimated. The experimental setup allows for the thermal characterization of up to 12 samples simultaneously in this mode. Second, the TES performance is evaluated by placing the device in the voltage-bias circuit (ETF configuration) and coupling it with an optical fiber. In this stage, the current flowing through the sensor is measured by varying the bias current and the bath temperature, regulated by a Proportional-Integral-Derivative (PID) controller. Superconducting

Quantum Interference Devices (SQUIDs) are used to read out the current variations. With this setup, we can illuminate and fully characterize 3 TESs simultaneously.

To send photons, a laser source with an attenuator is used to control the power sent through the fibers. Each fiber is manually aligned and glued to the TES using an inverted optical microscope.

Finally, a spectrum analyzer is used to measure noise frequency spectra, in order to record and compare measurement conditions.

Some details on the refrigerator used and measurements tecnique can be found in App. B.3

2.2.3 Optical Fiber Alignment with the Sample

The process of aligning the optical fiber to the TES, involves positioning the fiber onto the sample and securing it in place. This operation is carried out using an inverted optical microscope.

The TES devices developed at the INRiM laboratories consist of titanium and gold metallic films, while the electrodes are fabricated using niobium, aluminum, or titanium. The substrates on which the TES devices are deposited are made of silicon, covered with a silicon nitride layer. Both materials are transparent in the infrared range. By observing the TES chips with an inverted microscope equipped with an infrared light source, the niobium or titanium tracks and the TES itself can be identified as dark regions through the substrate. This happens since the the *Si* substrate is transparent to infrared light, while the TESs and their wirings are not.

The fiber alignment process is facilitated by micrometric screws, which allow fine positioning of the fiber along the three spatial directions. The fiber is held in a stable position using a dedicated clamp.

Initially, the fiber is cleaved to ensure that its section in contact with the TES is as smooth and perpendicular as possible to the surface. A continuous-wave laser operating at a wavelength of 1550 nm generates photons exiting the fiber. By adjusting the laser intensity, it becomes possible to observe an illuminated region corresponding to the fiber core (approximately 10 μm in diameter) when the fiber is sufficiently close to the sample. Additionally, a dark circular region, corresponding to the fiber cladding with a diameter of approximately 125 μm, becomes visible,

Fig. 2.12. Once the alignment is completed, the fiber is secured by applying small drops of adhesive using a syringe. The adhesive drops spreads along the fiber, reaching the sample. The drops are cured using ultraviolet (UV) light and then baked at 50 degrees for 24 hour to solidify it.

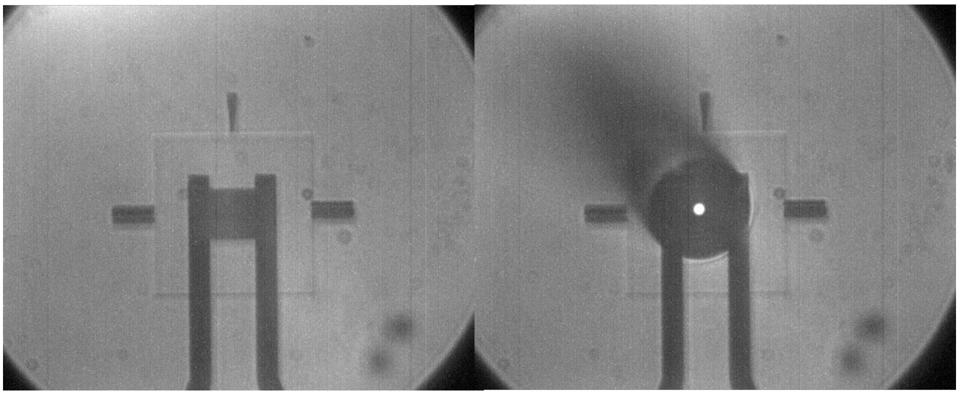

Fig. 2.12 Microscope image of a $(12 \times 12)\ \mu\mathrm{m}^2$ TES with the aligned fiber. The illuminated core of the fiber is visible.

Chapter 3

Fast response TESs

Part of the work described in this chapter has also been previously published in [43].

3.1 Abstract of the chapter

The SEQUME project [44] aims to demonstrate quantum advantage using high-brightness, high-efficiency entangled photon sources and high-purity single-photon sources. Within this framework, Transition-Edge Sensors (TESs) are required for low photon flux calibration, specifically necessitating Photon Number Resolving (PNR) capability at detection rates exceeding 2 MHz. These requirements translate into strict performance metrics: an energy resolution $\Delta E < 0.4\,\mathrm{eV}$, a detection efficiency greater than 90%, and an effective response time $\tau_{\mathrm{eff}} \approx 100\,\mathrm{ns}$.In this chapter, we investigate two primary strategies to achieve these speeds. First, we explore the fabrication of aluminum-based TESs (Al TESs), exploiting the lower specific heat capacity and higher critical temperature of aluminum compared to traditional titanium-gold (TiAu) bilayers. We present the characterization of Al strips and TESs, highlighting the challenges related to film quality and oxide formation. Second, we demonstrate the efficacy of introducing lateral gold banks to standard TiAu TESs. We prove that adding these thermal links significantly accelerates the detector recovery time to the order of hundreds of nanoseconds without compromising the structural integrity of the device.

3.2 Aluminum TESs

3.2.1 Motivations and complications

The initial idea was to fabricate TESs based on Aluminum instead of our usual TiAu. The advantages related to Al are given by an intrinsic higher T_C with respect to Ti, and thus an higher conductance G. Moreover, the specific heat capacity C of Al is lower than the one of the Ti.

In fact, the T_C of Al is ~ 1.2 K while the one of a Ti film is $\sim 400-500$ mK. Moreover, C is given by $C \propto (\gamma + \zeta T^2)TV$ where the free electrons contributes through γT thanks to the Sommerfeld constant γ and V is the volume. For C we have $\gamma_{Al}/(\gamma_{Ti}+\gamma_{Au}) = 1.35/(3.31+0.69)$ and $\zeta_{Al}/(\zeta_{Ti}+\zeta_{Au}) \propto 1.3/(1.18+21.8)$, while for $G = n\Sigma V T^{n-1}$ we have $\Sigma_{Al}/(\Sigma_{Ti}+\Sigma_{Au}) = 0.3/(1.5+2.4)$ [3].

If we calculate both C and G with a volume $V = 45$ nm $\times$ 100 μm^2 for an Al TES at $1\,K$ and a TiAu TES at 100 mK we obtain $C_{Al} = 1.5\ \frac{\text{fJ}}{\text{K}}$, $G_{Al} = 6750\ \frac{\text{pW}}{\text{K}}$ and $C_{TiAu} = 0.16\ \frac{\text{fJ}}{\text{K}}$, $G_{TiAu} = 5\ \frac{\text{pW}}{\text{K}}$. The characteristic times are $\tau_{TiAu} = 34\ \mu$s and $\tau_{Al} = 220$ ns. While, if we compare a Ti TES and an Al TES both with $T_C = 400$ mK and the same volume of before we obtain: $C_{Al} = 0.6\ \frac{\text{fJ}}{\text{K}}$, $G_{Al} = 173\ \frac{\text{pW}}{\text{K}}$, $\tau_{Al} = 3.4\ \mu$s and $C_{Ti} = 1.4\ \frac{\text{fJ}}{\text{K}}$, $G_{Ti} = 864\ \frac{\text{pW}}{\text{K}}$, $\tau_{Ti} = 1.6\ \mu$s, [45, 46].

These calculations show us that TiAu is limited in temperature and Ti alone is limited in ΔE because of C. Al seem to be a good trade-off between the energy resolution and recovery time due to its T_C and thermal capacitance. In addition, it is a metal easy to evaporate with an e-gun in an HV chamber and it is not expansive.

The comparison of the calculated thermal properties for the two material systems is summarized in Table 3.1.

Table 3.1 Comparison of calculated thermal properties for a standard TiAu TES and an Al TES. The values are estimated for a fixed device volume of $V = 45$ nm $\times$ 100 μm^2. The significant difference in the thermal time constant τ highlights the potential of Aluminum for high-speed detection.

Material	T_c (K)	**Heat Capacity** C (fJ/K)	**Thermal Cond.** G (pW/K)	**Time Constant** τ
TiAu	0.1	0.16	5	34 μs
Al	~ 1.0	1.50	6750	220 ns

The first 2 complications related to Al films are the well known oxidation of Al and the deviation of its properties depending on the growth of the Al grains of the film.

From [47], we can learn that Al films with well-coupled grains exhibit superconducting behavior that follows the BCS theory. In contrast, when the grains are poorly coupled, both the residual resistivity ratio (RRR) and the critical temperature (T_C) tend to increase.

Variations in T_C can be attributed to several factors. Among the minor contributions are the size of the aluminum grains and the specific deposition techniques employed. However, the most significant influence on the critical temperature is the nature of the substrate on which the aluminum is deposited.

Furthermore, it has been suggested that a coherent interaction of planar defects within the film [47] can formally lead to a $T_\mathrm{C} > 1.2$ K for an Al film.

Moreover, in [48] it is shown that the deposition of an Al film on a Ti layer using an Atomic Layer Deposition technique (ALD) is advantageous. Al films deposited with a titanium seed layer exhibit a strong (111) crystallographic orientation, regardless of the underlying substrate. This (111) orientation offers enhanced resistance to stress-induced migration and contributes to a longer operational lifetime when used as an electrode material in device applications. In fact, the superconducting transition temperature of these aluminum thin films is comparable to that of bulk aluminum, indicating high structural and electronic quality.

With these information, we initially decided to fabricate TiAl bilayers, with a 5 nm Ti layer under the Al layer that serves both as a growth seed and as an adhesion layer.

3.2.2 Results: superconductive transitions

We fabricated and characterized a series of samples containing Al TESs and test strips with varying dimensions and layer structures to optimize the superconducting properties. The deposited Al thicknesses range from 15 nm to 30 nm. The wiring consists of Nb or an Al/Nb bilayer with a Nb thickness of 100 nm or 150 nm, ensuring a wiring critical temperature $T_\mathrm{c} \sim 8 - 9$ K. The TESs are rectangular with side lengths varying from 3 μm to 12 μm, designed to minimize heat capacity C

and tune the normal resistance R_N. To improve uniformity, most chip masks (except SEQ1 and SEQ3) feature a central layout where TESs are arranged on two concentric circles equidistant from the chip center (Fig. 3.1). This design minimizes thickness variations due to the deposition profile.

Fig. 3.1 Central layout pattern of the chip mask. The TESs are placed equidistant from the chip center to minimize thickness gradients.

Table 3.2 summarizes the parameters and results for the "SEQ" sample series (1 to 10) and the second-generation "SEQB" samples. The latter feature an optimized contact pad layout for faster characterization.

Initial samples (SEQ1-SEQ5) utilized an evaporated Ti/Al bilayer with sputtered Nb wiring. As shown in Table 3.2 and Fig. 3.2, these samples exhibited anomalously high resistivities ($\rho \sim 15-19\ \mu\Omega$cm) compared to expected values ($6-12\ \mu\Omega$cm) and very low T_c. This indicates poor film quality and incomplete removal of the native Al oxide at the interface. Furthermore, TESs consistently showed higher resistivity and broader transitions than the corresponding strips (Fig. 3.4), confirming the presence of a resistive oxide barrier at the wiring contacts. This barrier likely forms a weak-link junction, as evidenced by the humped shape of the transition and its dependence on the excitation current (Fig. 3.3).

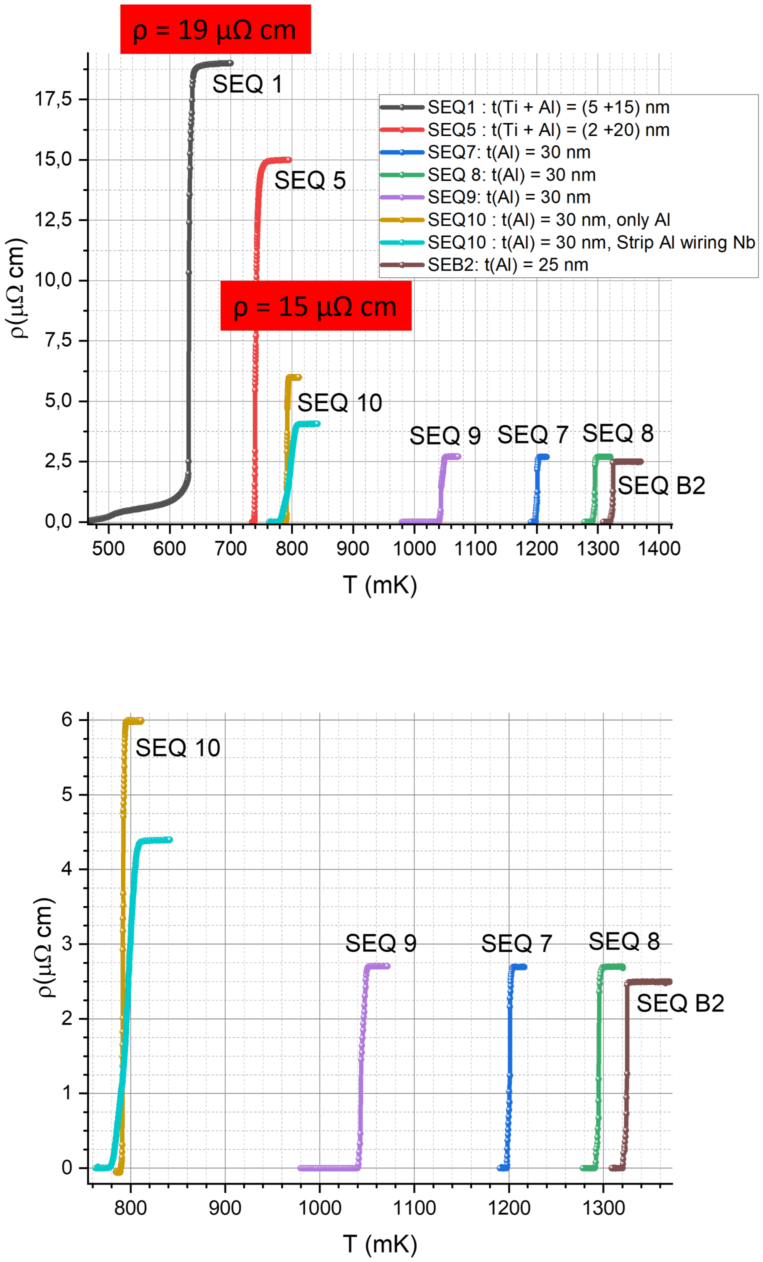

Fig. 3.2 Resistivity vs temperature of the strips in the SEQ samples. Top: all transitions. Bottom: zoom of the main region. Red labels indicate resistivity values far from literature expectations.

Sample SEQ	**Ti** (nm)	**Al** (nm)	**Sputter Etching** V_{BIAS}, P, t	T_{c} strip (mK)	ρ strip ($\mu\Omega$cm)	T_{c} TES (mK)	ρ TES ($\mu\Omega$cm)
1	5	15	640 V, 26 W, 2′	631 (5)	19	170 (15)	17.6
3	5	25	//	603 (12)	16	603 (12)	40.5
4	2	15	//	–	–	[400–1200]	130
5	2	20	//	741 (8)	15	[400–1200]	269
7	0	30	//	1202 (2.4)	2.7	1178 (97)	200
8	0	30	670 V, 26 W, 2’	1296 (4.2)	2.7	1050 (8.2)	6.4
9	0	30	624 V, 26 W, 5’	1024 (14)	2.7	∼780 (500)	6
10	0	30	748 V, 26 W, 7’	800 (12)	4.4	548 (17)	4.4
B1 (Nb first)	0	25	620 V, 25 W, 2’	1318 (4)	0.5	1320 (24)	0.5
B2	0	25	700 V, 25 W, 5’	1328 (3)	2.5	1312 (23)	5

Table 3.2 Summary of Al/Ti bilayer samples (SEQ), indicating Ti and Al thickness, applied sputter etching conditions (bias voltage V_{BIAS}, power P, and time t), and superconducting properties of both test strips and TESs: critical temperature T_{c}, transition width (in parentheses), and resistivity ρ.

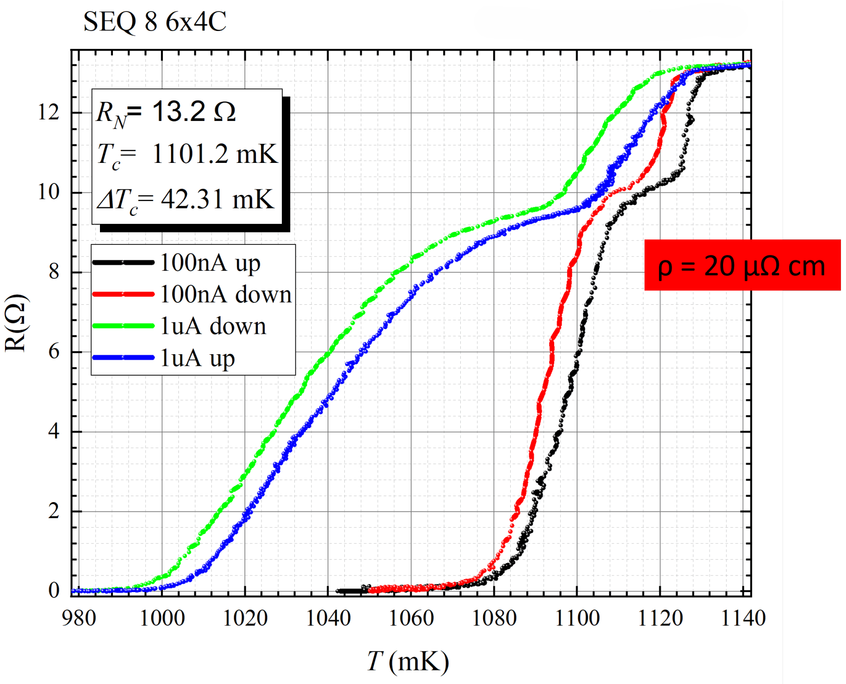

Fig. 3.3 Superconductive transition of an Al TES with a natural oxide layer. The humped shape and current dependence suggest weak-link behavior.

Subsequent samples (SEQ7-SEQ10) used sputtered Al without the Ti underlayer, with optimized sputter etching parameters. While strip properties improved, TESs still showed discrepancies. The breakthrough was achieved with samples SEQB1 and SEQB2, where we inverted the process by depositing the Nb wiring *before* the Al TES. This eliminated the issue of removing the robust Al oxide. Both samples showed well-behaved transitions with $T_\mathrm{c} \sim 1.32$ K and sharp widths ($\Delta T_\mathrm{c} \sim 3$ mK for strips), with $\rho_\mathrm{TES} \approx \rho_\mathrm{strip}$ in SEQB1.

The investigation of the proximity effect in these samples was motivated by the large coherence length $\xi(T)$ of Al near the transition. Recalling Eq. A.17 from Chapter 1, we estimated the specific coherence length for our sputtered Aluminum films. We assume the dirty limit condition ($l \ll \xi_0$), where l is the electron mean free path. Using the literature values for Fermi velocity $v_\mathrm{F} \approx 1.6 \times 10^8$ cm/s and a diffusion constant $D \approx 60\,\mathrm{cm}^2/\mathrm{s}$ (typical for thin films), we estimate $l = 3D/v_\mathrm{F} \approx 11$ nm. Consequently, the zero-temperature coherence length is $\xi(0) \approx 0.85\sqrt{\xi_0 l} \approx 116\,\mathrm{nm}$, where $\xi_0 = 0.18(\hbar v_\mathrm{F})/(k_\mathrm{B} T_\mathrm{c}) \approx 1.7\ \mu$m. Applying the temperature dependence described in Chapter 1, at the onset of the transition ($T \approx T_\mathrm{c} - \Delta T_\mathrm{c}$), the coherence length diverges, reaching values of $\xi \sim 2\ \mu$m. Since this length scale is comparable to the dimensions of our strips, the choice of wiring material and geometry becomes critical.

Given the large coherence length of aluminum, we further investigated the impact of Nb wiring on Al strips (samples SEQ10 and SEQB1) using the contact configurations detailed in Fig. 3.5. As shown in the transition curves in Fig. 3.6, the Nb wiring in SEQ10 induced a reduction in normal resistivity and a broadening of the transition width, consistent with the injection of Cooper pairs characteristic of the longitudinal proximity effect. The observed shift in T_c (14 mK), however, remained within experimental uncertainty. conversely, for SEQB1, where the contact pads were spaced further apart, all measurement configurations (2-wire and 4-wire across different segments) yielded compatible resistivity values, confirming the absence of spurious contact barriers

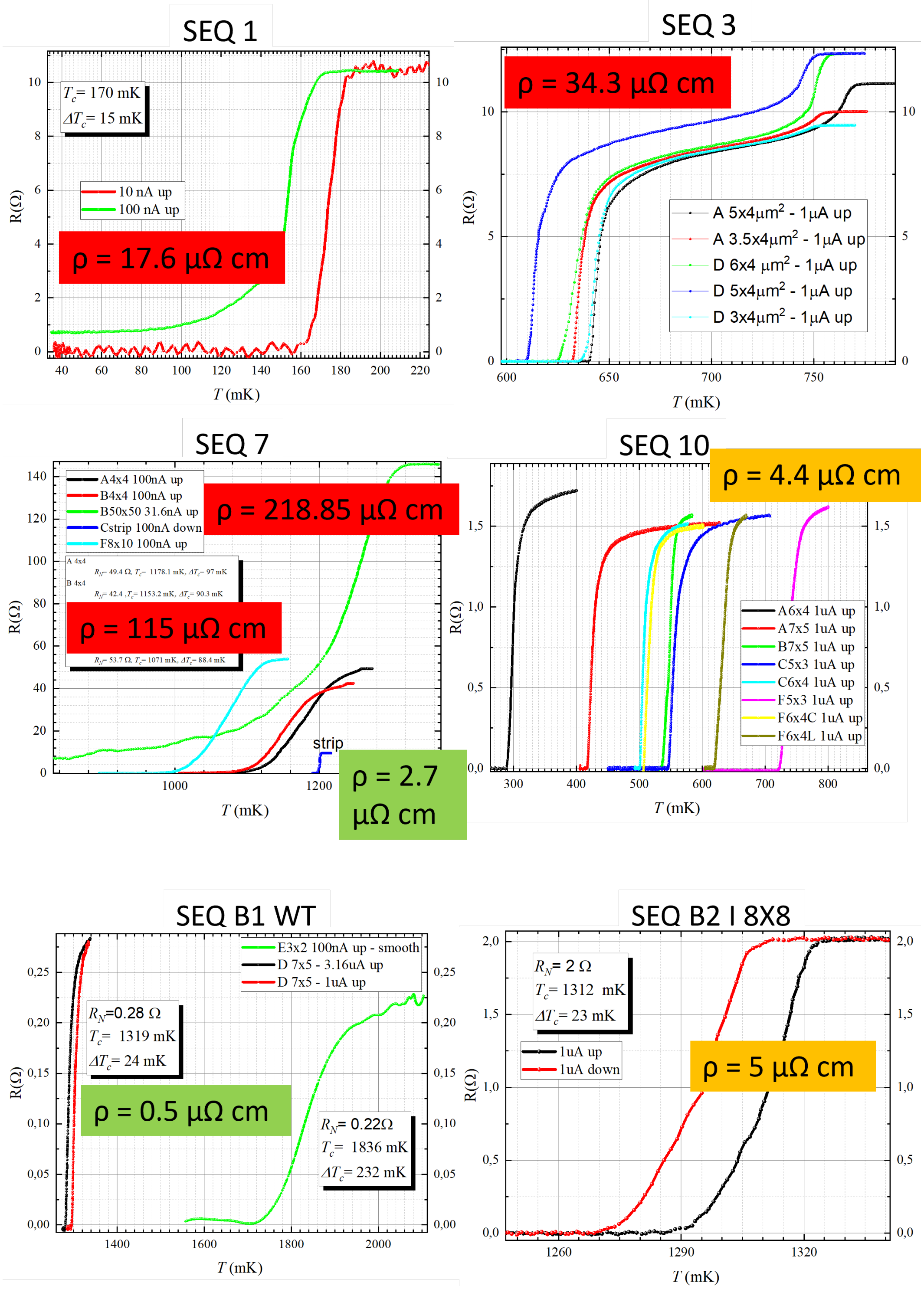

Fig. 3.4 *R* vs *T* measurements for TESs in samples SEQ1 to SEQB2. Early samples (SEQ1, SEQ3, SEQ7 TES) are affected by oxide. SEQB1 (Nb first) shows ideal sharp transitions at 1.3 K with low resistivity.

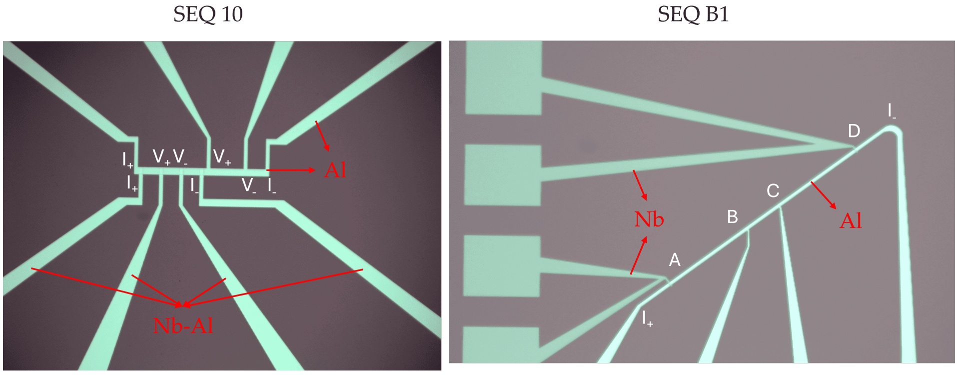

Fig. 3.5 Wiring configurations for Al strips in SEQ10 (left) and SEQB1 (right) used to study contact effects.

SEQ 10

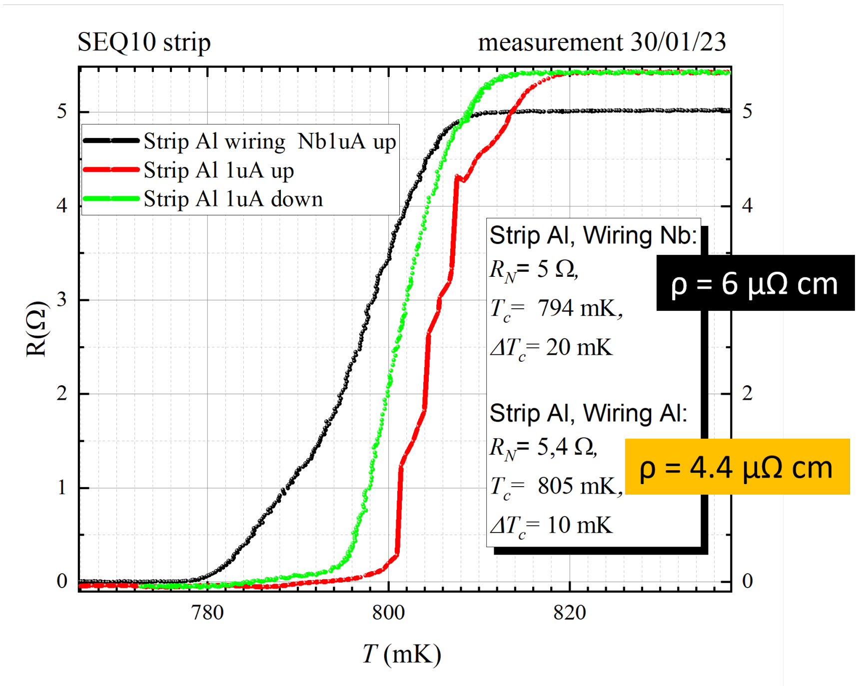

SEQ B1

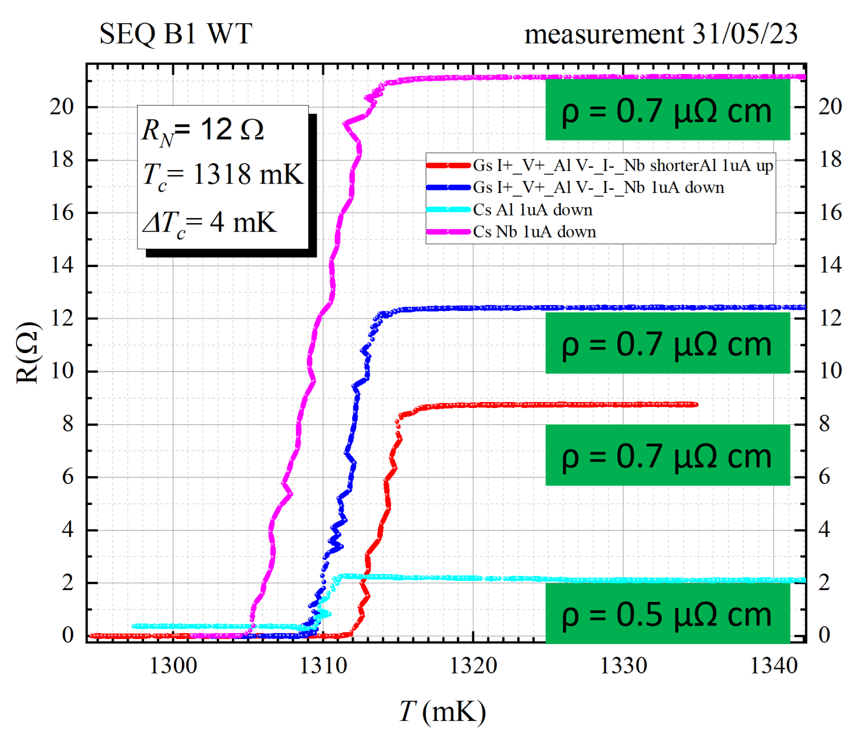

Fig. 3.6 Superconducting transitions for the strip configurations in Fig. 3.5. Top: SEQ10. Bottom: SEQB1.

The evolution of superconducting properties across the sample series is summarized in Fig. 3.7, showing the convergence of ρ, T_c, and ΔT_c towards expected literature values. This optimization effort enabled the realization of fast single-photon detectors, the results of which are discussed in the following subsection.

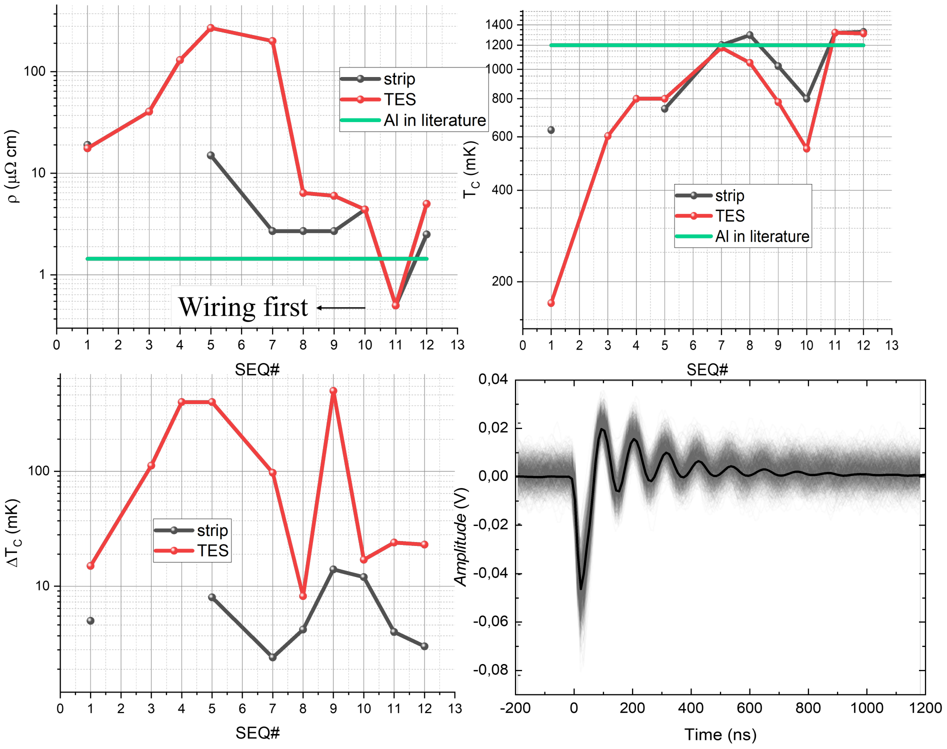

Fig. 3.7 From top left to bottom left: graphs in logarithmic scale of the resistivity ρ, critical temperature T_C and transition width ΔT_C of strips (black lines) and TESs (red lines) as a function of the number of chip "SEQ#" (considering SEQB1 as SEQ11 and SEQB2 as SEQ12). Green horizontal lines represents the values reported in literature. It can be noted that the values for TESs and strips converges both to values from literature and between each other. Bottom right: output signal during the photon detection for a TES of the SEQB1 sample polarized at the 60% of R_N. The oscillating signal is interpreted as the detector ringing due to electro-thermal instability ($\tau_{el} \sim \tau_{etf}$), from which we deduce an upper limit for the decay time of ~ 43 ns.

3.2.3 Results: photon detection

Our initial photon characterization was performed using a TES from the SEQ3 batch (area $3.5 \times 3\ \mu\text{m}^2$, $T_C = 603$ mK), prior to optimizing the Al film properties to match literature values. The device was coupled to a 1.6 μm core optical fiber for telecom wavelength detection, utilizing a 2 MHz low-pass filter. The results, shown in Fig. 3.8, demonstrated the potential of Al TESs for single-photon sensitivity, achieving an energy resolution of 0.3 eV. However, the measured pulse decay time was approximately 1 μs, which, while promising, was limited by the non-optimized film and the external filter, proving slower than state-of-the-art results [12, 13, 49].

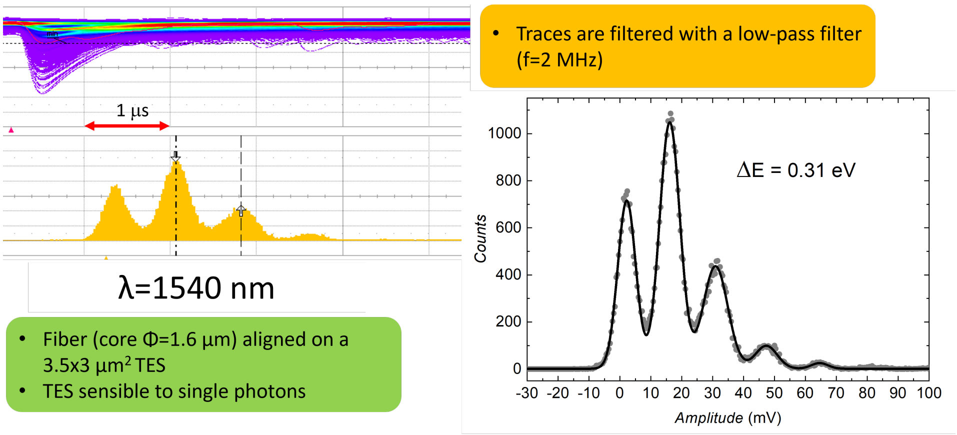

- Traces are filtered with a low-pass filter (f=2 MHz)

λ=1540 nm

- Fiber (core Φ=1.6 μm) aligned on a 3.5x3 μm² TES
- TES sensible to single photons

Fig. 3.8 SEQ3 TES photon counting. On top, the pulses measured with an oscilloscopes and a low pass filter of 2 MHz show overall pulses faster than 1 μs. On the bottom, the resulting histogram can discriminate single photons with $\lambda = 1540$ nm with a suitable energy resolution $\Delta E = 0.31$ eV.

A second characterization was conducted on a 7×7 μm^2 TES from the optimized SEQ8 batch. This device exhibited a normal resistance $R_\text{N} = 2.2\ \Omega$ ($\rho = 6.6\ \mu\Omega$cm), $T_\text{C} = 1047$ mK, and a sharp transition $\Delta T_\text{C} = 3$ mK (see Tab. 3.2).

In this case, we were unable to detect clean single-photon pulses with monotonic decay. Instead, all the photon absorption events revealed a strong oscillating response, as shown in Fig. 3.7 (bottom right). We interpret this behavior as a manifestation of electro-thermal instability, consistent with the theory described by Irwin and Hilton [4]. For a voltage-biased TES, stability requires specific conditions relating the electrical time constant τ_el and the effective thermal time constant τ_etf. Given the circuit inductance $L \approx 10$ nH and the device resistance, we estimate an electrical time constant $\tau_\text{el} = L/[R_\text{th} + R_0(1+\beta)] \approx 7.4$ ns (assuming $\beta \approx 0$). According to Irwin and Hilton, a TES can exhibit underdamped oscillations or instability when the loop gain $\mathscr{L}$ is high and the time constants are comparable. Specifically, for stability in the high-loop-gain limit, one typically requires τ_el to be significantly faster than

τ_{etf}. However, for our fast Al TESs, simulations suggest an intrinsic thermal time constant $\tau \sim 200$ ns, implying an effective decay time $\tau_{\text{etf}} = \tau/(\mathscr{L}+1)$ that can become extremely short.

If τ_{etf} approaches τ_{el}, the system enters an underdamped regime characterized by oscillations. The condition for critical damping or stability is roughly $\tau_{\text{etf}} > 5.8\,\tau_{\text{el}}$ [50]. In our case, this would imply a stability limit of $\tau_{\text{etf}} \approx 43$ ns. Since we observe oscillations, it is likely that the actual thermal response of the device is faster than this threshold ($\tau_{\text{etf}} < 43$ ns), violating the stability condition for our specific L. Attempts to stabilize the device by biasing it higher in the transition (60% of R_{N}) to reduce α (and thus $\mathscr{L}$) were insufficient to suppress the oscillations completely, confirming the extremely fast nature of these Al devices.

Furthermore, the observed oscillation frequency is close to the bandwidth limit of our dc-SQUID readout (~ 6 MHz). This could be another plausible explanation for which oscillations occurs and that prevents a resolved measurement of the fundamental pulse shape.

3.2.4 Conclusions for Al TESs

The study presented here highlights the potential of aluminum as a promising material for TES fabrication, offering a compelling compromise between thermal conductance and energy resolution. Thanks to its intrinsically higher critical temperature and lower specific heat compared to titanium and titanium-gold bilayers, Al allows for significantly faster thermal response times without excessively compromising energy sensitivity.

Our experimental results on the SEQ8 sample, interpreted through the Irwin-Hilton stability framework, suggest that optimized Al-based TESs can achieve thermal time constants in the deep sub-microsecond regime ($\tau_{\text{etf}} < 43$ ns), potentially challenging the bandwidth limits of standard SQUID readout electronics. This confirms their suitability for high-rate counting applications.

However, the development process also revealed critical challenges. The formation of a native aluminum oxide layer and variability in film grain structure significantly affect the reproducibility of T_{C} and resistivity, as seen in the SEQ1-SEQ5 batches. The data indicate that standard sputter etching is insufficient for oxide removal and that careful optimization of deposition parameters (e.g., sputtering power, substrate temperature) is required to achieve bulk-like film quality.

In conclusion, while Al TESs offer a path toward extremely fast single-photon detectors, realizing their full potential requires precise interface engineering and potentially the integration of customized readout circuits with higher critical inductance or bandwidth to manage the intrinsic speed and stability of the devices.

3.3 Gold banks

Another way to make faster TESs is to add additional Au structures [8, 13] to the TES. This is done in particular for thin W TESs, but is also exploited for thick TESs and MoCu TESs. However, an additional volume of Au can increase the thermal conductivity G even in thin AuTi TESs, albeit with an increase in thermal capacitance and a possible worsening of α.

3.3.1 Results

Our first design for this approach has been to cover the edges of the TESs with Au banks (separated stripes with a gap under the wirings or closed rings around the overall TES). The banks are 2 μm wide and 30 nm thick, designed to cover the TES surface for 1 μm and touch the substrate with the other half of the width, as shown in Fig. 3.9. This design has been conceived for three potential benefits:

- To increase G thanks to these Au thermal links between the Au on top of the TES and the substrate (results will be explained in this chapter);
- To affect the TES superconductive transition by modifying the proximity effect at the edge, and consequently the lateral proximity effect (results are shown in Ch. 5);
- To cover the exposed Ti at the edges to limit oxidation (this study is still ongoing and results will not be presented in this thesis).

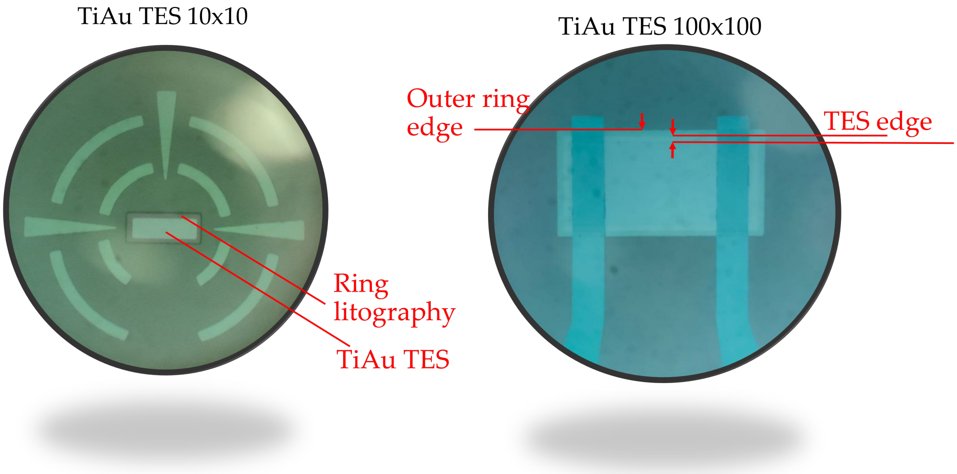

Fig. 3.9 On the left: TES area with the lithography of the banks/ring. On the right: fabricated $(100 \times 100)\ \mu\text{m}^2$ TES with TES area, wirings and banks/ring. The Au ring is half on the TES and half on the substrate, so as to cover the TES edges correctly. In the middle, between the inner and outer edge of the ring, it is possible to see the underlying edge of the TES itself.

We have fabricated and characterized two $(60 \times 60)\ \mu\text{m}^2$ TiAu TESs: the first with only one bank and the second with two banks. Both devices were characterized utilizing photons with a wavelength of $\lambda = 406$ nm.

To evaluate the thermal conductance G, we have used the power vs the bath temperature curve. This is an approximate way to evaluate G (and n) using the equilibrium condition for Joule power and dissipated power as $R_0 i_0^2 = k(T_0^n - T_{\text{bath}}^n)$, from which one can calculate G as $G = nkT_0^{n-1}$ (see Ch. 1).

For TESs with this area, two banks are estimated to affect the thermal capacitance by only 2 % of the total.

For the TES with one bank, G has been estimated as (413 ± 5) pW/K, which is 2 times greater than our previous TESs having the same structure, materials, geometries, and similar T_c. The transition, measured by the dc-SQUID in the photon counting setup, reveals a transition with no particular features, with $T_\text{c} \sim 123$ mK, $\Delta T_\text{c} = 1.2$ mK and a small R_N due to the gold bank in parallel with the TES.

The superconductive transition, the pulses generated by photons, and the histogram of the pulses for $\lambda = 406$ nm are shown in Fig. 3.10. The device is not excellent in terms of energy resolution and saturation energy, which are $\Delta E = 0.82$ eV and $E_\text{sat} = 4.27$ eV, but it excels in recovery time.

3.3.2 Results

Standard TES pulses are typically fitted with a two-exponential model describing the electrical rise time and the electro-thermal decay:

$$A(t) = A\left(e^{-\frac{t}{\tau_{\mathrm{el}}}} - e^{-\frac{t}{\tau_{\mathrm{etf}}}}\right). \tag{3.1}$$

However, the pulses from the TES with Au banks exhibit a distinctive "bump" or secondary feature in the decay tail (see Fig. 3.10) that cannot be accurately described by Eq. 3.1.

To interpret this behavior, we considered two main hypotheses: electro-thermal instability (Irwin-Hilton mechanism) or a multi-body thermal effect (Bennett model). As explained before, when the electrical time constant τ_{el} is comparable to the thermal time constant τ_{etf} in a high-loop-gain regime electro-thermal instability typically arise, leading to underdamped oscillations. While this mechanism can produce ringing, the observed feature is a relatively slow, damped modulation in the pulse tail rather than the high-frequency ringing characteristic of critical instability near the superconducting transition edge. Furthermore, the device remains stable under bias, suggesting that global electro-thermal instability is unlikely the primary cause.

Conversely, the two-body model developed by Bennett et al. [51] provides a compelling explanation. In this framework, the lateral gold banks act as auxiliary heat capacities thermally coupled to the main TES thermometer. Although photons are absorbed directly in the TES, the heat subsequently flows into these banks, which equilibrate on a different timescale compared to the primary TES-bath link. This creates a compound calorimeter system (TES + Banks). Under specific thermal coupling conditions, the solutions to the coupled differential equations can become complex conjugates, resulting in an underdamped thermal response. This manifests physically as a damped oscillation or "bumps" superimposed on the decay tail, exactly as observed.

Therefore, we fitted the single-bank data using a model derived from the Bennett framework, including a real component (rise and decay) and a damped oscillating component:

$$A(t) = A_0 + A\left(e^{-\frac{t-t_0}{\tau_{\mathrm{el}}}} - e^{-\frac{t-t_0}{\tau_{\mathrm{etf}}}}\right) + A_{\mathrm{osc}} e^{-\frac{t-t_0}{\tau_{\mathrm{osc}}}} \cos(\pi\omega_{\mathrm{osc}}(t - t_c)). \tag{3.2}$$

From this refined fit, we obtained an electrical rise time $\tau_{\mathrm{el}} = (180 \pm 3)$ ns and a thermal recovery time $\tau_{\mathrm{etf}} = (822 \pm 3)$ ns. The oscillatory component shows a decay constant $\tau_{\mathrm{osc}} = (582 \pm 3)$ ns. The quality of the fit supports the multi-body thermal interpretation, although a residual contribution from electro-thermal feedback dynamics cannot be entirely excluded without further impedance measurements.

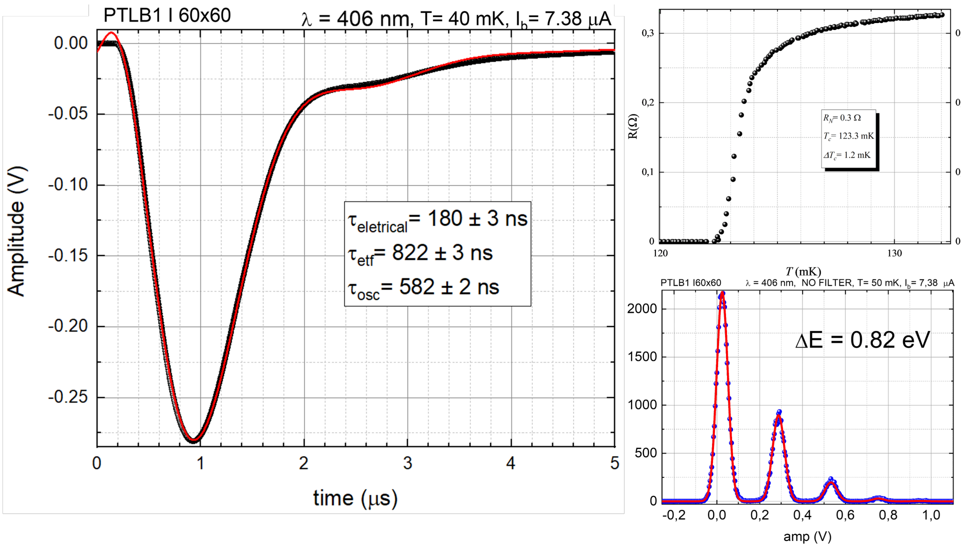

Fig. 3.10 Characterization results from a (60×60) μm^2 TiAu TES and one (2×60) μm^2 Au bank covering one of the edges. On the left, pulses for 1 (black), 2 (red) and 3 (green) photon detection events at $\lambda = 406$ nm. Both the rise and the electro-thermal time are (423 ± 11) ns and (426 ± 2) ns, respectively. On the right, its R *vs* T curve measured through a dc-SQUID in photon counting set-up with a $T_c \sim 123$ mK and the histogram from photon counting with $\Delta E = 0.82$ eV.

We performed a similar analysis for the TES with two banks (Fig. 3.11). In this case, the thermal conductance increased further to $G = (657 \pm 5)$ pW/K, suggesting its dependence by the banks. Since there are two distinct gold banks, the system should theoretically be described by a 3-body model (TES + Bank 1 + Bank 2). Assuming the two banks are nearly identical except for small fabrication defects, their individual responses can be modeled as two oscillations with slightly different frequencies, $\omega_3 = \langle\omega\rangle + d\omega$ and $\omega_4 = \langle\omega\rangle - d\omega$, and similar amplitudes. By factoring the common terms, the superposition of these two oscillations can be mathematically described by the product of two cosines, resulting in a modulation of the oscillation envelope. The fitting function thus becomes:

$$A(t) = A_0 + A\left(e^{-\frac{t-t_0}{\tau_{\mathrm{el}}}} - e^{-\frac{t-t_0}{\tau_{\mathrm{etf}}}}\right) + A_{\mathrm{osc}}e^{-\frac{t-t_0}{\tau_{\mathrm{osc}}}}\cos(\pi\omega_{\mathrm{osc}}(t-t_c))\cos(\pi d\omega_{\mathrm{osc}}(t-t_c)). \tag{3.3}$$

Fitting the experimental data with Eq. 3.3 yields a fast electrical rise time $\tau_{\mathrm{el}} = (43 \pm 3)$ ns and a thermal recovery time $\tau_{\mathrm{etf}} = (432 \pm 8)$ ns. The oscillation decay time is $\tau_{\mathrm{osc}} = (270 \pm 5)$ ns. The parameter related to the frequency difference, defined as $d\omega_{\mathrm{osc}} = d\omega/(\langle\omega\rangle^2 + d\omega^2)$, was found to be (-280 ± 5) ns.

The significantly reduced τ_{etf} compared to the single-bank device confirms that the gold banks effectively increase the thermal conductance to the substrate. Furthermore, the compatibility of the fitted model with the experimental data suggests that the complex pulse shape is consistent with the superposition of the thermal responses from the multiple gold bodies, providing a plausible description of the internal thermal dynamics.

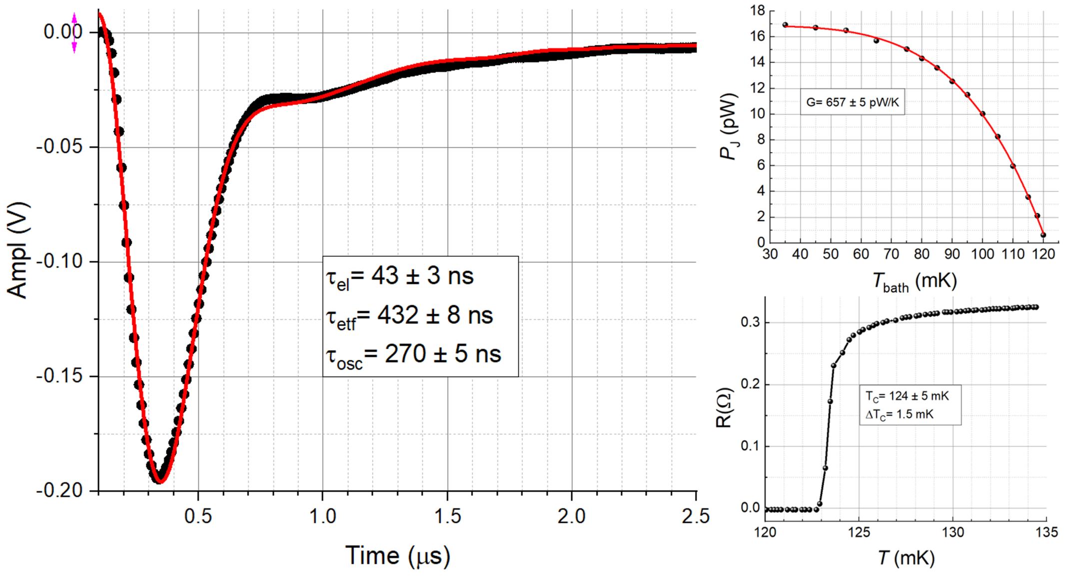

Fig. 3.11 Characterization results from a (60×60) μm^2 TiAu TES with Nb wiring and two (2×60) μm^2 Au banks covering the edges. On the left, pulse for 1 photon detection at $\lambda = 406$ nm; black represents the data, red represents the fit. The rise time is ~ 80 ns and the electro-thermal feedback time is 244 ns, half that of the single-bank device. On the top right, the Joule power vs T_{bath} from which we obtained $G = 657$ pW/K. On the bottom right, its R *vs* T curve measured through a dc-SQUID in photon counting set-up with a $T_{\mathrm{c}} \sim 124$ mK.

In conclusion, this type of gold bank appears to be advantageous, but only for larger TESs. The volume of these additional gold structures influences both G and C, but the effect on C is negligible for TESs where the bare C is much larger than the C of the banks. However, G can be increased by a factor of 4, leading the total pulse time to 1.3 μs for a (60×60) μm^2 TES made of 15 nm of Ti and 30 nm Au on a Si (500 μm)/ SiO$_2$ (140 μm)/ SiN$_x$ (480 μm).

It is worth noting that the pulses shown in Fig. 3.10 and Fig. 3.11 exhibit a characteristic long tail, deviating from a simple single-exponential decay. This behavior can be explained using the two-body analytical model developed by Bennett et al. [51]. In this framework, the lateral gold banks act as auxiliary heat capacities (absorbers) that are coupled to the main TES thermometer via a finite internal thermal conductance. Consequently, the device behaves as a compound calorimeter characterized by multiple time constants rather than a single thermal relaxation time. The observed tail arises from the internal thermalization process between the main TES film and these lateral banks, which equilibrate on a slower timescale compared to the primary feedback loop.

In addition to the previous samples, we have fabricated other TESs with titanium wirings. We have thermally and electrically characterized them, but unfortunately not optically, as they were unable to discriminate photons at 1540 nm. We believe that the origin of this limitation may be related to the confinement of quasi-particles, which depends on the energy gap difference between the TES and the wiring material. In this framework, the use of Ti wiring might not have provided sufficient quasi-particle confinement, leading to the loss of the PNR capability. These devices will be characterized at 406 nm in the near future to extrapolate their pulse times.

In the electrical characterization, we measured extremely sharp ΔT_c, between 1 mK and 2 mK, with a minimum of $\Delta T_c = 0.75$ mK for a (20×20) μm^2 TES.

While the thermal characterization of a (60×60) μm^2 device of this series was performed with the usual power vs bath temperature curve (Fig. 3.12), we obtained a value of G greater than the previous TESs, equal to (839 ± 126) pW/K. Since the time pulse does not depend on the energy, we expect this TES to have τ_{etf} close to 190 ns and $\tau_{\mathrm{tot}} \sim 1$ μs.

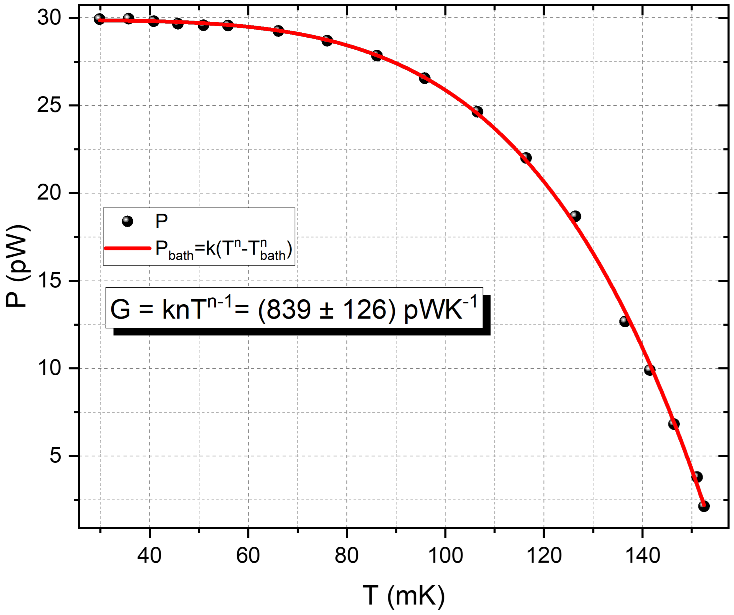

Fig. 3.12 Curve of the Joule power $P_{J0} = R_0 i_0^2$ vs the bath temperature T_{bath} for a $(60 \times 60)\ \mu\text{m}^2$ TiAu TES with Ti wiring and two $(2 \times 60)\ \mu\text{m}^2$ Au banks. R_0 and i_0^2 have been obtained by the i_0 vs I_{bias} curve.

3.3.3 Future Work and Discussion

The experimental results presented in this chapter demonstrate that lateral gold banks are a powerful tool for engineering detector speed. By introducing these additional structures, we achieved a significant increase in thermal conductance to the bath (G), reducing the effective recovery time τ_{eff} to the order of hundreds of nanoseconds.

However, the detailed pulse shape analysis revealed that these banks introduce additional complexity. The observed "bump" is best described by a multi-body thermal model, where the banks act as auxiliary heat capacities exchanging heat with the TES. While the fit results strongly favor this thermal interpretation, we acknowledge that the high speed of these devices pushes them towards the limits of electro-thermal stability. Therefore, a mixed regime where both multi-body thermal dynamics and electro-thermal feedback effects contribute to the pulse shape remains a possibility.

While the speed improvement is evident, the energy resolution obtained ($\Delta E \approx 0.82$ eV) suggests a trade-off. As discussed in [8], increasing G often leads to a reduction in the temperature sensitivity α, thereby worsening the energy sensitivity. For high-G devices, the increase in heat dissipation requires a higher bias current I_0, reducing the ratio I_{c0}/I_0 and consequently α (Eq. 1.31).

To mitigate this effect and optimize the bank design, we propose investigating two primary strategies:

- **Geometric Optimization of Banks:** Future fabrication runs will investigate Au structures with different geometries, areas, and thicknesses. The goal is to tune the thermal coupling between the TES and the banks to push the system from the underdamped (oscillating) regime towards a critically damped regime, eliminating the secondary "bump" while maintaining fast recovery.
- **High-Resistance Designs:** To counteract the reduction of α, we can adopt the approach of increasing the normal resistance R_N (e.g., via high aspect-ratio designs [8]). This reduces the necessary operating current I_0, restoring a higher I_{c0}/I_0 ratio and recovering α and energy resolution without sacrificing the high G provided by the banks.

In conclusion, while the current gold bank design successfully addresses the speed requirements for the SEQUME project, future work will focus on refining the bank geometry and TES aspect ratio to simultaneously achieve high speed, robust stability, and high energy resolution.

Chapter 4

Electron Detection

The results presented in this chapter have also been published in [52].

This chapter focuses on the optimization of Transition-Edge Sensors (TESs) for single-electron detection within the framework of the **PTOLEMY** project. We first outline the scientific goals of the project, specifically the detection of the Cosmic Neutrino Background (CνB). We then describe the fabrication and characterization of large-area TiAu TESs designed for this purpose. Unlike photon detection, electron detection involves complex scattering dynamics. We aim to demonstrate that standard TES temporal resolution is insufficient to discriminate Secondary Electrons (SE) from primary events based on timing alone. To this end, we present an analytical model describing the flight times and ranges of SEs and Back-Scattered Electrons (BSE). Finally, we develop a geometric cross-section model to estimate detection probability and propose design strategies to enhance the collection efficiency of primary electrons.

4.1 Project: PTOLEMY

The **PTOLEMY** [53] project is a groundbreaking experimental proposal aimed at detecting the cosmic neutrino background (CνB)—a sea of low-energy neutrinos that have permeated the universe since roughly one second after the Big Bang. These relic neutrinos are a direct prediction of the Big Bang model and are expected to be the oldest observable particles in the universe.

Unlike cosmic microwave background photons, which decoupled around 380,000 years after the Big Bang, relic neutrinos decoupled much earlier, making them a unique probe into the universe's infancy. However, due to their extremely low energy (on the order of 10^{-4} eV) and weak interactions, detecting them presents an enormous experimental challenge.

PTOLEMY aims to measure these neutrinos through the process of neutrino capture on tritium:

$$\nu_e + {}^3\mathrm{H} \rightarrow {}^3\mathrm{He} + e^-$$

This reaction has no energy threshold and results in an electron with an energy slightly above the endpoint of tritium beta decay. By precisely measuring the electron energy spectrum near this endpoint, PTOLEMY seeks to identify the excess events that would signify relic neutrino interactions.

This measurement would not only confirm a major prediction of the Standard Cosmological Model but also provide constraints on the absolute neutrino mass scale, the number of neutrino species, and potentially probe new physics beyond the Standard Model.

The project incorporates several advanced technologies:

- Graphene-based tritium targets for uniform and stable tritium deposition.
- Electromagnetic filters to pre-select electrons near the endpoint energy.
- TES for high-resolution calorimetric measurements.
- RF-based trigger and tracking systems to enhance event identification and background rejection.

The event rate is related to the number of tritium atoms in the target, to the cross section for neutrino capture on tritium and to the local density of relic neutrinos predicted by standard cosmology. The PTOLEMY collaboration estimates the expected event rate to be ~ 9.5 events/year for 100 g of tritium [54] from relic neutrino capture, with the relic neutrino density modeled as a uniform Fermi-Dirac number density throughout space. In terms of energy, the expected footprint of a relic neutrino capture is a peak in the emitted electron spectrum at an energy larger than the β-decay endpoint by twice m_ν [55].

The target for our TESs is the capability to detect low-energy electrons with an energy resolution of 0.1 eV at 10 eV (standard deviation $\sigma_\mathrm{e} = \frac{\Delta E_\mathrm{FWHM}}{\sqrt{8\ln 2}} = 50$ meV).

4.2 Fabrication and optical characterization

The TESs for PTOLEMY were fabricated using a TiAu bilayer with Nb wiring and an area of $100 \times 100\ \mu\mathrm{m}^2$. This large area was selected for the first phase of the project to ensure the collection of electrons, albeit at the expense of energy resolution. The first chip contained 4 TESs and a shield to prevent the substrate from charging due to electrons implanted at its surface, as shown in Fig. 4.1. One of the TESs was thermally characterized, showing a transition with $T_\mathrm{c} = 84$ mK and $\Delta T_\mathrm{c} = 1.5$ mK, and then optically characterized, revealing a $\Delta E_\mathrm{FWHM} = 4.06$ nm ($\sigma_\mathrm{e} = 1.72$ eV) and response times of $\tau_\mathrm{el} = (250 \pm 0.5)$ ns and $\tau_\mathrm{etf} = (9.48 \pm 0.03)\ \mu$s. The chosen wavelength was 406 nm, corresponding to 3.1 eV, which is the highest photon energy that we can transmit through the fiber.

The shield was realized with 300 nm of SiO_x covered by 30 nm of Au. The SiO_x deposition was performed in two steps to guarantee good isolation. Specifically, we deposited the first half and then let the sample rest in air for one hour. The exposure to an oxygen-rich environment ensures the oxidation of the SiO_x surface, closing potential conductive pinholes that arise from defects.

In the second chip, we realized 8 TESs with alternating areas of $100 \times 100\ \mu\mathrm{m}^2$ and $60 \times 60\ \mu\mathrm{m}^2$, similar to the first chip. The physical proximity of the TESs ensured good uniformity during deposition; thus, they show almost identical T_c, between 92.5 mK and 94 mK, and sharp transitions, with ΔT_c in the range $1-2$ mK. This second chip will be used for the next runs of electron detection.

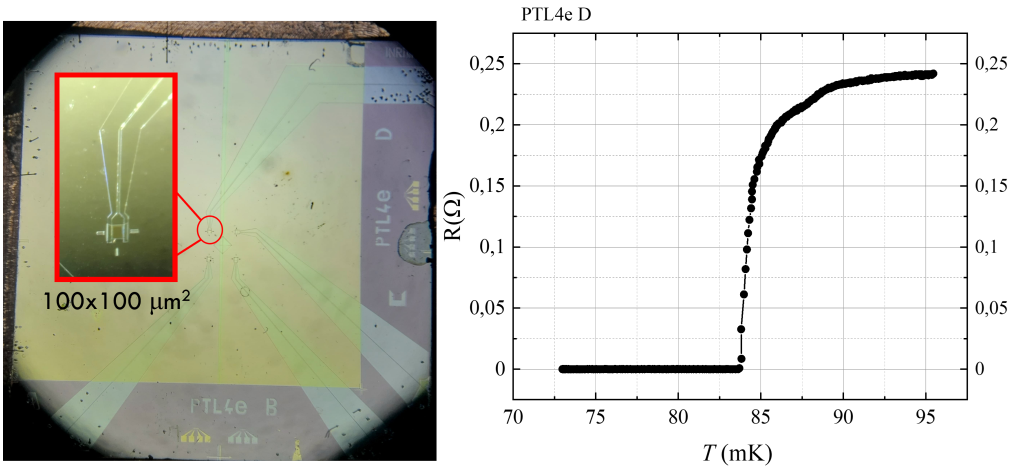

Fig. 4.1 On the left: first chip for the PTOLEMY project with four $100 \times 100\ \mu\mathrm{m}^2$ TESs. The top left TES has been used for electron detection, while the two on the right have been covered by the shield to measure the thermal effect of electrons absorbed by the shield without direct detection (since the electron source was much wider than the distance between the TESs). On the right: Superconductive transition of top left TES with a $T_\mathrm{c} = 84$ mK and $\Delta T_\mathrm{c} = 1.5$ mK.

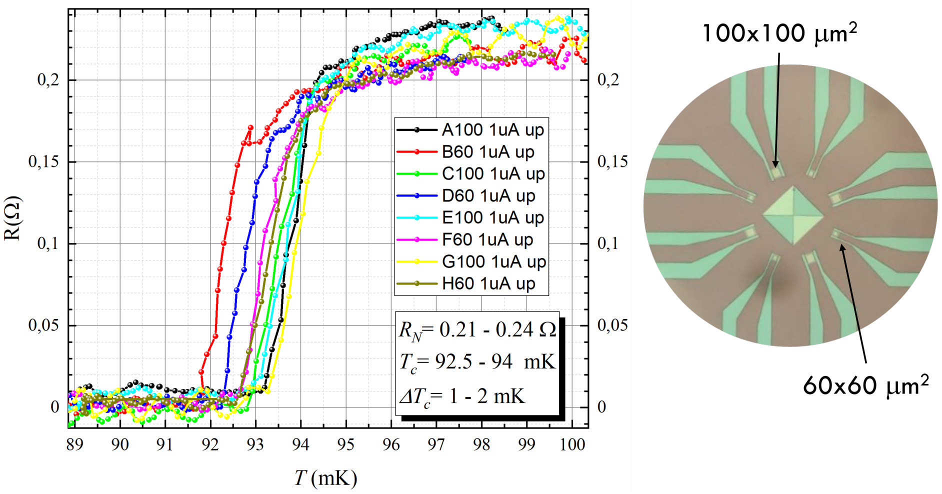

Fig. 4.2 On the left: superconductive transitions of the 8 TESs in the second chip for the PTOLEMY project, measured with a current of 1 μA. All the TESs show almost identical T_c, between 92.5 mK and 94 mK, and sharp transitions, with ΔT_c around $1-2$ mK. On the right: chip with all the TESs physically close to the center of the chip and with areas of $100 \times 100\ \mu\mathrm{m}^2$ or $60 \times 60\ \mu\mathrm{m}^2$. This physical proximity ensures good uniformity during the deposition and in the behavior of the various TESs.

4.3 Results

Electron detection with TESs has been demonstrated in [56] for electrons in the energy range $0.3-2$ keV achieving $\sigma_e = 17$ eV, and in [52] for energies < 100 eV, where we describe the work done so far. We succeeded in measuring electrons with energy $90-101$ eV with a resolution $\sigma_e = 0.8-1.8$ eV using shielded $100 \times 100\ \mu\text{m}^2$ TESs.

The measurement setup, schematically depicted in Fig. 4.3, consists of a cryogenic stage housing the detector and the source. Carbon Nanotubes (CNTs) act as the electron source, driven by a high voltage bias to generate field emission. To prevent charging effects on the insulating substrate, the TES wiring and substrate are protected by a grounded Au shield. The source plate and detector plate are separated by sapphire spacers, maintaining a precise source-to-detector distance of approximately 500 μm.

The detection counts are shown in the histogram on the right of Fig. 4.3. The peak on the far right corresponds to the full absorption of Primary Electrons (PE), while the counts at lower energies (amplitudes) are due to inelastically scattered electrons and Secondary Electrons (SE).

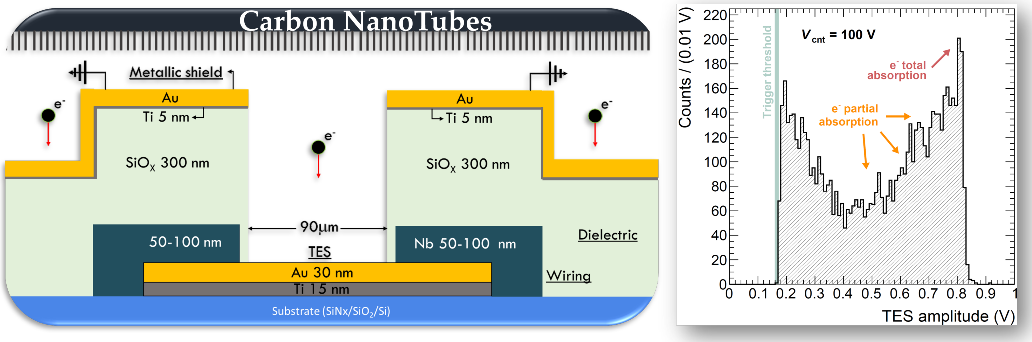

Fig. 4.3 Left: schematic of the measurement setup. Carbon nanotubes (CNTs) act as the electron source by applying high voltage, while the TES substrate and wiring are protected by a grounded Au shield. The TES plate and the CNT plate are separated by sapphire spacers. The CNT source was 3 mm^2 wide and placed 500 μm from the TES. Right: histogram obtained from electron detection with a $100 \times 100\ \mu\text{m}^2$ TES having the transition at $T_c = 84$ mK.

Most importantly, in [52] we showed that energy resolutions for photons and electrons are compatible for the same energies. Since the target energy resolution at

10 eV is a feasible goal, this is a promising result for incoming upgrades and allows us to study the energy resolution with photons before moving to electrons, greatly simplifying the work.

4.4 SE lifetimes and TES discrimination

The fundamental difference between photon detection and electron detection lies in the generation of inelastically scattered electrons and secondary electrons. We want to demonstrate that if a Primary Electron (PE) reaches the TES and generates Secondary Electrons (SE) or is reflected, these secondary events occur so rapidly that the TES is unable to distinguish them from the primary event.

Consider a small region close to the center of the TES. When an electron arrives, we have a simplified case of an electron generated by the CNT plane at a voltage V_{CNT} falling onto the TES held at 0 V. The energy measured by the TES for a fully absorbed primary electron is $E_{\mathrm{PE}} = e\Delta V = eV_{\mathrm{CNT}} - \phi_{\mathrm{TES}}$, where e is the electron charge and $\phi_{\mathrm{TES}} = 4.38 \pm 0.03$ eV is the work function of the TES [52]. A secondary electron or inelastically scattered electron (SE) emitted from the TES will have a fraction of this energy $E_{\mathrm{SE}} = rE_{\mathrm{PE}}$. We can remain generic by assuming $r \in [0,1]$ and calculating the flight time assuming a simple parabolic motion with a range that covers only the TES area. The flight time is given by the classical expression:

$$t = 2\sqrt{\frac{2\,r\,m_e}{E_{\mathrm{PE}}}}d, \tag{4.1}$$

where m_e is the mass of the electron and d is the distance between the CNT and the TES.

The current setup does not allow independent control of emission and acceleration energies. To overcome this limitation and study flight times more generally, we can conceptually introduce a decoupling plane between the CNT and the TES, as illustrated in Fig. 4.4. This plane allows us to distinguish between the voltage applied to generate electrons (V_{CNT}) and the voltage used to accelerate them toward the TES (V_{II}). In this generalized configuration, d represents the distance between the decoupling plane and the TES. The kinetic energy of the primary electron is regulated by the voltage of the decoupling plane as $E_e = eV_{\mathrm{I}} = e(V_{\mathrm{II}} + V_{\mathrm{CNT}} - \phi_{\mathrm{TES}})$, where

V_{CNT} is the voltage difference between the CNT and the decoupling plane, and V_{II} is the voltage difference between the decoupling plane and the TES. Moreover, we add a possible emission angle α between the SE trajectory and the TES surface. The flight-time equation is then modified as:

$$t = 2d\cos(\alpha)\sqrt{\frac{2m_e}{e}}\frac{\sqrt{rV_{\mathrm{I}}}}{V_{\mathrm{II}}}. \tag{4.2}$$

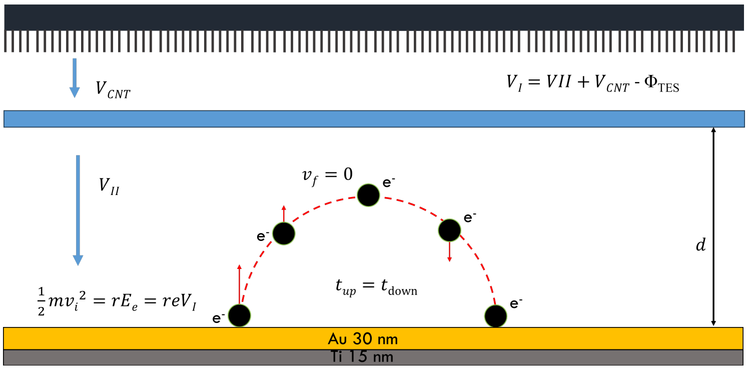

Fig. 4.4 Schematic of the motion of inelastically scattered electrons and secondary electrons in a set-up for electron detection with TES equipped with a decoupling plane. On top are the CNTs as electron source while on the bottom is the TiAu TES. In the middle there is the decoupling plane (light blue rectangle) at a distance d from the TES. If we consider only electrons with trajectory confined in the central region of the TES, we can simplify the problem with a parabolic motion in a constant and uniform electric field. Our setup in [52] was not equipped with a decoupling plane and can be represented simply by removing it, substituting $V_{\mathrm{I}} = V_{\mathrm{CNT}} - \phi_{\mathrm{TES}}$.

Using Eq. 4.1, we calculate the flight times as a function of the energy fraction r of the SE for various configurations, as shown in Fig. 4.5. Specifically, considering a PE with energy 100 eV (our measurement limit) and a CNT-TES distance of 1 mm (larger than our actual $d = (600 \pm 50)\ \mu$m), the green curve shows that the flight time is $t < 2$ ns even for a reflected PE ($r = 100\%$). Crucially, this satisfies the condition $t \ll \tau_{\mathrm{etf}}$, where $\tau_{\mathrm{etf}} = 9.48\ \mu$s for our device. This confirms that if a PE reaches the TES and is reflected or generates SEs, they return to the detector on a timescale much shorter than its thermal response time, making the events indistinguishable.

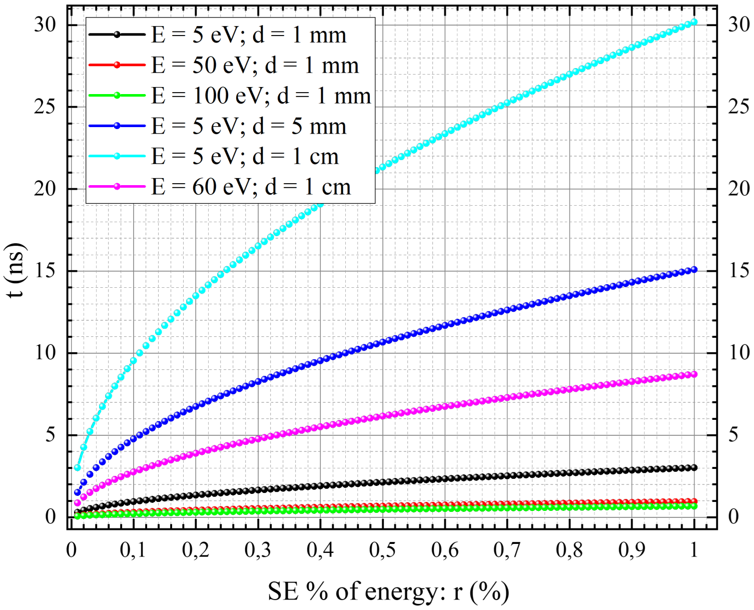

Fig. 4.5 Simulation of the flight times for inelastically scattered electrons and secondary electrons for different energies of the primary electron E generating them and distance between the CNT and the TES d. Even for energies as low as 5 eV and distances as large as 1 cm, the SEs have flight times smaller than $\sim$ 30 ns (light blue curve), which are negligible compared to our usual TES time responses.

In Eq. 4.1 and Fig. 4.5, we did not take into account the factor $\cos(\alpha)$ in Eq. 4.2 because the condition of a SE generated from the TES and falling back into the TES is $X \leq L$ (where L is the TES side), which leads to:

$$\alpha_{\max} = \frac{1}{2} \arcsin \frac{L}{4dr}. \tag{4.3}$$

In our case, the range X is:

$$X = 2rd \sin(2\alpha), \tag{4.4}$$

where α is the angle between the SE trajectory and the TES surface.

Considering r from 5% to 100%, we have $\cos \alpha_{\max} \geq 0.88$, which can be approximated to unity. This approximation has been taken considering a peak of secondary electrons at 6 eV as in Fig. 4.7.

4.5 SE range and SE from the shield

While the flight times are negligible, the range of the SEs is very large. In fact, for $d = 600\ \mu$m, in the worst-case scenario with $\alpha = \pi/4$ and $r = 1$, we can reach a range of $X = 1.2$ mm.

Then, the probability of a SE generated on the TES surface falling back onto the TES is shown in Fig. 4.6(left) and can be described with a geometrical cross-section of the form:

$$P_{\text{shield}\to\text{TES}}(r,\alpha) \propto \frac{A_{\text{TES}}}{A_C} = \frac{L^2}{\pi X^2} = \frac{L^2}{4\pi d^2}\frac{1}{r^2\sin^2 2\alpha}. \tag{4.5}$$

However, if the SE is generated outside, we need to consider the intersection area A_{int} between the TES and the circle of radius X. This term A_{int} depends on the distance between the TES and the point where the SE is generated (Fig. 4.6, right). Then, from energy conservation, we should note that for elastic scattering the input energy is equal to the final one, $E_{\text{PE}} = N_{\text{SE}}E_{\text{SE}}$. For inelastic scattering, the SE globally loses energy in the TES. Thus, the number of SEs with the same energy must satisfy $N_{\text{SE}} \leq 1/r$. Finally, we can assume a simple case using momentum conservation. If we consider only electrons moving in the vertical direction (perpendicular to the TES plane) and we assume that momentum conservation holds between the incident electron and the inelastically scattered electrons (at least in direction), $k_{\text{PE}} = \sum k_{\text{SE}}$, we can conclude that in the horizontal direction (along the TES plane) roughly each SE is associated with another SE moving in the opposite horizontal direction. That is, if one SE hits the TES, another one is moving away from the TES; thus, the probability is reduced by at least a factor of 2.

Then, the probability of a PE falling on the TES is $P_{\text{PE,TES}} = A_{\text{TES}}/A_{\text{CNT}} = L^2/(3\text{ mm})^2$, where we have that $4\pi d^2 = 4.5\text{ mm}^2 \sim A_{\text{CNT}}/2$. Only a fraction of these PEs is absorbed by the TES and not divided into SEs, but this means that the peak of the PE should be primarily formed by PEs generated by the source and directly detected by the TES. From Fig. 4.7, we can define a function representing the probability of measuring an electron with energy rE_{PE}, called $f(r)$, and with an angle α, called $f(\alpha)$. These functions will not be calculated here, but are required for the calculation of the final distribution of electrons detected by the TES in our detection configuration as a function of their energies. We can express $f(\alpha)$ as

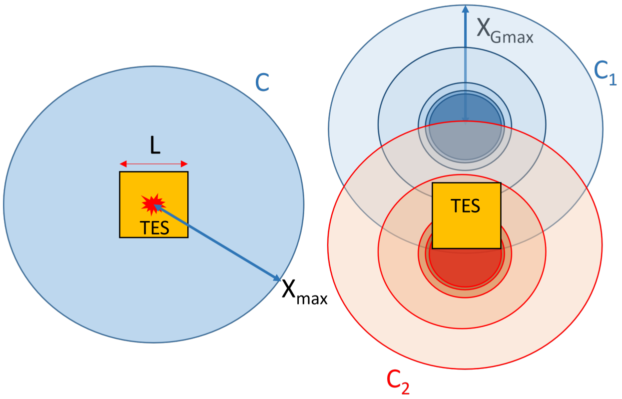

Fig. 4.6 On the left: representation of SEs generated from the center of the TES (yellow square at the center) with side $L = 90\ \mu$m and the maximal area C that can be covered in the worst case scenario in light blue, with $X_{\max} \sim 1.2$ mm being the maximal range of the SE trajectory. On the right: two areas on which the SEs fall if generated at the center of the red and blue circles outside the TES. The shade of color represents the number of SEs falling in that region. The blue circles C_1 indicate that generating points of SEs far enough from the TES have little influence on the final detection histogram, while those near the TES have a great influence on the shape of the histogram (red circles C_2).

$A\cos(\alpha/\alpha_C)$ [57–60], where A takes into account that the integral under the curve should be equal to 1. Since the electrons scattered or re-emitted from the TES are reflected back to it unless their angle is $\alpha \geq \alpha_{\max}$, the probability as a function of r for electrons only related to the TES is $P_{\text{TES}\to\text{TES}}(r) = f(r)$ with perfect energy and time discrimination. The probability for all the allowed angles is $F_\alpha = \int_{\alpha_{\max}}^{90^\circ} f(\alpha)d\alpha$. The overall probability is then $P_{\text{TES}\to\text{TES}}(r) = f(r)F_\alpha$.

From Fig. 4.7, we consider that $f(\alpha) = A\cos(\alpha/\alpha_C)$ is 0 at $\alpha \sim 40^\circ$, obtaining $\alpha_C \sim 40^\circ/(\pi/2) \sim 0.44$. From $\int_{\alpha_{\max}}^{90^\circ} f(\alpha)d\alpha = 1$, we obtain $A = 1/\alpha_C \sim 2.27$ and we can roughly approximate F_α as $1 - \sin(\alpha_{\max}/\alpha_C)$. Eq. 4.3 shows that in our case $\alpha_{\max}(r = 10\%) = 12.3^\circ$, while we have $\alpha_{\max}(r = 5\%) = 28.3^\circ$. Then, for $r > 10\%$ we can use the rough approximation $F_\alpha \sim 1 - \alpha_{\max}/\alpha_C$ and $\alpha_{\max} \sim L/(8dr)$, obtaining $F_\alpha \sim 1 - L/(8dr\alpha_C)$.

We can then remove the angle dependency from Eq. 4.5 by integrating the angle dependencies with $f(\alpha)$ as:

$$P_{\text{shield}\to\text{TES}}(r) = \frac{L^2}{4\pi d^2 r^2}\int_{\alpha_{\max}}^{90^\circ} \frac{f(\alpha)}{\sin^2 2\alpha} = \frac{L^2}{4\pi d^2 r^2} C_\alpha. \tag{4.6}$$

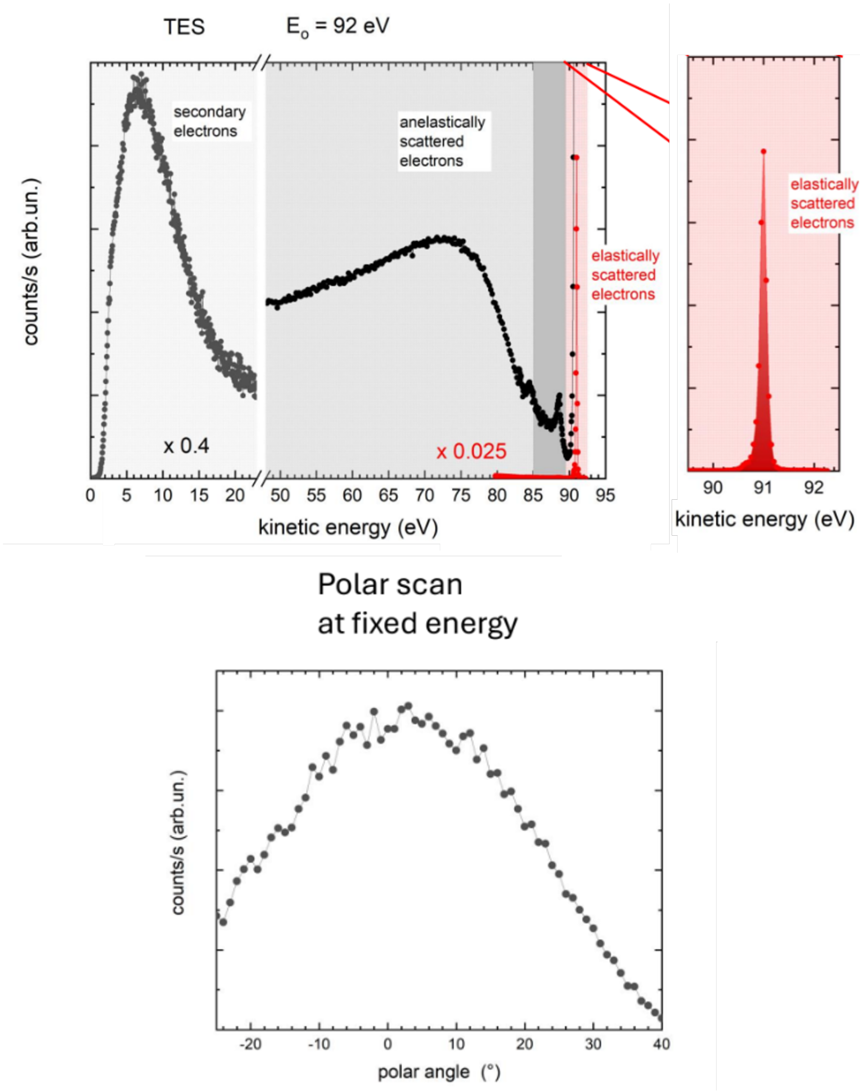

Fig. 4.7 Characterization of a TiAu film with the same thickness as our TESs, performed in Roma3. The measurement of electron reflectivity as a function of energy shows a Gaussian peak corresponding to the PE, an asymmetric dominant peak at 6 eV corresponding to secondary electrons, and a small peak related to inelastically scattered electrons with a long left tail. The measurement with respect to the angle at fixed energy shows that the maximum counts occur for angles close to the normal of the surface and decrease to 0 just above 40°.

Finally, we can sum together all the contributions:

$$P_{\text{detection}}(E) \sim \left[\frac{A_{\text{TES}}}{A_{\text{CNT}}} F\alpha f(rE_{\text{PE}}) + \frac{A_{\text{shield}}}{A_{\text{CNT}}} C\alpha \frac{L^2}{4\pi d^2 r^2} f(E_{\text{PE}}(r+\frac{h}{d}))\right] e^{-\frac{(E-rE_{\text{PE}})^2}{2\sigma}}, \tag{4.7}$$

where h is the distance between the shield and the TES, i.e., the SiO_x thickness $h \sim 300$ nm. This term accounts for the energy increase of electrons from the plane due to the free fall to the TES, equal to $eVh/d \sim E_{\text{PE}}/2000 \sim 50$ meV. Moreover, $A_{\text{shield}} \sim \pi X^2 - A_{\text{TES}} \sim 2d$, and σ can be attributed to the TES and the CNT for the PE. Finally, if the detection time of the TES is much larger than the flight time of the SE, as in our case, the first term simplifies as:

$$P_{\text{TES}\to\text{TES}}(E) \sim \frac{A_{\text{TES}}}{A_{\text{CNT}}} \left[I(E_{\text{PE}}) + X((1-r)E_{\text{PE}})\right] e^{-\frac{(E-rE_{\text{PE}})^2}{2\sigma}}, \tag{4.8}$$

where $I(E_{\text{PE}}) = 1 - F\alpha f(rE_{\text{PE}})$ is the number of electrons with energy E_{PE} and $X((1-r)E_{\text{PE}}) = F\alpha f((1-r)E_{\text{PE}})$ is the number of events detected as multiple electrons recollected by the TES with a loss of energy caused by a fraction of SEs escaping due to their emission angles. More importantly, long detection times mix the events of the two species of electrons (from TES to TES and from shield to TES).

From these considerations, we realized that the main contribution for the left peak comes from the SE generated in the Au shield, whatever the distribution of energy for the SE, and falling on the TES. We performed measurements reducing the source area and using a $60 \times 60\ \mu\text{m}^2$ TES and, in fact, we obtained a much cleaner histogram as in Fig. 4.8a (a). Compared to the previous histogram, here we can clearly see that the PE peak remains the highest peak until we move to low energy, where we find a left peak that we identify with the SE peak from the shield. This peak is very sharp and asymmetric (Fig. 4.8b (b)), similar to the one in Fig. 4.7.

4.6 Detection efficiency and future works

Achieving high efficiency in electron detection with TESs is a significant challenge because SEs cannot be avoided, and a simple uniform electric field perpendicular to the TES plane can confine them only in the vertical direction. This is a challenging

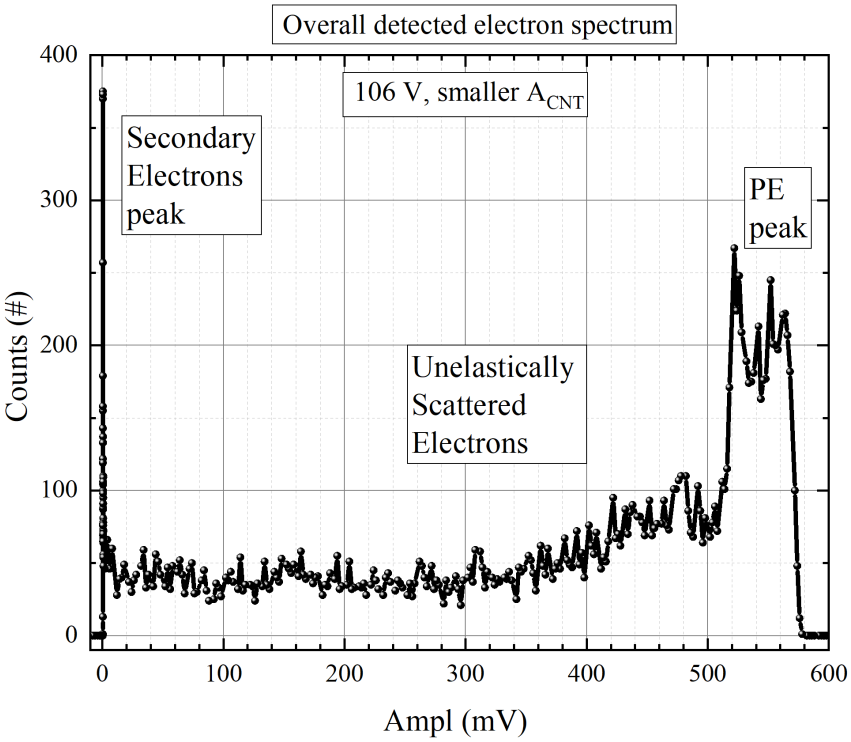

(a) Histogram for electron detection obtained with smaller CNT area with a $60 \times 60\ \mu m^2$ TES.

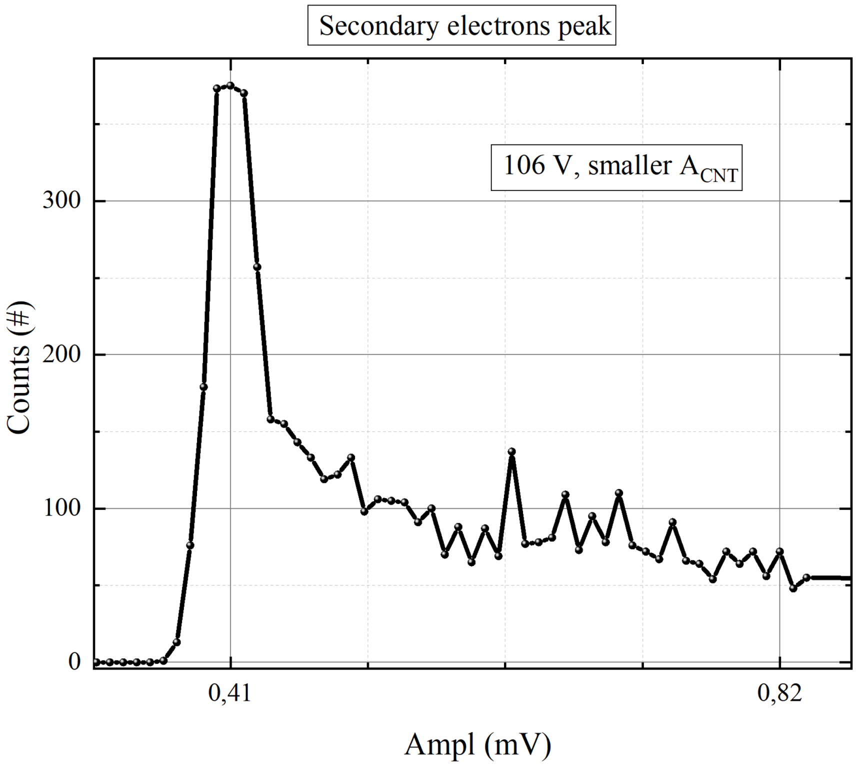

(b) SE peak zoomed from the second histogram obtained with smaller CNT area with a $60 \times 60\ \mu m^2$ TES.

Fig. 4.8 Results for smaller CNT area setup. (a) Full energy spectrum histogram. (b) Detail of the secondary electron peak.

target, but fundamental for the PTOLEMY project. For this task, we will try three main solutions.

The first is to reduce the electron source area in order to reduce the amount of SEs from outside and border regions of the TES. This could be achieved by reducing the CNT area or using a metallic nanometric tip as the electron source. Increasing the TES active area would also geometrically reduce the impact of border events; however, this approach is disfavored as it increases the sensor's heat capacity, thereby degrading the energy resolution, which is a critical constraint for the PTOLEMY experiment.

The second solution is to use a hemispherical cover as a decoupling electrode, where the pole is the electron source. In this solution, all secondary electrons and scattered electrons should experience a force parallel to their trajectories and fall back on the TES with their starting energy. The difficulties in this solution are the correct alignment and positioning. Moreover, the field produced by a hemispherical cover could suffer from inhomogeneity due to, at least, the need for a hole for the TES wiring. These solutions could work for an electron source near the TES, but in the final experiment, the electron will come from outside a cryostat, and so the TES needs a way to be intrinsically efficient.

The third idea is to modify the TES surface to create a nested structure. We can produce 3D gold poles, like those in [61], on top of the TES surface to increase the cross-section between SEs and the TES surface. With optimized parameters, a geometric trapping effect could emerge, significantly enhancing the capture probability (analogous to a particle trapped in a forest of pillars).

4.7 Conclusions

The PTOLEMY project represents a pioneering effort in the direct detection of relic neutrinos from the early universe, leveraging a combination of novel target design, high-precision energy filtering, and ultra-sensitive cryogenic detectors. While the expected event rate is extremely low—on the order of a few events per year—the scientific payoff in terms of cosmological and particle physics is significant.

This work has contributed to the fabrication and study of the first low-energy detection with TESs specifically designed for PTOLEMY's goals. The large-area fabricated TESs demonstrated excellent superconducting transitions and time responses, validating their potential for single-electron detection.

A key challenge remains the efficient discrimination of primary, secondary, and scattered electrons. We showed that SEs are emitted with sub-nanosecond delays, too short to be temporally separated from the primary signals by TESs with current time resolutions. This is an advantage for the electron detection. However, the large range of scattered electrons imposes strong constraints and complications on detector design and motivates further design strategies and geometric source-detector optimizations.

Future work will focus on enhancing intrinsic detection efficiency by engineering the TES geometry, improving the electron source collimation, and implementing novel shielding and decoupling configurations. These developments will be critical not only for relic neutrino detection, but also for broader applications in ultra-low energy particle calorimetry.

Chapter 5

Longitudinal and Lateral Inverse Proximity Effect

This chapter presents a systematic study of the longitudinal and lateral inverse proximity effects on the superconducting transition of thin-film TES devices. These effects, stemming from the physical configuration of the TES and its connections, have been shown to significantly modify the transition temperature T_c and its width ΔT_c, thus impacting device performance.

Unlike previous studies [62, 63], which focused on characterizing these effects for specific material combinations, this work provides a systematic comparison across three distinct wiring materials: Niobium (Nb), Titanium (Ti), and a Titanium-Aluminum (TiAl) bilayer, applied to TiAu and AuTi TES strips. Our primary goal is to highlight the differences between this work and previous literature by demonstrating how the choice of wiring material specifically alters the T_c scaling behavior. Furthermore, we aim to prove that utilizing a top Titanium layer in the TES structure effectively suppresses the longitudinal proximity effect, offering a pathway for more stable device engineering.

5.1 Longitudinal Proximity Effect

The longitudinal proximity effect arises from superconducting leads connected at the ends of the TES structure. When superconducting leads, typically made of niobium

(Nb), are attached to the TES, they enhance the superconducting order parameter along the length of the TES film. As shown by Sadleir et al. [62, 64], the shift in the critical temperature (δT_c) due to the longitudinal proximity effect scales inversely with the square of the distance L between these superconducting leads. This happens even for the transition width ΔT_c. This effect is quantified as:

$$\delta T_{\mathrm{c},l} \propto \frac{1}{L^2}, \tag{5.1}$$

$$\Delta T_{\mathrm{c},l} \propto \frac{1}{L^2}. \tag{5.2}$$

Thus, smaller spacing between superconducting leads significantly increases T_c and widens the transition width (ΔT) as shown in Fig. 5.1, degrading sensitivity and performances of the TES [65]. This effect is often related to a weak-link behavior because the TES and its wiring form a S'SS' junction. In fact, they often show Fraunhofer-like oscillations as a function of an applied magnetic field, [62].

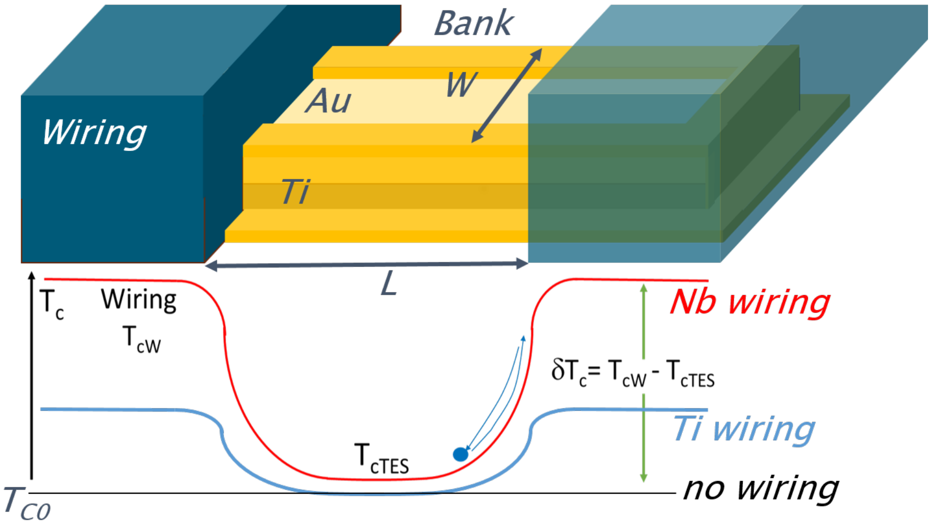

Fig. 5.1 On top: Schematic of the TiAu bilayer with gold banks and its wiring. L is the length or distance between the wirings and W is the width or distance between the edges of the bilayer. On bottom: T_c distribution respect to L given by the presence of the wiring.

5.2 Lateral inverse Proximity Effect

Conversely, the lateral inverse proximity effect is caused by normal metal structures, called "overhangs", situated laterally at the edges of the TES . This inverse proximity effect leads to a suppression of superconductivity, reducing the intrinsic T_c of the bilayer TES material [63]. Nagayoshi et al. have experimentally demonstrated this effect on Ti/Au TES bilayers with Au overhangs that arise during the etching process. They observed a significant decrease in T_c with decreasing TES width (W), which follows a scaling law similar to the one of the longitudinal proximity effect:

$$\delta T_c \propto -\frac{1}{W^2}. \tag{5.3}$$

This trend indicates that narrower TES structures suffer from a greater reduction in T_c and the usual widening of the ΔT_c related to a non-uniformity of the bilayer. This effect is critical for a fine tuning of the TES performances and to avoid that the superconductive transition is under the cryostat minimal temperature.

5.3 Material dependence

In [65], it has been shown that the longitudinal proximity effects vary on different type of wirings (Nb, Mo, Ti) and TESs (TiAu, MoAu, MoCu). In fact, the longitudinal proximity effect seems to be related to the difference between the wiring $T_{c,\mathrm{W}}$ and the TES $T_{c,\mathrm{TES}}$, the bigger this gap the higher the effect. For this study and in order to optimize out TESs, we choose wirings of niobium (Nb with $T_c = 9$ K), titanium (Ti with $T_c = 300 - 500$ mK) and aluminum (Al with $T_c = 1.2$ K) while the TiAu bilayer remains around 100 mK.

In addition, the bilayers tested are of two different kinds. The first is our usual TiAu, so that the interface between the wiring and the bilayer is with the gold, while the second is an AuTi bilayer, for which the interface is between the wiring and the titanium.

Lastly, the effect of the edge of the bilayer could, in principle, be given by gold "overhangs" or the exposed part of the titanium. In this study, we fabricated some Au banks that cover the edges for all the bilayer length, Fig. 5.1.

5.4 Design and measurements

We designed and fabricated three distinct chips to disentangle the longitudinal and lateral proximity effects and to study their dependence on the wiring material. We aim to verify if the scaling laws observed in literature hold for different material combinations and to quantify the suppression of these effects.

The chips are named "Nb", "Ti", and "TiAl" after their wiring materials. The detailed design parameters for the varying Length (L) and Width (W) series are summarized in Table 5.1. The first two chips (Nb and Ti) share the same TiAu bilayer structure (15 nm Ti / 30 nm Au). The third chip (TiAl) uses a tri-layer structure (5 nm Ti / 30 nm Au / 25 nm Ti) to avoid direct contact between Au and the Al wiring, preventing alloy formation. The wiring for this chip consists of 50 nm Ti and 150 nm Al. The native TiO_2 on the top Ti surface was removed via ion milling before wiring deposition. In the same chip, the L and W series are repeated identically with and without lateral gold rings (banks) to study edge effects. The strips with rings are indicated with the suffix "R".

Chip Name	Layer Structure	Variable Parameter	Fixed Parameter Condition
Nb	Ti(15)/Au(30)	$W \in [12, 350]$ μm $L \in [10, 300]$ μm	$L = 500$ μm $W = 100$ μm
Ti	Ti(15)/Au(30)	$W \in [12, 350]$ μm $L \in [10, 300]$ μm	$L = 500$ μm $W = 100$ μm
TiAl	Ti(5)/Au(30)/Ti(25)	$W \in [8, 150]$ μm $L \in [10, 200]$ μm	$L \in [300, 450]$ μm $W = 30$ μm (for $L < 10$ μm) $W = 60$ μm (for $10 < L < 95$ μm) $W = 100$ μm (for $L \geq 95$ μm)

Table 5.1 Summary of the geometric design parameters for the three fabricated chips. For the TiAl chip, the width W was adjusted in steps for the variable L series to accommodate the current range of the resistance bridge.

With these 3 chips, we were able to measure the longitudinal and lateral inverse proximity effects and compare the difference for different wirings on similar strips. Unfortunately, the Nb and Ti samples did not show any clear trend as a function of W. As shown in Fig. 5.2, the TiAu strips with Nb wiring had their T_c randomly spanning between 116 mK and 140 mK while increasing W, and the strip resistivities ρ followed a similar irregular behavior. Consequently, we will report only the analysis for features *vs* L for all samples.

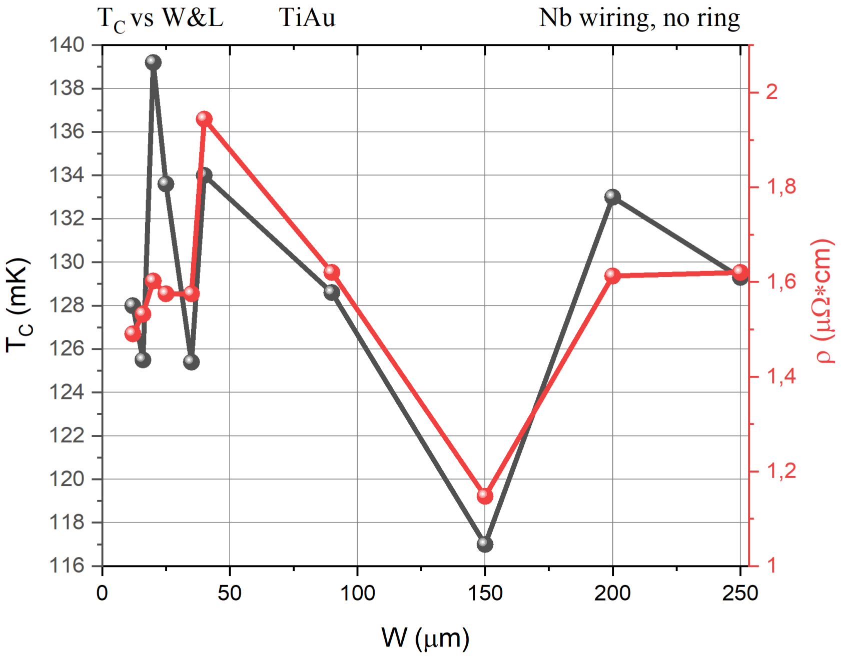

Fig. 5.2 Critical temperature T_c (black) and resistivity ρ (red) of TiAu strips with Nb wiring as a function of strip width W. No clear trend is observed, with T_c spanning randomly between 116 and 140 mK and ρ showing a similar irregular behavior.

As a first step, we verified the measurement conditions to isolate and properly address the proximity effects. We recall that T_c is influenced by the current density J flowing in a superconductor as $T_c(J) = T_c(0)(1-(J/J_c)^2)$ in the Ginzburg-Landau theory. Moreover, the Joule power dissipated in the TES P could lead to an increase of the local TES temperature, resulting in a lower measured T_c. If the measurement is performed too quickly or the Joule power is high, this could greatly affect the results. In all measurements, we used constant currents of $i = 1\ \mu$A or $i = 3.16\ \mu$A. The power P has been calculated as $P = R_N\, i^2$ and the current density as $J = i/(W\, t)$, where t is the total thickness of the strip.

Because the Nb and Ti samples are geometrically identical, Fig. 5.3 represents the conclusions for both. We can see that the trend in the T_c curve (black) cannot be described by variations in J or P. In fact, J is flat because the current and W are constant with respect to L, while P increases linearly due to the resistance R_N and its effect should be to decrease the T_c. An increase in P correspond to a decrease in T_c because the strip temperature would be actually higher than the one measured by the thermometer and, thus, the thermometer will be at a lower temperature when

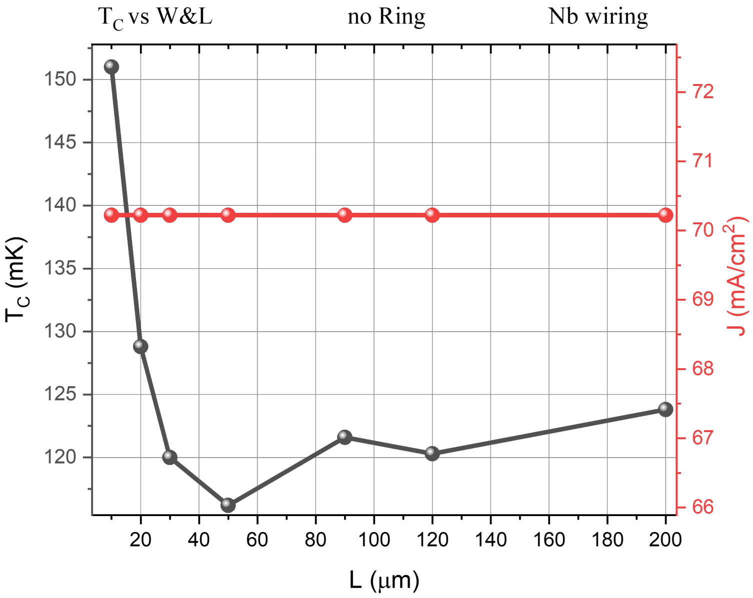

(a)

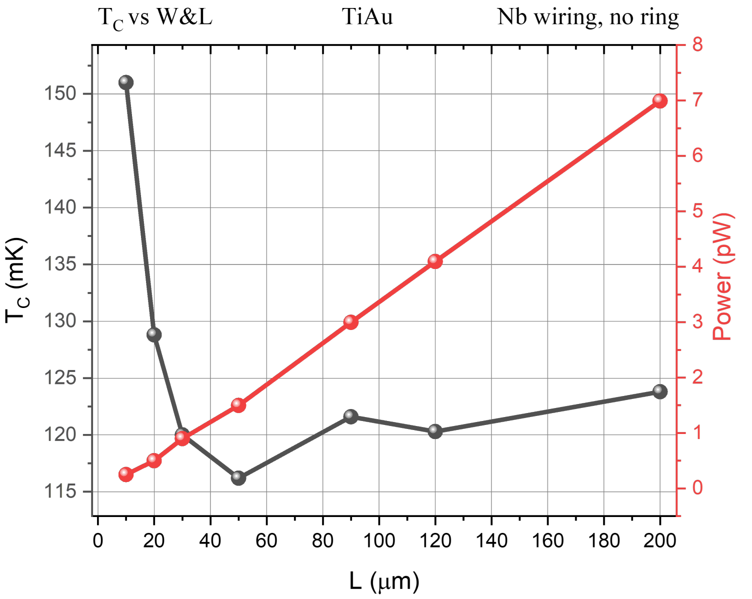

(b)

Fig. 5.3 Critical temperature analysis for the Nb sample. (a) T_c (black) and J (red) as a function of L. J is flat because the current and W are constant. (b) T_c (black) and Joule power P (red) as a function of L. P is linear with respect to L because R_N scales linearly with length.

the phase transition occurs. The slight increase in T_c can be explained by two mechanisms:

- The first involves a deviation in the effective current density J. If the actual conductive cross-section is larger than the nominal geometry (for instance, due to lithographic imperfections such as beam widening that create a series of "bulges" along the strip), the effective J would be lower than calculated. Physically, a reduction in current density is consistent with the observed increase in T_c.
- The second possibility relates to spatial non-uniformities in the film deposition. Since strips of similar lengths are often localized in specific regions of the chip, a spatial gradient in film properties could manifest as an apparent dependence on L.

However, the rising trend is quantitatively negligible respect to the drop in T_c for small L and becomes resolvable only in the regime where the longitudinal proximity effect is fully suppressed. Moreover, both these explanations cannot explain the the drop in T_c for small L because the first should behave monotonically and the second monotonically or randomly.

In the TiAl sample (Fig. 5.4), P and J show steps related to the design changes in W. Even here, the main T_c trend cannot be explained by P or J. However, in the final part of the curve, an unexpected rise of T_c appears. Since both J and P drop at those points (due to the larger width $W = 100\ \mu\text{m}$ for $L \geq 95\ \mu\text{m}$), we attribute this specific rise to the reduced heating/current density effects. Moreover, the unexpected step in T_c for the strips with $30\ \mu\text{m} \leq L \leq 70\ \mu\text{m}$ can be explained with local deposition non-uniformities. This is related to the strips positions on the chip, in fact strips with similar L are closer to each other respect to the other strips in the mask.

With these considerations suggesting that we are correctly isolating the proximity effects, we move to the results of the T_c vs L and ΔT_c vs L curves.

In Fig. 5.5, the critical temperature and transition widths for Nb wiring are shown for strips with and without Au rings. For both, clear trends as a function of L are visible. The effect of the rings (red curves) appears to be a slight reduction in T_c at the expense of a slight widening in ΔT_c.

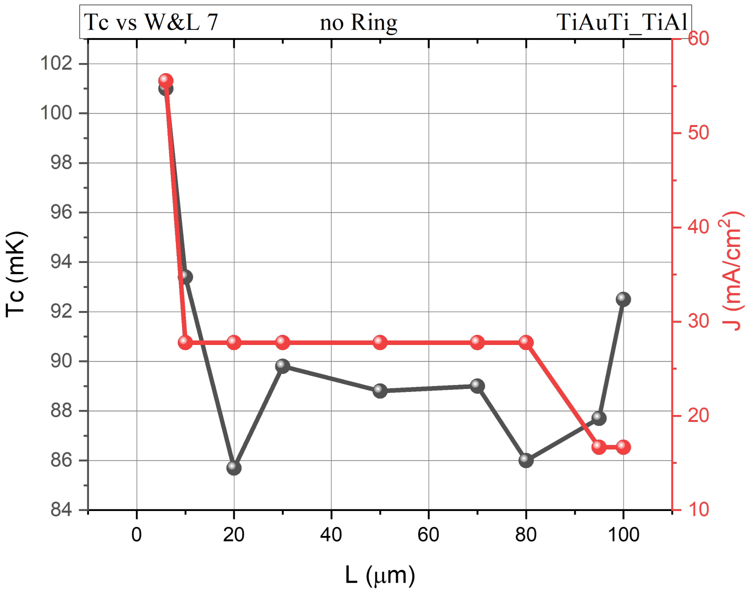

(a)

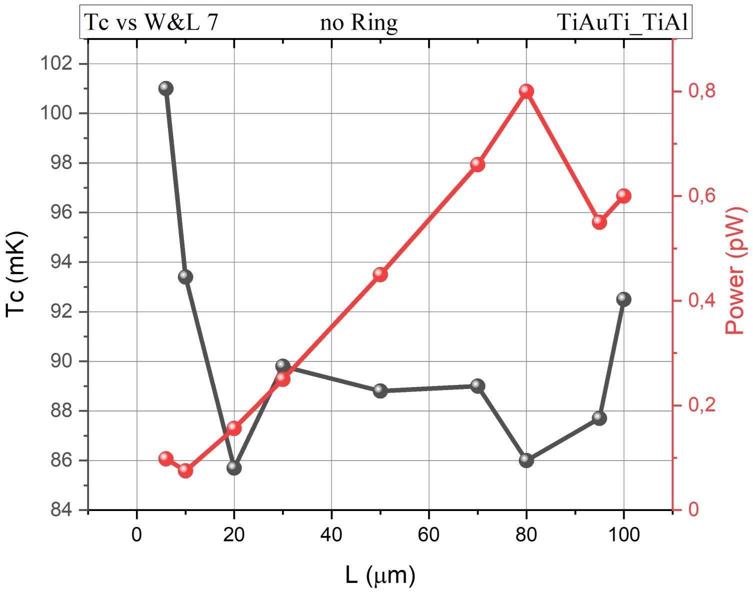

(b)

Fig. 5.4 Critical temperature analysis for the TiAl sample. (a) T_c (black) and J (red) as a function of L. J shows steps corresponding to the W design changes. (b) T_c (black) and Joule power P (red) as a function of L. The final rise in T_c correlates with the drop in power.

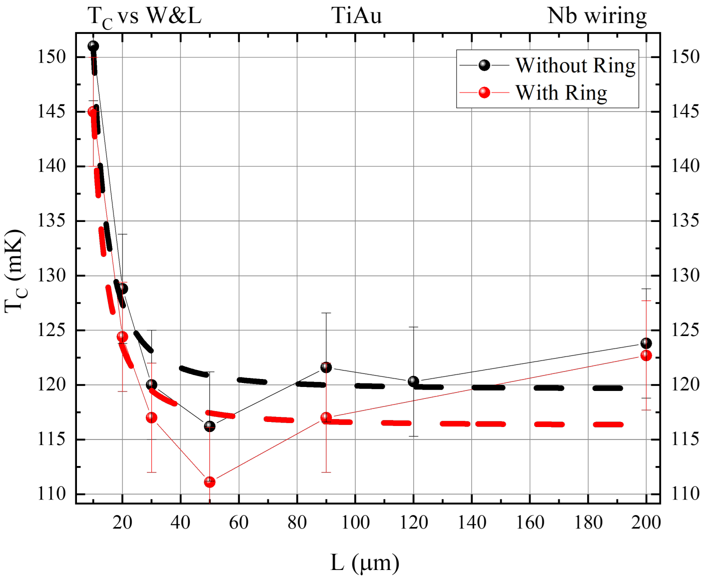

(a)

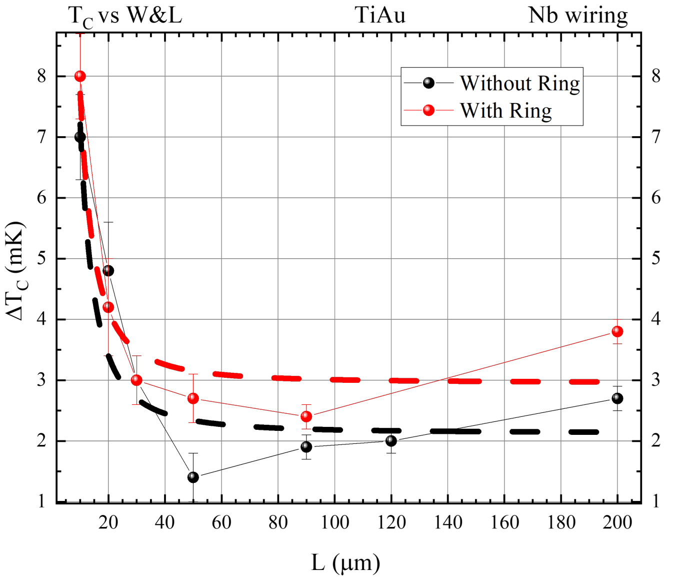

(b)

Fig. 5.5 Results for TiAu strips with Nb wiring. (a) T_c vs L with (red) and without (black) Au rings. (b) ΔT_c vs L. Dashed lines represent fits to $T_\mathrm{c} = T_{C0} + A/L^2$ and $\Delta T_\mathrm{c} = \Delta T_{C0} + a/L^2$.

In Fig. 5.6, the critical temperatures of the samples with Ti wiring are shown. Here, the strips with rings show higher critical temperatures. Since equivalent strips with and without rings are physically close on the chip, this effect is unlikely to be caused by deposition non-uniformity. Moreover, the resistance vs L curves overlap, suggesting no significant structural differences. The T_c uncertainties (not shown) are approximately 5 mK. Meanwhile, the transition width trend (Fig. 5.6b) is in agreement with the Nb case.

Finally, we measured the samples with TiAl wiring (without rings). Fig. 5.7 shows both T_c vs L and ΔT_c vs L. The trends are similar to the others, except for the final rise previously explained by the power/current density drop.

In all these curves, the dashed lines represent fits of the form $T_\mathrm{c} = T_{C0} + \frac{A}{L^2}$ or $\Delta T_\mathrm{c} = \Delta T_{C0} + \frac{a}{L^2}$ [63].

sample	Ring	T_{C0} $[mK]$	A $[\mu m^2/mK]$	ΔT_{C0} $[mK]$	a $[\mu m^2/mK]$
Nb	no	$119,6 \pm 1,4$	3124 ± 366	$2,1 \pm 0,2$	508 ± 138
Nb	yes	$116 \pm 2,3$	2874 ± 554	3 ± 2	476 ± 508
TiAl	no	$88,3 \pm 0,9$	454 ± 90	$1,1 \pm 0,3$	206 ± 30
Ti	no	$112,1 \pm 0,1$	2022 ± 100	$1,51 \pm 0,06$	1076 ± 40
Ti	yes	$121 \pm 0,3$	824 ± 293	$2,1 \pm 0,3$	1227 ± 293

Table 5.2 Table showing the parameters obtained by the $T_\mathrm{c} = T_{C0} + \frac{A}{L^2}$ and $\Delta T_\mathrm{c} = \Delta T_{C0} + \frac{a}{L^2}$ fits for Nb, Ti and TiAl samples.

Comparing the values of A, a, T_{C0}, and ΔT_{C0} from Tab. 5.2, we can conclude that:

- For both Ti and Nb wiring with TiAu TES, both A and a are compatible, meaning that the Au rings do not significantly reduce or increase the lateral inverse proximity effect.
- For TiAu TES with Nb wiring, both T_{C0} and ΔT_{C0} are compatible, while for the Ti wiring this is no longer true. This could be explained by the fact that the Nb wiring effect is stronger (since its T_c is higher) and dominates any possible effects given by the Au rings. This does not happen with the Ti wiring sample, on which the Au rings have a slightly detrimental effect.
- T_{C0} and ΔT_{C0} for different samples are completely dominated by differences during the deposition process. For this reason, we cannot compare them across

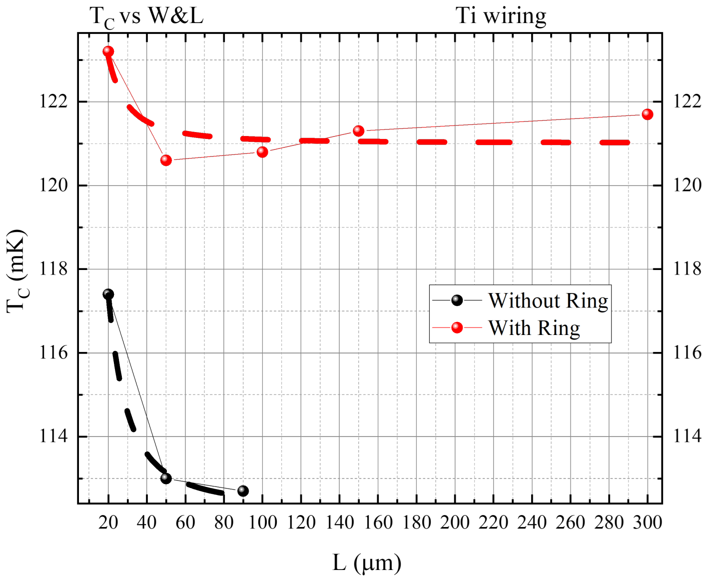

(a)

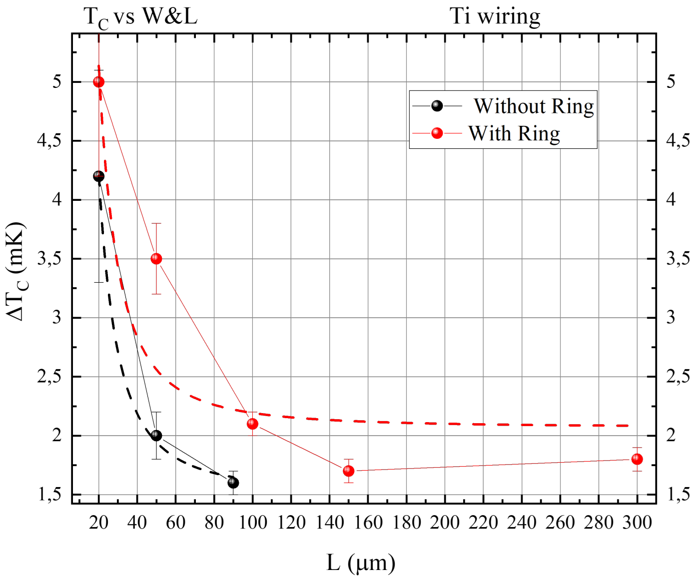

(b)

Fig. 5.6 Results for TiAu strips with Ti wiring. (a) T_c vs L with (red) and without (black) Au rings. (b) ΔT_c vs L. Dashed lines represent fits to the longitudinal proximity effect model.

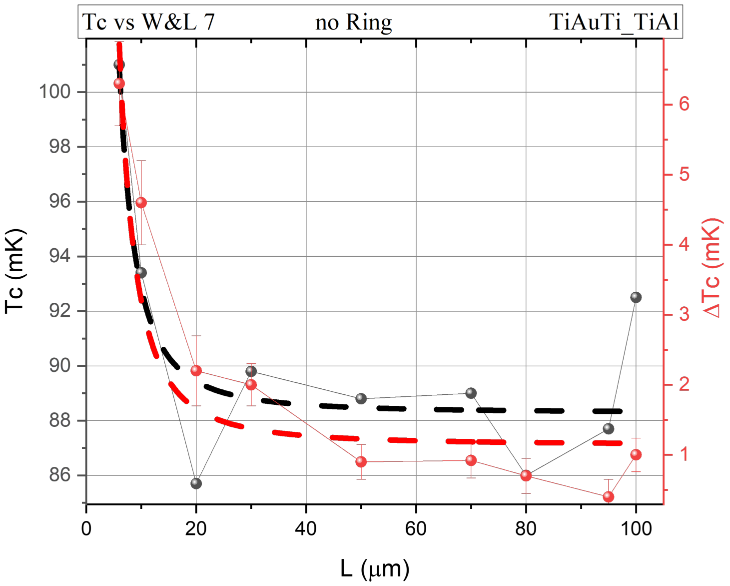

Fig. 5.7 T_c (black) and ΔT_c (red) *vs* L of AuTi strips with wirings in TiAl. The dots represent the measured data, while the dashed lines represent the fit of the equation $\Delta T_c = \Delta T_{C0} + a/L^2$.

different samples. However, the Nb and Ti samples were fabricated under similar conditions and show similar T_{C0} and ΔT_{C0}.

- The parameter A is higher with Nb wiring, followed by Ti wiring without rings, Ti with rings, and finally TiAl wiring. The last two are compatible. The low value of A in the AuTi TES with TiAl wiring is suspected to be caused by the different TES structure or contacts. This is consistent because TiAl wiring has the T_c of Al alone, and we expect A to decrease with the T_c gap between wiring and TESs.
- On the other hand, a is higher in the Ti wiring case, then in the Nb case, and finally in the AuTi with TiAl wiring. Again, we suspect that the major contribution in the last case is due to properties related to the contacts, while the Ti and Nb cases seem to suggest that a should decrease while increasing the T_c gap.

In Fig. 5.8, the resistivity ρ plots are shown for all samples. We can note that:

- None of the ρ curves is flat except for the one with Ti wiring (bottom left), which shows only fluctuations. All other curves show that ρ increases with L

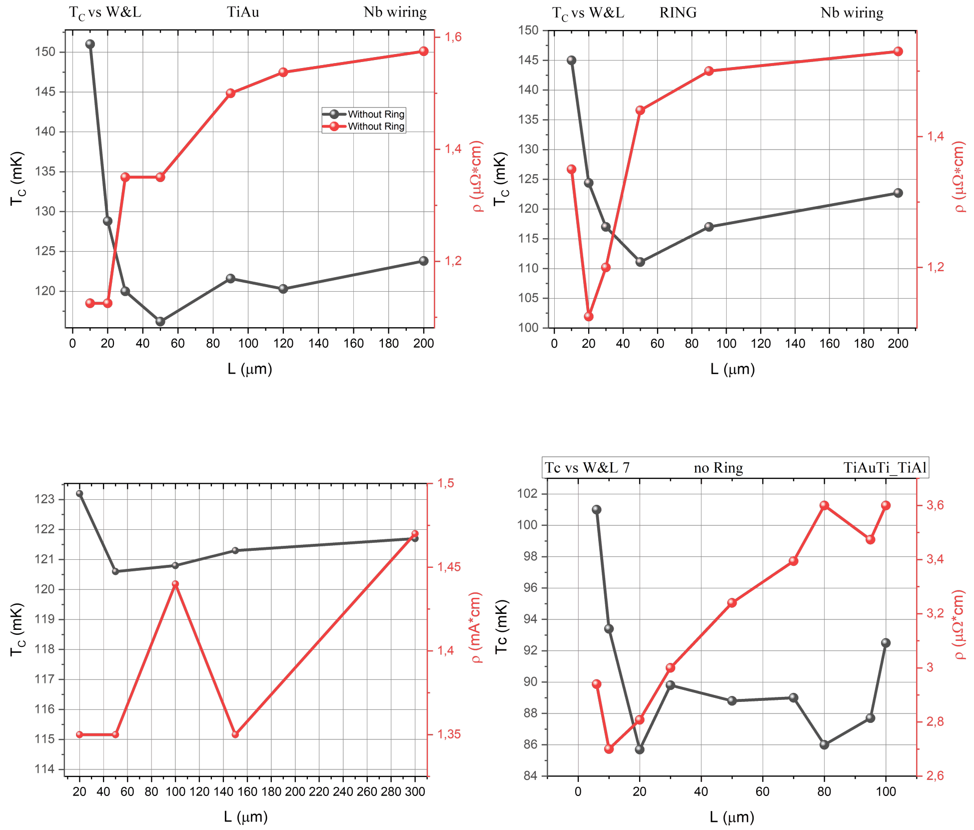

Fig. 5.8 Plots of the resistivity ρ (red) with the relative T_c curve (black) as a function of L. Top left: Nb without ring. Top right: Nb with rings. Bottom left: Ti sample without ring. Bottom right: TiAl case without rings.

on average—in an almost linear way for the TiAl case (bottom right) and with a concave increasing function for the Nb wiring (top).

- Moreover, in both TiAl and Nb wiring cases, the final increasing trend of the T_c curve seems to be correlated to the ρ curve. The relationship is likely not due to intrinsic film properties (as strips were deposited in the same run for each sample type) but rather to the proximity effect. This is compatible with the fact that the closer the wirings are to each other, the smaller the resistivity due to the presence of Cooper pairs injected from the superconducting leads, as discussed in Ch. 3.

This behavior can be understood by modeling the total conductivity σ as the superposition of the normal channel (Drude model) and the superconducting channel (London theory). The resistivity ρ is therefore inversely related to the densities of normal electrons (n_n) and Cooper pairs (n_s) injected by the wiring:

$$\rho \approx \frac{1}{\sigma_\mathrm{Drude} + \sigma_\mathrm{London}} \propto \frac{1}{An_\mathrm{n} + Bn_\mathrm{s}}, \tag{5.4}$$

where A and B are coefficients related to scattering times and effective masses. Consequently, a higher n_s (shorter L) leads to lower ρ and higher T_c, confirming that both the critical temperature and resistivity trends are manifestations of the longitudinal proximity effect.

- The ρ in the TiAl wiring case spans a higher range of values compared to the other two samples. Since the intrinsic ρ of the strips should be around $1-2\ \mu\Omega\mathrm{cm}$ in all cases, we can see that the Nb and Ti wiring cases are behaving well. Meanwhile, the resistivity of the TiAl sample is higher, and this difference can be explained by a "dirty" interface (oxide residue) that limits the longitudinal proximity effect.

5.5 Conclusions

The longitudinal and lateral proximity effects significantly modify the transition temperature T_c and its width ΔT_c in thin-film bilayer TES devices, directly impacting detector performance. This study systematically investigated these effects by fabricating and characterizing three distinct chip designs ("Nb", "Ti", and "TiAl").

We validated the measurement conditions by analyzing the trends of Joule power and current density. At short lengths (L), the behavior of resistivity ρ and critical temperature T_c is consistent and well-explained by the longitudinal proximity effect. The injection of Cooper pairs from the superconducting wiring into the bilayer leads to a simultaneous decrease in resistivity and an increase in T_c, following the expected $1/L^2$ scaling. However, the magnitude of this effect varies with the wiring material; specifically, the TiAl sample showed a reduced effect compared to expectations, which we attribute to a thin oxide layer on the Ti surface acting as a barrier, limiting the proximity effect.

At large lengths (L), where the proximity effect fades, we observe a different behavior: a slight increase in both T_c and ρ. The increase in resistivity with length is attributable to the statistical distribution of film defects or inhomogeneities, which naturally accumulate in longer strips. However, the presence of defects would typically degrade superconductivity and lower the T_c; therefore, statistical defects cannot explain the observed rise in critical temperature. Similarly, self-heating effects can be ruled out as the cause of this trend. Since the measurements were performed at constant current, the Joule power $P \propto R \propto L$ is highest for the longest strips. If self-heating were dominant, it would raise the strip temperature above the bath temperature, leading to an apparent decrease in T_c. Since we observe the opposite trend (a rise), self-heating is negligible at higher L (and thus at lower). A possible explanation for the slight T_c rise at large L could be related to the current density J. If the effective conductive cross-section were larger than the nominal geometry (e.g., due to current redistribution effects or lithographic problems for which strips are actually more series of bulges caused by widening of the laser spot), the effective J would be lower, which is physically consistent with an increase in T_c. Another explanation could be related to deposition non-uniformities on the chip and for which a gradient appears respect to L, but is actually related to the strips positions on the chip (long strips are close to each other and far from short strips in the masks). The bulges collection hypothesis could be verified with SEM images. In any case the rising effect for long strip is negligible since it should be monotonous and it is visible only after the LoPE is absent.

Crucially, the fact that the trend at large L (slight rise) is qualitatively different and driven by mechanisms distinct from those at small L allows us to isolate the longitudinal proximity effect. This confirms that the steep variation observed at short lengths is indeed the genuine signature of the proximity effect.

Conversely, the lateral inverse proximity effect was not clearly observed in our measurements; no significant correlation between T_c and strip width W was found in the first two samples. This suggests that either the effect is weak in these specific geometries or that the fabrication process resulted in interfaces that masked the effect.

Future improvements will include the fabrication and characterization of a TiAu TES with TiAl wirings to further explore the suppression of the longitudinal effect. Overall, these results provide a framework for optimizing superconducting detectors by carefully selecting wiring materials and geometries to tailor the transition properties.

Chapter 6

TES efficiency

6.1 Abstract of the chapter

Maximizing photon absorption is critical for applications ranging from dark matter searches to quantum optics. For TESs, achieving high System Detection Efficiency (SDE) requires minimizing reflection at the device interface. While multi-layer dielectric Anti-Reflection (AR) coatings are a standard solution, Plasmonic Metasurfaces offer a promising alternative for achieving high absorption in thin metallic films.

This chapter addresses the enhancement of photon detection efficiency through two approaches. First, we discuss the design and fabrication of a traditional dielectric AR coating (SiO_x/TiO_2), reporting measured efficiencies of up to 85%. Second, we introduce the theory of Grating-Coupled Surface Plasmon Polaritons (GC-SPP). We present numerical simulations for both gold and aluminum nanogratings, predicting absorption rates exceeding 95% at specific target wavelengths. Finally, we report the ellipsometric characterization of fabricated test structures, proving that optical micro-gratings can successfully reduce reflectivity to below 5% in the target spectral range.

6.2 Guiding projects and ideas

In the following chapter, our work on the optimization of detection efficiency will be shown. We have simulated and fabricated a sample with an antireflective coating on top of a TES. The TES itself has been redesigned with Ti on top in order to reduce the total reflectivity and make the required antireflective coating simpler. Then, we performed simulations to design optical and plasmonic gratings for TESs with Au on top. In fact, the Au layer on top of the Ti one has the advantage to protect the Ti from oxidation, since Au is an inert metal. Gratings are necessary since the Au reflectivity is too high to make possible simple antireflective coatings designs and are used to additionally decrease the reflectivity. The simulations and designs have been made for the telecom wavelengths ($\lambda = [1540, 1550]$ nm) and for the wavelengths relevant to two projects. $\lambda = [630, 690]$ nm are the wavelengths for a project in the Next Generation EU plan with PNRR funds. The project aim to measure pressure variation that will produce the generation of photons from nano-diamonds color centers. These photons will be detected by highly efficient TESs. Meanwhile, $\lambda = [780, 800]$ nm and $\lambda = 1300$ nm are the wavelengths related to the STAR project (**S**uperconducting **T**ES **A**rrays with energy number **R**esolution), a PNRR cascading project coming from the NQSTI project in the framework of quantum technologies.

6.3 Hints on System Detection Efficiency

The setup used to measure the system detection efficiency (SDE) is based on a configuration similar to that in [66–68, 43]. It includes a laser source, calibrated photodiode, two optical attenuators, and fiber connections. The laser beam is split into two beams: one path is used to monitor the power with a powermeter, while the other is attenuated to single-photon levels and directed into the cryostat through an optical fiber aligned with the TES. The SDE quantifies the probability that a photon entering the cryostat is detected by the TES, accounting for internal losses and misalignments. Measurements were performed at $\lambda = (690 \pm 5)$ nm using Keysight attenuators and a ThorLabs S150C photodiode.

We performed measurements for a TES with antireflective coatings using this cryogenic setup, while the plasmonic efficiency study is in a preliminary stage and only films with plasmonic structures measured via ellipsometer will be shown.

6.4 Anti-reflection Coating

One widely explored solution is the implementation of dielectric anti-reflective (AR) coatings. These coatings, based on interference effects, aim to minimize reflectivity at the target wavelength and enhance the net optical absorption of the sensor.

Multilayer coatings enable the optimization of the AR performance by stacking alternating layers with high and low refractive index materials. These can be tailored to create broad or multiple-band suppression of reflectance. In practical devices, AR coatings are often designed using optimization algorithms, such as in the software Macleod [69], to match the required spectral characteristics. The theory can be found in App. A.4.1.

6.4.1 Design and fabrication

Our first design for a high efficiency TES for wavelengths around 690 nm is made of an AuTi bilayer (Au 26 nm and Ti 34 nm) with an anti-reflection coating made of only 2 layers of SiO_x and TiO_2. The Ti layer on top of the Au layer has been chosen to reduce the intrinsic reflectivity of the TES bilayer and allow a simpler anti-reflection coating design. We used SiO_x and TiO_2 due to their stable optical properties and compatibility of their deposition with evaporators designed for superconductor deposition. The anti-reflective coatings is realized with 8 nm of SiO_x upon the TES and 50 nm of TiO_2 on top of that Fig. 6.1a . No mirrors or cavities between the TES and the SiN_x substrate have been used in this case. We applied this design to a $60 \times 60\ \mu\mathrm{m}^2$ with a 95 mK critical temperature as in Fig. 6.1b).

6.4.2 Results

The TES with the AR coating has been optically characterized with a laser of wavelength 690 nm. The total attenuation has been set to 30 dB to measure a low number of photons per pulse. From the histogram of the measured single photon pulses, both the energy resolution and the SDE have been calculated. The SDE can be measured as:

$$SDE = \frac{\mu_{\mathrm{TES}}}{\mu_{ref}}, \tag{6.1}$$

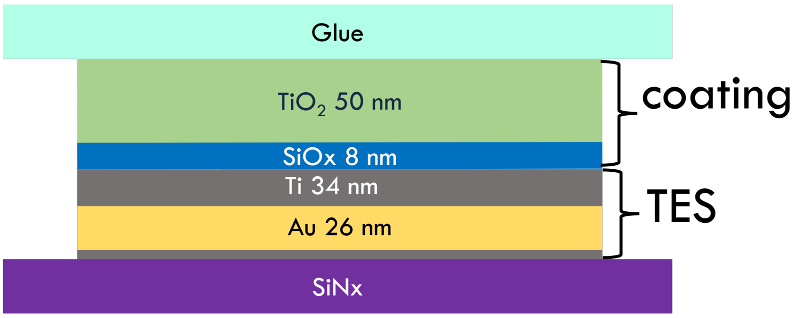

(a) Structure of the overall TES and anti-reflective coating design.

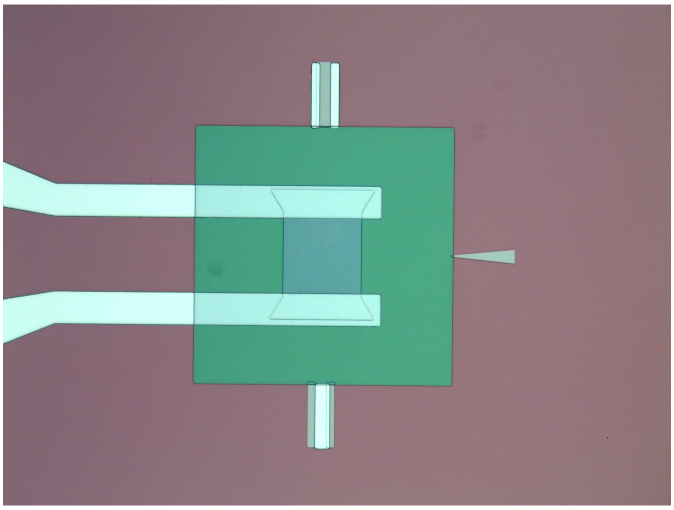

(b) Microscope capture of the fabricated TES with the anti-reflective coating from above. The large green square is the dielectric coating. Under the clean room lights, the coating on the SiN_x appear in a green shade, while on the TES look of a gray shade.

Fig. 6.1 Design and microscope capture of the fabricated TES and anti-reflective coating.

where μ_{TES} is the average number of photons per pulse detected by the TES and μ_{ref} the average number of photons in the fiber. The value of μ_{ref} can be measured from the photodiode monitor and the characterization of the branches from the laser source to the TES and to the photodiode as in [68, 43]. Meanwhile, μ_{TES} can be obtained by the well known formula of Gaussian functions per each pulse convoluted with the Poissoniana distribution of the laser statistic:

$$F(x;\mu,\sigma) = A\sum_{n=0}^{\infty}\frac{\mu^n e^{-\mu_{\mathrm{TES}}}}{n!}\cdot\frac{1}{\sqrt{2\pi}\sigma_n}\exp\left(-\frac{(x-x_n)^2}{2\sigma_n^2}\right) \tag{6.2}$$

From the fit in Fig. 6.2 we obtained $\mu_{\mathrm{TES}} = 1,6$, $\sigma_1 = 0,005$ V, $X_0 = 0,003$ V and $X_1 = 0,016$ V. The energy resolution can be calculated as $\Delta E = 2\sqrt{2\ln 2}\,\sigma_i/(X_1 - X_0) = 0.9$ eV. It is worth noting that this value is consistent with the resolution obtained for similar devices in Chapter 3 ($\Delta E \approx 0.82$ eV). The apparent lack of peak separation in the histogram compared to previous measurements is primarily due to the lower energy of the incident photons used here ($\lambda = 690$ nm $\rightarrow E_\gamma \approx 1.8$ eV) compared to the characterization at 406 nm ($E_\gamma \approx 3.05$ eV). Since these energy resolutions are close, but the measurements are done with different incident energies, the ratio between the peak separation (determined by E_γ) and the peak width (ΔE) is significantly reduced at 690 nm, leading to the observed overlapping of the photon peaks.

While, the obtained value for SDE is $(85 \pm 6)\%$ with a confidence level of the 95%. This value doesn't reach the required values ($> 90\%$) for most of the projects and this is probably due to a wrong thickness of the SiO_x layer. In fact, measurements of a large area on the chip designated for ellipsometric characterizations revealed a slight shift in the maximum absorption peak and thickness measurements show a total thickness 2 nm lower than expected. On the other hand, the large uncertainty on the SDE is given by the large uncertainty of a commercial photodiode used during the characterization of the setup.

6.5 Plasmonic Metasurfaces

Plasmonic metasurfaces and optical gratings on TESs are a poorly investigated field. Here, I try an attempt in simulating some structure for TES with high photon

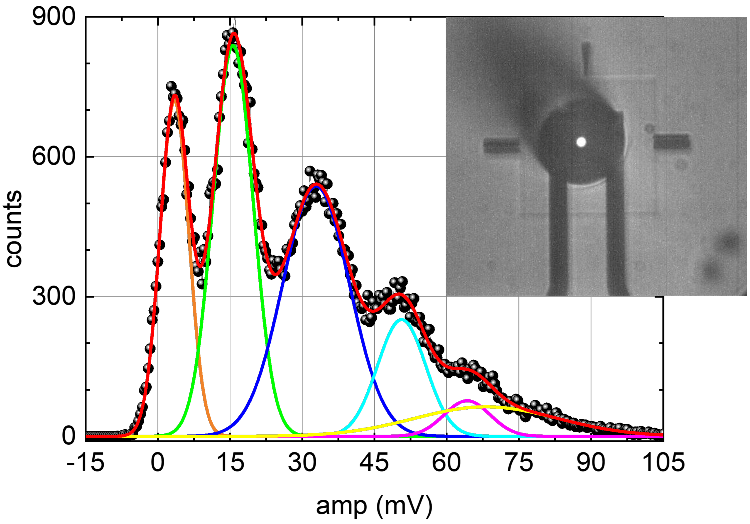

Fig. 6.2 Histogram of the TES with AR coating at 690 nm. The peaks has been analyzed and we obtained an energy resolution of $\Delta E = 0.9$ eV for the peak of 1 photon. The small picture shows the TES with a fiber aligned at the center of it.

detection using plasmonic gratings and the realization of optical gratings on thin TiAu bilayers. The theory can be found in App. A.4.2.

6.5.1 Design and simulations

We made various simulations of Au gratings on a TiAu continuous bilayer with and without a mirror structure made of SiO_2 and Au for different λ and α. Moreover, we simulated Al gratings followed by the same mirror structure to create a superconductive photon absorber linked to the TES. Before showing the simulation results, we bring some preliminary considerations:

Polarization Sensitivity: The interaction between incident photons and plasmonic gratings in literature is highly polarization-dependent. Transverse magnetic (TM) polarized photons, with their electric fields oriented perpendicular to the grating lines, strongly couple to SPP modes, significantly enhancing absorption. Conversely, transverse electric (TE) polarized photons interact weakly, resulting in substantially lower absorption efficiency [70]. This polarization dependency could be restrictive in some applications and with standard optical fibers. However, it grants the possibility to detect light with only one polarization, useful in some experiments and possibly reducing noise related to stray or reflected photons. Moreover, this dependency could disappear for some grating design and lower angles. In our simulations, we focused on the TE polarization only and we measured both the polarizations reflection.

Optimization of Plasmonic Gratings

To engineer plasmonic gratings effectively, key geometric parameters—including grating period, fill factor, metal thickness, and dielectric environment—must be optimized. Numerical techniques such as Finite-Difference Time-Domain (FDTD) simulations and neural-network-assisted methods are frequently employed for this optimization process [71]. By fine-tuning these parameters, one can precisely achieve a sharp resonance condition, significantly enhancing photon-to-SPP coupling efficiency. Consequently, metasurfaces exhibit minimal reflection. Adding a mirror structure or using thick and opaque materials under the plasmonic grating, one can achieve negligible transmission at the resonant wavelength, resulting in near-perfect absorption [72]. We adopted and modified the simple comsol model [73] and used the Wave Optics package in COMSOL Multiphysics 6.2. Moreover, we create 2 dimensional maps for absorbance or reflection varying 2 parameters at a time while fixing the others. We select the couple of parameters for the best results for each couple and repeated the process until we converge at the desired values. Most of the refractive indexes used for the simulations are obtained from tables of the refractive indexes as a function of the incident wavelength of single material layers measured via ellipsometer. While the others comes from [74]. In Tab. 6.1, I report the approximate values of the real parts of the refractive indexes n (or phase velocities) and the extinction coefficients k (imaginary parts) of the materials used in the simulations at the wavelengths required by our guiding projects.

Table 6.1 Real and imaginary parts of the refractive indexes (n,k) of the different materials at the different wavelengths used in the simulations.

Material	(n;k)	(n;k)	(n;k)	(n;k)
λ	630 nm	$780-808$ nm	1300 nm	$[1540, 1550]$ nm
Ti	(3,58; 3,33)	(4,1; 3,1)	(4,4; 3,1)	(4,4; 3,1)
Au	(0,23; 3,51)	(0,19; 5)	(0,43; 9,08)	(0,6; 10,9)
Al	(1,05; 6,15)	(1,95; 6,94)	(1,34; 10,8)	(1,72; 12,8)
SiO_x	(2; 0)	(1,96; 0)	(1,92; 0)	(1,92; 0)
TiO_2	(2,44; 0,016)	(2,4; 0,0001)	(2,4; 0)	(2,36; 0)
SiN_x	(2,18; 0,002)	(2,16; 0,0011)	(2,13; 0,0005)	(2,13; 0,0005)

In addition, the grating geometries have been taken simple as infinitely periodic squares with perfectly sharp corners. We are aware that real geometries will be smoother and this may cause broader, but less intense scattering lobes, especially in regimes where edge effects dominate due to the attenuation of high-frequency components in the Fourier domain.

The simulations in this thesis are of 4 kinds: the firsts are simple Au gratings on top of the TiAu TES, the seconds are simple Au gratings covered by an AR coating and the thirds are Al absorbers to be connected to the TES. Under all of this a cavity in SiO_x and a mirror in Au or Al are used to suppress the transmittance. The fourth kind are Al or Au gratings on top of a SiO_x or TiO_2 layer upon a TiAuTi TES exploiting a proper nanopatterning to increase the the light-to-heat conversion [75, 76]. The first two kinds are limited by the ratio between the volume of the Au grating and the volume of the Ti in the TES because of the proximity effect, while the third are limited by the fact that the photon absorption will happen outside the TES. The external absorbers rely on the energy down-conversion from the grating-absorber to the TES due to the difference in the energy gaps before the lost of its energy [77]. A possible loss of the absorbed energy could happen to phonons flowing from the absorber to the substrate and we eventually need to fabricate the absorber on a membrane.

In Fig. 6.3 is shown what usually appear in this type of simulations. On the top we can see the typical condensation of the electric field while getting closer to the grating, where the red "bubbles" are the space region on which the electric field density is higher. On the bottom, it is shown a map of the total reflectivity R with respect to the width of the grating wires w_{gr} and to the width of the trenches (or distance between the wires) a in the case of an Au grating with a layer of $\mathrm{TiO_2}$ on top as an AR coating. The scattered features are given by the grating itself, in fact the GC-SPP act on the reflectivity with specific combinations of a and w_{gr}. This dots in R are usually arranged in parallel lines with a minimum of R at some point and R progressively increasing on the same line and moving far from the minimum. The continuous variations of R are given by the continuous layers, both by the AR layers and by the TES layers and by the mirror and cavity. The map for cavity and mirror is usually monotonically changing in the mirror layer t_{mirror} (with T decreasing while increasing t_{mirror}) and periodically changing with the thickness of the cavity t_{cav}. The thickness of the GC-SPP t_{gr} usually act with a maximum at some precise values and progressively decreasing moving far from there. While the map for the TES layers

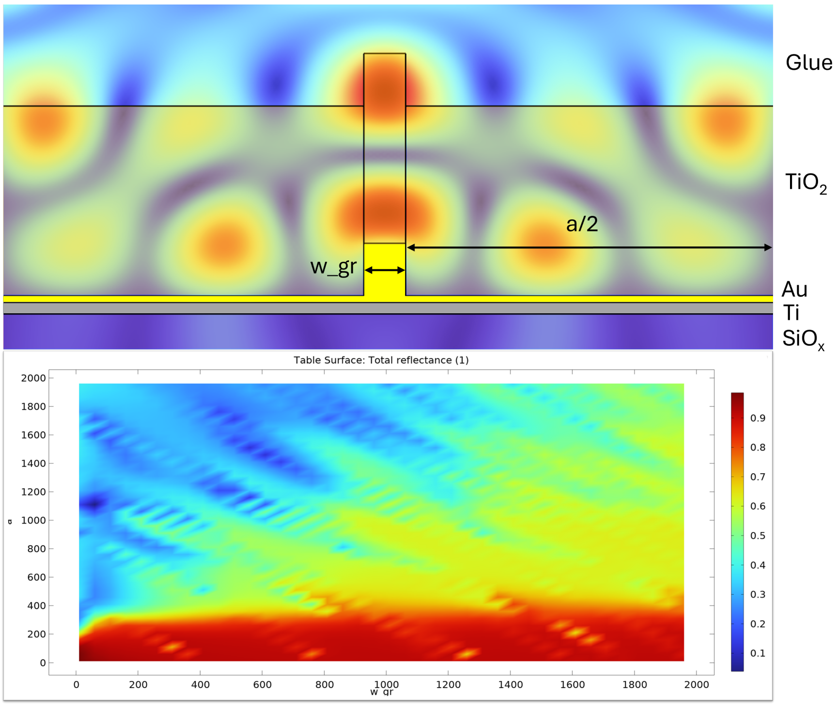

Fig. 6.3 Typical maps resulting during the simulations, in particular for a TES with a GC-SPP covered by an AR coating. Top plot, the electric field density with the usual condensation of the field while reaching the grating. Bottom plot, a typical map of the total reflectance vs the parameters a and w_{gr} of the grating indicated in the figure on the left. The scale for a and w_{gr} are in nanometers, while the legend of color scale is in the right part of the image.

are usually continuous, with R increasing with the thickness of the more reflective layer (Al or Au).

Validation of the Comsol model

The first necessary step is to compare the simulations of a simple TiAu film between the Comsol model created for plasmonic gratings, the MacLeod software used for AR Coatings and some external software such as [78].

As reported in Fig. 6.4, all the simulations of the basic stack Glue-Au 30 nm-Ti 15 nm-Si_3N_4 500 nm-Si are in agreement in terms of values for R *vs* λ at $\alpha = 0°$, even if Comsol shows additional features. At the interested λ for the projects, the values of R are the same, but for $\lambda = 800$ nm. At that wavelength Comsol and KLA agree and differ from MacLeod by a 5% of reflectivity. In terms of angles, MacLeod and Comsol agree under 1% of reflectivity in the range $\alpha \in [0°, 15°]$, that are the possible angles incident on the TES due to the spread of light from the optical fiber. The Comsol model has been considered enough in agreement and then used as basic model for the the GC-SPP simulations.

I will now proceed to show the best obtained simulations in COMSOL for GC-SPP for TES high efficiency, indicating with $t_{\text{namelayer}}$ the thickness of each layer. The function R,A and T *vs* λ are all calculated at an angle $\alpha = 0°$, while upon the top structure (GC-SPP or AR coating) we considered a medium with $n = 1.5$ simulating the glue between the sample and the optical fiber. The simulated polarization is TE.

Au grating for $\lambda = 630$ nm

In this simulation we obtained an absorption of $A = 99.5\%$ at a wavelength $\lambda = 630$ nm and an incident angle of $\alpha = 0°$ using an Au grating directly on top of the TES.

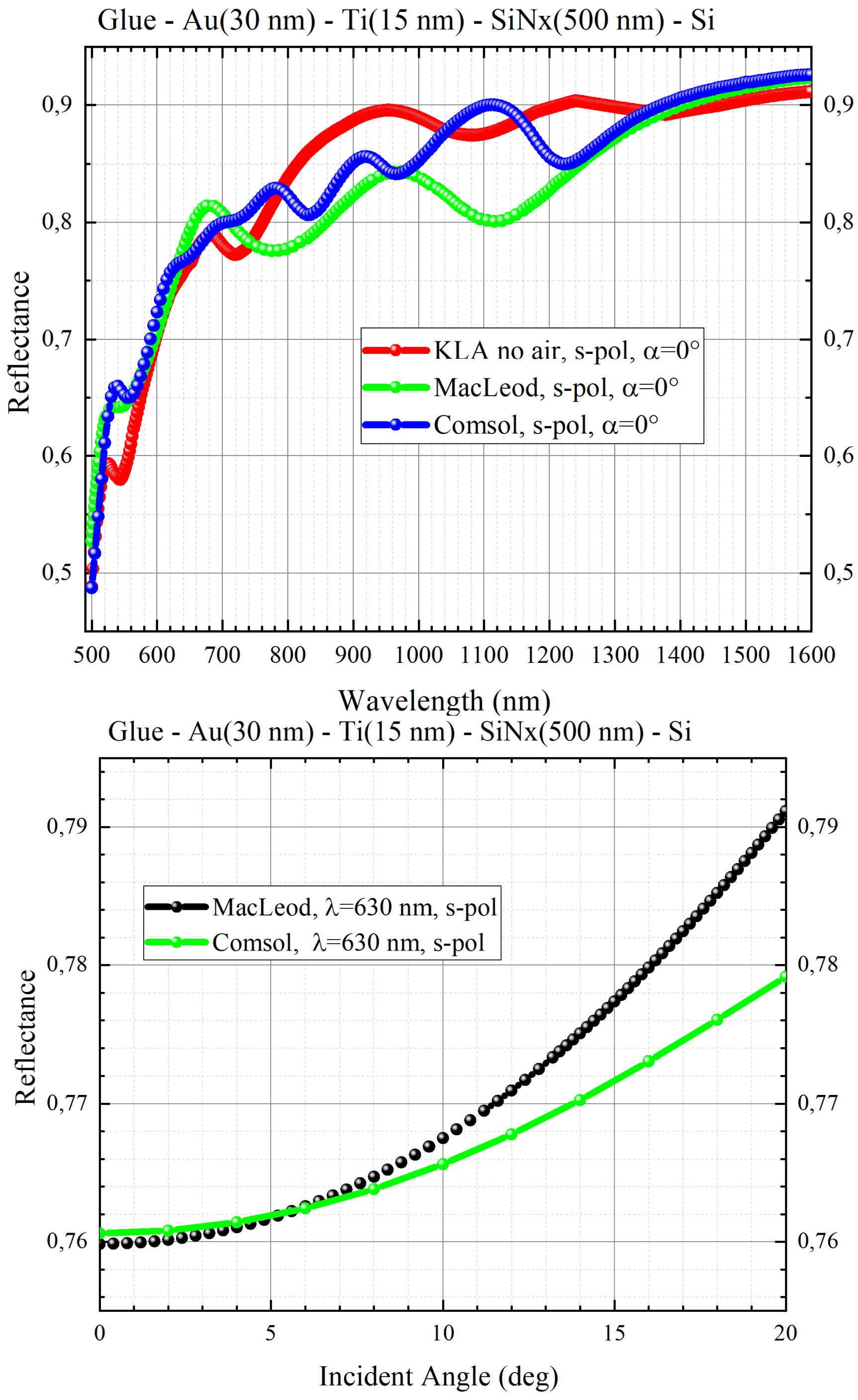

Fig. 6.4 Reflectivity R of the following stack: Glue-Au 30 nm-Ti 15 nm-Si_3N_4 500 nm-Si as a function of the wavelength λ at an angle of 0° with Comsol, [78] and MacLeod. Then, R as a function of the angle α at $\lambda = 630$ nm with Comsol and MacLeod with the s polarization.

Table 6.2 Optimized geometric parameters for the Au grating structure on AuTi TES designed for $\lambda = 630$ nm and normal incidence ($\alpha = 0°$).

Parameter	Value [nm]
a	210
w_{gr}	160
$t_{\mathrm{TiO_2}}$	65
t_{SiO_x}	20
t_{gr}	65
t_{Au}	10
t_{Ti}	22
t_{cav} (TiO_2)	40
t_{mirror} (Au)	60

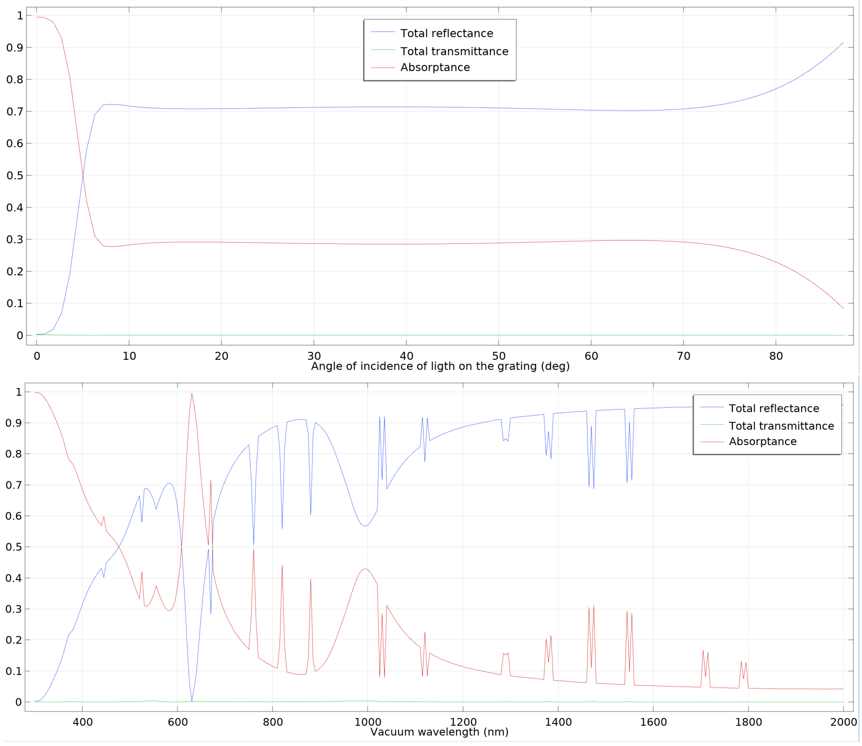

Fig. 6.5 On the top: simulation of R, T, A *vs* α at $\lambda = 630$ nm for an Au grating on top of a TiAu TES and a cavity on a mirror with a TE polarization and covered by an AR coating in SiO_x and TiO_2. On the bottom: simulation of R, T, A *vs* λ at $\alpha = 0°$ for the same structure.

Au grating for $\lambda = 1550$ nm

In this simulation we obtained an absorption of $A = 93\%$ at a wavelength $\lambda = 1550$ nm and an incident angle of $\alpha = 0°$ using an Au grating directly on top of the TES.

Table 6.3 Optimized geometric parameters for the Au grating structure on AuTi TES designed for $\lambda = 1550$ nm and normal incidence ($\alpha = 0°$).

Parameter	Value [nm]
a	1870
w_{gr}	1620
t_{gr}	90
t_{Au}	40
t_{Ti}	25
t_{cav}	30
t_{mirror}	25

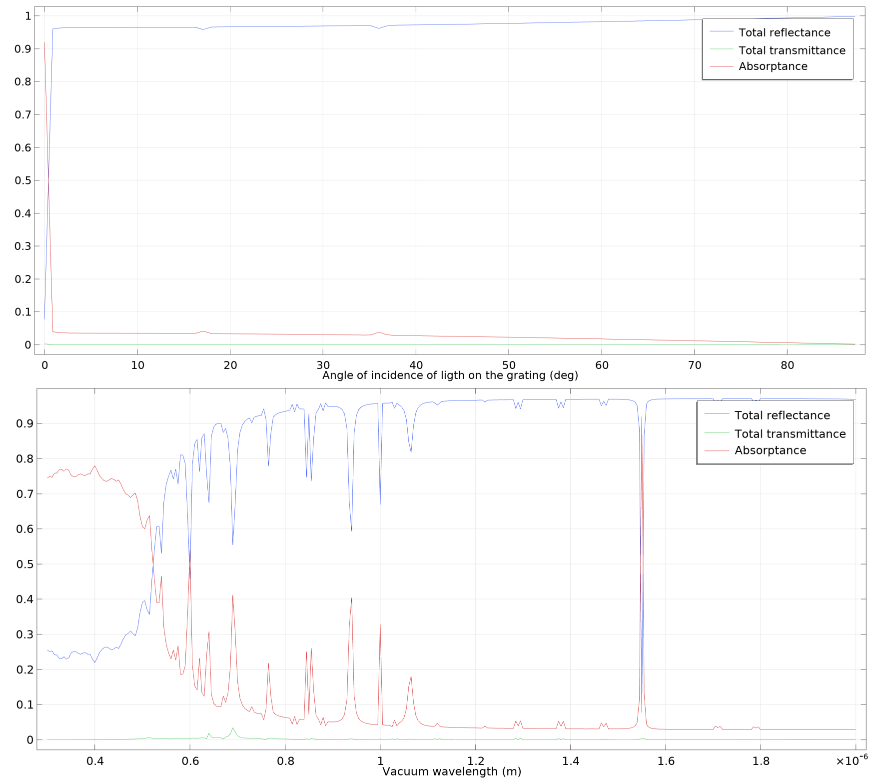

Fig. 6.6 On the top: simulation of R, T, A *vs* α at $\lambda = 1550$ nm for an Au grating on top of a TiAu TES and a cavity on a mirror with a TE polarization. On the bottom: simulation of R, T, A *vs* λ at $\alpha = 0°$ for the same structure.

Al optical grating on Ti for $\lambda = 808$ nm

In this simulation we obtained an absorption of $A = 91\%$ at a wavelength $\lambda = 808$ nm and an incident angle of $\alpha = 0^\circ$ using an Al grating directly on top of a Ti layer.

Table 6.4 Optimized geometric parameters for the Al optical grating on Ti layer at $\lambda = 808$ nm.

Parameter	Value [nm]
a	5000
w_{gr}	1500
t_{gr}	170
t_{Ti}	15
t_{cav}	260
t_{mirror}	80

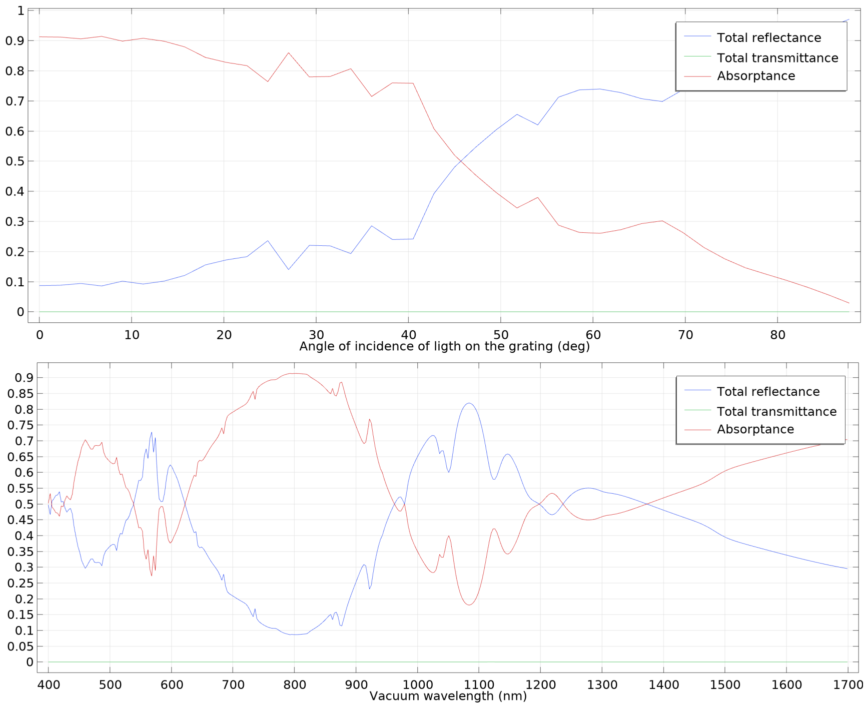

Fig. 6.7 On the top: simulation of R, T, A *vs* α at $\lambda = 808$ nm for an Al optical grating on top of a Ti TES and a cavity on a mirror with a TE polarization. On the bottom: simulation of R, T, A *vs* λ at $\alpha = 0^\circ$ for the same structure.

Al absorber for $\lambda = 630$ nm

In this simulation we obtained an absorption of $A = 97\%$ at a wavelength $\lambda = 630$ nm and an incident angle of $\alpha = 0^\circ$ with an Al grating on top of a mirror and a SiO_x cavity.

Table 6.5 Optimized geometric parameters for the Al absorber structure at $\lambda = 630$ nm.

Parameter	Value [nm]
a	340
w_{gr}	40
t_{gr}	80
t_{cav}	230
t_{mirror}	60
$t_{\text{adhesion Ti}}$	5

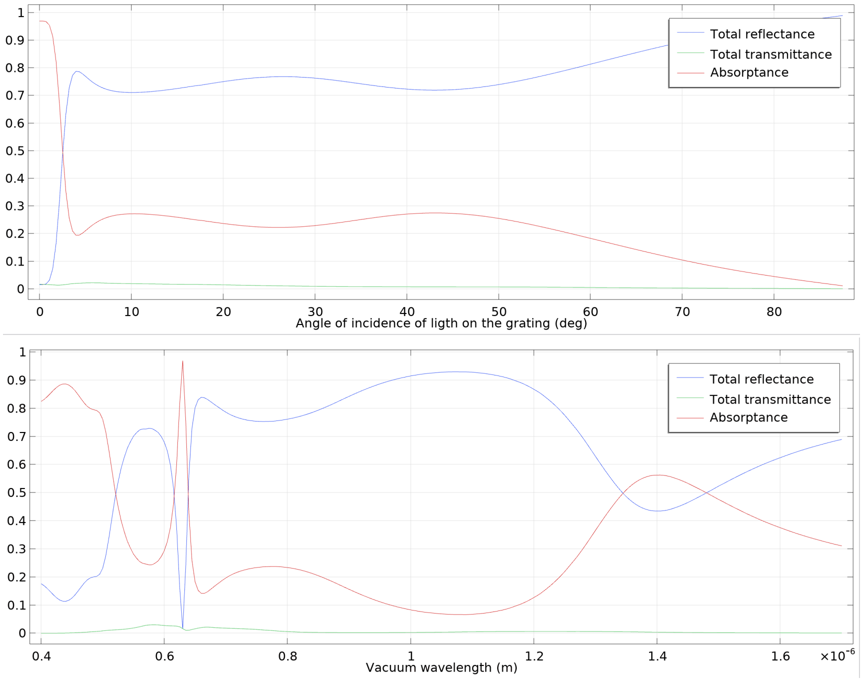

Fig. 6.8 On the top: simulation of R,T,A *vs* α at $\lambda = 630$ nm for an Al grating on top of a cavity on a mirror with a TE polarization that should work as an absorber for a TES. On the bottom: simulation of R,T,A *vs* λ at $\alpha = 0^\circ$ for the same structure.

Al absorber for $\lambda = 780$ nm

In this simulation we obtained an absorption of $A = 95\%$ at a wavelength $\lambda = 778$ nm, $A = 96\%$ at a wavelength $\lambda = 1186$ nm, $A = 80\%$ at a wavelength $\lambda = 610$ nm with an Al grating on top of a mirror and a SiO_x cavity. The incident angle is $\alpha = 0^\circ$ and the refractive index of the medium above the grating is $n = 1$.

Table 6.6 Optimized geometric parameters for the Al absorber structure at $\lambda = 780$ nm.

Parameter	Value [nm]
a	320
w_{gr}	220
t_{gr}	110
t_{cav}	220
t_{mirror}	60
$t_{\mathrm{adhesion\ Ti}}$	5

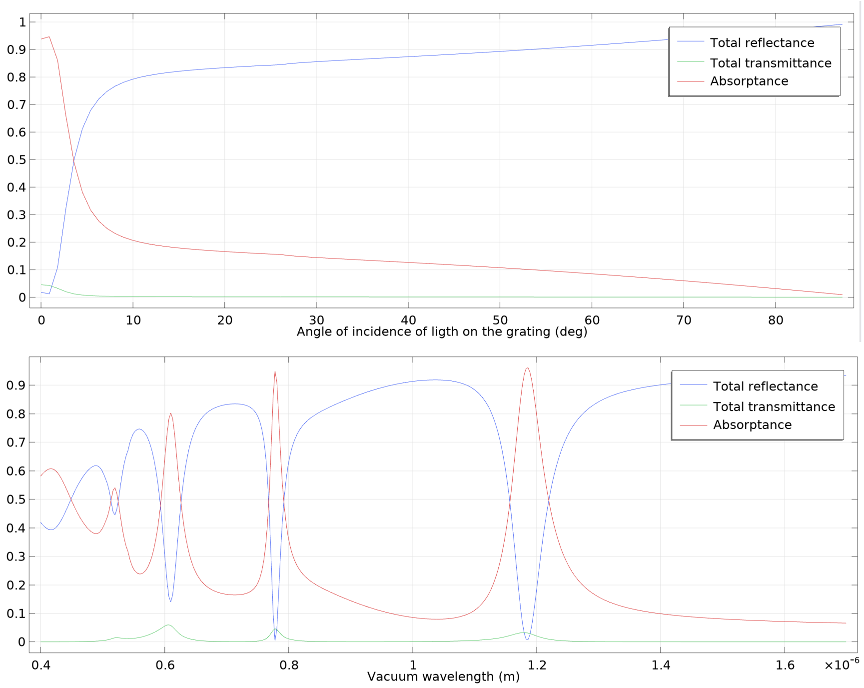

Fig. 6.9 On the top: simulation of R, T, A *vs* α at $\lambda = 780$ nm for an Al grating on top of a cavity on a mirror with a TE polarization that should work as an absorber for a TES. On the bottom: simulation of R, T, A *vs* λ at $\alpha = 0^\circ$ for the same structure.

Al absorber for $\lambda = 1300$ nm

In this simulation we obtained an absorption of $A = 97\%$ at a wavelength $\lambda = 1300$ nm with an Al grating on top of a mirror and a SiO_x cavity. The incident angle is $\alpha = 0^\circ$ and the refractive index of the medium above the grating is $n = 1.5$.

Table 6.7 Optimized geometric parameters for the Al absorber structure at $\lambda = 1300$ nm.

Parameter	Value [nm]
a	1260
w_{gr}	1480
t_{gr}	190
t_{cav}	194
t_{mirror}	60
$t_{\mathrm{adhesion\ Ti}}$	5

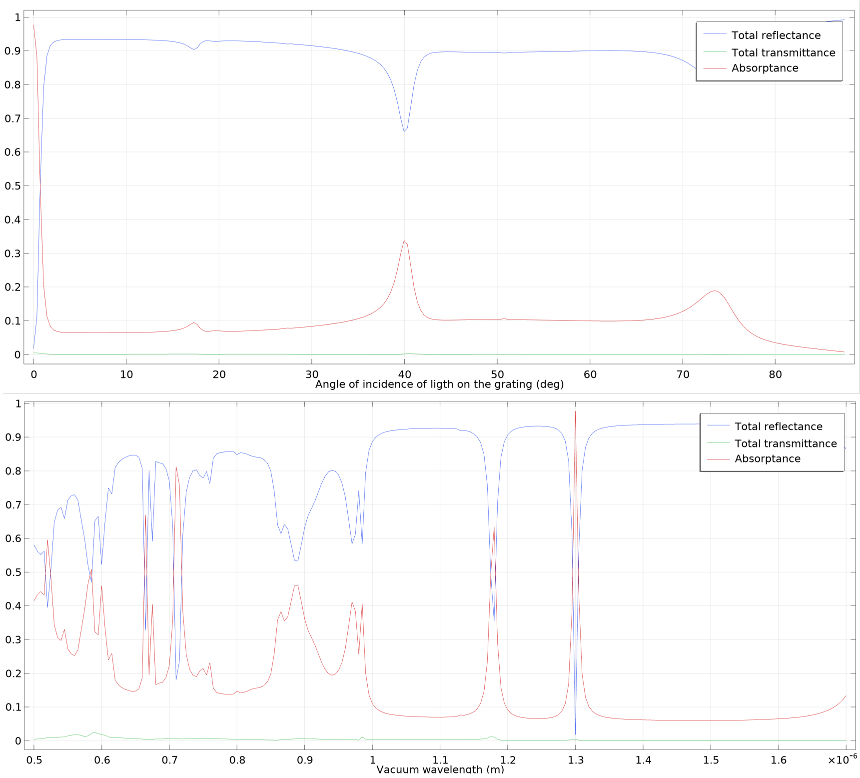

Fig. 6.10 On the top: simulation of R, T, A *vs* α at $\lambda = 1300$ nm for an Al grating on top of a cavity on a mirror with a TE polarization that should work as an absorber for a TES. On the bottom: simulation of R, T, A *vs* λ at $\alpha = 0^\circ$ for the same structure.

Al/Au GC-SPP + single oxide layer on TiAuTi TESs

In this simulations we obtained high absorption (around $A = 95\%$) for different wavelengths ($\lambda = 798$ nm, $\lambda = 630$ nm, $\lambda = 1540$ nm with an Al or Au grating on top of a single oxide layer of SiO_x or TiO_2. Under the GC-SPP and the oxide there is the TiAuTi tri-layer used for TESs also with AR coatings as in Fig. 6.11. The incident angle is $\alpha = 0°$ and the refractive index of the medium above the grating is $n = 1.5$.

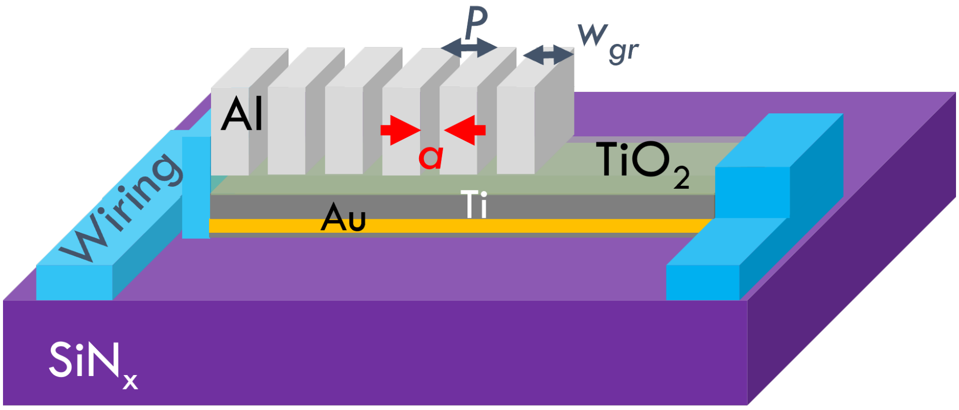

Fig. 6.11 Schematic of the TES covered by the oxide layer and by the Al GC-SPP on top.

The parameters for the 3 different wavelengths can be found in he following table. The columns are divided for each wavelength, while in the row are indicated the materials, in addition to the usual thicknesses.

Table 6.8 Optimized geometric parameters for Al/Au gratings on TiAuTi TES with single oxide layer.

Parameter	Value [nm]	Value [nm]	Value [nm]
λ	630	798	1540
$Absorption$	95%	95%	90%
a	610	820	660
w_{gr}	390	600	310
Grating material(t_{gr})	$Al(120)$	$Al(210)$	$Au(100)$
Oxide(t_{oxide})	$\mathrm{SiO}_x(50)$	$\mathrm{TiO}_2(30)$	$\mathrm{TiO}_2(130)$
$t_{\mathrm{adhesion\ Ti}} - t_{\mathrm{Au}} - t_{\mathrm{Ti}}$	$5-20-35$	$5-20-35$	$5-20-35$

In Fig. 6.12 are shown the maps from which I extrapolated the parameters for Tab. 6.8 related to $\lambda = 798$ nm and the absorption respect to the wavelength spectrum. In Fig. 6.13 is shown the absorption function respect to λ at $\alpha = 0°$.

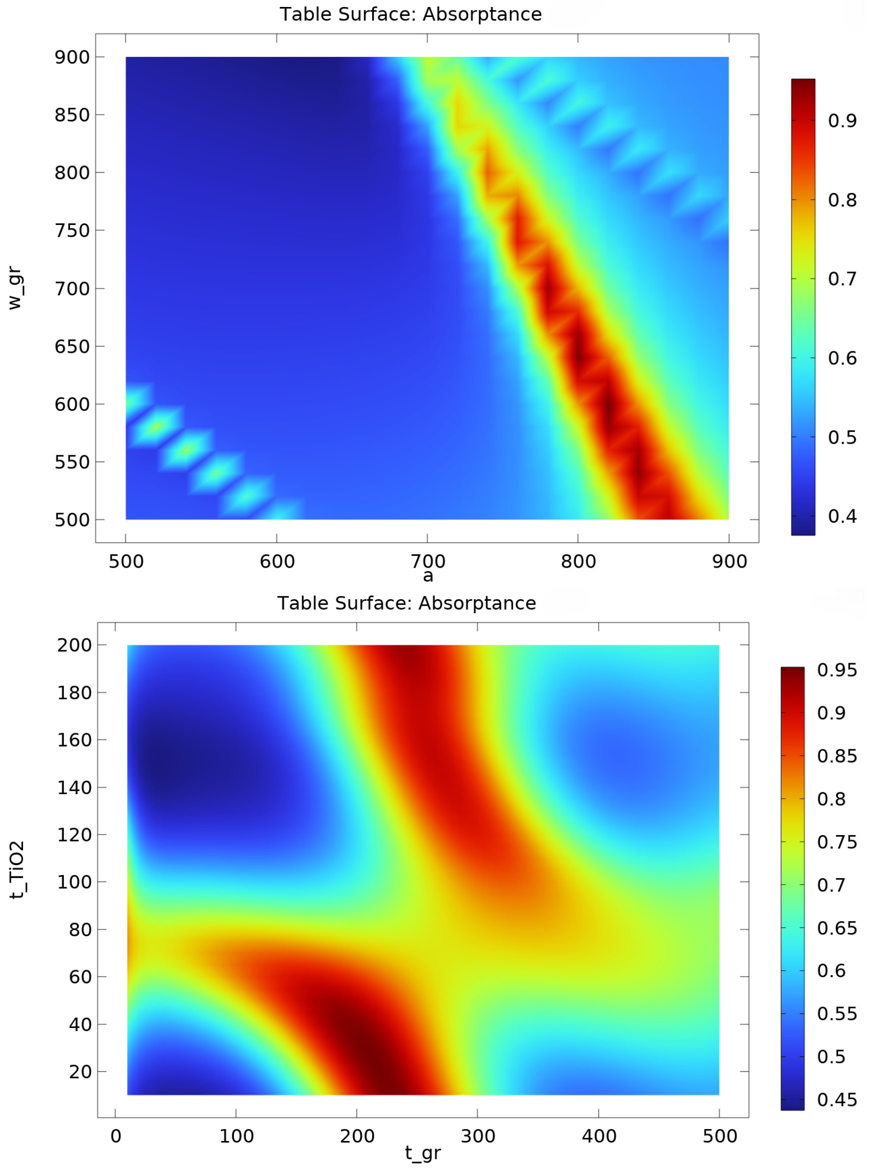

Fig. 6.12 On the top: simulated map of A *vs* a, w_{gr} at $\lambda = 798$ nm, $\alpha = 0°$ for an Al grating on top of a TiO_2 layer on a TiAuTi TES with a TE polarization. On the bottom: simulation map of A *vs* $t_{\mathrm{gr}}, t_{\mathrm{TiO_2}}$ at $\lambda = 798$ nm, $\alpha = 0°$ for the same structure. For both: dark red means highest absorption, while dark blue lowest absorption.

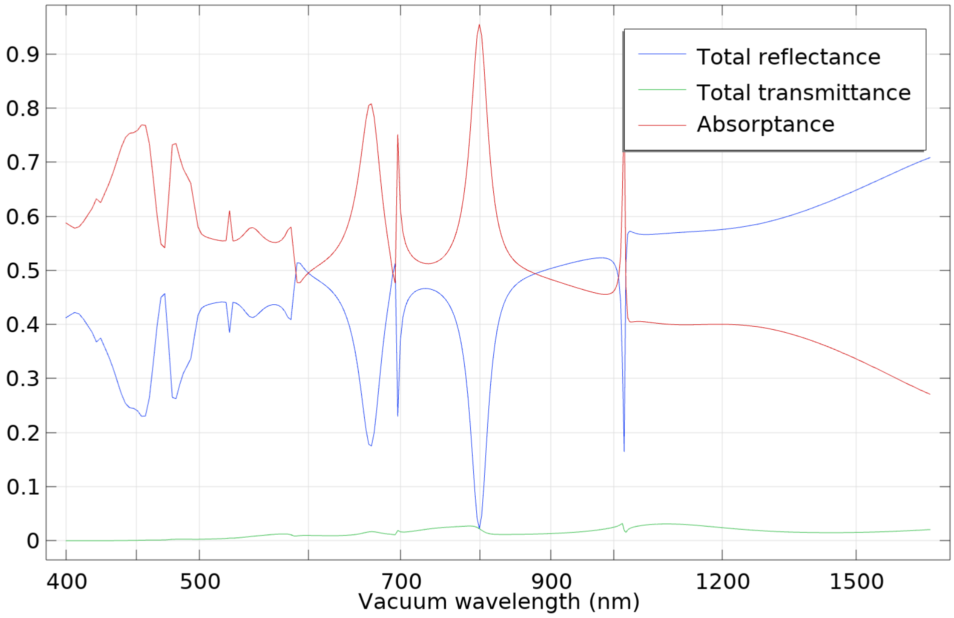

Fig. 6.13 simulation of R, T, A *vs* λ at $\alpha = 0°$ for an Al grating on top of a TiO_2 layer on a TiAuTi TES.

6.5.2 Fabrication and results of μm$-$gratings test structures

Among the many simulations performed, three representative samples were fabricated for experimental testing. These samples have μm$-$gratings made via laser writing and have no mirrors or cavity. Moreover, the refractive index of the external medium considered is $n = 1$. They have been optically characterized only measuring R via ellipsometer and so has areas large at least 3×3 mm^2 each and angles of interrogation between 20° and 80°. They are named Sample1 and Sample2 and will be explained here. In all the samples, there are different areas with different grating geometries with name in the form *column* $w_{\mathrm{gr}} - a$. The film C0 is the reference film without any additional layer or structure on the basic TiAu bilayer and is used as a reference for the effects of the gratings on that film. The film C∞ has a continuous Au layer with a thickness equal to t_{gr} and is used has upper limit for R as a grating with fill factor of 100%.

Sample1

Sample 1 has been simulated as periodic linear stripes with AR coating and optimized to have $A = 55\%$ at 630 nm and $\alpha = 0$. Because the peak of this sample disappeared at higher angles, the following results are reported only to show the methodology used in these studies. The structure is:

Table 6.9 Geometric parameters for the Au grating and AuTi TES (Sample 1).

Parameter	Value [nm]
a	6000
w_{gr}	5000
t_{SiO_x}	10
t_{TiO_2}	55
t_{gr}	60
t_{Au}	60
t_{Ti}	25

The films present in this sample are the following:

Table 6.10 List of different grating patterns on the fabricated samples. Various geometries and dimensions were tested.

Name	Form	w_{gr} $[\mu m]$	a $[\mu m]$
A5-6	linear stripes	5	6
B∞	flat layer	∞	0
C0	none	0	∞
A□5-6	squares in a squared lattice	5	6
BO5-6	circles in an hexagonal lattice	5	6
A10-30	linear stripes	10	30
BCH5-6	10 concentric circular crowns in a hexagonal lattice	5	6
B⊕5-6	10 concentric circular crowns in a cross lattice	5	6

However, because of the impossibility to characterize the sample at angle 0° via ellipsometer, we performed simulations for angles $\geq 20°$ and we discovered that there were no more resonances at 630 nm, but only a peak at 690 nm. Then, we measured that peak to understand if the combination of AR coating and the optical μm$-$grating with our fabrication facilities were consistent with simulations.

In Fig. 6.14, the simulated A maps of the Sample 1 vs different couples of parameters are shown for $\lambda = 630$ nm, $\alpha = 0°$ and $n = 1$. In the top left map, the chosen parameter are the one in the red dot that represent the better couple of lateral parameters of the grating. In this study, there was only one stretched dot in which the combination of $a = 5\ \mu$m and $w_{\rm gr} = 6\ \mu$m was slightly better than the combination $a = 5\ \mu$m and $w_{\rm gr} = 5\ \mu$m. In the top right map, the red horizontal stain represents the better thickness for the grating while varying the thickness of Au. A slightly increases with the thickness of Au and we chose the minimum amount for which the variation in A was consistent. In the bottom left map, the simulation suggest that A is better with higher thicknesses of both the Ti and Au layer. However, this is not fully compatible with our thin film TESs and we chose a compromise for this test, reducing the amount of Au and selcting 40 nm of Ti. In the bottom right map, the better couples of dielectric thicknesses are shown in red dots. We chose ($t_{\rm SiO_x} = 10$ nm, $t_{\rm TiO_2} = 55$ nm) to limit the amount of deposited dielectrics.

In Fig. 6.15, simulation of our $a = 6\ \mu$m and $w_{\rm gr} = 5\ \mu$m Au grating covered in $\mathrm{TiO_2/SiO}_x$ results in a peak in the absorbance at $\lambda = 690$ nm and $\alpha \sim 74°$. The minimum R from the simulation is $R \sim 30\%$.

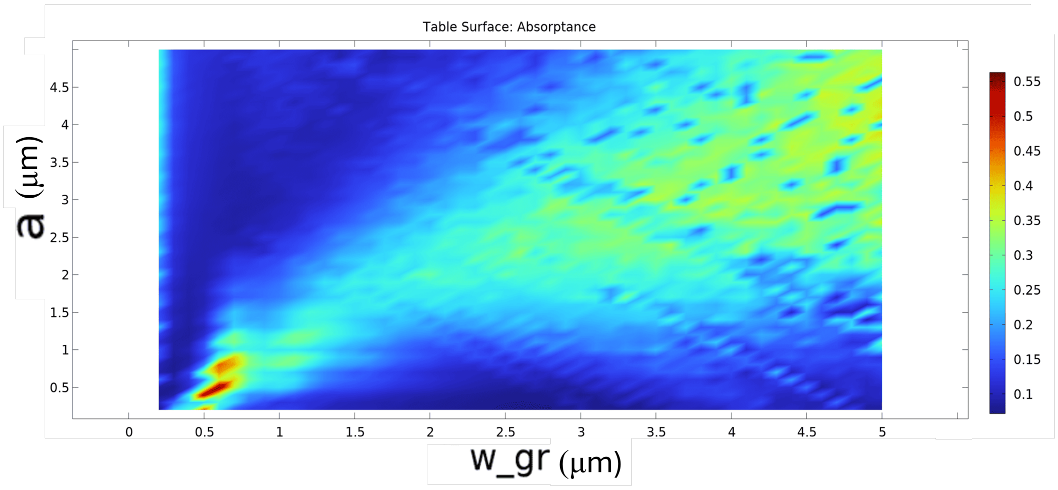

(a) Absorptance vs lateral parameters of the grating (a, w_{gr})

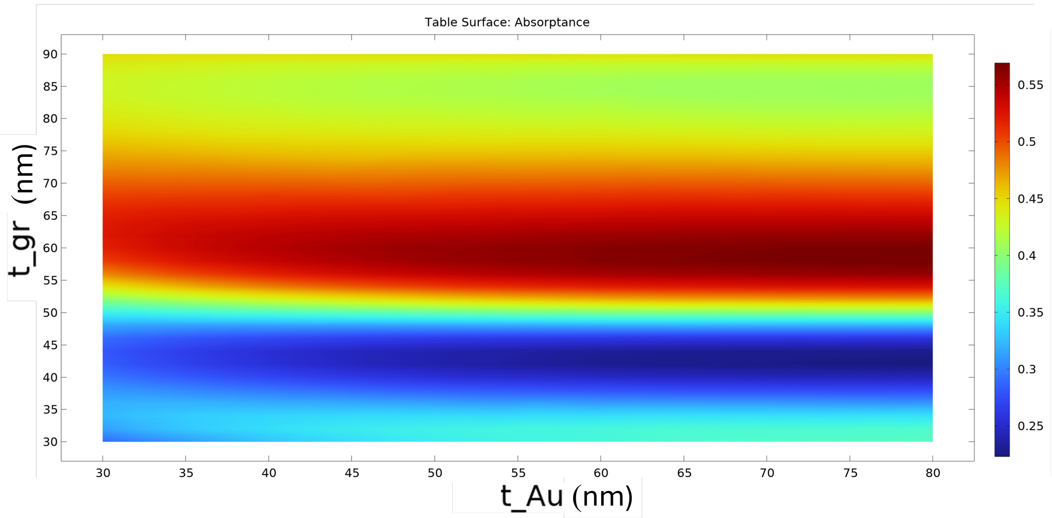

(b) Absorptance vs grating and Au thicknesses (t_{gr}, t_{Au})

Fig. 6.14 (Continued on next page...)

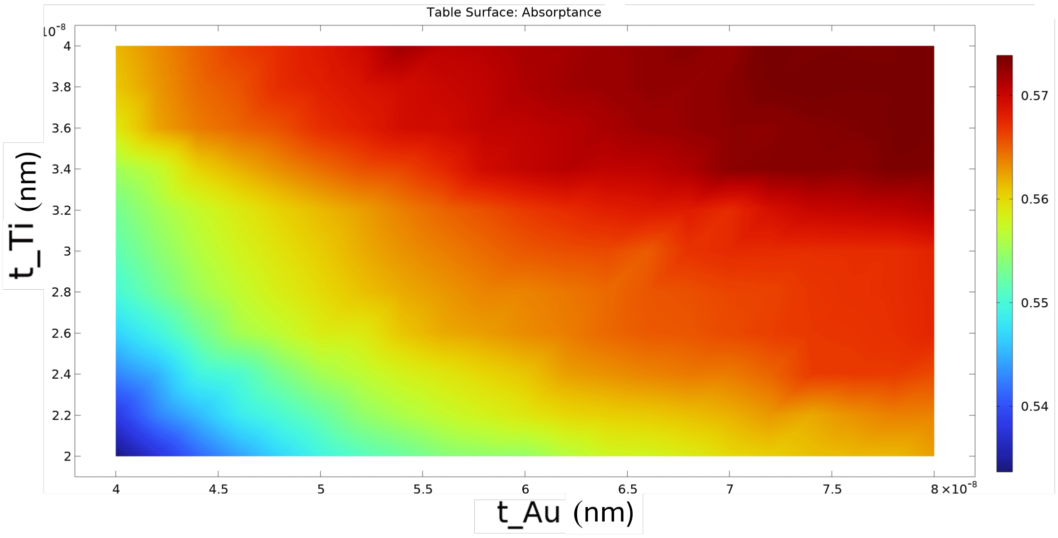

(c) Absorptance vs Ti and Au thicknesses of the TES (t_{Au}, t_{Ti})

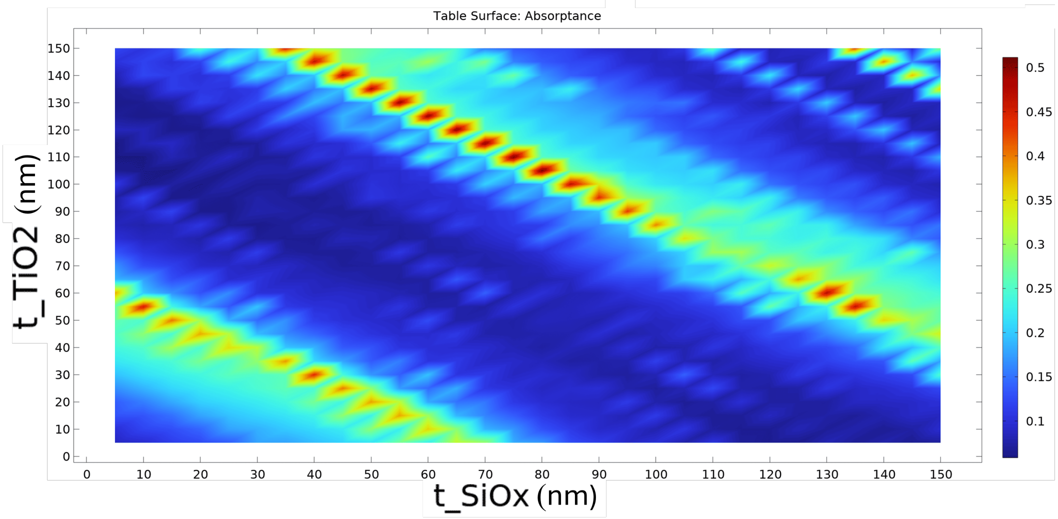

(d) Absorptance vs dielectric thicknesses (t_{TiO_2}, t_{SiO_x})

Fig. 6.14 Simulated A maps of the Sample 2 vs different couples of parameters for $\lambda =$ 630 nm, $\alpha = 0°$ and $n = 1$. (a) A vs lateral grating parameters. (b) A vs grating/Au thicknesses. (c) A vs Ti/Au thicknesses. (d) A vs dielectric thicknesses.

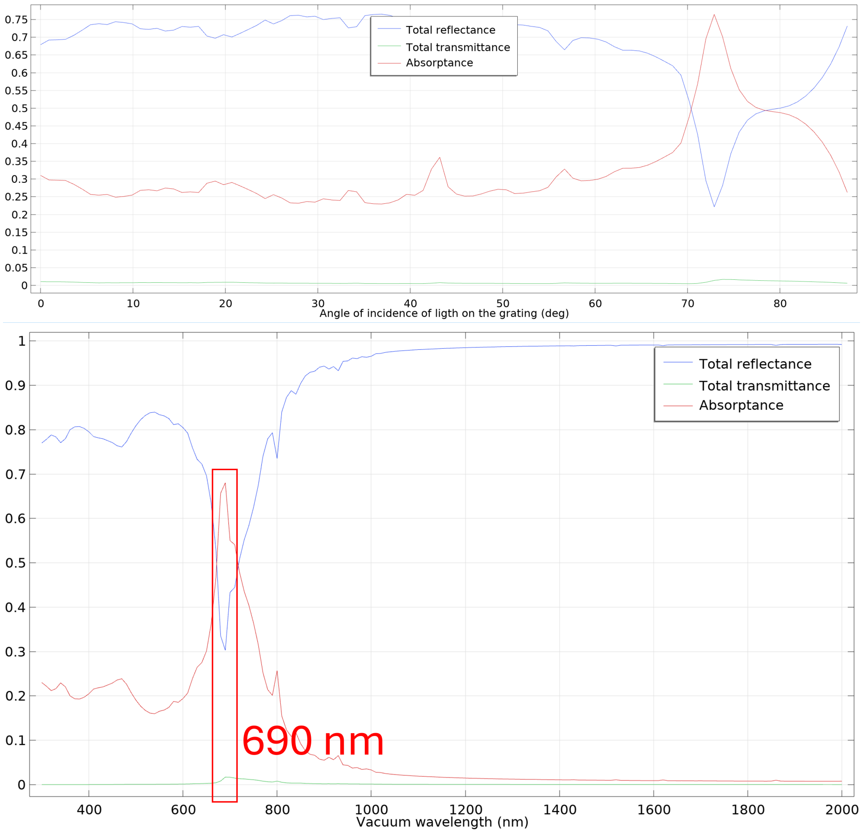

Fig. 6.15 Simulated R(blue), T(green) and A(red) vs the angle of incidence at $\lambda = 690$ nm and vs λ at $\alpha = 74^\circ$ for $a = 6\ \mu$m and $w_{\mathrm{gr}} = 5\ \mu$m from top to bottom.

In Fig. 6.16 different patterns indicated in Tab. 6.10 are shown. These patterns was done as variant patterns from the linear stripes, but keeping unchanged the periodicity, fill factor, structure and thicknesses. The crowns had the function to reduce possible dependencies from the polarization adding a rotational invariance, while the hexagonal lattice had the function to reproduce the grating pattern from 1 axis to 3, adding an invariance for periodic translations. In the same figure we can see the measurement of R *vs* λ at $\alpha = 20^\circ$ for the different films and none of them differ from the basic film C0, but for a 10% overall reduction in R decreasing above $\lambda = 1\ \mu$m for the patterned films. This simply implies that we were far from the correct investigation conditions.

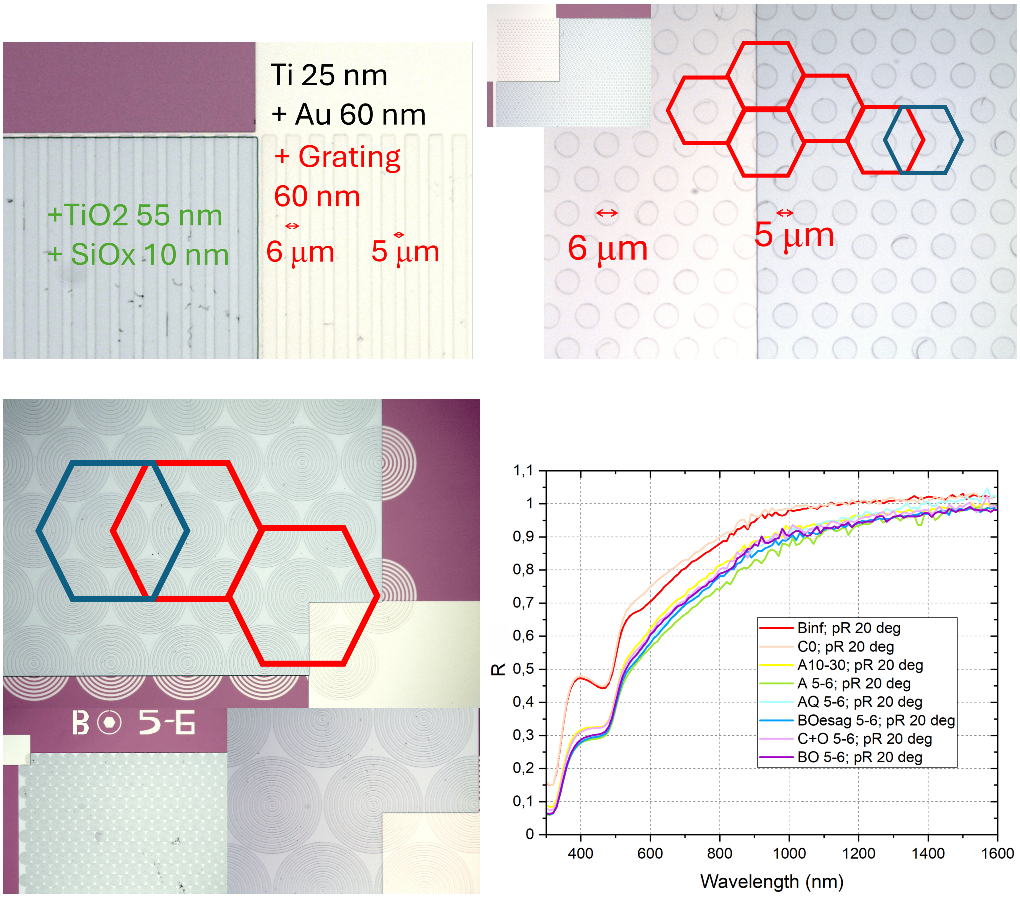

Fig. 6.16 From top to bottom: images of the films realized in the Sample 1 from the linear stripes simulated pattern, to the circles in hexagonal lattice to the concentric circular crowns in the hexagonal lattice. In the bottom right: measured R *vs lambda* at $\alpha = 20^\circ$ for the different films. None of them differ from the basic film at that angle.

Fig. 6.17 shows the main features from this sample:

- at higher angles, the μm−gratings do not show additional polarization dependencies respect to the film and AR coating ones;
- the angle at which a peak appear in the measurements is shifted from the one from simulations. This could be due to wrong thicknesses of some deposited layer ;

- simulations for A5-6 suggest that the peak appear at 690 nm (at lower wavelength respect to C0, A10-30 and B∞) and is narrower and deeper than the other simulated films;
- the measured peaks appear at the λ of the A5-6 peak, but with lower depth and at a different angle (in the R *vs* λ plot).

We can infer 2 different conclusions:

1. the measured peak can be caused by the AR coating and the optical gratings does not contribute. The difference in the dielectric thicknesses respect to simulations are the cause for the shift (in both angle and wavelength) and enhancement of the peak.
2. the peak is caused by the optical μm$-$gratings since it appears at the correct λ, but chamferings due to fabrication processes or errors in the deposited thicknesses have caused a decrease in the depth of the peak and a shift in the incident angle at which it appears. Discrepancies between simulations and experimental results may arise from fabrication uncertainties, particularly in layer thicknesses (crucial in simulations), deviations in grating width and corner rounding, and slight refractive index variations in deposited thin films compared to nominal values. Additionally, the simple 2D geometry assumed in simulations cannot fully capture 3D fabrication defects.

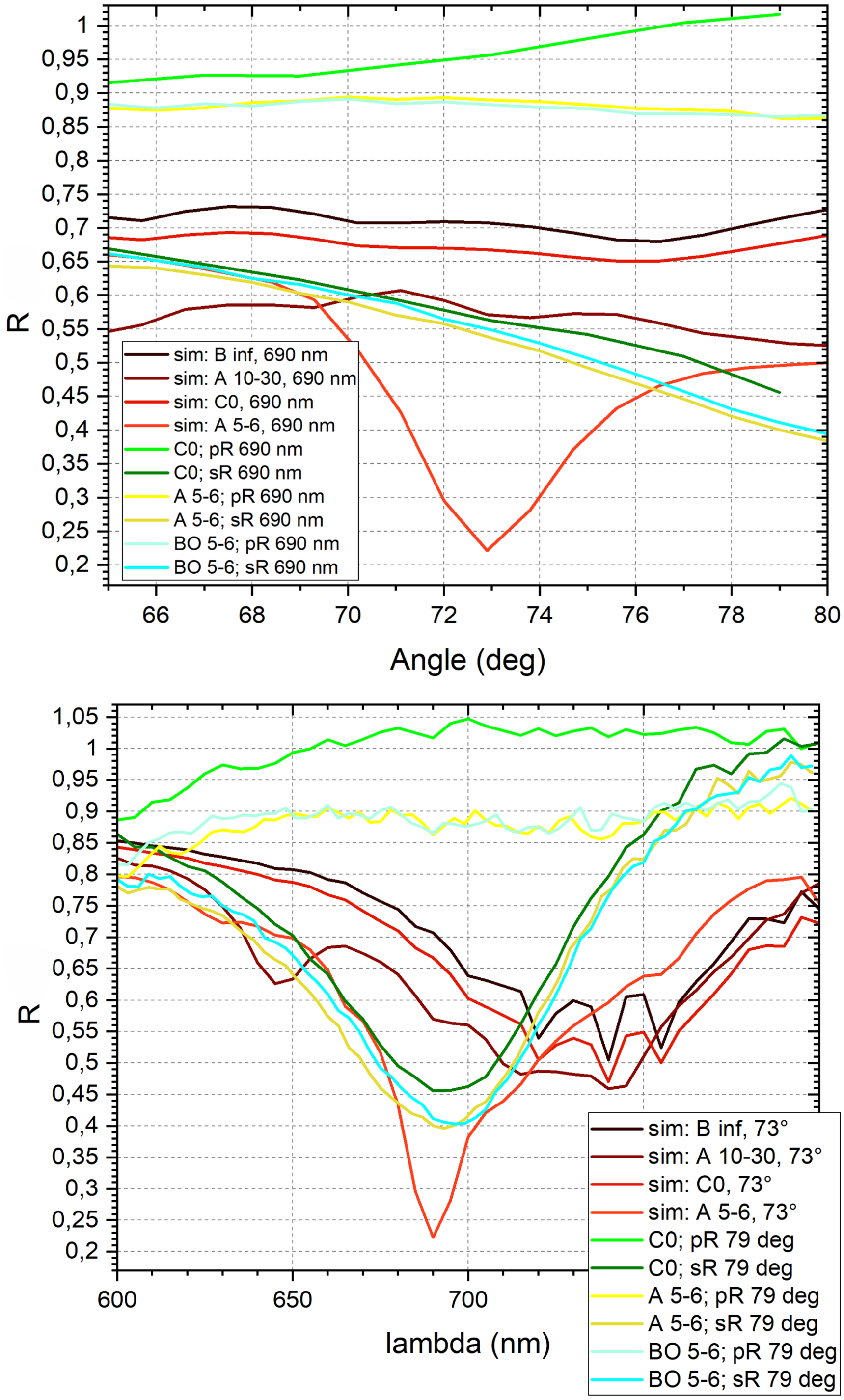

Fig. 6.17 From top to bottom: simulated (black and red) and measured (green, light blue, yellow) R vs the angle of incidence at $\lambda = 690$ nm and vs λ at $\alpha = 73°$ and $79°$ for the films C0, B∞, A5-6 and BO5-6.

Because of these complications, we decided to produce a new sample without AR coating on top to simplifies the analysis.

Sample2

Sample 2 has been simulated as periodic linear stripes and optimized to have $A = 48\%$ at 630 nm and $\alpha = 0$. The structure is:

Table 6.11 Geometric parameters for the structure of Sample 2.

Parameter	Value [nm]
a	8000
w_{gr}	2000
t_{gr}	115
t_{Au}	40
t_{Ti}	40

The films present in this sample are the following:

Table 6.12 List of different grating patterns on Sample 2.

Name	Form	w_{gr} $[\mu m]$	a $[\mu m]$
A8-2	linear stripes	8	2
B2-8	linear stripes	2	8
C0	none	0	∞
A3.5-5	linear stripes	3.5	5
C2-8	concentric circular crowns	2	8
A10-10	linear stripes	10	10
B100-100	linear stripes	100	100
CO2-8	circles in a hexagonal lattice	2	8

For the Sample2, the interrogated wavelengths are from 300 nm to 800 nm. Simulations and measurements of the film C0 are shown in Fig. 6.18a. Simulations of R *vs* λ for C0 at $\alpha = 20^\circ$ for TE waves have the same smooth trend of the measurements, but the real film show a $R = 20\%$ at 450 nm instead of the 45% of the simulations and then converge for higher λ. The reason for this difference could related to deposition, but they seem to affect the results between our region of interest $(600 - 700\ \text{nm})$ only from a 10% to a 5%.

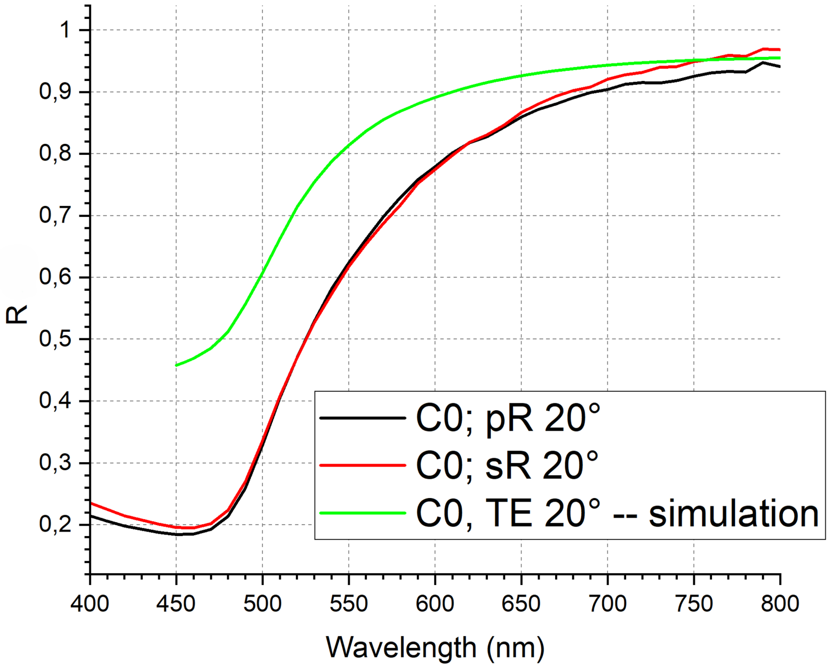

(a) R *vs* λ of the film C0 at $\alpha = 20°$. The green curved is the simulation for TE wave, while red and black curves are the measurements via ellipsometer for the 2 polarizations. The curves have the same trend, but at low λ are different and they start to converge at higher wavelengths. This difference can be caused by difference in the material refractive indexes or real thicknesses of the film.

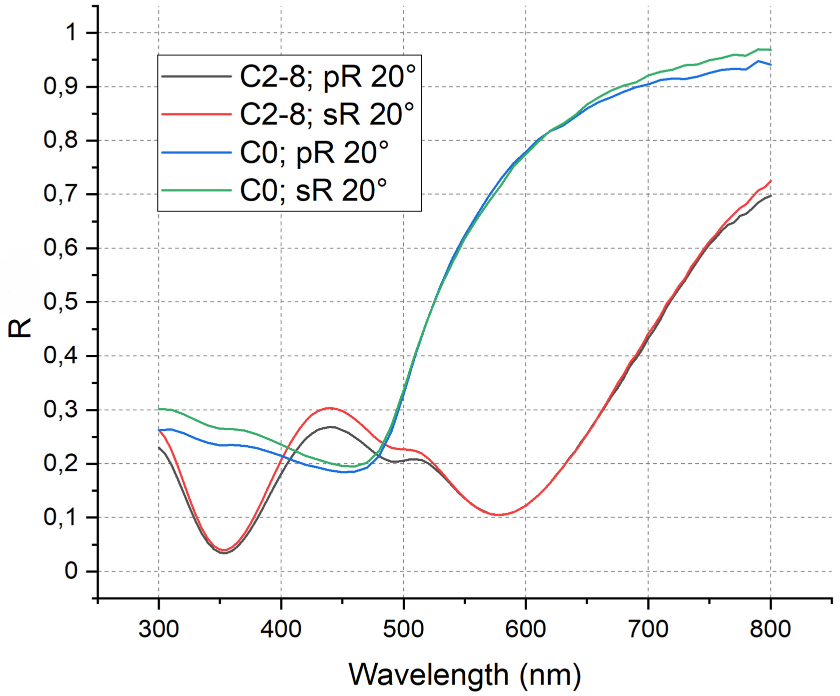

(b) Measured R *vs* λ of the films C0 and C2-8 at $\alpha = 20°$. The concentric circular crowns grating in C2-8 greatly reduce R from the 75% to the 10% at 580 nm.

Fig. 6.18 R *vs* λ for flat film: simulations and measurements. R *vs* λ measurements for flat film and concentric circular crowns grating.

Fig. 6.18b show the difference between the flat film C0 and the film with concentric circular crowns C2-8. The concentric circular crowns scheme has been adopted to reduce the dependency from the polarization, being rotationally invariant on the film plane. There are no consistent differences between the 2 polarizations and, in particular, the reflectivity drops from the 70% for C0 to the 10% for the C2-8 at 580 nm. In the region of interest ($600-700$ nm) we have that the R of the C2-8 film grows from below 15% to 45%. That is very low compared to the values from 75% to 90% of the basic film C0.

In the Fig. 6.19, R *vs* λ of A10-10, B100-100, A8-2 and CO2-8 are shown for $\alpha = 20°$ and $\alpha = 40°$. The simulations for B100-100 and A8-2 mostly follow the one of C0, while A10-10 goes to 70% after $\sim$ 600 nm (instead of 90%) and have a drop from 90% to 56% at 645 nm. The circles in the hexagonal lattice in the CO2-8 film have not been simulated, but realized to create a periodicity in 3 axis instead of the 2 of the linear stripes in addition to a rotational symmetry of 60°. Since C0 has reflectivities 10% lower than the simulations and $R = 20\%$ just above 450 nm, all the measurements have lower values than expected. In fact, A10-10 reflects less than the 10% between the 450 nm ans 500 nm for the p-polarization at $\alpha = 40°$ and has a drop to the 15% at 645 nm (larger, but lower than the simulated 56%). The film B100-100 is similar to C0, but R remain confined under the 70% after 550 nm instead of growing to the 90%. This phenomenon didn't appear during the simulations and is considered as a simple corrugation of the film, without resonances or matching conditions, but generically increasing scatterings and reducing the reflection. The opposite happens with the A8-2 film, whose grating is complementary to the 2-8 grating, that after 600 nm act as a mirror reaching $R \geq 90\%$. All these films act similarly from what we expected if related to the differences between the C0 film and its simulations. However, the major differences could be caused by the presence of imperfections, roundings and chamferings of the corners of the gratings. Probably because of these fabrication problems, the small 2 μm circles doesn't show any optical grating behavior, but act as simple corrugations better than the one in B100-100. One can see that R is lowered to 50% at 600 μm instead of the 70% of the B100-100 film and the 80% of C0.

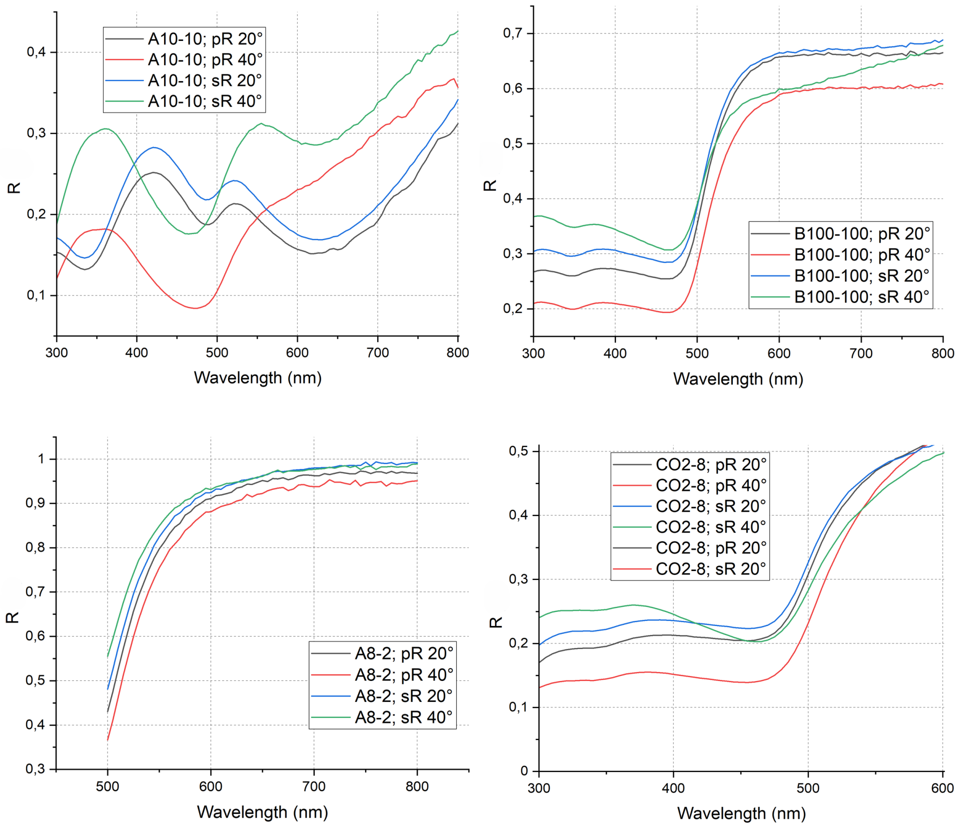

Fig. 6.19 Measured R *vs* λ of the films A10-10, B100-100, A8-2 and C02-8. A10-10, B100-100 and A8-2 films act similarly from what we expected if related to the differences between the C0 film and its simulations. A10-10 has resonances similar to the simulate ones, while B100-100 act only as a corrugation, while A8-2 as a mirror. CO2-8 differ from the linear stripes B2-8 and act simply as corrugation better than B100-100.

The B2-8 film is shown in Fig. 6.20a with an evident resonant minimum between 600 nm and 700 nm at $\alpha = 20^\circ$ and $\alpha = 40^\circ$. The reflectivity drops under the 5% and the overall R remains under the 40% even at $\lambda = 1\ \mu$m. There are no great differences between the 2 polarizations (specially in the range $\lambda \in [600\,\text{nm}, 800\,\text{nm}]$) and the minimum seem to shift to the right while increasing α. The minimum was expected at $(\lambda = 630\ nm, \alpha = 0^\circ)$ and we measured it at $(\lambda = 640\ nm, \alpha = 20^\circ)$ and $(\lambda = 680\ nm, \alpha = 40^\circ)$. This result suggest that, in a merely optical point of view, μm$-$gratings can be competitive with the classical AR coatings. In fact, the dependence on the polarization doesn't appear so limiting and the absorbance can be greater than the 90%. However, a fine tuning to regulate the thickness of gold needed for the μm$-$gratings resonance while not destroying the T_C of thin film TESs is required and the effect on ΔT_C is not already known.

Finally, Fig. 6.20b show an overview of all the films. The "mirror" A8-2 film has the higher *R*, followed by the vanilla film C0. Then from the corrugation films (B100-100, CO2-8, A3.5-5) and finally by optical μm$-$gratings films A10-10, C 2-8 and B2-8. The takeaway message is is that the polarization does not act much on *R* for our gratings at low angles and that *R* can be lowered to the 4% at 640 nm and 20°. Moreover, the solution of circles in a hexagonal lattice act as simple corrugations and lost the optical grating properties due to fabrication complications or because overlapping in the periodicity of grating and lattice. Lastly, the concentric circular crown act good, but not as the standard linear stripe solution. Since there no dependencies on the polarization for low angles, the rotational invariance is not useful and the complication of aligning the fiber to the center of the crowns can be avoided with this optical μm$-$gratings.

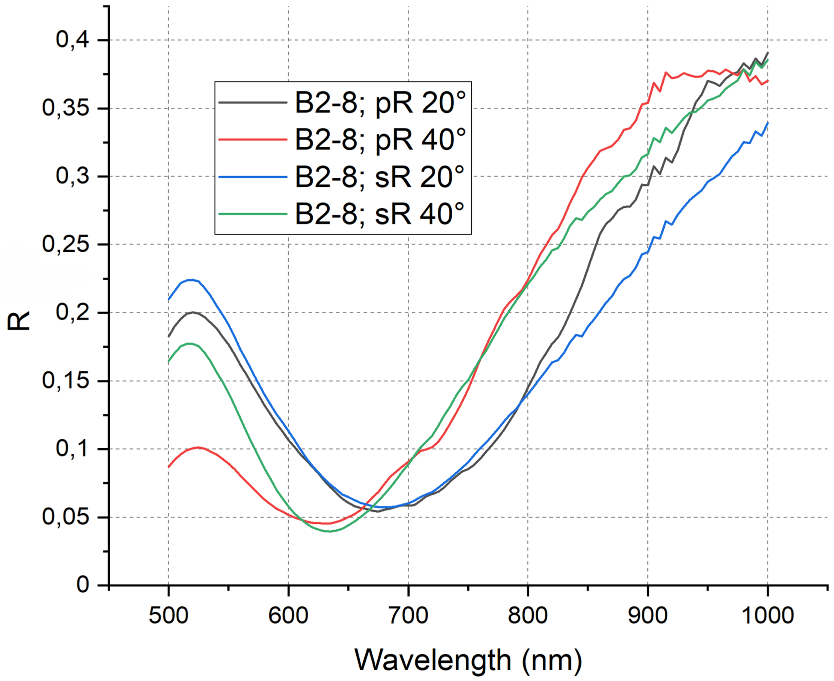

(a) Measured R *vs* λ of the film B2-8. A large resonant drop in R can be seen between 600 nm and 700 nm at $\alpha = 20^\circ$ and $\alpha = 40^\circ$. This drop is attributed to the simulated μm−gratings resonance. The reflectivity drops under the 5% and the overall R remains under the 40% even at $\lambda = 1\ \mu$m.

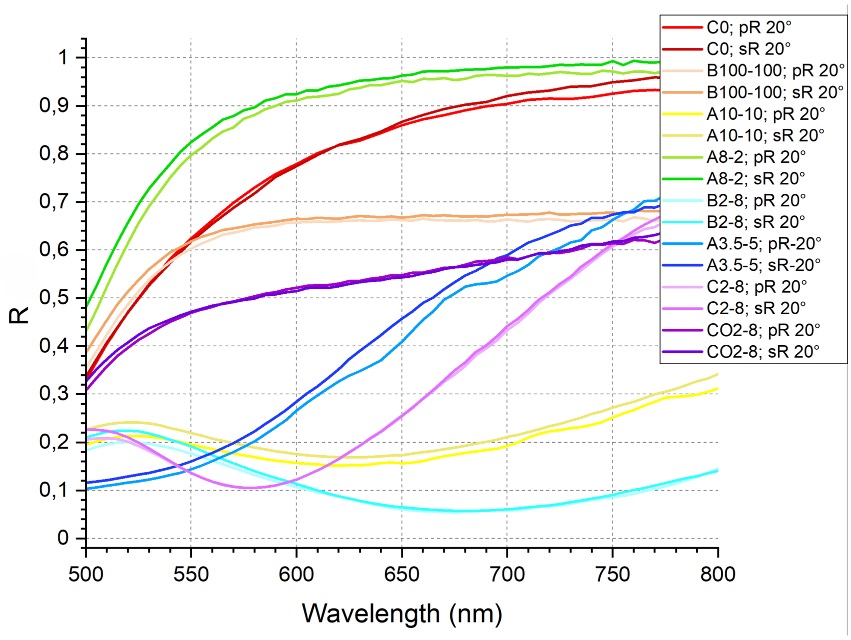

(b) Overview of all the films in the Sample2. The higher R is given by the "mirror" A8-2 (green), with a grating complementary to the one minimizing R to the 5% for optical grating resonance B2-8 (light blue). The uncorrugated film without grating C0 (red) is just below A8-2 and above the other films. The B100-100 (orange), CO2-8 (purple) and A3.5-5 (blue) act as corrugations without resonances, but still decreasing R to 70% and 50%, respectively. A10-10 (yellow), C2-8 (pink) show resonance in the region $550 - 700$ nm between 10% and 20%. At 20°, none of these gratings or corrugations show substantial differences in the polarization behaviors.

Chapter 7

Conclusions and Future Perspectives

This thesis presented a comprehensive study on the design, fabrication, and optimization of Transition-Edge Sensors (TESs) tailored for advanced applications in quantum optics and fundamental physics. The work spanned from the fundamental investigation of superconducting proximity effects to the engineering of high-speed, high-efficiency, and electron-sensitive detectors. The research was driven by the specific requirements of four major frameworks: the **SEQUME** project, aiming for fast single-photon detection for quantum communication, the **PTOLEMY** project, focused on low-energy electron calorimetry for neutrino physics and the the **STAR** project, a project in the framework of quantum technologies requiring almost unitary detection efficiency.

7.1 Summary of Key Discoveries

The experimental and simulation activities led to several key findings regarding TES physics and performance optimization:

- **High-Speed TES Engineering (SEQUME):** To overcome the inherent speed limitations of standard TESs, we investigated two approaches. While aluminum-based TESs showed limitations related to film quality and oxide formation, we successfully used a design based on **lateral gold banks** applied to TiAu bilayers. This geometric modification proved to be a game-changer: it increased the thermal conductance to the bath significantly, reducing the effective recovery time τ_{eff} to the order of hundreds of nanoseconds (down to ~ 200 ns), a four-fold improvement compared to standard designs, without compromising the structural integrity of the device.

- **Low-Energy Electron Detection (PTOLEMY):** We successfully fabricated and characterized large-area TiAu TESs capable of detecting low-energy electrons ($10-100$ eV) with high energy resolution. Crucially, we developed an analytical model describing the dynamics of Secondary Electrons (SE) and Back-Scattered Electrons (BSE). We proved that the flight times of SEs are on the sub-nanosecond scale, making them temporally indistinguishable from primary events using current TES readout bandwidths. This discovery shifts the focus of background rejection from temporal discrimination to geometric optimization, suggesting the necessity of source collimation and active shielding.

- **Physics of Longitudinal Proximity Effects:** We performed a systematic study of the longitudinal proximity effects, which are critical for tuning the transition temperature T_c with small devices. We confirmed the $1/L^2$ scaling law for the longitudinal effect induced by superconducting leads. However, a key discovery was the strong dependence on the contact between wiring material and TESs (TiAu or AuTi): Niobium leads on Au induce a strong proximity effect, whereas Titanium leads on Au showed a weaker effect, but an insufficient particle confinement. Then, we analyzed Titanium-Aluminum (TiAl) leads on Ti, resulting in a suppressed effect likely due to interface oxidation acting as a weak barrier.

- **Photon Absorption Efficiency:** To maximize quantum efficiency, we explored both dielectric, gratings and plasmonic solutions. We achieved a system detection efficiency (SDE) of $\sim 85\%$ using traditional SiO_x/TiO_2 AR coatings. More innovatively, we modeled and designed Grating-Coupled Surface Plasmon Polariton (GC-SPP) structures. Our simulations predict absorption rates exceeding 95% at target wavelengths ($630, 780, 1300, 1550$ nm). Experimental characterization of fabricated test micrometric gratings confirmed the presence of resonant absorption dips, validating the model despite fabrication tolerances.

7.2 Future Perspectives

The results obtained in this thesis open several pathways for future research and technological development:

- **Integration of Plasmonics and Fast Designs:** The immediate next step is the integration of the optimized plasmonic nanogratings directly onto the fast "gold-bank" TESs. This combination aims to produce a device that is simultaneously fast (~ 100 ns) and highly efficient ($> 95\%$), meeting the strict requirements of many quantum communication protocols and quantum technologies.
- **Advanced Electron Calorimetry:** For the PTOLEMY project, future iterations will focus on implementing the proposed geometric solutions to mitigate secondary electron loss. This includes the testing of "decoupling planes" to separate generation and acceleration voltages and the use of nanometric tip sources to spatially confine the primary electron beam away from the detector edges.
- **Material Optimization:** The study on proximity effects suggests that further control over the wiring-TES interface is needed. Future fabrication runs will test TESs with Au on top and TiAl wirings to conclude the study. This allows for more precise T_c engineering for small TESs considering: the material of the leads such to both properly confine the quasi-particle generated from the particle detection and minimize the longitudinal proximity effect; the material of the TES in direct contact with the wirings that can present or not a contact barrier weakening the longitudinal proximity effect.

In conclusion, this thesis has advanced the state of the art of TES technology by providing robust ideas for speed, models for photon detection efficiency and particle discrimination. These developments not only serve the specific goals of our projects, but also contribute to the broader field of superconducting detectors, offering versatile tools for the precision measurement of single quanta of energy.

References

[1] Hobey Garrone. Caratterizzazione di rivelatori superconduttivi ”transition-edge sensor”come contatori di fotoni. *Master Thesis*, Università di Torino, 2021.

[2] C. Enss. *Cryogenic Particle Detection*. Springer, Berlin, 2005.

[3] Guglielmo Ventura and Lara Risegari. *The art of cryogenics: low-temperature experimental techniques*. Elsevier, 2010.

[4] Kent D Irwin and Gene C Hilton. Transition-edge sensors. *Cryogenic particle detection*, pages 63–150, 2005.

[5] NA Wakeham, JS Adams, SR Bandler, S Beaumont, JA Chervenak, AM Datesman, ME Eckart, FM Finkbeiner, R Hummatov, RL Kelley, et al. Thermal fluctuation noise in mo/au superconducting transition-edge sensor microcalorimeters. *Journal of Applied Physics*, 125(16), 2019.

[6] Shuo Zhang, Megan E Eckart, Felix T Jaeckel, Kari L Kripps, Dan McCammon, Kelsey M Morgan, and Yu Zhou. Mapping of the resistance of a superconducting transition edge sensor as a function of temperature, current, and applied magnetic field. *Journal of applied physics*, 121(7), 2017.

[7] J. N. Ullom and D. A. Bennett. Review of superconducting transition-edge sensors for x-ray and gamma-ray spectroscopy. *Superconductor Science and Technology*, 2015.

[8] Kelsey M Morgan, Christine G Pappas, Douglas A Bennett, Johnathon D Gard, James P Hays-Wehle, Gene C Hilton, Carl D Reintsema, Daniel R Schmidt, Joel N Ullom, and Daniel S Swetz. Dependence of transition width on current and critical current in transition-edge sensors. *Applied Physics Letters*, 110(21), 2017.

[9] M. de Wit, L. Gottardi, E. Taralli, K. Nagayoshi, M. Ridder, H. Akamatsu, and J. van der Kuur. Transition edge sensors for dc operation and low magnetic field sensitivity. *IEEE Transactions on Applied Superconductivity*, 34(3):1–5, 2024.

[10] Kaori Hattori, Toshio Konno, Yoshitaka Miura, Sachiko Takasu, and Daiji Fukuda. An optical transition-edge sensor with high energy resolution. *Superconductor Science and Technology*, 35(9):095002, 2022.

[11] Xiaolong Xu, Xiaoying Sun, Jian Chen, Mauro Rajteri, Hobey Garrone, Carlo Pepe, Wan Li, Jinjin Li, Mingyu Zhang, Tianjia Bu, et al. Development of ti/au transition-edge sensors for single-photon detection. *IEEE Transactions on Applied Superconductivity*, 34(3):1–4, 2024.

[12] L Lolli, Emanuele Taralli, Mauro Rajteri, T Numata, and D Fukuda. Characterization of optical fast transition-edge sensors with optimized fiber coupling. *IEEE transactions on applied superconductivity*, 23(3):2100904–2100904, 2013.

[13] Ruslan Hummatov, Adriana E Lita, Tannaz Farrahi, Negar Otrooshi, Samuel Fayer, Matthew J Collins, Malcolm Durkin, Douglas Bennett, Joel Ullom, Richard P Mirin, et al. Fast transition-edge sensors suitable for photonic quantum computing. *Journal of Applied Physics*, 133(23), 2023.

[14] Adriana E Lita, Aaron J Miller, and Sae Woo Nam. Counting near-infrared single-photons with 95% efficiency. *Optics express*, 16(5):3032–3040, 2008.

[15] Daiji Fukuda, Go Fujii, Takayuki Numata, Kuniaki Amemiya, Akio Yoshizawa, Hidemi Tsuchida, Hidetoshi Fujino, Hiroyuki Ishii, Taro Itatani, Shuichiro Inoue, et al. Titanium-based transition-edge photon number resolving detector with 98% detection efficiency with index-matched small-gap fiber coupling. *Optics express*, 19(2):870–875, 2011.

[16] Laura Manenti, Carlo Pepe, Isaac Sarnoff, Tengiz Ibrayev, Panagiotis Oikonomou, Artem Knyazev, Eugenio Monticone, Hobey Garrone, Fiona Alder, Osama Fawwaz, et al. Dark counts in optical superconducting transition-edge sensors for rare-event searches. *Physical Review Applied*, 22(2):024051, 2024.

[17] William B Doriese, Kelsey M Morgan, Douglas A Bennett, Edward V Denison, Colin P Fitzgerald, Joseph W Fowler, Johnathon D Gard, James P Hays-Wehle, Gene C Hilton, Kent D Irwin, et al. Developments in time-division multiplexing of x-ray transition-edge sensors. *Journal of low temperature physics*, 184:389–395, 2016.

[18] Daniel Swetz. Highly scalable transition-edge sensor arrays for optical to near-infrared astronomy. *NASA APRA Proposal*, page 104, 2021.

[19] Paul Szypryt, Douglas A Bennett, Ian Fogarty Florang, Joseph W Fowler, Andrea Giachero, Ruslan Hummatov, Adriana E Lita, John AB Mates, Sae Woo Nam, Galen C O'Neil, et al. Kinetic inductance current sensor for visible to near-infrared wavelength transition-edge sensor readout. *Communications Engineering*, 3(1):160, 2024.

[20] J. Zmuidzinas. Superconducting microresonators: Physics and applications. *Annual Review of Condensed Matter Physics*, 3:169–214, 2012.

[21] H. G. LeDuc and et al. Titanium nitride films for ultrasensitive microresonator detectors. *Applied Physics Letters*, 97(10):102509, 2010.

[22] Jennifer Pearl Smith, John I Bailey, Aled Cuda, Nicholas Zobrist, Benjamin A Mazin, et al. Mkidgen3: Energy-resolving, single-photon-counting mkid readout on an rfsoc. *arXiv preprint arXiv:2406.09764*, 2024.

[23] Pieter J. de Visser, Steven A.H. de Rooij, Vignesh Murugesan, David J. Thoen, and Jochem J.A. Baselmans. Phonon-trapping-enhanced energy resolution in superconducting single-photon detectors. *Phys. Rev. Appl.*, 16:034051, Sep 2021.

[24] W. Guo, X. Liu, Y. Wang, Q. Wei, L. F. Wei, J. Hubmayr, J. Fowler, J. Ullom, L. Vale, M. R. Vissers, and J. Gao. Counting near infrared photons with microwave kinetic inductance detectors. *Applied Physics Letters*, 110(21), May 2017.

[25] Can Yang, Mengting Si, and Lixing You. Superconducting x-ray detectors. *Science China Information Sciences*, 63(8):180502, 2020.

[26] Danica Marsden, Benjamin A Mazin, Bruce Bumble, Seth Meeker, Kieran O'Brien, Sean McHugh, Matthew Strader, and Eric Langman. Optical lumped element microwave kinetic inductance detectors. In *High Energy, Optical, and Infrared Detectors for Astronomy V*, volume 8453, pages 62–70. SPIE, 2012.

[27] K Kouwenhoven. *Visible to Near-Infrared Kinetic Inductance Detectors: Energy-Resolving Single Photon Detectors*. PhD thesis, Delft University of Technology, 2024.

[28] J. J. A. Baselmans, B. S. Karasik, R. den Hartog, and A. V. Verhoeve. Kinetic inductance detectors for sub-millimeter astronomy. In *Proceedings of SPIE*, volume 8452, page 84520F. International Society for Optics and Photonics, 2012.

[29] GN Gol'Tsman, O Okunev, G Chulkova, A Lipatov, A Semenov, K Smirnov, B Voronov, A Dzardanov, C Williams, and Roman Sobolewski. Picosecond superconducting single-photon optical detector. *Applied physics letters*, 79(6):705–707, 2001.

[30] Boris Korzh, Qing-Yuan Zhao, Jason P Allmaras, Simone Frasca, Travis M Autry, Eric A Bersin, Andrew D Beyer, Ryan M Briggs, Bruce Bumble, Marco Colangelo, et al. Demonstration of sub-3 ps temporal resolution with a superconducting nanowire single-photon detector. *Nature Photonics*, 14(4):250–255, 2020.

[31] J Chang. *Detecting Single Photons with Superconducting Nanowires*. PhD thesis, Delft University of Technology, 2021.

[32] Jeff Chiles, Ilya Charaev, Robert Lasenby, Masha Baryakhtar, Junwu Huang, Alexana Roshko, George Burton, Marco Colangelo, Ken Van Tilburg, Asimina Arvanitaki, Sae Woo Nam, and Karl K. Berggren. New constraints on dark photon dark matter with superconducting nanowire detectors in an optical haloscope. *Phys. Rev. Lett.*, 128:231802, Jun 2022.

[33] Chandra M Natarajan, Michael G Tanner, and Robert H Hadfield. Superconducting nanowire single-photon detectors: physics and applications. *Superconductor science and technology*, 25(6):063001, 2012.

[34] L Zhang, L Kang, J Chen, Y Zhong, Q Zhao, T Jia, C Cao, B Jin, W Xu, G Sun, et al. Ultra-low dark count rate and high system efficiency single-photon detectors with 50 nm-wide superconducting wires. *Applied Physics B*, 102(4):867–871, 2011.

[35] V. B. Verma, J. Chiles, et al. Low-noise single-photon counting superconducting nanowire detectors at infrared wavelengths up to 29 μm. *Optica*, 10(12):1672–1677, 2023.

[36] J. Chang et al. Efficient mid-infrared single-photon detection using superconducting nbtin nanowires with high time resolution. *Photonics Research*, 10(4):1063–1070, 2022.

[37] Binjie Zhao, Zigang Deng, Zunxiang Hu, Yu Liu, Shuai Zhang, and Jun Zheng. Levitation force characteristics of high-temperature superconducting bulks in a high magnetic field. *IEEE Transactions on Applied Superconductivity*, 30(4):1–5, 2020.

[38] Yonit Hochberg, Ilya Charaev, Sae-Woo Nam, Varun Verma, Marco Colangelo, and Karl K Berggren. Detecting sub-gev dark matter with superconducting nanowires. *Physical review letters*, 123(15):151802, 2019.

[39] Bakhrom G Oripov, Dana S Rampini, Jason Allmaras, Matthew D Shaw, Sae Woo Nam, Boris Korzh, and Adam N McCaughan. A superconducting nanowire single-photon camera with 400,000 pixels. *Nature*, 622(7984):730–734, 2023.

[40] Jun Gao, Jin Chang, Bruno Lopez Rodriguez, Iman Esmaeil Zadeh, Val Zwiller, and Ali W Elshaari. From pixels to camera: Scaling superconducting nanowire single-photon detectors for imaging at the quantum-limit. *arXiv preprint arXiv:2505.24725*, 2025.

[41] Hao Hao, Qing-Yuan Zhao, Ling-Dong Kong, Shi Chen, Hui Wang, Yang-Hui Huang, Jia-Wei Guo, Chao Wan, Hao Liu, Xue-Cou Tu, et al. Improved pulse discrimination for a superconducting series nanowire detector by applying a digital matched filter. *Applied Physics Letters*, 119(23), 2021.

[42] Veronika R Meyer. Measurement uncertainty. *Journal of Chromatography A*, 1158(1-2):15–24, 2007.

[43] Carlo Pepe. *Development of Superconducting Single-Particle Detector Transition-Edge Sensor*. PhD thesis, Politecnico di Torino, 2024.

[44] Sequme: Single and entangled photon sources for quantum metrology. Available at https://sequme.cmi.gov.cz/.

[45] Hobey Garrone, Carlo Pepe, Alessandro Reineri, Eugenio Monticone, Roberto Filippo, and Mauro Rajteri. Simulation software for transition-edge sensor performance prediction. *IEEE Transactions on Applied Superconductivity*, 32(4):1–6, 2022.

[46] INRiM. free tes simulator online software. Available at https://tes.inrim.it/.

[47] K Yu Arutyunov, EA Sedov, VV Zavialov, A Stavrinidis, G Stavrinidis, Z Chatzopoulos, A Adikimenakis, G Konstantinidis, N Florini, P Chatzopoulou, et al. The critical temperature of superconducting aluminum films. *Physics of Metals and Metallography*, 124(1):53–57, 2023.

[48] Sameh Okasha, Yoshiaki Sekine, Satoshi Sasaki, and Yuichi Harada. Atomic layer deposition of aluminum (111) thin film by dimethylethylaminealane precursor. *Thin Solid Films*, 732:138784, 2021.

[49] D Fukuda, G Fujii, A Yoshizawa, H Tsuchida, RMT Damayanthi, H Takahashi, S Inoue, and M Ohkubo. High speed photon number resolving detector with titanium transition edge sensor. *Journal of Low Temperature Physics*, 151:100–105, 2008.

[50] Kent D Irwin, Gene C Hilton, David A Wollman, and John M Martinis. Thermal-response time of superconducting transition-edge microcalorimeters. *Journal of Applied Physics*, 83(8):3978–3985, 1998.

[51] Douglas A Bennett, Robert D Horansky, AS Hoover, NJ Hoteling, MW Rabin, DR Schmidt, Daniel S Swetz, LR Vale, and Joel N Ullom. An analytical model for pulse shape and electrothermal stability in two-body transition-edge sensor microcalorimeters. *Applied physics letters*, 97(10), 2010.

[52] Carlo Pepe, Benedetta Corcione, Francesco Pandolfi, Hobey Garrone, Eugenio Monticone, Ilaria Rago, Gianluca Cavoto, Alice Apponi, Alessandro Ruocco, Federico Malnati, et al. Detection of low-energy electrons with transition-edge sensors. *Physical Review Applied*, 22(4):L041007, 2024.

[53] E Baracchini, MG Betti, M Biasotti, A Bosca, F Calle, J Carabe-Lopez, G Cavoto, C Chang, AG Cocco, AP Colijn, et al. Ptolemy: A proposal for thermal relic detection of massive neutrinos and directional detection of mev dark matter. *arXiv preprint arXiv:1808.01892*, 2018.

[54] S Betts, WR Blanchard, RH Carnevale, C Chang, C Chen, S Chidzik, L Ciebiera, P Cloessner, A Cocco, A Cohen, et al. Development of a relic neutrino detection experiment at ptolemy: princeton tritium observatory for light, early-universe, massive-neutrino yield. *arXiv preprint arXiv:1307.4738*, 2013.

[55] A Apponi, MG Betti, M Borghesi, A Boyarsky, N Canci, G Cavoto, C Chang, V Cheianov, Y Cheipesh, W Chung, et al. Heisenberg's uncertainty principle in the ptolemy project: A theory update. *Physical Review D*, 106(5):053002, 2022.

[56] Kunal Patel. *Transition-edge sensors for electron spectroscopy*. PhD thesis, University of Cambridge, 2024.

[57] HJJoAP Seiler. Secondary electron emission in the scanning electron microscope. *Journal of Applied Physics*, 54(11):R1–R18, 1983.

[58] JLH Jonker. The angular distribution of the secondary electrons of nickel. *Philips Res. Rep*, 6(5):372–387, 1951.

[59] Neal Nickles, RE Davies, and John R Dennison. Applications of secondary electron energy-and angular-distributions to spacecraft charging. In *Proceedings of the 6th Spacecraft Charging Technology Conference*, page 275, 2000.

[60] Mauro Ciappa, Emre Ilgünsatiroglu, and Alexey Yu Illarionov. Monte carlo simulation of emission site, angular and energy distributions of secondary electrons in silicon at low beam energies. *Microelectronics Reliability*, 52(9-10):2139–2143, 2012.

[61] Mario Malerba, Alessandro Alabastri, Ermanno Miele, Pierfrancesco Zilio, Maddalena Patrini, Daniele Bajoni, Gabriele C Messina, Michele Dipalo, Andrea Toma, Remo Proietti Zaccaria, et al. 3d vertical nanostructures for enhanced infrared plasmonics. *Scientific reports*, 5(1):16436, 2015.

[62] John E Sadleir, Stephen J Smith, Simon R Bandler, James A Chervenak, and John R Clem. Longitudinal proximity effects in superconducting transition-edge sensors. *Physical review letters*, 104(4):047003, 2010.

[63] K Nagayoshi, M de Wit, E Taralli, S Visser, ML Ridder, L Gottardi, H Akamatsu, D Vaccaro, MP Bruijn, J-R Gao, et al. Lateral inverse proximity effect in ti/au transition edge sensors. *Journal of Low Temperature Physics*, 209(3):540–547, 2022.

[64] John E Sadleir, Stephen J Smith, Ian K Robinson, Fred M Finkbeiner, James A Chervenak, Simon R Bandler, Megan E Eckart, and Caroline A Kilbourne. Proximity effects and nonequilibrium superconductivity in transition-edge sensors. *Physical Review B—Condensed Matter and Materials Physics*, 84(18):184502, 2011.

[65] ML Ridder, K Nagayoshi, MP Bruijn, L Gottardi, E Taralli, P Khosropanah, H Akamatsu, J van der Kuur, K Ravensberg, S Visser, et al. Study of tes detector transition curve to optimize the pixel design for frequency-division multiplexing readout. *Journal of Low Temperature Physics*, 199:962–967, 2020.

[66] Sebastian MF Raupach, Ivo Pietro Degiovanni, Hristina Georgieva, Alice Meda, Helmuth Hofer, Marco Gramegna, Marco Genovese, Stefan Kück, and Marco López. Detection rate dependence of the inherent detection efficiency in single-photon detectors based on avalanche diodes. *Physical Review A*, 105(4):042615, 2022.

[67] Hristina Georgieva, Alice Meda, Sebastian MF Raupach, Helmuth Hofer, Marco Gramegna, Ivo Pietro Degiovanni, Marco Genovese, Marco López, and Stefan Kück. Detection of ultra-weak laser pulses by free-running single-photon detectors: modeling dead time and dark counts effects. *Applied Physics Letters*, 118(17), 2021.

[68] Federico Malnati. *Rivelazione di particelle con i Transition-edge Sensors: dai fotoni agli elettroni*. PhD thesis, Università degli studi di Torino, 2023-2024.

[69] Thin Film Center Inc. Thin film center provides optical thin film software for design and analysis of optical coatings and consulting for the coating industry. Available at https://www.thinfilmcenter.com.

[70] Tahir Iqbal, Saba Khalil, Mohsin Ijaz, Khalid Nadeem Riaz, Muhammad Isa Khan, Muhammad Shakil, Azeem Ghulam Nabi, Muhammad Javaid, Muhammad Abrar, and Sumera Afsheen. Optimization of 1d plasmonic grating of nanostructured devices for the investigation of plasmonic bandgap. *Plasmonics*, 14:775–783, 2019.

[71] Sergio G Rodrigo, Carlos Pobes, Marta Sánchez Casi, Luis Martín-Moreno, and Agustín Camón Lasheras. Neural network assisted design of plasmonic nanostructures on superconducting transition-edge-sensors for single photon detectors. *Optics Express*, 30(8):12368–12377, 2022.

[72] VG Kravets, F Schedin, and AN Grigorenko. Plasmonic blackbody: Almost complete absorption of light in nanostructured metallic coatings. *Physical Review B—Condensed Matter and Materials Physics*, 78(20):205405, 2008.

[73] www.comsol.com/trademarks. *Plasmonic Wire Grating*. Available at https://doc.comsol.com/6.1/doc/com.comsol.help.models.woptics.plasmonic_wire_grating/plasmonic_wire_grating.html.

[74] Refractive index database. Available at https://refractiveindex.info/?shelf=3d&book=metals&page=titanium.

[75] Alessandro Alabastri, Mario Malerba, Eugenio Calandrini, Alejandro Manjavacas, Francesco De Angelis, Andrea Toma, and Remo Proietti Zaccaria.

Controlling the heat dissipation in temperature-matched plasmonic nanostructures. *Nano letters*, 17(9):5472–5480, 2017.

[76] Gabriele C Messina, Mario Malerba, Pierfrancesco Zilio, Ermanno Miele, Michele Dipalo, Lorenzo Ferrara, and Francesco De Angelis. Hollow plasmonic antennas for broadband sers spectroscopy. *Beilstein Journal of Nanotechnology*, 6(1):492–498, 2015.

[77] A Kozorezov. Energy down-conversion and thermalization in metal absorbers. *Journal of Low Temperature Physics*, 167(3):473–484, 2012.

[78] Spectral thin film reflectance calculator for thin-film stacks. Available at https://www.kla.com/products/instruments/reflectance-calculator?wmin=300&wmax=700&wstep=1&angle=0&pol=s&units=nm&mat[]=Air&d[]=0&mat[]=SiO2&d[]=500&mat[]=Au&d[]=30&mat[]=Ti&d[]=15&mat[]=Si3N4&d[]=0&sptype=r.

[79] J. Bardeen, L. N. Cooper, and J. R. Schrieffer. Theory of superconductivity. *Phys. Rev.*, 108:1175–1204, Dec 1957.

[80] J.M. Martinis, G. C. Hilton, K.D. Irwin, and D.A. Wollman. Calculation of tc in a normal-superconductor bilayer using the microscopic-based usadel theory. *National Institute of Standards and Technology*, 2000.

[81] R. Boucher, T. May, ThWagner, V. Zakosarenko, S. Anders, and H. G. Mayer. Structural and electrical properties of aupd/mo bi-layer films for transition edge sensors. *Institute for Physical High Technology*, 2005.

[82] J Beyer and D Drung. A squid series array dc current sensor. *Superconductor Science and Technology*, 21(9):095012, 2008.

[83] John Clarke and Alex I Braginski. Fundamentals and technology of squids and squid systems. *(No Title)*, 2004.

[84] JAB Mates, Daniel T Becker, Douglas A Bennett, BJ Dober, JD Gard, JP Hays-Wehle, JW Fowler, GC Hilton, CD Reintsema, DR Schmidt, et al. Simultaneous readout of 128 x-ray and gamma-ray transition-edge microcalorimeters using microwave squid multiplexing. *Applied Physics Letters*, 111(6), 2017.

[85] Paul Szypryt, SR Meeker, G Coiffard, N Fruitwala, B Bumble, G Ulbricht, AB Walter, M Daal, C Bockstiegel, G Collura, et al. Large-format platinum silicide microwave kinetic inductance detectors for optical to near-ir astronomy. *Optics Express*, 25(21):25894–25909, 2017.

[86] Aditya Kher, PK Day, Byeong Ho Eom, Jonas Zmuidzinas, and HG Leduc. Kinetic inductance parametric up-converter. *Journal of Low Temperature Physics*, 184:480–485, 2016.

[87] Johnathon D Gard, Daniel T Becker, Douglas A Bennett, Joseph W Fowler, Gene C Hilton, JAB Mates, Carl D Reintsema, Daniel R Schmidt, Daniel S Swetz, and Joel N Ullom. A scalable readout for microwave squid multiplexing of transition-edge sensors. *Journal of Low Temperature Physics*, 193:485–497, 2018.

[88] Zahraa Hummam Mohammed. The fresnel coefficient of thin film multilayer using transfer matrix method tmm. In *IOP Conference Series: Materials Science and Engineering*, volume 518, page 032026. IOP Publishing, 2019.

[89] William L Barnes, Alain Dereux, and Thomas W Ebbesen. Surface plasmon subwavelength optics. *nature*, 424(6950):824–830, 2003.

[90] Francisco J Garcia-Vidal, Luis Martin-Moreno, TW Ebbesen, and L Kuipers. Light passing through subwavelength apertures. *Reviews of Modern Physics*, 82(1):729–787, 2010.

[91] Junxi Zhang, Lide Zhang, and Wei Xu. Surface plasmon polaritons: physics and applications. *Journal of Physics D: Applied Physics*, 45(11):113001, 2012.

[92] Divagar Murugan, Marcel Tintelott, Madaboosi S Narayanan, Xuan-Thang Vu, Tetiana Kurkina, César Rodriguez-Emmenegger, Ulrich Schwaneberg, Jakub Dostalek, Sven Ingebrandt, and Vivek Pachauri. Recent advances in grating coupled surface plasmon resonance technology (advanced optical materials 34/2024). *Advanced Optical Materials*, 12(34):2470110, 2024.

[93] Jianjun Cao, Yuan Sun, Yan Kong, and Weiying Qian. The sensitivity of grating-based spr sensors with wavelength interrogation. *Sensors*, 19(2):405, 2019.

[94] Siqi Long, Jianjun Cao, Yueke Wang, Shumei Gao, Nianxi Xu, Jinsong Gao, and Wenjie Wan. Grating coupled spr sensors using off the shelf compact discs and sensitivity dependence on grating period. *Sensors and Actuators Reports*, 2(1):100016, 2020.

[95] Mikhail A Kats, Romain Blanchard, Patrice Genevet, and Federico Capasso. Nanometre optical coatings based on strong interference effects in highly absorbing media. *Nature materials*, 12(1):20–24, 2013.

[96] Kevin M McPeak, Sriharsha V Jayanti, Stephan JP Kress, Stefan Meyer, Stelio Iotti, Aurelio Rossinelli, and David J Norris. Plasmonic films can easily be better: rules and recipes. *ACS photonics*, 2(3):326–333, 2015.

[97] Gururaj V Naik, Vladimir M Shalaev, and Alexandra Boltasseva. Alternative plasmonic materials: beyond gold and silver. *Advanced materials*, 25(24):3264–3294, 2013.

[98] Huakang Yu, Yusi Peng, Yong Yang, and Zhi-Yuan Li. Plasmon-enhanced light–matter interactions and applications. *npj Computational Materials*, 5(1):45, 2019.

[99] N. D. Mermin N.W. Ashcroft. *Solid State Physics*. Saunders Collage Publishing, 1976.

[100] Heinz Faether. *Surface Plasmons on*. Springer Tracts in Modem Physics 111, 1988.

[101] Vasily V Temnov, Ulrike Woggon, José Dintinger, Eloise Devaux, and Thomas W Ebbesen. Surface plasmon interferometry: measuring group velocity of surface plasmons. *Optics letters*, 32(10):1235–1237, 2007.

[102] DS Kim, SC Hohng, V Malyarchuk, YC Yoon, YH Ahn, KJ Yee, JW Park, J Kim, QH Park, and Ch Lienau. Microscopic origin of surface-plasmon radiation in plasmonic band-gap nanostructures. *Physical Review Letters*, 91(14):143901, 2003.

[103] Donald L Smith and David W Hoffman. Thin-film deposition: Principles and practice, 1996.

Appendix A

Additional materials on superconductivity and optics

In this appendix, we outline the fundamental principles of superconductivity necessary to understand the physics necessary to TESs. We provide a brief overview of the BCS theory and the London equations, followed by a description of the proximity effect, which is crucial for engineering the critical temperature of the bilayer films used in this work. We then describe the operation of dc-SQUIDs, the readout devices used for our sensors. Finally, we will introduce the principles of anti-reflection coatings and plasmonic gratings.

A.1 Some elements of superconductivity

Some materials have the ability to transition to a state called superconductivity below a critical temperature T_c. For low T_c, the phenomenon of superconductivity is explained by the formation of Cooper pairs, a bound state of two electrons due to an attractive interaction. These pairs no longer behave as fermions, but as bosons. The binding energy of Cooper pairs allows them to move without resistance, avoiding scattering events and thus making the material a perfect conductor, as shown in Fig. A.1a. The formation of these pairs was first explained in 1957 by Bardeen, Cooper, and Schrieffer with the BCS theory [79]. The binding energy of the two electrons in each Cooper pair is due to interactions with positive ions in the lattice mediated by phonons. When an electron moves in a superconductor, the positive ions in the lattice are attracted to it. Because the electron moves faster than the ions can respond, a region of positive charge is generated. This region, in turn, attracts a second electron. The resulting binding energy is called the superconducting energy gap of the material. In a superconductor described by BCS theory, the transition temperature T_c is related to the superconducting energy gap E_gap in the weak-coupling limit by the relation [79]:

$$E_\mathrm{gap} \approx \frac{7}{2} k_\mathrm{B} T_\mathrm{c}. \tag{A.1}$$

In addition to perfect conductivity at temperatures lower than T_c, another characteristic aspect of superconductivity is the Meissner-Ochsenfeld effect, whereby the system's free energy is minimized when any external magnetic field is expelled from the superconducting sample, as shown in Fig. A.1b. A magnetic field applied to a superconductor is exponentially shielded by a supercurrent of Cooper pairs induced on its surface. The state transition can also occur relative to the critical values of two other quantities: magnetic field and current density, as shown in Fig. A.2.

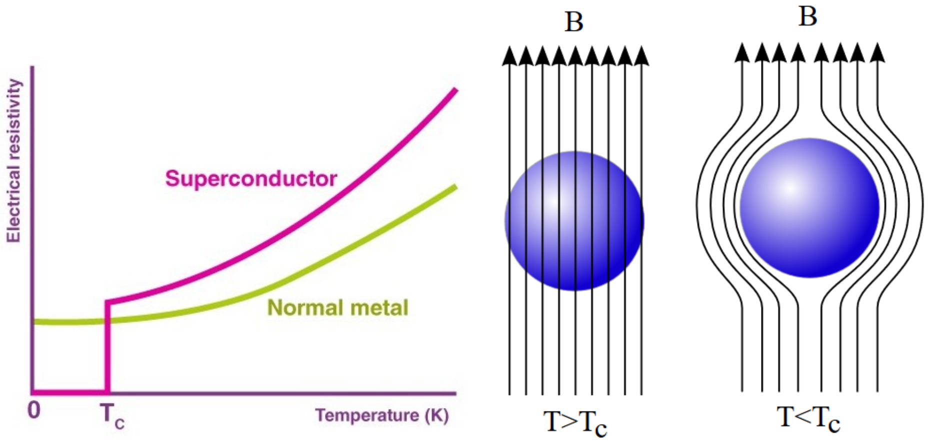

(a) Resistance as a function of temperature during the transition from the normal to the superconducting state.

(b) Illustration of the Meissner effect in a superconducting material

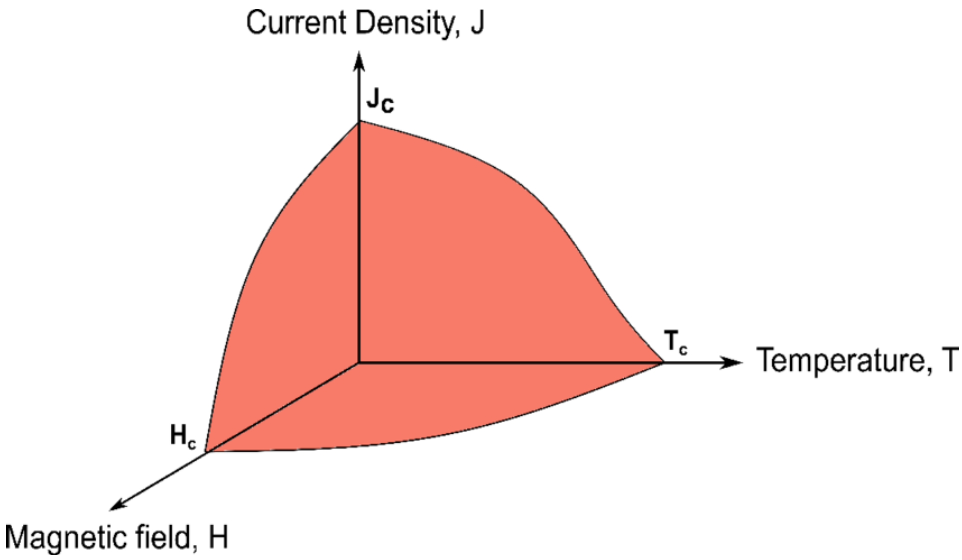

Fig. A.2 Phase diagram of the superconducting state for temperature, current density, and applied magnetic field. The superconducting region is the blue volume.

A.1.1 London Equations

The London equations are the simplest constitutive relations that describe superconductivity. The first equation describes the absence of resistance starting from the Drude model, which describes the motion of electrons in a material:

$$m\frac{d}{dt}\mathbf{v} = -e\mathbf{E} - m\frac{\mathbf{v}}{\tau}, \tag{A.2}$$

where e, m, and $\mathbf{v}$ are the electron's charge, mass, and velocity, respectively; $\mathbf{E}$ is the electric field and τ is the relaxation time, i.e., the average time between two collisions of an electron with the ions in the crystal lattice. The two-fluid model allows us to represent two different groups of electrons: those in the normal state and those in the superconducting state. At temperatures above the critical temperature, all electrons are normal; below it, they become superconducting, always conserving the total number of electrons. The subscript s will refer to superconducting electrons. Since τ^{-1} is proportional to the electrical resistivity ρ and the resistivity in a superconductor is zero, we can assume $\tau \to \infty$, simplifying the Drude equation to Eq. A.3:

$$m\frac{d}{dt}\mathbf{v_s} = -e_s\mathbf{E}. \tag{A.3}$$

Given a volumetric density of superconducting electrons n_s in the material, and defining the current density as:

$$\mathbf{J_s} = -n_s e_s \mathbf{v}, \tag{A.4}$$

we can write the first London equation from Eq. A.3 as follows:

$$\frac{d}{dt}\mathbf{J_s} = \frac{n_s e_s^2}{m_s}\mathbf{E}. \tag{A.5}$$

The second London equation serves to describe the Meissner-Ochsenfeld effect and the associated perfect diamagnetism, which is absent in the first equation. From Faraday's law:

$$\nabla \times \mathbf{E} = -\frac{d}{dt}\mathbf{B}, \tag{A.6}$$

and from the first London equation we obtain:

$$\frac{d}{dt}\left(\nabla \times \mathbf{J_s} + \frac{n_s e_s^2}{m_s}\mathbf{B}\right) = 0. \tag{A.7}$$

Inside the superconductor, there are no currents if its thickness is greater than the London penetration depth λ_L, and magnetic fields are excluded. Thus, we obtain the second London equation:

$$\nabla \times \mathbf{J_s} = -\frac{n_s e_s^2}{m_s}\mathbf{B}. \tag{A.8}$$

Using Maxwell's equations:

$$\nabla \times \mathbf{E} = -\frac{d}{dt}\mathbf{B}, \tag{A.9}$$

$$\nabla \times \mathbf{B} = \mu_0 \mathbf{J_s} + \frac{1}{c^2}\frac{d}{dt}\mathbf{E}, \tag{A.10}$$

and the mathematical property of the curl:

$$\nabla \times \nabla \times \mathbf{B} = \nabla(\nabla \cdot \mathbf{B}) - \nabla^2 \mathbf{B}, \tag{A.11}$$

we obtain the following equation:

$$(\nabla^2 - \frac{1}{c^2}\frac{d^2}{dt^2})\mathbf{B} = \frac{\mathbf{B}}{\lambda_L^2}, \tag{A.12}$$

where λ_L is the London penetration depth given by:

$$\lambda_L = \sqrt{\frac{m_s}{\mu_0 n_s e_s^2}}. \tag{A.13}$$

For simplicity, setting $\frac{d}{dt}\mathbf{B} = 0$, $\nabla = \partial_x$, and an external magnetic field along an axis perpendicular to x, indicated as $B(0)$, we obtain:

$$B(x) = B(0)e^{-x/\lambda_L}, \tag{A.14}$$

as shown in Fig. A.3.

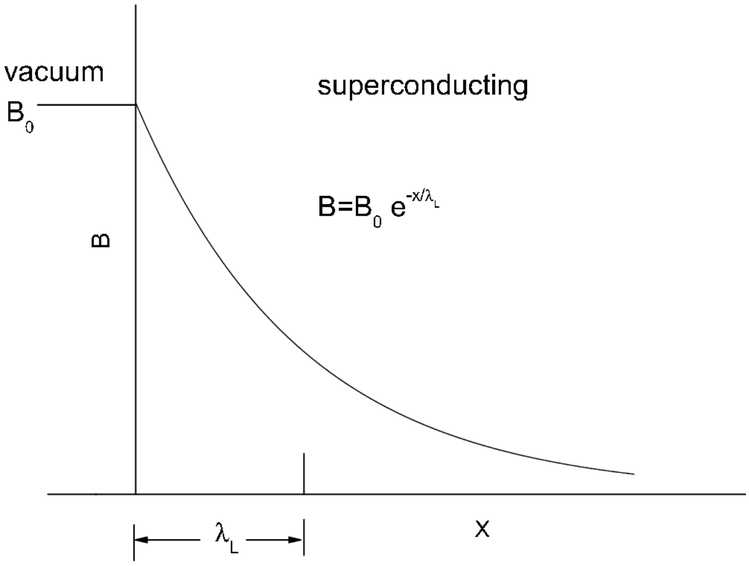

Fig. A.3 Penetration of a constant magnetic field along the x-axis at the interface with the superconductor, reaching the value $B(0)$ at $x = \lambda_L$.

A.1.2 BCS Theory

In 1957, Bardeen, Cooper, and Schrieffer proposed a microscopic theory of superconductivity (BCS theory) that quantitatively predicts the properties of superconductors at low critical temperatures [79]. The central concept is the formation of "Cooper pairs," bound states of two electrons with opposite spin and momentum ($k\uparrow, -k\downarrow$) mediated by an attractive electron-phonon interaction.

While the normal ground state of an electron gas consists of a Fermi sea filled up to the Fermi energy E_F, Cooper demonstrated that this state is unstable in the presence of even a weak attractive potential. The instability leads to the formation of a new ground state separated from the excited states by an energy gap, E_gap. This gap represents the binding energy required to break a Cooper pair and is directly related to the critical temperature. In the weak-coupling limit, this relationship is given by:

$$E_\mathrm{gap}(0) \approx 3.528 k_\mathrm{B} T_\mathrm{c}. \tag{A.15}$$

The existence of this gap explains the exponential dependence of the specific heat and the perfect conductivity observed in the superconducting state. For the purpose of TES operation, the most relevant aspect of BCS theory is this temperature-dependent energy gap, which determines the ultimate energy resolution limit of the detector and the confinement of quasiparticles when different superconducting materials are in contact.

A.1.3 Proximity Effect

For a superconductor, the attraction between electrons is a consequence of the electron-phonon interaction, an idea confirmed by the isotopic effect, from which it follows that $T_\mathrm{c} \propto M^{-\alpha}$, where M is the mass of the lattice ion. However, in the context of TES (Transition Edge Sensors), superconducting materials are interfaced with normal metallic materials. For two-layer TES, it is possible to predict and regulate the critical temperature based on the parameters of the materials used and the geometries of the two layers.

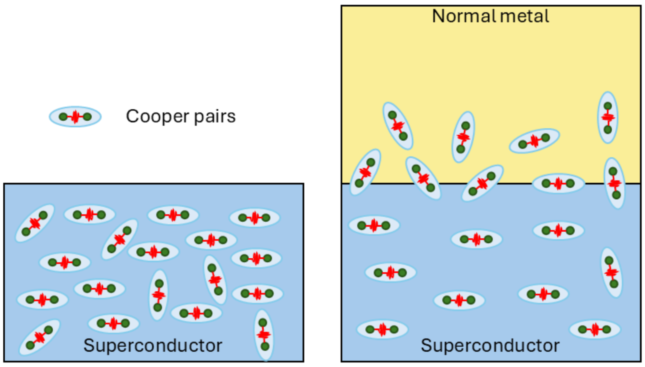

Fig. A.4 On the left, a superconductive layer with its Cooper pairs under its critical temperature. On the right, a bilayer of a superconductive film on the bottom and a normal metal on top. In this case, the density of Cooper pairs is reduced because the Cooper pairs from the superconductor can occupy a bigger volume.

The approach used is that of Usadel [80, 81], which describes the behavior of superconductors in the "dirty limit" (where the electron mean free path is smaller than the coherence length). The core concept is that Cooper pairs can diffuse from the superconductor into the normal metal, while normal electrons diffuse into the superconductor. This leads to a spatially varying order parameter $\Delta(x)$ and, consequently, a suppression of the critical temperature T_c of the bilayer system compared to the intrinsic critical temperature T_c0 of the isolated superconductor.

The spatial behavior of this effect is described by the variation of the superconducting order parameter $\Delta(x)$. At the interface between the superconductor (S) and the normal metal (N), the density of Cooper pairs does not drop abruptly to zero. Instead, the order parameter leaks into the normal metal and is suppressed within the superconductor near the boundary. In the normal metal, the probability of finding Cooper pairs decays exponentially with the distance x from the interface. This decay is characterized by a specific length scale, the *coherence length* in the normal metal, denoted as ξ_n. In the diffusive limit (dirty limit), which typically applies to our thin films, ξ_n is given by:

$$\xi_{\mathrm{n}} = \sqrt{\frac{\hbar D_{\mathrm{n}}}{2\pi k_{\mathrm{B}} T}}, \tag{A.16}$$

where D_{n} is the diffusion coefficient of the normal metal.

Furthermore, within the superconductor itself, the order parameter varies over a characteristic scale known as the Ginzburg-Landau coherence length $\xi(T)$. This length diverges near the critical temperature T_{c} following the relation:

$$\xi(T) = \frac{\xi(0)}{\sqrt{1 - \frac{T}{T_{\mathrm{c}}}}}, \tag{A.17}$$

where $\xi(0)$ depends on the material purity. In the dirty limit, $\xi(0) \approx 0.85\sqrt{\xi_0 l}$, where l is the mean free path and ξ_0 is the intrinsic BCS coherence length. The interplay between the film thicknesses and these coherence lengths determines the strength of the proximity effect.

By solving the Usadel equations with appropriate boundary conditions at the interface, one obtains an equation relating the critical temperature T_{c} in the presence of a normal metal to $T_{\mathrm{c}0}$. For thin films (where the thickness is much smaller than the coherence length), the critical temperature can be approximated as:

$$\frac{T_{\mathrm{c}}}{T_{\mathrm{c}0}} = \left[\left(\frac{k_{\mathrm{B}} T_{\mathrm{c}0}}{1.13\hbar\omega_D} \right)^2 + \left(\frac{k_{\mathrm{B}} T_{\mathrm{c}0}}{1.13\tau} \right)^2 \right]^{\frac{\alpha}{2}}, \tag{A.18}$$

where α depends on the ratio of the thicknesses d and the density of states n of the normal (n) and superconducting (s) layers: $\alpha = \frac{d_n n_n}{d_s n_s}$. This relationship is fundamental for tuning the T_{c} of TES devices by adjusting the thickness of the normal metal layer (e.g., Gold) on top of the superconductor (e.g., Titanium), as depicted in Fig. A.5.

A.2 DC SQUID

The theoretical principles of superconductivity discussed in the previous sections are a basic set of knowledge for understandin TESs. In this section, magnetic flux quantization and the Josephson effect will be explained as crucial mechanisms in

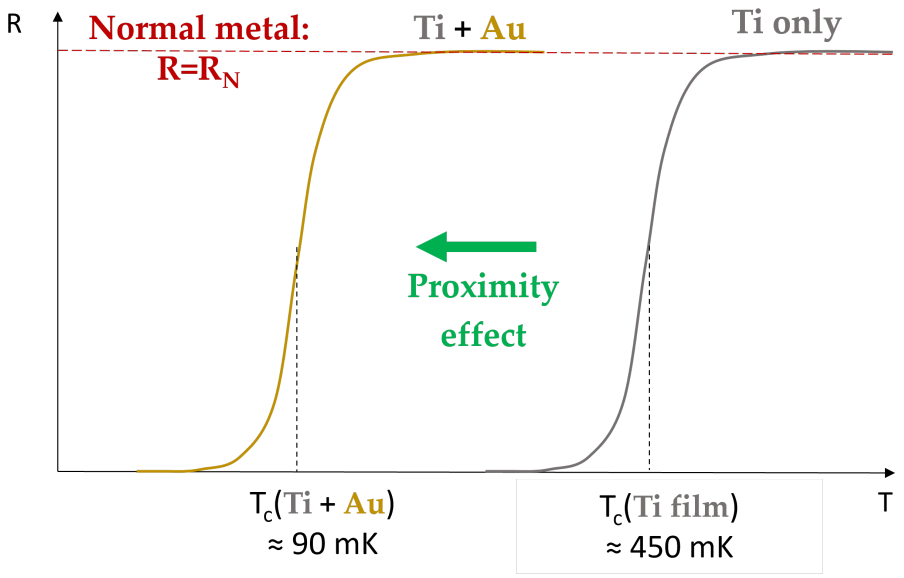

Fig. A.5 Transition of a Titanium thin layer (gray) translated to lower values adding a gold thin layer on top of it (yellow).

the operation of Superconducting Quantum Interference Devices (SQUIDs). These devices are extremely sensitive magnetic flux sensors and are essential for the readout of TESs. Before detailing the specific TES operation, it could be useful to introduce the working principles of the DC SQUID, as it serves as the fundamental current-sensing element in our experimental setup.

A.2.1 Magnetic Flux Quantization

A fundamental property of superconductivity, derived from the macroscopic quantum nature of the condensate, is flux quantization. The macroscopic wavefunction describing the Cooper pairs must be single-valued. This imposes a constraint on the phase of the wavefunction around any closed superconducting loop. Consequently, the magnetic flux Φ threading a closed superconducting loop cannot take arbitrary values but is quantized in integer multiples of the flux quantum Φ_0:

$$\Phi = n\Phi_0, \tag{A.19}$$

where n is an integer and $\Phi_0 = \frac{h}{2e} \approx 2.068 \times 10^{-15}\,\mathrm{Wb}$. This principle is central to the operation of SQUIDs, which convert magnetic flux into measurable voltage signals.

A.2.2 Josephson Junction

The Josephson effect appears whenever there is a weak coupling between superconductors, for example at the interface between two superconductors separated by a thin insulating layer as shown in Fig. A.6. This results in a non-zero overlap of the macroscopic wavefunctions.

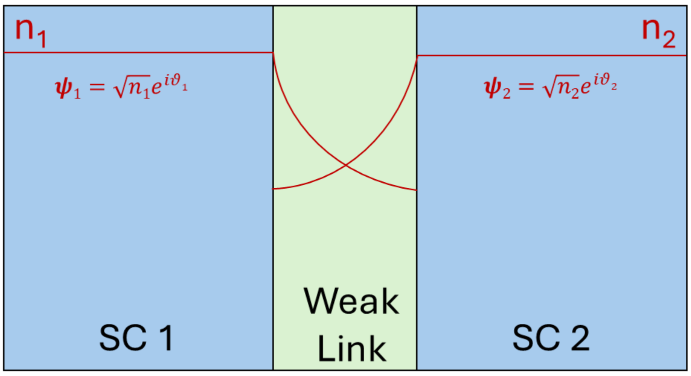

Fig. A.6 Two superconductors with wavefunctions Ψ_1 and Ψ_2 separated by an insulating barrier. The top curves represent the Cooper pair densities n_1, n_2 as a function of position.

For a potential difference at the interface $\Delta V = 0$, a DC supercurrent I_s flows through the junction, dependent on the phase difference $\Delta\theta = \theta_2 - \theta_1$ between the two superconductors:

$$I_s = I_c \sin(\Delta\theta), \tag{A.20}$$

where I_c is the critical current of the junction. When a voltage $\Delta V \neq 0$ is applied, the phase difference evolves in time according to:

$$\frac{d(\Delta\theta)}{dt} = \frac{2e}{\hbar}\Delta V. \tag{A.21}$$

This results in an AC supercurrent oscillating at the Josephson frequency $\omega_J = \frac{2e\Delta V}{\hbar}$.

A.2.3 DC SQUID Operation

The device used in TES measurements is the DC SQUID, which simultaneously exploits the quantization of magnetic flux in a superconducting loop and the Josephson junctions. A DC SQUID consists of a superconducting loop interrupted by two Josephson junctions, allowing it to sense extremely small changes in magnetic flux. The total current is the sum of the contributions from the two junctions. Assuming identical junctions, applying a magnetic flux to the loop results in an interference pattern where the maximum critical current of the SQUID modulates with the applied flux:

$$I_{\text{max}}(\Phi) = 2I_{\text{c}}\left|\cos\left(\pi\frac{\Phi}{\Phi_0}\right)\right|. \tag{A.22}$$

When the device is biased with a current $I > I_{\text{max}}$, the voltage across the SQUID varies periodically with the applied magnetic flux with a period of Φ_0. This allows the SQUID to act as an extremely sensitive flux-to-voltage transducer.

A.2.4 Flux-Locked Loop DC SQUID

The mode of operation of the SQUID in question is the Flux-Locked Loop (FLL) mode, which involves the use of a feedback circuit to keep the flux inside the SQUID constant, as shown in Fig. A.7 and as explained in [[82], [83]]. The SQUID is coupled with an input coil, which measures variations in the magnetic flux it generates. Additionally, it is current-biased as previously described and referenced to a constant voltage value through a comparator. Furthermore, it is also magnetically coupled to a feedback coil. Any variation of the flux in the SQUID will result in a voltage change, which passes through the comparator and is compensated by the feedback circuit. The voltage read at the device output is the voltage applied to the feedback circuit, which, when applied to the feedback resistance R_{fb}, generates a current that, in turn, is converted into a magnetic field by the feedback inductance L_{fb} until the flux linked to the SQUID returns to the operating point. The advantages offered by reading signals in this way include the linearization of the response and a gain given by:

$$G = \frac{M_{\mathrm{fb}}}{M_{\mathrm{in}}} R_{\mathrm{fb}}, \tag{A.23}$$

where $M_{\mathrm{fb}}, M_{\mathrm{in}}$ are the mutual inductances of the feedback and input inductances.

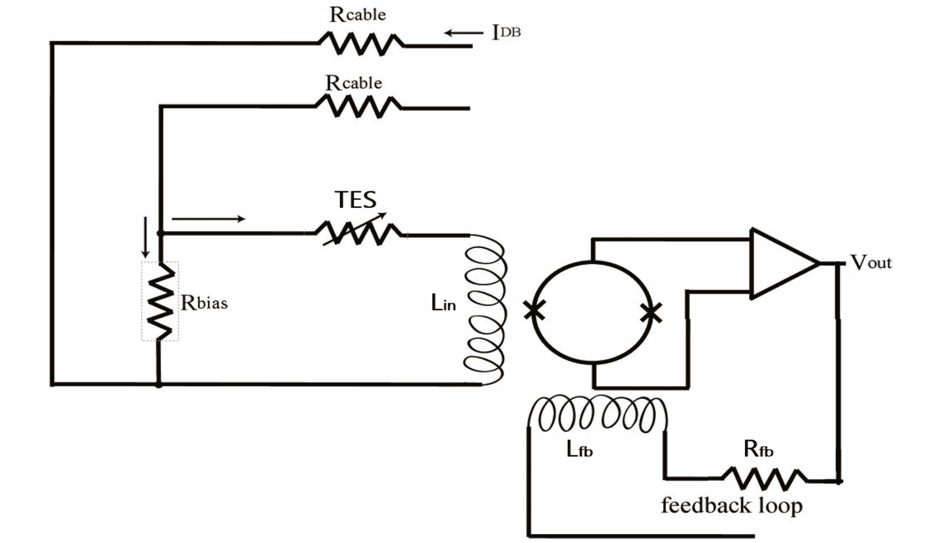

Fig. A.7 Configuration of the FLL DC SQUID with an input coil coupled to the SQUID, carrying the TES current, and a feedback circuit.

A.2.5 Advantages of SQUID Readout for TESs

The dc-SQUID is the readout device of choice for Transition-Edge Sensors due to its unique compatibility with the physical properties of the detector. First, TESs are low-impedance devices (typically $R_{\mathrm{TES}} < 1\,\Omega$ even in the transition). The superconducting input coil of a SQUID offers a naturally matched low-impedance load, essential for efficient signal transfer and voltage-biased operation. Second, SQUIDs are the most sensitive magnetic flux sensors available, translating to an extremely low current noise floor (typically few $\mathrm{pA}/\sqrt{\mathrm{Hz}}$). This allows them to resolve the minute current variations generated by single-photon events in the TES loop. Finally, SQUIDs operate at cryogenic temperatures compatible with the TES working stage, minimizing thermal noise and simplifying the cold-stage assembly.

A.3 Advantages of KICS over dc-SQUID-based Readout

A promising result for fast TESs, particularly beneficial for large-scale TES arrays, is the one obtained in [19] using Kinetic Inductance Current Sensors (KICS) instead of dc-SQUIDs. KICSs are superconducting resonator-based devices similar to KIDs that leverage the nonlinear kinetic inductance of a superconducting resonator to measure currents with high sensitivity. Unlike dc-SQUIDs, which require complex fabrication and significant space, KICS are smaller and less expensive. They can be galvanically connected to TESs and do not require external bias current, since they are dissipationlessly self-biased through a loop made with an aluminum strip called a Superconductive Switch that traps a persistent current through flux quantization, allowing for continuous frequency tunability.

One of the primary limitations of TES readouts using dc-SQUIDs is the need for multiplexing to manage large pixel arrays. Current multiplexing techniques such as time-division multiplexing (TDM), frequency-division multiplexing (FDM), and microwave dc-SQUID multiplexing (μMUX) introduce trade-offs in speed, bandwidth, and scalability.

KICS overcomes these challenges through several key advantages [19]:

- **High-speed Readout:** The speed of a KICS is set by its resonator bandwidth, making it inherently faster than dc-SQUID-based techniques, particularly for high-speed applications.
- **Microwave Frequency-Division Multiplexing:** Unlike μMUX, which relies on RF-SQUIDs with complex flux ramp modulation, KICS can be directly read out with microwave techniques similar to those used in Microwave KIDs (mKIDs), enabling simpler multiplexing [20].
- **Simplified Fabrication:** KICS requires only a single superconducting layer for its resonator structures, whereas dc-SQUIDs need highly uniform Josephson junctions, complicating large-scale fabrication [84].

- **Compact Design:** dc-SQUID-based readout cells typically require $> 0.4\,\mathrm{mm}^2$ per channel due to large coupling coils and noise-mitigation structures. KICS devices can be as small as $0.02\,\mathrm{mm}^2$, significantly reducing the footprint of large TES arrays [85].
- **Self-Biased Operation:** KICS employs a persistent current biasing method using superconducting switches, eliminating the need for active bias lines that can introduce excess noise [86].
- **Low-Noise Performance:** The readout noise of KICS, measured at $1.4\,\mathrm{pA}/\sqrt{\mathrm{Hz}}$, is significantly lower than the TES noise at operating frequencies, ensuring minimal degradation of detector performance [19].
- **Scalability for Large Arrays:** With an effective bandwidth of 250 MHz per readout line, KICS allows for multiplexing factors of over 1000 pixels per channel, surpassing the 500-pixel limit of μMUX and the $\sim$40-pixel limit of TDM/FDM [84, 87].

The KICS represents a promising alternative to dc-SQUID-based readouts for TES arrays, particularly in applications where high-speed, low-noise operation is critical. The self-biasing scheme, compact design, and simplified fabrication process make KICS a promising candidate for next-generation readouts for TESs. At the time of this thesis, the demonstration of the multiplexed readout of TES arrays with multiple KICS devices coupled to a shared microwave transmission line has yet to be performed.

A.4 Anti-reflective coatings and plasmonic gratings

A.4.1 Principles of Anti-reflection Coating

The fundamental concept behind Anti-reflection (AR) coatings is the destructive interference of reflected waves at the interface between materials of different refractive indices. I will now provide a brief description of the theory for a thin film as in Fig. A.8. We indicate with E_0 the amplitude of the electric field of the incident light and with k_0 its wave vector coming from air or glue indicate by the refractive index n_0. The subscript 1 indicates the first thin film layer of the anti-reflective coating with thickness l_1, while the subscripts t and r indicate the progressive or regressive wave. This formulation can be quickly declined for a multi-layer of which the i-th layer has thicknesses l_i, refractive indexes n_i and in which there are progressive waves (E_{it}, k_{it}) and regressive waves (E_{ir}, k_{ir}). Finally, we indicate the reflected wave in the 0-th medium with (E_R, k_R) and the wave transmitted after the TES and mirror with (E_T, k_T).

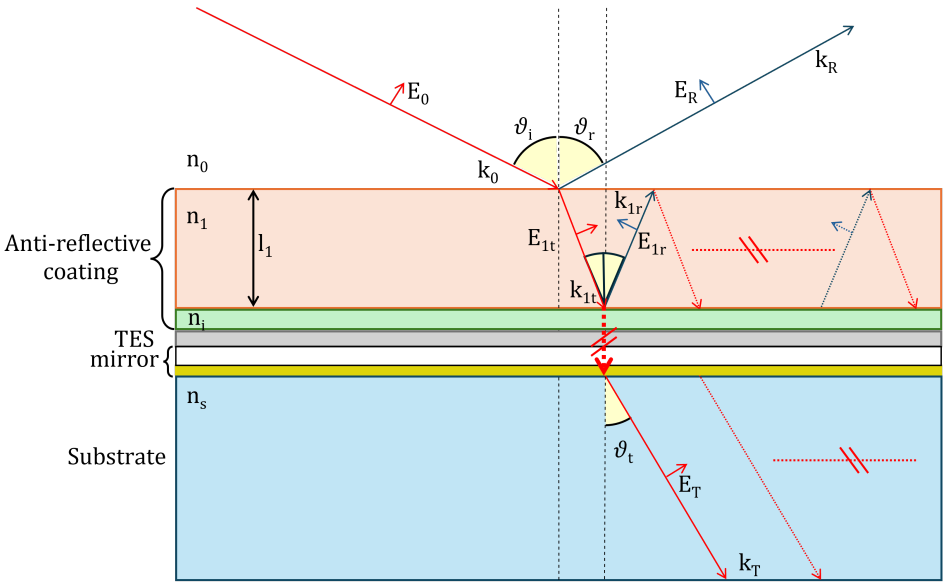

Fig. A.8 Schematic for the light propagation and structure of a TES with anti-reflective (AR) coating and mirror. The incident light from the medium 0 (E_0, k_0) can be reflected (E_R, k_R) or transmitted in the first anti-reflective layer. The i-th layer has thickness l_i and refractive index n_i with progressive waves (E_{it}, k_{it}) and regressive waves (E_{ir}, k_{ir}). Under the AR coating, there is our TES, followed by a mirror to reduce transmitted wave in the substrate (E_T, k_T). Dotted arrows indicate greater orders of reflection and transmission.

We recall the following basic concepts and definitions:

- the refractive index in a medium is $n_i = \frac{c}{v_i}$, where c is the speed of light in vacuum and v_i is the one in a medium,
- we can write a monochromatic plane wave as $E_z = E_{0,z} \exp i(K_z r - \omega_z t)$
- the wave vector is $k_i = n_i k = 2\pi n_i \lambda^{-1}$, where λ is the wavelength of the incident light,
- the optical thickness is $L_i = n_i l_i$,

- the ratio of the incident angle θ_{it} and the refraction angle θ_{ir} at the interface of 2 media i and j is given by the Snell's law $\frac{\sin\theta_{ir}}{\sin\theta_{it}} = \frac{n_j}{n_i}$
- the total reflectance R, transmission T and absorbance A are related by the closure relation $A+R+T=1$.

For boundary conditions, the tangential components of the electric field E and the magnetic field H are continuous at each interface. For each interface between the layer i and the subsequent j, we have:

$$\begin{cases} E_{it} + E_{ir} = E_{jt} + E_{jr} \\ E_{it}e^{ik_il_i} + E_{ir}e^{-ik_il_i} = E_{jt} \\ H_{it} - H_{ir} = H_{jt} - H_{jr} \\ H_{it}e^{ik_il_i} - H_{ir}e^{-ik_il_i} = H_{jt} \end{cases}$$

The regressive and progressive waves have exponential phase factors with opposite signs moving in opposite directions of the same medium. If we propagate to the various interfaces, use the Maxwell laws and a matrix formalism, we can write [88]:

$$\begin{pmatrix} E_0 \\ H_0 \end{pmatrix} = \begin{bmatrix} m_{00} & m_{01} \\ m_{10} & m_{01} \end{bmatrix} \begin{pmatrix} E_s \\ H_s \end{pmatrix} = M \begin{pmatrix} E_s \\ H_s \end{pmatrix} = \prod_{i=1}^{N} M_i \begin{pmatrix} E_s \\ H_s \end{pmatrix}, \tag{A.24}$$

where the matrix of the i-th layer is:

$$M_i = \begin{bmatrix} \cos\delta_i & i\gamma_i \sin\delta_i \\ i\gamma_i^{-1}\sin\delta_i & \cos\delta_i \end{bmatrix} \tag{A.25}$$

and in which :

$$\delta_i = k_i l_i \cos\theta_i \tag{A.26}$$

and

$$\gamma_i = \begin{cases} \dfrac{\eta_i}{\cos\theta_i} & TE\ mode \\ \eta_i \cos\theta_i & TM\ mode \end{cases}$$

with $\eta_i = \frac{n_i c}{\varepsilon_i \varepsilon_0}$.

So, for the 2 polarizations s (TE mode) and p (TM mode) we can finally calculate the reflectance and the transmittance as $R = \left|r\right|^2$ and $T = \left|t\right|^2$, where r and t can be calculated through the matrix M for the 2 polarizations as:

$$\begin{aligned} r &= \frac{E_R}{E_0} = \frac{(m_{00}+P_s m_{01})P_0 - (m_{10}+P_s m_{11})}{(m_{00}+P_s m_{01})P_0 + (m_{10}+P_s m_{11})} \\ t &= \frac{E_T}{E_0} = \frac{2P_0}{(m_{00}+P_s m_{01})P_0 + (m_{10}+P_s m_{11})}. \end{aligned} \tag{A.27}$$

The terms P_0 and P_s contains the difference for the 2 polarizations and are by the first and last medium, respectively:

$$P_0 = \begin{cases} \dfrac{\eta_0 \cos\theta_0}{z_0} & TE\ mode \\ \dfrac{\cos\theta_0}{\eta_0 z_0} & TM\ mode \end{cases}$$

$$P_s = \begin{cases} \dfrac{\eta_0 \cos\theta_s}{z_0} & TE\ mode \\ \dfrac{\cos\theta_s}{\eta_s z_0} & TM\ mode \end{cases}$$

where we have $z_0 = \sqrt{\frac{\mu_0}{\varepsilon_0}}$, where ε_0 and μ_0 are the electric permittivity and magnetic permeability in vacuum.

Recent experimental works have demonstrated significant improvement in photon absorption of TESs with AR coatings. For instance, in [14], a Ti/Au TES integrated with an SiO_2/TiO_2 bilayer AR coating achieved a system detection efficiency above 95% at $\lambda = 1550$ nm. Similar high-efficiency results were obtained by [15], who reported over 98% absorption using carefully engineered dielectric stacks on TESs.

In conclusion, AR coatings provide a robust and passive method to increase efficiency without modifying the TES structure or requiring resonance-based effects. However, their efficiency strongly depends on TESs areas and fiber-TES alignments, since the TES should be larger than the core of the fiber and the fiber should be placed inside the TES areas.

A.4.2 Principles of Plasmonic Metasurfaces

When light reaches the interface between a dielectric and a flat metal from the dielectric side, the incident photons have a momentum $\hbar k_{\mathrm{d}} = \frac{h}{\lambda} n_{\mathrm{d}}$ and are mostly reflected following the Snell's law $n_{\mathrm{d}} \sin\theta = n_{\mathrm{m}} \sin\theta_R$, conserving the momentum. Differently, light propagating in the metal has a direction given by θ_T and a momentum $\hbar k_{\mathrm{m}} = \frac{h}{\lambda} n_{\mathrm{m}}$. Since usually one has $n_{\mathrm{d}} > n_{\mathrm{m}}$ for visible, near-visible and telecom wavelengths, θ_T has a maximum value equal to 90°, corresponding to a critical value for the incident angle as $\theta_C = \frac{n_{\mathrm{m}}}{n_{\mathrm{d}}}$. The momentum along the surface for $\theta > \theta_C$ is higher than $\hbar k_{\mathrm{m}}$, the supported value in the metal. This generate evanescent fields (oscillating electric field spatially decaying in both media from the interface) cause surface charges to oscillate and radiate into the metal.

By structuring metallic surfaces into periodic gratings, it is possible to couple incident photons effectively into surface plasmon polaritons (SPPs) through the evanescent fields, significantly increasing photon absorption at targeted wavelengths and angles [89, 71]. Sensors with this gratings are called Grating Coupled Surface Plasmon Resonance sensors (GC-SPR sensors).

Surface plasmon polaritons (SPPs) are collective oscillations of electrons at the interface between a dielectric and a metal, which can strongly confine and enhance electromagnetic fields. The dispersion relation governing SPP propagation at a planar interface is given by:

$$k_{\mathrm{SPP}} = \frac{\omega_p}{c} \sqrt{\frac{\varepsilon_{\mathrm{m}} \varepsilon_{\mathrm{d}}}{\varepsilon_{\mathrm{m}} + \varepsilon_{\mathrm{d}}}} = \frac{\omega_p}{c} n_{\mathrm{SPP}} \tag{A.28}$$

where ε_{m} and ε_{d} represent the complex dielectric permittivities of the metal and dielectric materials, respectively, ω_p is the plasma frequency for that material, and c is the speed of light in vacuum [89, 90].

This follows considering a p-polarized electromagnetic wave propagating in the x direction with the usual monochromatic plane wave equation for the electric $E_{xz}(x)$ and magnetic $H_y(x)$ fields in the $x - z$ and y directions, respectively. Because we have waves in media, we need to take into account the term $\exp(-k_{z,medium} z)$. Using the notation F_j such that $F_j \delta(j,y) = (0, H_y, 0)$ and $F_j \delta(j,xz) = (E_x, 0, E_z)$ we have $F_{\mathrm{medium}} = F_{\mathrm{j,medium}} \exp(-k_{\mathrm{z,medium}} z) \exp i(k_j j - \omega t)$. Using the Maxwell's equations and and the boundary conditions at the interface we obtain:

$$k_{zd}^2 = k_x^2 - \varepsilon_{\mathrm{d}} k^2$$
$$k_{zm}^2 = k_x^2 - \varepsilon_{\mathrm{m}} k^2$$
$$\frac{k_{zd}}{k_{zm}} = -\frac{\varepsilon_{\mathrm{d}}}{\varepsilon_{\mathrm{m}}}.$$

Substituting k_x with k_{SPP} we obtain Eq. A.28 as in [91].

Due to the mismatch between photon momentum in a dielectric medium (k_{d}) and the SPP momentum ($k_{\mathrm{SPP}} > k_{\mathrm{d}}$), direct excitation of SPPs in a flat metallic layer from photons is not straightforward. This mismatch can be compensated using periodic grating structures, which provide the additional momentum needed.

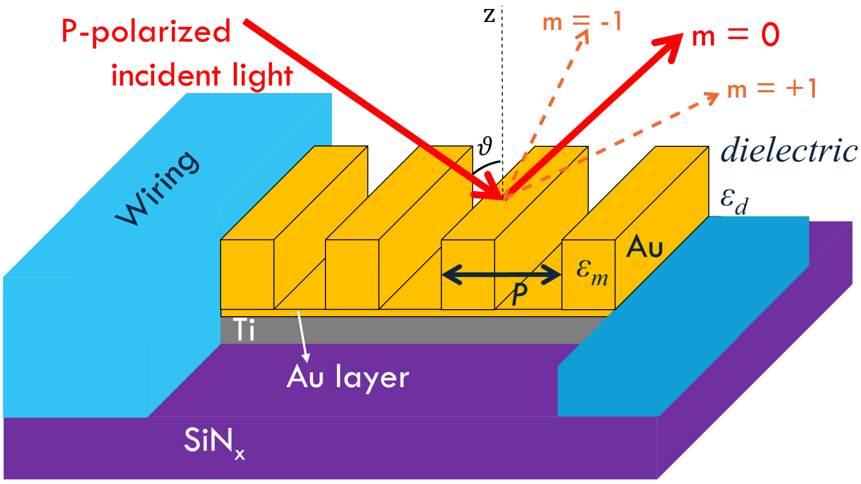

Fig. A.9 Schematic for the grating coupling for Single Plasmon Polaritons and photons. The incident light from the dielectric medium has momentum k_{d} and $k_{zd} = k_d \sin\theta$ in the z direction (along the normal to the grating plane). The grating here is made of gold with thickness h and periodicity P. The relative dielectric constants are ε_{d} for the dielectric medium and ε_{m} for the metallic layer. The diffracted light is represented in various orders labeled by the value m. The plasmonic grating is, here, represented on top of an AuTi TES on its SiN$_x$ substrate. It is also possible to image the grating not on the TES and a mirror under the TES or under the grating like in Fig. A.8.

We consider a metallic film with grating in the xy direction under a dielectric medium with refractive index n_{d} (that in dielectrics is equivalent to ε_{d}) as in Fig. A.9. To transfer the energy from the photon to the SPPs we need to couple their momenta in the z direction. The wavevector momentum of the incident photon in z direction is:

$$k_{zd} = k_0 n_{\mathrm{d}} \sin\theta, \tag{A.29}$$

while the wavevector of the diffracted light of order m can be given by:

$$k_G = mG = m\frac{2\pi}{P}, \tag{A.30}$$

where P is the grating period.

The resonance condition for coupling photons into SPPs via a grating is described by the equation [92]:

$$k_{\mathrm{SPP}} + \Delta n^{SP}_{eff} = k_{zd} \pm k_G, \tag{A.31}$$

where Δn^{SP}_{eff} takes into account the difference of the effective indices of the surface plasmon (SP) due to, for example, AR coating or prism-based Kretschmann configuration upon the grating.

With the grating only and substituting $\omega_p/c = \lambda$ and $\varepsilon_{\mathrm{d}} = n_{\mathrm{d}}^2$, we can write [93, 94]:

$$\sin\theta + m\frac{\lambda}{P} = \pm\sqrt{\frac{\varepsilon_{\mathrm{m}} n_{\mathrm{d}}^2}{\varepsilon_{\mathrm{m}} + n_{\mathrm{d}}^2}}. \tag{A.32}$$

When photons match this resonance condition, they couple efficiently into SPPs, drastically reducing reflectivity at the resonant wavelength and achieving a black body-like behavior for optimized structures [95, 72]. It is important to note that, once selected the materials and the grating periodicity, the matchable wavelengths are limited due to $\sin\theta$ function that is limited in the range $[0,1]$. In fact we have $m\lambda = P(\pm n_{\mathrm{SPP}} - \sin\theta)$ that for $m = 1$ is limited in the range $\left[Pf(n_{\mathrm{SPP}} - 1), P(1 + n_{\mathrm{SPP}})\right]$, where $f(n_{\mathrm{SPP}} - 1) = 0$ if $n_{\mathrm{SPP}} < 1$ and $f(n_{\mathrm{SPP}} - 1) = n_{\mathrm{SPP}} - 1$ if $n_{\mathrm{SPP}} > 1$.

The choice of material for the plasmonic grating significantly impacts the performance of the metasurface. Ideal materials exhibit a large negative real part and a minimal imaginary part of their dielectric permittivity. Silver has superior plasmonic properties, but its tendency to oxidize limits its practicality, making Au the preferred choice for its chemical stability [96, 97]. Because Ag and Au are expensive, copper and aluminum are valid choices, but both suffer from chemical instability under atmospheric conditions. Metals have plasmon resonance in the visible and NIR because their plasma frequency values corresponds to the ω in these region, while Si and other semiconductors have ω_P corresponding to the microwave region, [98]. In fact, we can write $\omega_P = \sqrt{\frac{N_e e^2}{\varepsilon_0 m^*}}$, where N_e is the density of carriers and m^* their effective mass. Then we consider that $m^* = h^2 \left(\frac{d^2E}{dk^2}\right)^{-1} \sim 1.1\ m_e$ in Au,Al and Ag [99] and that for those metals N_e typical values are around $10^{22} - 10^{23}$ cm^{-3}. The resulting ω_P falls in the region of the spectra between NIR and UV for these flat metals.

At telecom wavelengths, the values of n_{SPP} for different metal-dielectric combinations can be approximated with $n_{\text{SPP}} \sim n_{\text{d}}$ because one has $\varepsilon_{\text{m}} \gg n_{\text{d}}^2$. This can be verified considering the values found in [78]: $\varepsilon_{\text{m}}(Ag) = -125.53 + i3.2$, $\varepsilon_{\text{m}}(Al) = -236 + i48$, $\varepsilon_{\text{m}}(Au) = -111.8 + i10.8$ and $n_{\text{d}}(Air) = 1$, $n_{\text{d}}(Glue) = 1.5$, $n_{\text{d}}(SiO_2) = 1.44$, $n_{\text{d}}(TiO_2) = 2.45$. For $\theta = 0$ we can compute the grating period for a specific λ as $P = \frac{m\lambda}{\pm n_{\text{d}}}$. This approximation is valid only for $\lambda \sim P$, $\theta = 0$ and if $\varepsilon_{\text{m}} \gg n_{\text{d}}^2$ because, in general, we have $P = P(\theta, \lambda)$ and $\varepsilon_{\text{m}} = \varepsilon_{\text{m}}(\lambda), \varepsilon_{\text{d}} = \varepsilon_{\text{d}}(\lambda)$.

Once the photons are converted into SPP modes they have an oscillating frequency:

$$\omega_{\text{SPP}} = \frac{\omega_P}{\sqrt{1 + \varepsilon_{\text{m}}}}, \tag{A.33}$$

following from the free electron form of the dielectric constant $\varepsilon_{\text{m}} = 1 - \frac{\omega_P^2}{\omega^2}$. The penetration depth in the media of the SPP in the direction normal to the interface is given from $d_{SPP,medium} = \frac{1}{k_{z,medium}}$, for which the electric field is $E_{\text{SPP}}(d_{SPP,medium}) \propto E_{\text{SPP}}(0)e^{-k_{z,medium}d_{SPP,medium}}$. With the notation for the real and imaginary parts of the permittivities as $\varepsilon_{\text{m}} = \varepsilon'_{\text{m}} + i\varepsilon''_{\text{m}}$ and $\varepsilon_{\text{d}} = \varepsilon'_{\text{d}} + i\varepsilon''_{\text{d}}$, the solution is:

$$d_{SPP,medium} = \frac{1}{k_0}\sqrt{\left|\frac{\varepsilon_{\text{d}} + \varepsilon'_{\text{m}}}{-(\varepsilon'_{medium})^2}\right|}, \tag{A.34}$$

for both the medium. Since $\varepsilon_{\text{d}} \ll \varepsilon_{\text{m}}$ it follows the the SPP penetration depth is larger in the dielectric than in the metal.

Since ε_{medium} are complex numbers, from Eq. A.33 and Eq. A.28 we can derive that both the wavelength and the frequency are complex and given by [100]:

$$\begin{aligned}
n_{\mathrm{SPP}} &= n'_{\mathrm{SPP}} + n''_{\mathrm{SPP}} = \sqrt{\frac{\varepsilon'_{\mathrm{m}}\varepsilon_{\mathrm{d}}}{\varepsilon'_{\mathrm{m}}+\varepsilon_{\mathrm{d}}}} + i\left(\sqrt{\frac{\varepsilon'_{\mathrm{m}}\varepsilon_{\mathrm{d}}}{\varepsilon'_{\mathrm{m}}+\varepsilon_{\mathrm{d}}}}\right)^{3}\frac{\varepsilon''_{\mathrm{m}}}{2(\varepsilon'_{\mathrm{m}})^{2}}\\
k_{\mathrm{SPP}} &= k'_{\mathrm{SPP}} + ik''_{\mathrm{SPP}} = k_0\left(n'_{\mathrm{SPP}} + in''_{\mathrm{SPP}}\right)\\
\omega_{\mathrm{SPP}} &= \omega'_{\mathrm{SPP}} + i\omega''_{\mathrm{SPP}} = \omega_0\left(1 + in''_{\mathrm{SPP}}\right)\ .
\end{aligned}$$

The SPP mode can propagate on a flat surface in a limited range due to gradual attenuation from the losses caused by absorption in the metal. The decrease during the propagation along a direction in the x-y plane is expressed by the real part in the exponent of the plane wave expression $e^{-k''_{\mathrm{SPP}}x}$. Using Eq. A.4.2, we can obtain propagation length L_{SPP} due to the ohmic losses:

$$L_{\mathrm{SPP}} = \frac{1}{2k''_{\mathrm{SPP}}} = \frac{\lambda}{2\pi}\left(\sqrt{\frac{\varepsilon'_{\mathrm{m}}+n_{\mathrm{d}}^{2}}{\varepsilon'_{\mathrm{m}}n_{\mathrm{d}}^{2}}}\right)^{3}\frac{\varepsilon'^{2}_{\mathrm{m}}}{\varepsilon''_{\mathrm{m}}}, \tag{A.35}$$

In the same manner, we can calculate the SPP life-time from the dissipative term $e^{-2\omega''_{\mathrm{SPP}}t}$ as:

$$\tau_{\mathrm{SPP}} = \frac{1}{2\omega''_{\mathrm{SPP}}} = \frac{1}{\omega_0}\left(\sqrt{\frac{\varepsilon'_{\mathrm{m}}+n_{\mathrm{d}}^{2}}{\varepsilon'_{\mathrm{m}}n_{\mathrm{d}}^{2}}}\right)^{3}\frac{\varepsilon'^{2}_{\mathrm{m}}}{\varepsilon''_{\mathrm{m}}}, \tag{A.36}$$

Considering a wavelength of 1530 nm we can roughly calculate the penetration depth, propagation length and life-time for various interfaces as in Tab. A.1.

Table A.1 Calculated SPP penetration depths, propagation length and life-times at 1530 nm for different metal-oxide combinations.

Interface	$d_{SPP,m}(\mu\mathrm{m})$	$d_{SPP,d}(\mathrm{nm})$	$L_{\mathrm{SPP}}(\mu\mathrm{m})$	$\tau_{\mathrm{SPP}}(\mathrm{ps})$
Au-Air	23	2563	28	0.9
Au-glue/SiO_2	23	1705/1776	15	0.5
Au-TiO_2	23	1040	71	0.2
Al-Air	16	3733	280	0.9
Al-glue/SiO_2	16	2486/2590	152	0.5
Al-TiO_2	16	1519	72	0.2

All this calculation for L_{SPP} and τ_{SPP} are considered in a flat media. In a corrugated metal we need to consider that the SPP could loss energy re-emitting photons because of the grating, reducing both L_{SPP} and τ_{SPP}. In addition, rough surface increase the SPP scattering reducing the propagation of the SPPs even more.

The group velocity is $v_{\mathrm{gr}} = \frac{d\omega'_{\mathrm{SPP}}}{dk'_{\mathrm{SPP}}}$ and can be estimated with transmission measurements of slit-groove nano-structures in broadband optical spectroscopy [101].

Meanwhile, from [102], the propagation length and the life-time are related by the phase velocity as $L_{\mathrm{SPP}} = v_{ph}\tau_{\mathrm{SPP}}$ and in a grating the phase velocity can estimated by $v_{ph} = \frac{P}{\lambda_{peak}}\,c$, where λ_{peak} is the measured wavelength at which a resonance peak appears and c the speed of light in vacuum. The phase velocity can be calculated from Eq. A.4.2 as:

$$v_{ph} = \frac{\omega'_{\mathrm{SPP}}}{k'_{\mathrm{SPP}}} = \frac{\omega_0}{k_0 n'_{\mathrm{SPP}}} = \frac{c}{n'_{\mathrm{SPP}}} \tag{A.37}$$

and, if we consider a photon perpendicular to the grating, Eq. A.32 reduce to $m\frac{\lambda}{P} = \pm n'_{\mathrm{SPP}}$, we obtain $v_{ph} = \frac{c}{n'_{\mathrm{SPP}}} = \frac{P}{\lambda_{peak}}\,c$ for $m = 1$. This will be useful in the attempt to describe the plasmonic resonance with a Lorentzian line shape.

The Lorentzian describes the spectral shape of many resonances and could take the form:

$$A_{\mathrm{SPP}} = \frac{a}{(k - k_{peak})^2 + (\Gamma/2)^2}, \tag{A.38}$$

where A_{SPP} represent the efficiency in the excitation of a SPP due to an incident photon, a is the efficiency amplitude related to the coupling strength and Γ the Full Width at Half Maximum (FWHM) of the peak. While $k = 2\pi\lambda^{-1}n_{\mathrm{d}}\sin(\theta)$ is the momentum of the interrogated photon and k_{peak} the momentum at which the peak occur or the one for which the grating has been designed.

If the peak (described by the subscript *peak*) is mainly generated by the homogeneus broadening of SPP, the FWHM is $\Gamma = \frac{2\hbar}{\tau_{SPP,peak}}$. It become larger if there are contributions from the inhomegeneus broadening caused by structural imperfections [102] and radiative losses due to grating outcoupling. TESs could, in principle, measure the Joule heating caused by SPP absorption and so we can consider a FWHM given by the sum of different contribution as $\Gamma = \Gamma_{abs} + \Gamma_{imp} + \Gamma_{out}$, in which Γ_{imp}

and Γ_{out} are given by imperfections and outcoupling. While Γ_{abs} is the width related to SPP absorption and so the most relevant for TESs detection.

Exploiting the phase velocity, we can rewrite Γ as $\frac{2\hbar}{\tau_{SPP,peak}} = \frac{2\,\hbar\, v_{ph,peak}}{L_{SPP,peak}}$ and then recall that $L_{SPP,peak} = \frac{1}{2k''_{SPP,peak}} = \frac{\lambda_{peak}}{4\pi n''_{SPP,peak}}$ and that $v_{ph} = \frac{c}{n'_{SPP,peak}}$. The computation leads to:

$$\Gamma/2 = hc\frac{n''_{SPP,peak}}{n'_{SPP,peak}}\lambda_{0,peak}^{-1}, \tag{A.39}$$

where $\lambda_{0,peak}$ is the wavelength in $k_{peak} = \frac{2\pi}{\lambda_{0,peak}} n_{\mathrm{d}} \sin\theta_{peak}$.

Then, we can obtain k_{peak} immediately from Eq. A.32 as:

$$k_{peak} = \pm k_{0,peak}\; n_{SPP,peak} - m\frac{2\pi}{P}. \tag{A.40}$$

Finally, the peak depend both on the angle of incidence and on the wavelength and they are related by:

$$\sin\theta_{peak} = \pm\frac{n'_{SPP,0}}{n_{\mathrm{d}}} - \frac{m}{n_{\mathrm{d}}}\frac{\lambda_{0,peak}}{P}. \tag{A.41}$$

If the grating is optimized for $\theta_{peak} = 0$, Eq. A.39 and Eq. A.40 become simpler because Eq. A.41 directly relate the grating period P and the real part of the SPP equivalent refractive index obtaining:

$$\begin{aligned}
&mG = \pm k_0 n_{SPP,peak} = \pm\frac{2\pi}{\lambda_{peak}} n_{SPP,peak} \\
&\lambda_{peak} = \frac{P}{m}\; n_{SPP,peak} \\
&\Gamma = hc\;\frac{m}{P}\frac{\varepsilon''_m}{(\varepsilon'_m)^2}\; n_{SPP,peak},
\end{aligned}$$

recalling that $n''_{\mathrm{SPP}} = (n'_{\mathrm{SPP}})^3 \frac{\varepsilon''_m}{2(\varepsilon'_m)^2}$ from Eq. A.4.2.

Finally, we can turn the Lorentzian resonance peak in a Lorentzian reflectivity dip as $R = R_{bg} - A_{\mathrm{SPP}}$. For a grating optimized for λ_p and $\theta = 0$ we obtain:

$$R = R_{bg} - \frac{4a}{16\pi^2 \left(\lambda n_{\mathrm{d}} \sin\theta - \frac{m}{P\, n_{SPP,p}}\right)^2 + \left(hc\, \frac{m}{P} \frac{\varepsilon_m^{"}}{(\varepsilon_m')^2}\, n_{SPP,p}\right)^2}. \tag{A.42}$$

Using an ad hoc mirror under the grating to avoid transmission losses we can consider $T = 0, A = 1 - R$, $R_{bg} = 1$ and so $A = A_{\mathrm{SPP}}$, meaning the the total absorbance is due only to the Lorentzian plasmonic resonance. The only remaining free parameter is the coupling efficiency a, that is crucial in the final calculation and that must be find experimentally

Appendix B

Elements of TES fabrication and measurements

B.1 Additional material on fabrication procedures

B.1.1 Facilities: UHV and HV evaporators

Both the HV and UHV deposition systems employ thermal evaporation. In the UHV system, an e-gun is used for Ti, while Au is evaporated by an effusion cell.

The UHV deposition system at INRiM consists of two chambers dedicated to Ti-Au TES deposition. The load-lock chamber (atmospheric pressure to $\sim 10^{-7}$ mbar) houses the sample on a rotary platform and includes an argon Ion Milling system. The main deposition chamber (base pressure 10^{-10} mbar) houses the Ti and Au sources. A gate valve connects the chambers, and a magnetic transfer arm moves the sample. The sample can be positioned over the Ti crucible and then translated to the Au effusion cell in $15-25$ s. This rapid transfer under UHV prevents Ti oxidation, ensuring a high-quality interface.

Fig. B.2 shows the deposition chamber interior. The effusion cell can be heated to $1385\,^{\circ}$C and stabilized, while the e-gun current is modulated for Ti evaporation. Shutters control deposition: the effusion cell has a manual shutter, while the Ti crucible has both an automatic shutter (controlled by the microbalance) and a manual

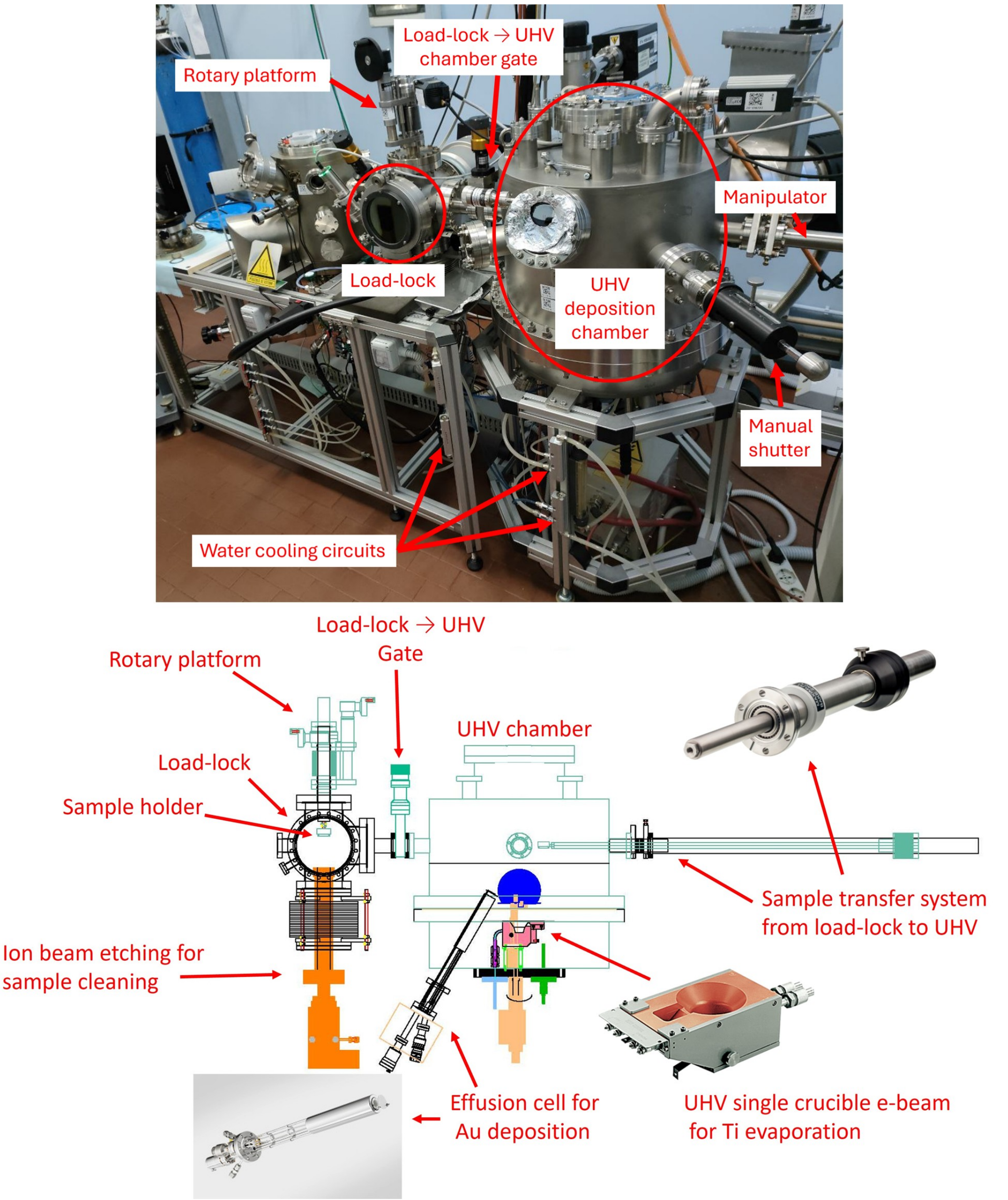

Fig. B.1 External view (top) and schematic (bottom) of the evaporation chamber where Ti and Au for TESs are deposited. Left: load-lock chamber with Argon Ion Milling system. Right: deposition chamber with e-gun (Ti) and effusion cell (Au).

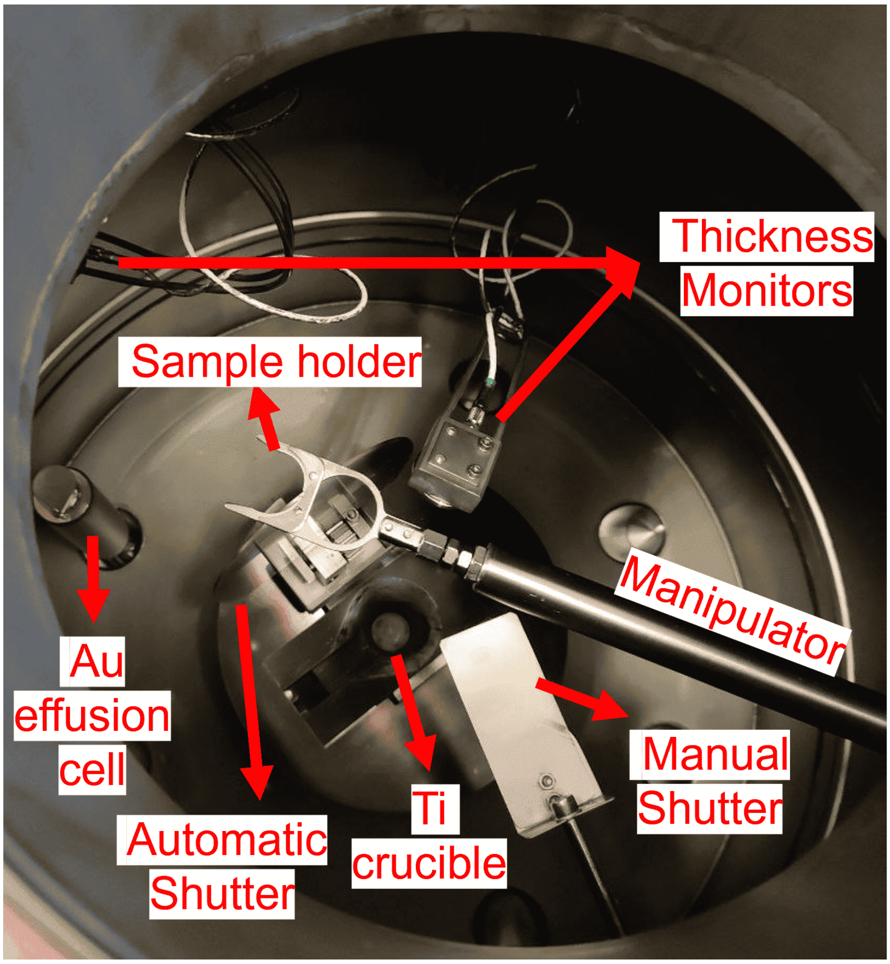

Fig. B.2 Interior of the UHV deposition chamber: center-bottom, Ti crucible for e-gun evaporation; left, Au effusion cell chimney; above sources, shutters; top, magnetic transfer arm and quartz crystal microbalances.

shutter for rate adjustment. Two quartz crystal microbalances monitor the thicknesses of Ti and Au.

The HV evaporator is used for various materials (nanospheres, plasmonic structures, AR coatings, Al wiring). Its load-lock lacks a sputter etching module, but it features a multi-pocket crucible for e-gun evaporation. The system base pressure is $\sim 7 \times 10^{-8}$ mbar. It deposits superconductors (Al, V, Ti), inert metals (Au), and oxides (SiO_2, TiO_2). Magnetic materials are avoided. Fig. B.3 shows the HV chamber with the multi-pocket crucible. A motorized linear translator positions the sample. Controlled oxygen injection allows reactive evaporation for depositing TiO_2 and SiO_2 from TiO or SiO at $\sim 10^{-4}$ mbar.

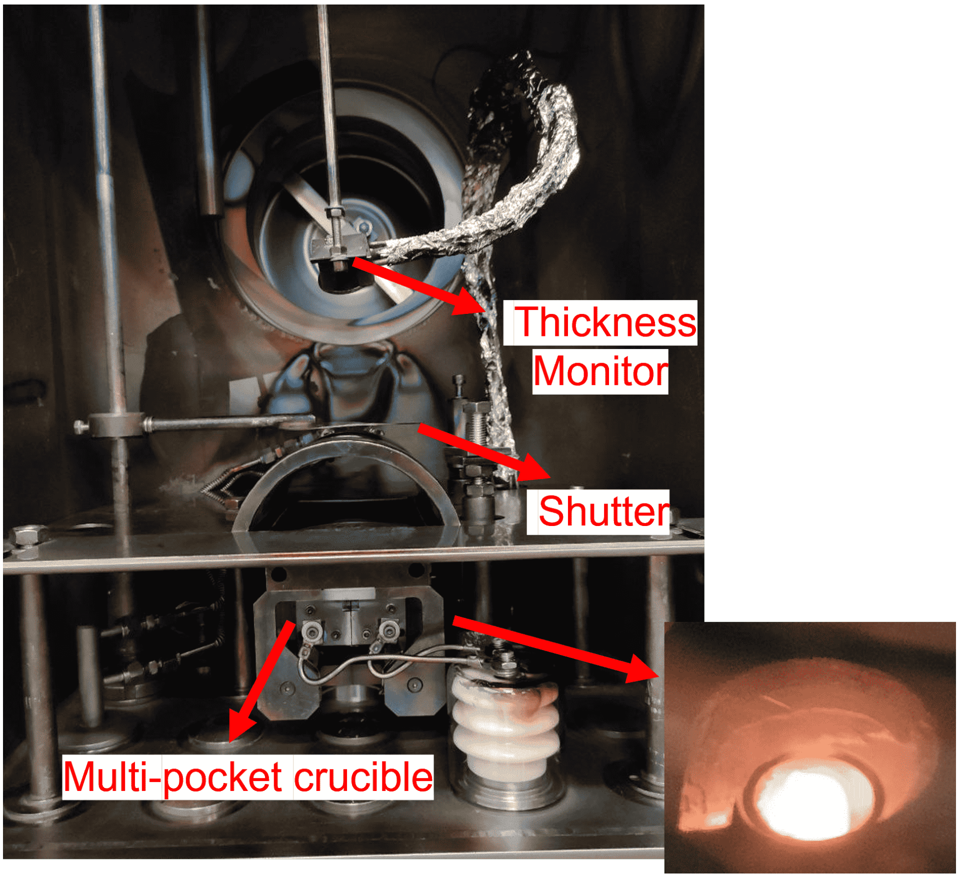

Fig. B.3 Interior of the HV deposition chamber showing the multi-pocket crucible, manual shutter, and quartz crystal thickness monitor. Bottom right: crucible with melting material under e-gun heating.

Both systems use water cooling for the chamber and components.

B.1.2 O_2 Plasma Etching

O_2 plasma etching is a dry etching technique to remove organic layers (photoresist residues). The process occurs in a plasma reactor at $\sim 10^{-3}$ mbar, where oxygen is ionized (Fig. B.4). Reactive species (O^+, O_2^+, radicals) break down organic compounds into volatile by-products (CO, CO_2, H_2O) which are pumped away.

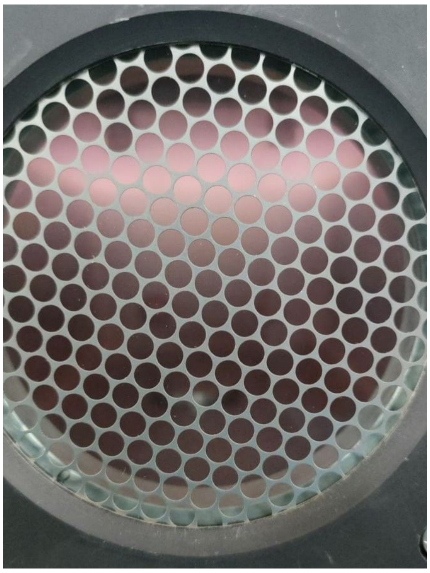

Fig. B.4 O_2 plasma in the plasma matrix showing its typical white-grey color. The sample is at the bottom.

The Plasma Matrix system controls gas flow, RF power, pressure, and time. The procedure includes:

- **Purge:** N_2 line purge for 5 minutes (no RF).
- **Pre-etching:** O_2 plasma ignition to clean the chamber. Matching network tuning minimizes reflected RF power and maximizes DC bias for stability.
- **Cleaning:** Sample loaded and exposed to plasma for 80 s at 40 W.

This ensures consistent cleaning without degrading the photoresist pattern, crucial for interface quality.

B.1.3 Ion Milling (Sputter Etching)

Ion milling (sputter etching) is a physical dry etching technique using focused inert gas ions (Ar^+) to remove material. It is used here for thin film cleaning. Ions accelerated by an electric field impinge on the surface, physically sputtering atoms. The sputtering yield Y approximates to:

$$Y \propto \frac{E}{U_s}, \tag{B.1}$$

where E is ion energy and U_s is surface binding energy. Ion milling is highly anisotropic, enabling vertical etching. It cleans contact areas and removes native oxides (e.g., on Ti, Nb, Al) before top electrode deposition or cleans the SiN_x surface. Parameters are optimized to avoid damage. Etching is performed from bottom to top to prevent redeposition.

B.1.4 Thermal Evaporation Methods

E-beam evaporation is used for superconducting films, optical coatings, and microelectronic devices [103]. A high-energy electron beam heats and evaporates the target material. It is ideal for refractory metals (Ti, W, Mo) and dielectrics. High kinetic energy of evaporated species ensures dense, adherent films.

The process operates under HV/UHV. The beam, generated by a thermionic emitter and steered by magnetic fields, focuses on the target. Evaporated atoms travel ballistically to the substrate. The deposition rate R is estimated by the Hertz-Knudsen equation:

$$R = \frac{\alpha P_{\mathrm{sat}}}{\sqrt{2\pi m k_B T}}, \tag{B.2}$$

where α is sticking coefficient, P_{sat} vapor pressure, T temperature, and m atomic mass. E-beam allows rapid, high-purity growth with fine rate control via beam power.

The effusion cell (Fig. B.5) is used for gold in UHV ($< 10^{-9}$ mbar). It consists of a crucible heated by a resistive filament. Gold atoms evaporate thermally and form a molecular beam. The rate is controlled by temperature (PID). We use ~ 0.7 /s.

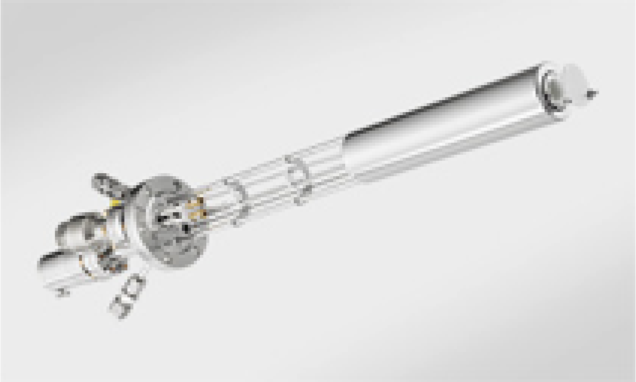

Fig. B.5 Effusion cell for gold evaporation, comprising a crucible inside a metallic tube, resistive heater, thermal shielding, water cooling, and PID control. The chimney defines the beam direction.

The effusion cell with a chimney provides a smooth, uniform coating. Thermal evaporation follows a modified Knudsen's cosine law:

$$I(\theta) = I_0(\cos\theta)^n, \tag{B.3}$$

where $I(\theta)$ is the flux at angle θ. The chimney collimates the flux, improving uniformity but reducing rate. The uniformity cone is defined by:

$$\frac{\Delta t}{t_0} \approx 1 - \cos^n(\theta_{max}), \tag{B.4}$$

where t_0 is central thickness and θ_{max} is the maximum emission angle. In our UHV evaporator, the source-to-substrate distance is $d = 22$ cm, ensuring 96% uniformity for 1-inch samples (Fig. B.6).

B.2 Elements of ellipsometry

B.2.1 Ellipsometer

Ellipsometry determines the complex refractive index and thickness of thin films by measuring the change in polarization state (Ψ, Δ) of reflected light. The ratio of

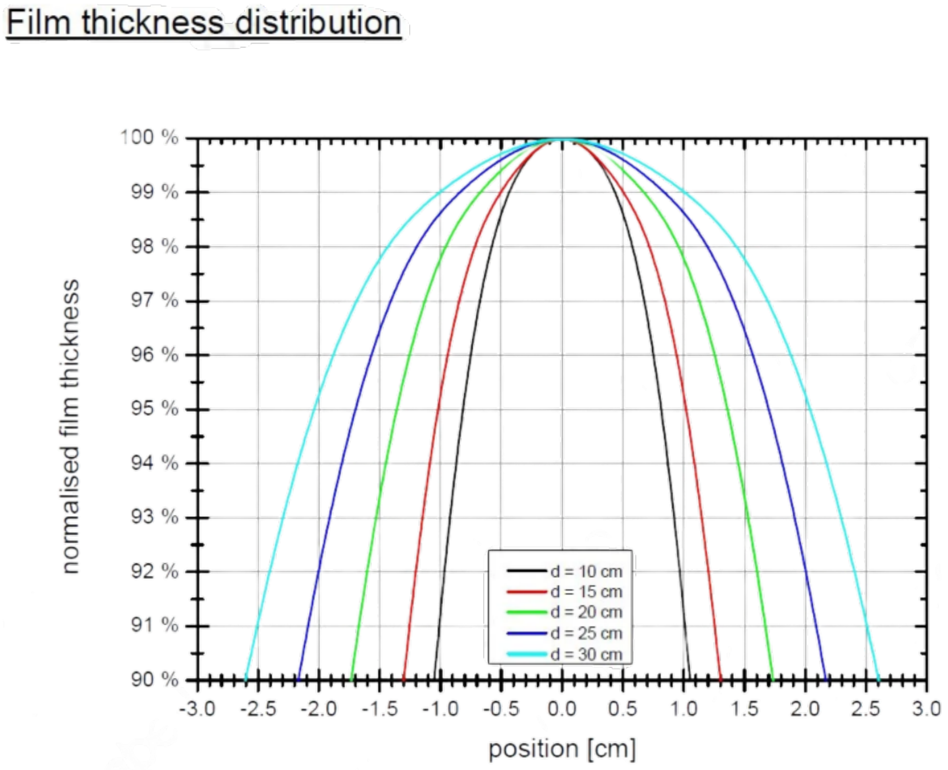

Fig. B.6 Film thickness distribution profiles for Au deposition using the evaporation chimney. Curves show normalized thickness vs. lateral position for different distances d. For our system ($d = 22\,\mathrm{cm}$), uniformity is $\sim 96\%$ for 1-inch samples.

reflection coefficients for p- and s-polarization is:

$$\frac{r_p}{r_s} = \tan(\Psi)e^{i\Delta}. \tag{B.5}$$

Fresnel equations describe reflection and transmission (Fig. B.7) based on refractive indices n_1, n_2 and angles θ_i, θ_t (Snell's Law: $n_1 \sin\theta_i = n_2 \sin\theta_t$).

For s-polarized light:

$$r_s = \frac{n_1\cos\theta_i - n_2\cos\theta_t}{n_1\cos\theta_i + n_2\cos\theta_t}, \quad t_s = \frac{2n_1\cos\theta_i}{n_1\cos\theta_i + n_2\cos\theta_t}. \tag{B.6}$$

For p-polarized light:

$$r_p = \frac{n_2\cos\theta_i - n_1\cos\theta_t}{n_2\cos\theta_i + n_1\cos\theta_t}, \quad t_p = \frac{2n_1\cos\theta_i}{n_2\cos\theta_i + n_1\cos\theta_t}. \tag{B.7}$$

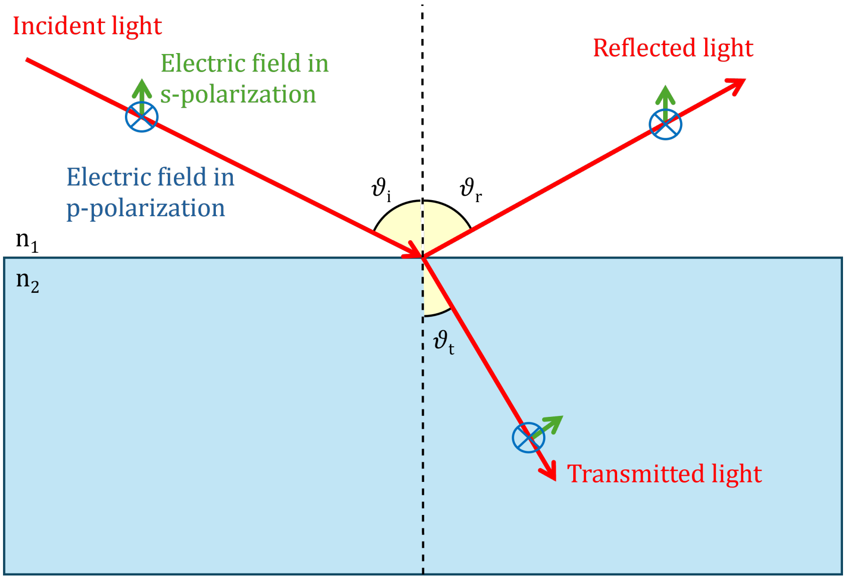

Fig. B.7 Reflection and transmission of light at an interface. Incident θ_i, reflected θ_r, and transmitted θ_t angles follow Snell's Law.

For absorbing materials, $\tilde{n} = n + ik$. By measuring Ψ and Δ versus wavelength $(200-1700\,\text{nm})$ and angle $(20^\circ - 80^\circ)$, we extract n, k and thickness.

B.2.2 Experimental Procedure

A J.A. Woollam V-VASE ellipsometer was used.

1. **Lamp ignition:** Xe lamp activated 1 hour prior for stabilization.
2. **Calibration:** Performed using a standard Silicon substrate. The sample is aligned in the xy plane and centered along z to maximize signal. System calibration records intensity and gain.
3. **Sample Positioning:** Sample positioned and alignment verified (Fig. B.8).
4. **Data Acquisition:** Reflectance (R_s, R_p) or ellipsometric data acquired for plasmonic gratings (Sec. 6.5) or AR coatings/TiAu bilayers (Sec. 6.4).

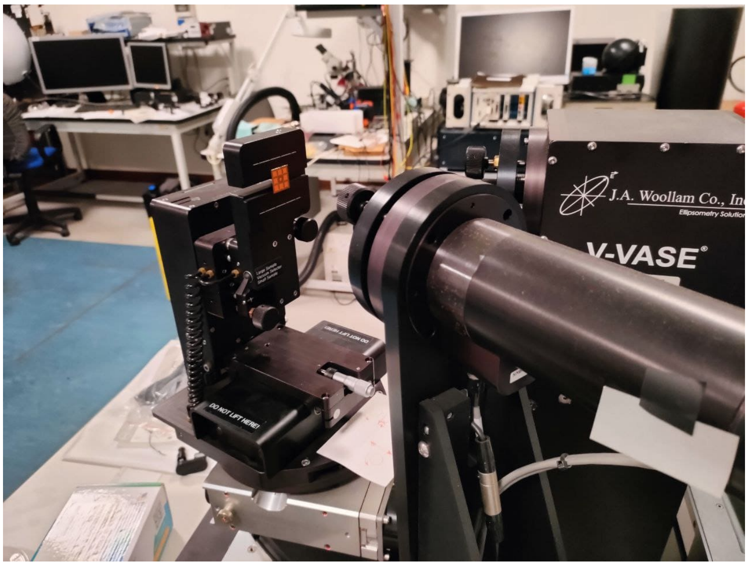

Fig. B.8 Ellipsometer measurement of a sample with Si/SiNx substrate, TiAu bilayers, and gold gratings.

B.3 Elements of cryogenics

B.3.1 Adiabatic Demagnetization Refrigerator Cryostat

The fundamental instrument for characterization is the cryostat. The cryostat used is an "Adiabatic Demagnetization Refrigerator" (ADR). The ADR in the INRiM laboratory for TES measurements and its schematic are shown in Fig. B.9. Thermal insulation from the external environment is achieved through thermal shields and vacuum isolation. The basic mechanism follows the principle of Dewar flasks: through vacuum, there is no heat transfer by convection or conduction, only by radiation. The latter process is minimized using reflective shields. The vacuum is achieved using a turbo-molecular pump and a dry pre-vacuum mechanical pump.

The ADR system at INRiM cools down to approximately 3 K using a pulse-tube cryocooler, illustrated in Fig. B.10. The compressor piston moves periodically, increasing and decreasing the pressure in the tube. The initial temperature inside the cryostat is ambient temperature T_H. As shown in the figure, when the piston moves to the right, gas is pushed towards the regenerator.

The regenerator is made of a material with high heat capacity but low thermal conductivity along the gas flow direction. It retains the heat from the gas it contacts,

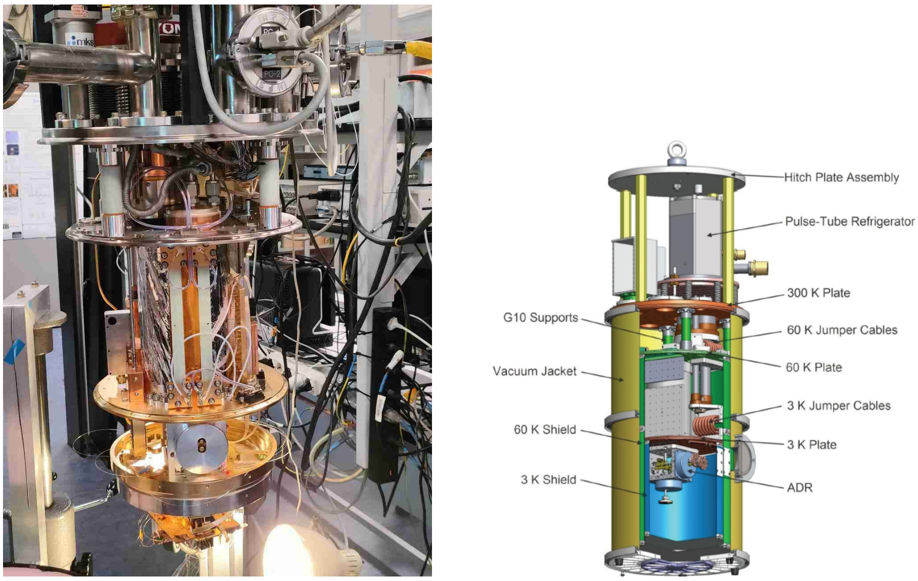

(a) Overall view of the ADR cryostat.

(b) Schematic of the ADR cryostat.

Fig. B.9 ADR Cryostat and its schematic.

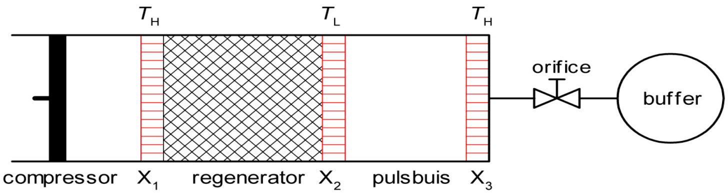

Fig. B.10 The pulse-tube cryocooler consists of: a compressor for the ambient temperature T_H, heat exchangers X_1, X_2, X_3, a regenerator, a pulse tube operating at low temperatures T_L, a flow resistance, and a buffer volume.

so the gas entering at temperature T_H exits at a lower temperature T_L. The gas then leaves the heat exchanger at T_L and enters the high-pressure adiabatic region of the tube. In this region, temperature variations are solely linked to pressure changes. The same gas returns due to the pressure drop induced by the piston.

Simultaneously, gas from a buffer volume enters the same adiabatic tube region at T_H under low pressure and exits at a higher temperature under high pressure. Since the gas from the buffer volume exits at a higher temperature, the gas from the compressor exits at a lower temperature.

The cryostat consists of three temperature stages: 300 K, 60 K, and 3 K. Instrumentation cables pass through these stages to the sample holder platform.

The ADR device contains a superconducting magnet coil through which current i flows. The coil generates a magnetic field on paramagnetic salts when current is applied. The paramagnetic salts used are "gadolinium gallium garnet" (GGG) and "ferric ammonium alum" (FAA). When subjected to specific magnetothermal cycles, these salts exchange their thermal and magnetic entropy, cooling the surrounding environment. To perform the correct magnetization cycle enabling this cooling effect, a cold source must be connectable and disconnectable to the salts via a thermal switch. Finally, these salts are in contact with the sample platform via a "cold finger." The minimum achievable temperature is approximately 28 mK. Here, the TESs are located with the terminal of the fiber, Fig. B.11.

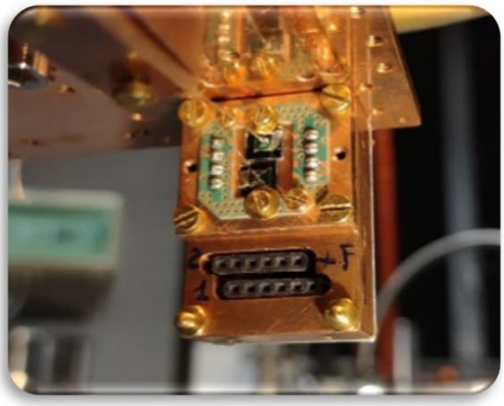

Fig. B.11 Sample mounting stage with TES and optical fiber.

The thermal cycle of the salts is illustrated in Fig. B.12, using normalized entropy S as a function of temperature and where R is the universal gas constant. The process is controlled by adjusting the current and thermal switches.

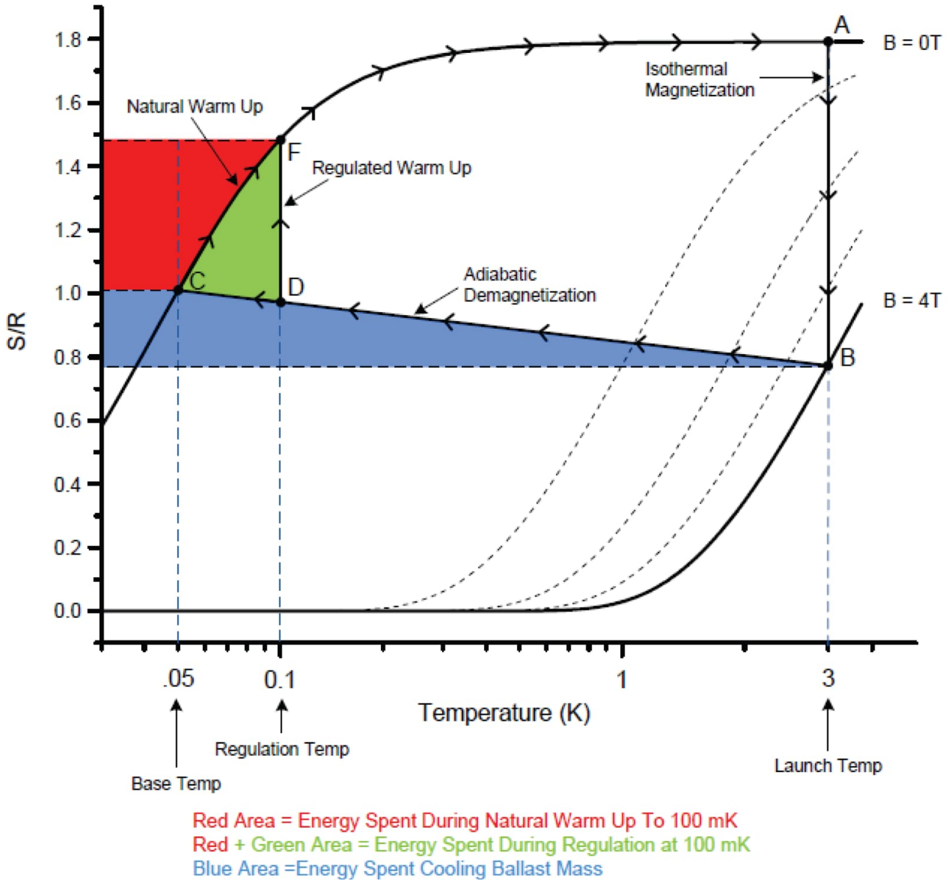

Fig. B.12 Magnetization cycle of paramagnetic salts.

Initially, at state A, the salts are at approximately 3 K with zero magnetic field ($B = 0\ T$), zero current ($i = 0$ A), and the thermal switch closed, connecting the cold source and salts.

Increasing the coil current raises the magnetic field on the salts, leading to isothermal magnetization. At point A, the thermal entropy remains unchanged, as the salts are in thermal equilibrium with the source. However, the magnetic field aligns atomic spins, reducing magnetic entropy until reaching state B. This state is characterized by maximum magnetic field, unchanged temperature from A, maximum coil current, and a closed switch.

After stabilizing for a few dozen minutes to reach thermal equilibrium, the switch is opened, disconnecting the source from the salts, making them adiabatic. The current and thus the magnetic field are then reduced, causing adiabatic demagnetization. Consequently, atomic spins regain random orientation at the expense of thermal energy, reaching point C, characterized by the minimum temperature ($T \approx 28$ mK in this case), with zero current and field, and an open switch.

Over time, the salts experience heating due to entropy redistribution, requiring cycle repetition. If maintaining the minimum temperature is unnecessary, the system can be stabilized at a higher temperature. An adiabatic demagnetization from point D to F conserves energy and preserves the salts' cooling power.

B.3.2 Four-Wire Measurement Technique

To accurately measure the superconducting transition, the four-wire sensing technique is employed. This method is essential for precisely measuring small resistance values, as it eliminates the influence of lead and contact resistances, which can otherwise introduce significant errors, especially when measuring superconducting samples.

The four-wire technique, illustrated in Fig. B.13, utilizes four contacts on the sample. Two contacts are dedicated to injecting the current, while the other two measure the resulting voltage drop across the sample. This separation between the current supply and voltage measurement ensures that the measured voltage is not affected by the resistance of the wires and contacts.

Denoting the resistance values of the voltmeter, wires, contacts, and the superconducting sample as R_V, R_f, R_c, and R_s, respectively, the currents flowing in the circuit are i through wires 1 and 4, i_V through wires 2 and 3, and i_s through R_s. Assuming that the wire resistances are equal and that the contact resistances are also equal, the voltage drops across the sample can be represented as:

$$i = i_V + i_s, \quad V_{2,3} = i_s R_s = i_V(2R_c + 2R_f + R_V). \tag{B.8}$$

Thus, the voltage measured by the voltmeter is:

$$V = i_V R_V = V_{2,3} - i_V(2R_c + 2R_f). \tag{B.9}$$

If the condition $R_V \gg R_s, R_c, R_f$ holds, we can approximate:

$$i_V = \frac{i_s R_s}{R_V}. \tag{B.10}$$

From this, the measured resistance is given by:

$$R_{\text{measured}} = \frac{V}{i} = \left[1 - \frac{2(R_c + R_f)}{R_V}\right]\left(\frac{1}{R_s} + \frac{1}{R_V}\right)^{-1} \approx R_s. \tag{B.11}$$

This technique enables the measurement of extremely small resistance values, even approaching zero, since the resistance of the measuring instrument is significantly larger than other resistances present in the system. In particular, it is invaluable for studying the superconducting transition, where resistance rapidly drops to zero as the sample enters the superconducting state.

By employing this four-wire technique, the resistance of the superconducting sample is measured as a function of temperature to identify its T_c. As the temperature decreases and approaches T_c, the resistance of the sample drops sharply, ultimately reaching a negligible value in the fully superconducting state.

In practical measurements, a small alternating current (AC) is injected into the sample in order to avoid thermoelectric forces that arise due to the temperature variations occurring in the measurement circuit. The resulting voltage is measured using a high-impedance voltmeter to ensure that all injected current flows through the sample.

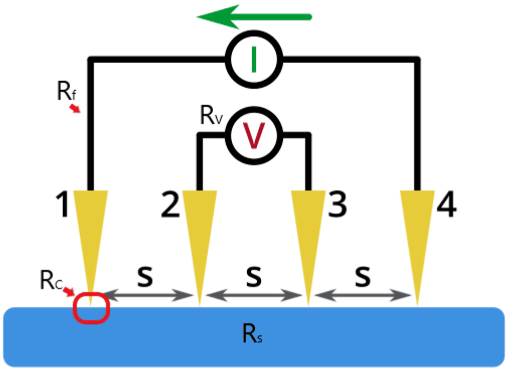

Fig. B.13 Four-terminal resistance measurement schematic. Two contacts are used to inject current, while voltage measurements are taken using two separate contacts, preventing the influence of wire and contact resistances.

This technique, combined with precise temperature control and shielding from electromagnetic interference, provides a reliable means to investigate the superconducting transition and characterize the electrical properties of the material under study.